# Inclusion of nuclear quantum effects in thermal conductivity prediction from path integral techniques




Benjamin Sutherland

Brasenose College

University of Oxford

A thesis submitted for the degree of

*Doctor of Philosophy*

Michaelmas 2022

# Inclusion of nuclear quantum effects in thermal conductivity prediction from path integral techniques

Benjamin Sutherland

Brasenose College
University of Oxford

*A thesis submitted for the degree of Doctor of Philosophy*

Michaelmas 2022

## Abstract

Path integral based methods to approximately include quantum mechanical effects in the motion of nuclei have thus far appeared insufficient to describe the thermal conductivity of a system from the Green-Kubo relation. In this thesis the possible reasons for this are examined, and an approach to improve the estimation of the thermal conductivity using path integral methods is developed.

The thesis begins by considering how the thermal diffusivity, the ratio of the thermal conductivity and the heat capacity, may be related to the equilibrium density fluctuations within a liquid, using the theory of linearised hydrodynamics. Application of this to liquid parahydrogen using centroid molecular dynamics (CMD) showed that the CMD estimate of the thermal diffusivity is accurate, but that the CMD estimate of the heat capacity is not. This is used to propose a means to correct the CMD estimate of the Green-Kubo thermal conductivity, allowing for an efficient and accurate determination of the thermal conductivity in both liquid parahydrogen and normal liquid helium.

Following this, the same methodology is applied to the calculation of the CMD thermal conductivity in liquid water. The agreement with experiment is found to be less convincing, which may partly be due to the use of an inaccurate potential model.

The thesis finishes by showing that the thermal conductivity may be determined from the equilibrium density fluctuations at temperatures above 30 K for crystalline Lennard-Jones argon in the classical limit. At lower temperatures, the fraction of the signal dependent on the thermal conductivity is found to become very small, but it is shown in this case that the equilibrium local temperature fluctuations may be used instead. However, extension of this to an accurate path integral based method for quantum mechanical thermal conductivity prediction in a crystalline solid appears to be a very challenging problem that is beyond the scope of this thesis.

# Acknowledgements

To begin I would like to express my deepest gratitude to my supervisor, David Manolopoulos, for his enduring support and insights over the past four years. Particularly helpful was the manner in which he adjusted to the changes in working we have experienced over the past couple of years - he really made the effort to make what was a very difficult time easier than it otherwise would have been.

I would also like to thank Mariana Rossi and the Max-Planck Institute for the opportunity to spend two months working in Berlin towards the beginning of my DPhil. Although the project which we were working on at the time did not end up making it into this thesis directly, the insights gained were (after a few unsuccessful diversions) instrumental in motivating the work which is contained here.

My thanks also go out to all members of the Manolopoulos group for many helpful discussions, both scientific and otherwise. Particular thanks go to Joe, for his knowledge and experience which proved invaluable in helping me solve some of the problems encountered during my DPhil, and for his work on the centroid potentials of mean force of liquid water which enabled us to perform some of the calculations in this thesis.

Thanks should also go to EPSRC for their funding support as well as to the TMCS CDT.

Finally, I would like to thank my friends and family. Although I know at times it can be difficult for me to show it, their support means the world to me and I would not have made it here without them.

# List of publications

## The following publication is directly related to the work within this thesis

*Nuclear quantum effects in thermal conductivity from centroid molecular dynamics*, B. J. Sutherland, W. H. D. Moore and D. E. Manolopoulos, J. Chem. Phys., **154**, 174104 (2021)

# Declaration of authorship

This thesis is entirely the result of my own work except where otherwise indicated in the text. In particular, some of the results contained within Chapters 4 and 5 of this thesis were obtained in collaboration with other researchers, and where this is relevant this will be clearly indicated in the text.

# Contents


**1 Introduction** **1**

**2 Nuclear quantum effects in molecular dynamics simulations** **4**
2.1 Path Integral Molecular Dynamics . . . . . 5
2.1.1 Algorithms for PIMD . . . . . 9
2.2 Centroid Molecular Dynamics . . . . . 13
2.3 Ring Polymer Molecular Dynamics . . . . . 17

**3 Classical methods for thermal conductivity** **19**
3.1 Introduction . . . . . 19
3.2 The Linearised Hydrodynamic Equations . . . . . 22
3.3 The Green-Kubo relation . . . . . 29
3.3.1 Formulation of the heat flux vector . . . . . 35
3.3.2 Applying the Green-Kubo relation in practice and other methods for thermal conductivity . . . . . 38
3.3.3 Quantum generalisations of the Green-Kubo method . . . . 40
3.4 Thermal conductivity from density fluctuations . . . . . 43
3.4.1 Thermal conductivity from local temperature fluctuations . 50

**4 Thermal conductivity of quantum liquids** **53**
4.1 Introduction . . . . . 53
4.2 Silvera-Goldman parahydrogen . . . . . 54
4.2.1 The CMD potential of mean force . . . . . 55
4.2.2 Equilibrium density fluctuations . . . . . 67
4.2.3 Returning to the Green-Kubo relation . . . . . 77
4.3 Normal liquid helium . . . . . 82

**5 Thermal conductivity of liquid water** **89**
5.1 Introduction . . . . . 89
5.2 The q-TIP4P/F model . . . . . 92
5.3 Quantum mechanical heat capacities . . . . . 95
5.4 Centroid potentials of mean force . . . . . 98
5.5 Green-Kubo thermal conductivity . . . . . 104

**6 Thermal conductivity of classical solids** **120**
6.1 Introduction . . . . . 120
6.2 Hydrodynamic theory of solids . . . . . 121
6.3 Application to Lennard-Jones argon . . . . . 129

6.3.1 Thermal conductivity from the Green-Kubo relation . . . . . 130
6.3.2 Equilibrium density fluctuations . . . . . 134
6.4 Temperature fluctuations . . . . . 144

**7 Conclusions** **154**

**Bibliography** **159**

# 1 Introduction

Heat transport is often one of the foremost considerations when determining the optimal materials to be used in the development of new components and devices.[1] As electronic components become increasingly smaller, effective management of the heat which is generated by them, either by insulation or by conduction, has become more and more important.[2–4] Due to this, it is especially desirable to be able to predict and understand the heat transfer properties of a substance using computer simulations. The transport coefficient associated with heat transfer, the thermal conductivity, has however proved particularly difficult to calculate, even with classical simulations.[5; 6]

Thermal transport in insulators is dominated by the motion of the atomic nuclei. A complete description of the mechanisms of heat transfer in insulators therefore requires the consideration of nuclear quantum effects in the dynamics. Although for many applications these nuclear quantum effects will prove not to play a significant role in the thermal conductivity of the material, there do exist situations where the nuclear quantum effects on the thermal conductivity are far from negligible. This is particularly apparent in the experimentally observed peak in the temperature dependence of the thermal conductivity at low temperatures, which arises from the diminishing quantum mechanical heat capacity.[7; 8] In addition, nuclear quantum effects are believed to be important, even at ambient temperatures, in substances like

silicon.[9] Further, the temperature dependent behaviour of the thermal conductivity of water and that of heavy water is qualitatively different,[10] likely due to the fact that nuclear quantum effects are greater in water than they are in heavy water.[11]

Approximate path integral based approaches, such as centroid molecular dynamics (CMD)[12–17] and ring polymer molecular dynamics (RPMD),[18] have been remarkably successful in including nuclear quantum effects in many dynamical properties such as the diffusion constant.[19–23] Unfortunately, attempts to use these methods to incorporate nuclear quantum effects into the thermal conductivity prediction have on the whole not been as fruitful,[19; 24; 25] likely due to the increased complexities in the operators involved in its calculation.[19] Whilst nuclear quantum effects may be included in the special case of crystalline solids when anharmonic effects are small through the use of the anharmonic lattice dynamics method,[26; 27] we are not aware of any approach which is capable of capturing the nuclear quantum effects within strongly anharmonic systems or within disordered media such as liquids or glasses. Evidently there are still significant gaps in our understanding of how quantum mechanical effects within the nuclear motion affect the theoretical prediction of the thermal conductivity. The ability to accurately predict these effects would be desirable for obtaining the heat management properties required for devices which need to operate in low temperature regimes where these nuclear quantum effects would be expected to be important, with superconductors being a notable example.[28] Therefore, in this thesis we aim to investigate whether it is possible to use path integral based approaches to successfully include nuclear quantum effects in the prediction of the thermal conductivity, focussing primarily on the liquid phase.

This thesis will be structured as follows. In Chapter 2 we briefly introduce some of the background theory necessary to understand how nuclear quantum effects are incorporated into molecular dynamics simulations through the use of path integrals. In Chapter 3 we present the classical theory of linearised hydrodynamics within the liquid phase, which may be used to relate the thermal conductivity to the equilibrium fluctuations of the local density and the local temperature. We

then apply this theory to calculate the quantum mechanical thermal diffusivity from the equilibrium density fluctuations in liquid parahydrogen in conjunction with CMD in Chapter 4, finding excellent agreement with experiment. This is used to motivate a scheme for correcting the CMD thermal conductivities found from the generalisation of the classical Green-Kubo method, which were previously found to be inaccurate. With this we are able to efficiently and accurately describe the thermal conductivity of liquid parahydrogen and liquid helium using CMD. Following this, in Chapter 5 we apply this approach to the more challenging example of liquid water. In Chapter 6 we show how the thermal conductivity can be determined in classical crystalline solids from the equilibrium local density and the local temperature fluctuations. The thermal conductivities obtained from these fluctuations are shown to agree reasonably well with those obtained from the classical Green-Kubo method. Finally, we provide some concluding remarks and avenues for future investigation in Chapter 7.

# 2

# Nuclear quantum effects in molecular dynamics simulations

The success of the classical molecular dynamics technique,[29; 30] based on generating nuclear trajectories by integration of Newton's equations of motion, as a sampling tool for prediction of physical processes cannot be overstated. However, despite the wide range of applicability, there exist many situations where a simple classical treatment of the nuclear motion is insufficient to describe the system accurately. Obvious examples of this include systems consisting of light nuclei at low temperatures - such as liquid parahydrogen and liquid helium.[22; 31] In addition, nuclear quantum effects persist up to ambient temperatures in systems where motion of light nuclei is important in characterising the interactions adequately (hydrogen bonding in liquid water,[32; 33] for example).

In this Chapter, we will present a means by which quantum mechanical effects in the nuclear motion may be included in simulations by utilising the path integral formulation of quantum mechanics proposed by Feynman.[34] We will show how the quantum mechanical partition function is isomorphic to a classical partition function in an extended phase space, allowing for extension of classical molecular dynamics to path integral molecular dynamics (PIMD),[35] and discuss how this may be used to compute quantum mechanical ensemble averages of static properties

exactly. After this, we will also introduce two approximate methods which make use of this idea for the calculation of quantum mechanical dynamical properties. The first of these being centroid molecular dynamics (CMD), which we will use extensively throughout this thesis, and the second being a brief discussion of the closely related ring polymer molecular dynamics (RPMD).

## 2.1 Path Integral Molecular Dynamics

The crucial step in constructing Feynman's aforementioned classical isomorphism for the quantum mechanical partition function

$$\mathcal{Z} = \mathrm{Tr}\left[e^{-\beta\hat{H}}\right] = \int d\mathbf{x}\, \langle \mathbf{x}|e^{-\beta\hat{H}}|\mathbf{x}\rangle\,, \tag{2.1}$$

with a set of positions $\mathbf{x}$, the inverse temperature $\beta = \frac{1}{k_B T}$, and Hamiltonian $\hat{H} = \hat{T} + \hat{V}(\mathbf{x})$, where $\hat{T}$ and $\hat{V}(\mathbf{x})$ being the kinetic and potential energy operators, respectively, is to utilise the identity

$$e^{-\beta\hat{H}} = \left(e^{-\beta_P\hat{H}}\right)^P, \tag{2.2}$$

with $P$ being a positive integer and $\beta_P = \frac{\beta}{P}$.

We can then make use of an approximation to factor the exponential into kinetic and potential components. One simple way to do this is to use the symmetric Trotter splitting[36; 37]

$$e^{-\beta_P\hat{H}} = e^{-\frac{1}{2}\beta_P\hat{V}}e^{-\beta_P\hat{T}}e^{-\frac{1}{2}\beta_P\hat{V}} + \mathcal{O}\left(\beta_P^3\right), \tag{2.3}$$

where an error term of $\mathcal{O}(\beta_P^3)$ must be added since, in general, the quantum mechanic kinetic energy and potential operators, $\hat{T}$ and $\hat{V}$ respectively, do not commute. With this, Eq. 2.1 becomes

$$\mathcal{Z} = \mathrm{Tr}\left[\left(e^{-\frac{1}{2}\beta_P\hat{V}}e^{-\beta_P\hat{T}}e^{-\frac{1}{2}\beta_P\hat{V}}\right)^P\right] + \mathcal{O}\left(\beta_P^2\right), \tag{2.4}$$

where the associated error term vanishes as $1/P^2$ in the limit of large $P$. By inserting a set of $P-1$ identity operators of the form

$$\hat{1} = \int d\mathbf{x}^{(i)}\, |\mathbf{x}^{(i)}\rangle\, \langle \mathbf{x}^{(i)}|\,, \tag{2.5}$$

between each of the $P$ products inside of the trace we can then reexpress this as, relabelling $\mathbf{x} \equiv \mathbf{x}^{(0)}$,

$$\mathcal{Z} \approx \int d\mathbf{x}^{(0)} \dots d\mathbf{x}^{(P-1)} \prod_{i=0}^{P-1} \langle \mathbf{x}^{(i)} | e^{-\frac{1}{2}\beta_P \hat{V}} e^{-\beta_P \hat{T}} e^{-\frac{1}{2}\beta_P \hat{V}} | \mathbf{x}^{(i+1)} \rangle \,, \tag{2.6}$$

where $\mathbf{x}^{(i)} = \left(x_1^{(i)}, x_2^{(i)}, \dots, x_{3N}^{(i)}\right)$, and $N$ is the number of particles in the system. The notation $\int d\mathbf{x}^{(0)} \dots d\mathbf{x}^{(P-1)}$ is understood to mean an integral over all possible values of each of the $3NP$ coordinates within $\mathbf{x}^{(0)}$ to $\mathbf{x}^{(P-1)}$ and we have also adopted the cyclic convention that $\mathbf{x}^{(P)} \equiv \mathbf{x}^{(0)}$. In this thesis we will always adopt the notation of using superscript indices to differentiate between the different coordinate sets, or "replicas", introduced here, and subscript indices to label the different degrees of freedom within each replica.

We then have to evaluate a set of $P-1$ terms of the form $\langle \mathbf{x}^{(j)} | e^{-\frac{1}{2}\beta_P \hat{V}} e^{-\beta_P \hat{T}} e^{-\frac{1}{2}\beta_P \hat{V}} | \mathbf{x}^{(j+1)} \rangle$, with $j \in [0, P-1]$. It is easy to show that

$$\langle \mathbf{x}^{(j)} | e^{-\frac{1}{2}\beta_P \hat{V}} e^{-\beta_P \hat{T}} e^{-\frac{1}{2}\beta_P \hat{V}} | \mathbf{x}^{(j+1)} \rangle = e^{-\frac{1}{2}\beta_P \left[ V\left(\mathbf{x}^{(j)}\right) + V\left(\mathbf{x}^{(j+1)}\right) \right]} \langle \mathbf{x}^{(j)} | e^{-\beta_P \hat{T}} | \mathbf{x}^{(j+1)} \rangle \,. \tag{2.7}$$

We can split up the remaining integral into a product of integrals in each degree of freedom, as $\langle \mathbf{x}^{(j)} | e^{-\beta_P \hat{T}} | \mathbf{x}^{(j+1)} \rangle = \prod_{i=1}^{3N} \langle x_i^{(j)} | e^{-\beta_P \hat{p}_i^2/(2m_i)} | x_i^{(j+1)} \rangle$, where $\hat{p}_i$ and $m_i$ are the momentum operator and the mass associated with the $i^{\text{th}}$ degree of freedom, respectively. We proceed by inserting a complete set of momentum

eigenstates inside each, as follows

$$\begin{aligned}
&\langle \mathbf{x}^{(j)}|e^{-\beta_P \hat{T}}|\mathbf{x}^{(j+1)}\rangle = \prod_{i=1}^{3N}\int dp_i \,\langle x_i^{(j)}|e^{-\beta_P \frac{\hat{p}_i^2}{2m_i}}|p_i\rangle\,\langle p_i|x_i^{(j+1)}\rangle \\
&= \prod_{i=1}^{3N}\int dp_i \,\langle x_i^{(j)}|p_i\rangle\, e^{-\beta_P \frac{p_i^2}{2m_i}}\,\langle p_i|x_i^{(j+1)}\rangle \\
&= \prod_{i=1}^{3N}\int dp_i \frac{1}{2\pi\hbar} e^{-\beta_P \frac{p_i^2}{2m_i}+\frac{ip_i}{\hbar}\left(x_i^{(j)}-x_i^{(j+1)}\right)} \\
&= \frac{1}{(2\pi\hbar)^{3N}}\prod_{i=1}^{3N}\left(\frac{2\pi m_i}{\beta_P}\right)^{\frac{1}{2}} e^{-\frac{1}{2}\beta_P m_i\omega_P^2\left(x_i^{(j+1)}-x_i^{(j)}\right)^2} \\
&= \frac{1}{(2\pi\hbar)^{3N}}\prod_{i=1}^{3N}\left(\frac{m_i}{m_i'}\right)^{\frac{1}{2}}\int dp_i^{(j)}\, e^{-\frac{\beta_P}{2m_i'}\left(p_i^{(j)}\right)^2-\frac{1}{2}\beta_P m_i\omega_P^2\left(x_i^{(j+1)}-x_i^{(j)}\right)^2} \\
&= \frac{\prod_{i=1}^{3N}\left(\frac{m_i}{m_i'}\right)^{\frac{1}{2}}}{(2\pi\hbar)^{3N}}\int d\mathbf{p}^{(j)}\, e^{-\beta_P\sum_{i=1}^{3N}\left[\frac{1}{2m_i'}\left(p_i^{(j)}\right)^2+\frac{1}{2}m_i\omega_P^2\left(x_i^{(j+1)}-x_i^{(j)}\right)^2\right]},
\end{aligned} \tag{2.8}$$

where we have introduced the convenient notation $\omega_P = 1/(\beta_P\hbar)$. We have also made use of the fact that when reintroducing the integral over momenta we are under no obligation to use the same mass as the physical particle mass, $m_i$. In fact, in some of the techniques we will introduce later in this Chapter, it will be advantageous for us to be able to use a value of the mass associated with the reintroduced momenta, $m_i'$, of our own choosing. Making such a change merely alters the prefactor in front of the partition function, which will cancel out in the computation of observable averages and thus not affect the final result. As such, the momenta introduced here are often referred to as "fictitious momenta".[38] The masses associated with the harmonic spring terms in Eq. 2.8 must remain the physical masses, $m_i$.

Inserting this into our equation for $\mathcal{Z}$, Eq. 2.6, we arrive at the following classical-like expression

$$\mathcal{Z} \approx \frac{\prod_{i=1}^{3N}\left(\frac{m_i}{m_i'}\right)^{\frac{P}{2}}}{(2\pi\hbar)^{3NP}}\int d\mathbf{x}\, d\mathbf{p}\, e^{-\beta_P\mathcal{H}(\mathbf{p},\mathbf{x})}, \tag{2.9}$$

where the "ring polymer Hamiltonian" is

$$\mathcal{H}(\mathbf{p},\mathbf{x}) = \mathcal{H}_P(\mathbf{p},\mathbf{x}) + \sum_{j=0}^{P-1} V\left(\mathbf{x}^{(j)}\right), \tag{2.10}$$

and the "free ring polymer Hamiltonian", $\mathcal{H}_P(\mathbf{p},\mathbf{x})$, is given by

$$\mathcal{H}_P(\mathbf{p},\mathbf{x}) = \sum_{j=0}^{P-1}\sum_{i=1}^{3N}\frac{1}{2m_i'}\left(p_i^{(j)}\right)^2 + \frac{1}{2}m_i\omega_P^2\left(x_i^{(j+1)} - x_i^{(j)}\right)^2, \tag{2.11}$$

and where Eq. 2.9 becomes exact in the $P \to \infty$ limit. This is the discretised form of the Feynman path integral partition function. The connection to "path integrals" becomes more obvious in the continuous form that Feynman originally presented,[34] as

$$\mathcal{Z} = \oint \mathcal{D}\mathbf{x}(\tau)\, e^{-\frac{S[\mathbf{x}(\tau)]}{\hbar}}, \tag{2.12}$$

where $S[q(\tau)]$ is the action functional given by

$$S[\mathbf{x}(\tau)] = \int_0^{\beta\hbar} d\tau \sum_{i=1}^{3N}\frac{m_i}{2}\dot{x}_i^2(\tau) + V(\mathbf{x}(\tau)), \tag{2.13}$$

where the overdot denotes a time derivative and the notation $\oint \mathcal{D}\mathbf{x}(\tau)$ denotes a path integral over all possible closed paths $x(\tau)$. We will not present a full derivation of the continuous form here, and instead just note that the two forms are equivalent in the $P \to \infty$ limit. The discrete form is the version which is more directly connected to the algorithms used to perform PIMD in practice, and so this notation will be favoured for this thesis. However, in providing the theoretical basis behind the centroid molecular dynamics method, to be presented in the following Section, the continuous form will prove particularly useful.

In undertaking this procedure, we have expressed the quantum-mechanical partition function in a form resembling a classical partition function, albeit with a Hamiltonian in an extended phase space of a set of $P$ replicas or "beads" denoted by the index $j$, and with neighbouring replicas connected by harmonic springs of frequency $\omega_P$. Since the beads are connected in a cyclic fashion (i.e. that $\mathbf{x}_{P+1} = \mathbf{x}_1$), the partition function resembles that of a classical ring polymer in this extended phase space.[39] PIMD takes advantage of this isomorphism in order to utilise classical molecular dynamics methods within the extended phase space to sample the quantum mechanical statistics.

### 2.1.1 Algorithms for PIMD

In order to evolve the trajectories generated by the Hamiltonian in Eq. 2.11 via

$$\frac{d\mathbf{p}}{dt} = -\frac{\partial \mathcal{H}\left(\mathbf{p},\mathbf{x}\right)}{\partial \mathbf{x}}, \tag{2.14}$$

and

$$\frac{d\mathbf{x}}{dt} = \frac{\partial \mathcal{H}\left(\mathbf{p},\mathbf{x}\right)}{\partial \mathbf{p}}, \tag{2.15}$$

it will be helpful to perform a coordinate transformation from the bead representation to the normal mode representation of the ring polymer, in which the harmonic spring terms between neighbouring beads naturally become decoupled. This can be accomplished using the transformation matrix

$$C_{jk} = \begin{cases} \frac{1}{\sqrt{P}} & k = 0 \\ \sqrt{\frac{2}{P}}\cos\left(\frac{2\pi jk}{P}\right) & 1 \leq k \leq \frac{P}{2} - 1 \\ (-1)^j \frac{1}{\sqrt{P}} & k = \frac{P}{2} \\ \sqrt{\frac{2}{P}}\sin\left(\frac{2\pi jk}{P}\right) & \frac{P}{2} + 1 \leq k \leq P - 1, \end{cases} \tag{2.16}$$

if $P$ is even. This transformation may be accomplished efficiently by using the Fast Fourier Transform (FFT) technique available in most mainstream programming languages. The FFT is normally most efficient if the length of the array to be transformed (in this case, $P$) factors into only the product of small primes, and so it is typical to choose a value of $P = 2^n$, where $n$ is a positive integer. For this reason, whilst it is not difficult to use a version of the transformation matrix in Eq. 2.16 applicable to odd $P$, we will not do so here. Using this transformation, the normal mode momenta, $\tilde{\mathbf{p}}^{(k)}$, and positions, $\tilde{\mathbf{x}}^{(k)}$ are given by

$$\tilde{p}_i^{(k)} = \sum_{j=0}^{P-1} p_i^{(j)} C_{jk} \quad \text{and} \quad \tilde{x}_i^{(k)} = \sum_{j=0}^{P-1} x_i^{(j)} C_{jk}. \tag{2.17}$$

In the normal mode representation, the free ring polymer Hamiltonian of Eq. 2.11 becomes

$$\mathcal{H}_P\left(\mathbf{p},\mathbf{x}\right) = \sum_{k=0}^{P-1}\sum_{i=1}^{3N} \frac{1}{2m_i'}\left(\tilde{p}_i^{(k)}\right)^2 + \frac{1}{2} m_i \omega_k^2 \left(\tilde{x}_i^{(k)}\right)^2, \tag{2.18}$$

with the normal mode frequency $\omega_k = 2\omega_P \sin\left(\frac{k\pi}{P}\right)$. It is also worth emphasising that the $k = 0$ normal mode of the positions is closely associated to the average position, or the centroid, of the beads in each ring polymer,

$$\bar{\mathbf{x}} \equiv \frac{1}{P}\sum_{j=0}^{P-1}\mathbf{x}^{(j)} = \frac{1}{\sqrt{P}}\tilde{\mathbf{x}}^{(0)}, \tag{2.19}$$

with a similar equation holding for the momenta and the centroid momenta. For this reason the $k = 0$ normal mode is referred to as the "centroid mode", and the $k \geq 1$ normal modes as the "internal modes" of the ring polymer.

The advantage of the normal mode transformation is that it is more convenient to propagate the ring polymer part of the total Hamiltonian using these coordinates. It also allows us to apply thermostats to the normal modes directly when simulating in the canonical $NVT$ ensemble. This allows us to attach harsher thermostats to the stiff high-frequency internal modes of the ring polymer to allow for better ergodicity in phase space exploration, whilst attaching a gentler thermostat to the centroid mode.[40]

One way to generate trajectories within PIMD that sample the path integral $NVT$ ensemble is to use a "BAOAB" type splitting of the integrator. Here, "B" refers to evolving the momenta under the forces from the external potential for half a time step,

$$p_i^{(j)}\left(t + \frac{\Delta t}{2}\right) = p_i^{(j)}(t) - \frac{\Delta t}{2}\frac{\partial V\left(\mathbf{x}^{(j)}\right)}{\partial x_i^{(j)}}, \tag{2.20}$$

where the forces are evaluated in the bead representation and "A" refers to an exact free ring polymer evolution for half a time step in the normal mode representation,

$$\begin{pmatrix}\tilde{x}_i^{(k)}\left(t+\frac{\Delta t}{2}\right)\\ \tilde{p}_i^{(k)}\left(t+\frac{\Delta t}{2}\right)\end{pmatrix} = \begin{pmatrix}\cos\left(\frac{\omega_k\Delta t}{2}\right) & \frac{1}{m_i\omega_k}\sin\left(\frac{\omega_k\Delta t}{2}\right)\\ -m_i\omega_k\sin\left(\frac{\omega_k\Delta t}{2}\right) & \cos\left(\frac{\omega_k\Delta t}{2}\right)\end{pmatrix}\begin{pmatrix}\tilde{x}_i^{(k)}(t)\\ \tilde{p}_i^{(k)}(t)\end{pmatrix}, \tag{2.21}$$

where this results in an ordinary velocity Verlet type integration of the centroid mode (for which $\omega_k = 0$). We have also assumed here that the fictitious masses associated with the momenta are taken to be the same as the physical masses for simplicity. The "O" step refers to evolving the momenta under an applicable thermostat for a full time step in order to keep the system in the $NVT$ ensemble.

It was recently discovered that the exact free ring polymer evolution used in Eq. 2.21 is not "strongly stable" in the context of the overall BAOAB scheme and can therefore lead to nonergodicity in phase space exploration for large time steps $\Delta t$. Therefore it is better to use the Cayley transformed propagator proposed by Korol *et al.*[41]. The form of this propagator applicable to the BAOAB splitting (or rather the "BCOCB" splitting if the Cayley propagator is used) can be written as[42]

$$\begin{pmatrix} \tilde{x}_i^{(k)}\left(t+\frac{\Delta t}{2}\right) \\ \tilde{p}_i^{(k)}\left(t+\frac{\Delta t}{2}\right) \end{pmatrix} = \frac{1}{\sqrt{1+\omega_k^2\left(\frac{\Delta t}{2}\right)^2}} \begin{pmatrix} 1 & \frac{\Delta t}{2m_i} \\ -m_i\omega_k^2\frac{\Delta t}{2} & 1 \end{pmatrix} \begin{pmatrix} \tilde{x}_i^{(k)}(t) \\ \tilde{p}_i^{(k)}(t) \end{pmatrix}. \tag{2.22}$$

The BCOCB splitting has been found to give better stability of integration than other schemes and allows for a larger time step to be used.[42] For this reason, we will use the BCOCB scheme in all PIMD simulations performed within this thesis.

For operators which depend solely on position, $\hat{A}(\mathbf{x})$, the corresponding estimator $A_P$ in the PIMD framework may be found by simply taking the average of the observable over the different replicas

$$A_P(\mathbf{x}) = \frac{1}{P}\sum_{i=1}^{P} A\left(\mathbf{x}^{(i)}\right), \tag{2.23}$$

and the ensemble average $\langle A\rangle$ then being given by

$$\langle A\rangle = \lim_{P\to\infty} \frac{\int d\mathbf{x}\, d\mathbf{p}\, e^{-\beta\mathcal{H}(\mathbf{p},\mathbf{x})} A_P(\mathbf{x})}{\int d\mathbf{x}\, d\mathbf{p}\, e^{-\beta\mathcal{H}(\mathbf{p},\mathbf{x})}}, \tag{2.24}$$

with the integral being understood to be over all coordinates in the extended system.

Ensemble averages of operators which have momentum dependence may also typically be calculated within PIMD, although their estimators are often more complex. For example, the kinetic energy is most efficiently computed using the centroid virial estimator[43]

$$T_{CV} = \frac{N}{2\beta} + \frac{1}{2P}\sum_{j=0}^{P-1}\sum_{i=1}^{3N}\left(x_i^{(j)} - \bar{x}_i\right)\frac{\partial V\left(\mathbf{x}^{(j)}\right)}{\partial x_i^{(j)}}. \tag{2.25}$$

Whether a general momentum dependent operator can be calculated efficiently by PIMD will depend on the particular form of the operator in question and the computational feasibility of evaluating the corresponding estimators, with the heat capacity being a more difficult example.[44]

Since one must evaluate the potential and forces within each of the replicas to generate the trajectories required, PIMD is at least $P$ times less efficient than classical molecular dynamics, with $P$ being however many replicas are required to converge the observable of interest to the quantum mechanical result with sufficient accuracy. However, many techniques have been developed to help alleviate this issue. Multiple time-stepping procedures[45; 46] and ring-polymer contraction schemes[47] may be used to minimise the number of times that the forces need to be evaluated, enhanced thermostats[40] can be attached to improve sampling during the simulation and parallelisation of the force evaluation loop across the different replicas may also easily be exploited to decrease the overall simulation time. Another approach to improve efficiency is to use a higher-order splitting of the Boltzmann operator than the Trotter splitting used in Eq. 2.3. These include the Suzuki-Chin[48] and Takahashi-Imada[49] splittings, which both have an associated error of $\mathcal{O}\left(\beta_P^4\right)$ and so would require fewer replicas to be used to converge onto the correct result. Although in principle these require computation of the Hessian as well as the forces to evaluate trajectories, a scheme for evaluating the Hessian terms in PIMD with the Suzuki-Chin splitting using finite difference has been developed which only requires a factor of two more force evaluations than the typical Trotter factorisation[50] - and so this would be desirable when the number of beads required to reach convergence in the Trotter scheme is becoming impractically large.

With these techniques in hand, PIMD now stands as an efficient tool to calculate the quantum ensemble average of static equilibrium properties in condensed phase systems. However, the success of classical molecular dynamics lies not only in the fact that it may be used to determine static properties, but that dynamical information from the trajectories generated may also be used to compute time correlation functions. The classical time correlation function for two observables $A$ and $B$, $C_{AB}\left(t\right)$, is given by

$$C_{AB}\left(t\right) = \left\langle A\left(0\right) B\left(t\right)\right\rangle = \frac{\int d\mathbf{p}\, d\mathbf{x}\, A\left(\mathbf{p}\left(0\right), \mathbf{x}\left(0\right)\right) B\left(\mathbf{p}\left(t\right), \mathbf{x}\left(t\right)\right) e^{-\beta\mathcal{H}}}{\int d\mathbf{p}\, d\mathbf{x}\, e^{-\beta\mathcal{H}}}, \tag{2.26}$$

where $\mathcal{H} = \mathcal{H}\left(\mathbf{p}, \mathbf{x}\right)$ is the classical Hamiltonian.

Many properties of physical interest are related to correlation functions of this form. These include, but are not limited to, transport coefficients which are related to correlation functions via various Green-Kubo relations. For example, the diffusion constant, $D$, is related to the velocity autocorrelation function by

$$D = \frac{1}{3N}\int_0^\infty dt \sum_{i=1}^{N} C_{\mathbf{v}_i\cdot\mathbf{v}_i}(t)\,. \tag{2.27}$$

Therefore, it is desirable for our method for computing quantum observables to also be useful for calculating the corresponding quantum time correlation functions, given in standard form as

$$C_{AB}(t) = \frac{1}{\mathcal{Z}}\mathrm{Tr}\left[e^{-\beta\hat{H}}\hat{A}e^{\frac{i\hat{H}t}{\hbar}}\hat{B}e^{-\frac{i\hat{H}t}{\hbar}}\right], \tag{2.28}$$

where we have used the Heisenberg time evolved form of the operator $\hat{B}(t) = e^{\frac{i\hat{H}t}{\hbar}}\hat{B}e^{-\frac{i\hat{H}t}{\hbar}}$.

However, PIMD cannot be used for this purpose. This is because the fictitious momenta introduced in the partition function of Eq. 2.9 exist only as a tool to explore the correct phase space distribution, and do not necessarily have any bearing on the real dynamics of the system. Nevertheless, various methods have been proposed to extend PIMD to allow for generation of information on the *approximate* quantum dynamics. Of these, the two most prominent are centroid molecular dynamics (CMD),[12–17] to be discussed in the next section, and ring polymer molecular dynamics (RPMD),[18] which will be mentioned briefly afterwards.

## 2.2 Centroid Molecular Dynamics

At the core of CMD are the centroid variables, where the centroid position $\bar{\mathbf{x}}$ of Eq. 2.19 is given in continuous form by

$$\bar{\mathbf{x}} = \frac{1}{\beta\hbar}\int_0^{\beta\hbar} d\tau \mathbf{x}[\tau] \sim \lim_{P\to\infty}\frac{1}{P}\sum_{i=1}^{P}\mathbf{x}_i, \tag{2.29}$$

with a similar expression holding for the centroid momentum, $\bar{\mathbf{p}}$.

To begin our discussion of the theoretical basis of CMD, we present the continuous path-integral quantum partition function of Eq. 2.12 in a slightly different form as

$$\mathcal{Z} = \int d\mathbf{x}_c \oint \mathcal{D}\mathbf{x}\,(\tau)\,\delta\,(\bar{\mathbf{x}} - \mathbf{x}_c)\,e^{-\frac{S[\mathbf{x}(\tau)]}{\hbar}}, \tag{2.30}$$

where the delta function $\delta\,(\bar{\mathbf{x}} - \mathbf{x}_c)$ restricts the path integral to all closed paths with centroid position $\mathbf{x}_c$, and then integration over all $\mathbf{x}_c$ recovers the integral over all possible closed paths. The advantage of expressing the partition function in this form is that one can then introduce a centroid potential $V_c$ such that

$$e^{-\beta V_c(\mathbf{x}_c)} = \left(\frac{2\pi\beta\hbar^2}{m_i}\right)^{\frac{3N}{2}} \oint \mathcal{D}\mathbf{x}\,(\tau)\,\delta\,(\bar{\mathbf{x}} - \mathbf{x}_c)\,e^{-\frac{S[\mathbf{x}(\tau)]}{\hbar}}, \tag{2.31}$$

and so the partition function could be expressed as

$$\mathcal{Z} = \left(\frac{m_i}{2\pi\beta\hbar^2}\right)^{\frac{3N}{2}} \int d\mathbf{x}_c\,e^{-\beta V_c(\mathbf{x}_c)} \tag{2.32}$$

$$= \frac{1}{(2\pi\hbar)^{3N}} \int d\mathbf{p}_c\,d\mathbf{x}_c\,e^{-\beta\left[\sum_{i=1}^{3N}\frac{p_{c,i}^2}{2m_i} + V_c(\mathbf{x}_c)\right]}, \tag{2.33}$$

which is in the form of a classical partition function in the centroid variables $\mathbf{x}_c$ and $\mathbf{p}_c$. This idea has formed the basis of several attempts to define an effective classical potential to incorporate quantum effects by devising approximate forms for the centroid potential - most notably in the Feynman-Hibbs[34] and the Feynman-Kleinert[51] potentials. CMD is a later iteration of this idea, which attempts to calculate the forces associated with the centroid potential exactly. The centroid variables are propagated using the classical equations of motion with forces given by

$$\mathbf{F}_c = -\frac{dV_c\,(\mathbf{x}_c)}{d\mathbf{x}_c}. \tag{2.34}$$

We can evaluate the derivative in the expression above by differentiating both sides of Eq. 2.31 with respect to $\mathbf{x}_c$ and rearranging to give

$$\frac{dV_c\,(\mathbf{x}_c)}{d\mathbf{x}_c} = \frac{1}{\beta\hbar}\frac{\oint \mathcal{D}\mathbf{x}\,(\tau)\,\delta\,(\bar{\mathbf{x}} - \mathbf{x}_c)\,e^{-\frac{S[\mathbf{x}(\tau)]}{\hbar}}\frac{\partial S[\mathbf{x}(\tau)]}{\partial\bar{\mathbf{x}}}}{\oint \mathcal{D}\mathbf{x}\,(\tau)\,\delta\,(\bar{\mathbf{x}} - \mathbf{x}_c)\,e^{-\frac{S[\mathbf{x}(\tau)]}{\hbar}}}, \tag{2.35}$$

and noting that the expression on the right hand side of the equation above is simply a path integral ensemble average with the centroids constrained at $\mathbf{x}_c$, which we will denote with the notation $\langle \dots \rangle_c$, we can then write

$$\frac{dV_c(\mathbf{x}_c)}{d\mathbf{x}_c} = \frac{1}{\beta\hbar}\left\langle \frac{\partial S[\mathbf{x}(\tau)]}{\partial \bar{\mathbf{x}}} \right\rangle_c . \tag{2.36}$$

Next, to compute the derivative on the right hand side in the equation above, we note that $\frac{\partial \mathbf{x}(\tau)}{\partial \bar{\mathbf{x}}} = 1$ and that $\frac{\partial \dot{\mathbf{x}}(\tau)}{\partial \bar{\mathbf{x}}} = 0$ (from expressing $\mathbf{x}(\tau)$ in terms of its Fourier components), and using the definition of $S[\mathbf{x}(\tau)]$ in Eq. 2.13 we arrive at

$$\frac{dV_c(\mathbf{x}_c)}{d\mathbf{x}_c} = \left\langle \frac{1}{\beta\hbar}\int_0^{\beta\hbar} d\tau \frac{dV(\mathbf{x}(\tau))}{d\mathbf{x}(\tau)} \right\rangle_c \sim \lim_{P\to\infty} \left\langle \frac{1}{P}\sum_{i=1}^{P} \frac{dV\left(\mathbf{x}^{(i)}\right)}{d\mathbf{x}^{(i)}} \right\rangle_c , \tag{2.37}$$

with the latter equation being given in discretised form. So, the forces generated by this centroid potential are just the thermal averages of the forces on the centroid modes with the centroids constrained at positions $\mathbf{x}_c$.

The critical issue with this expression is that computing the centroid mean force requires performing a full centroid constrained PIMD simulation at each point in phase space visited by the trajectory, which is computationally infeasible. Therefore, what is typically done instead is that the masses of the non-centroid normal modes are adjusted so that they oscillate at a much faster frequency than the centroid mode. The mass of the centroid mode must remain set to that of the physical particle mass so that it represents the classical motion of said particle on the effective mean force potential. This enforces a partial adiabatic separation between the centroid and the internal modes of the ring-polymer, and is thus termed partially adiabatic centroid molecular dynamics[17] (PACMD). The centroid potential of mean force is then calculated "on the fly" during the simulation by the rapid oscillations of the internal modes, whilst the comparatively slow motion of the centroid moves along this potential. Depending on the degree which the internal mode masses have to be shifted in order to achieve this partial adiabatic separation, this may mean that a very small timestep would have to be used in order to correctly integrate the equations of motion for the high frequency oscillations of these modes. Another approach for simple potentials would be to precompute the centroid potential of

mean force in a PIMD simulation and then use that to perform classical molecular dynamics upon. This has been done via "force-matching" by Hone *et al.*[21] to compute the velocity autocorrelation function for liquid parahydrogen.

The dynamics of the centroid along the centroid potential of mean force can then be used to evaluate time correlation functions of observables, $C_{AB}(t)$. It may be shown that the classical correlation functions generated from CMD most closely approximate the Kubo transformed quantum time correlation function,[52]

$$\tilde{C}_{AB}(t) = \frac{1}{\beta \mathcal{Z}} \int_0^\beta d\lambda \, \mathrm{Tr}\left[ e^{-(\beta-\lambda)\hat{H}} \hat{A} e^{-\lambda \hat{H}} e^{\frac{i\hat{H}t}{\hbar}} \hat{B} e^{-\frac{i\hat{H}t}{\hbar}} \right]. \tag{2.38}$$

This Kubo transformed correlation function is related to the standard form of the quantum time correlation function, given in Eq. 2.28, by

$$G_{AB}(\omega) = \frac{\beta\hbar\omega}{1 - e^{-\beta\hbar\omega}} \tilde{G}_{AB}(\omega), \tag{2.39}$$

where $G_{AB}(\omega)$ is the Fourier transform of the standard quantum correlation function $C_{AB}(t)$,

$$G_{AB}(\omega) = \int_{-\infty}^{\infty} e^{-i\omega t} C_{AB}(t), \tag{2.40}$$

and $\tilde{G}_{AB}(\omega)$ that of the Kubo transform $\tilde{C}_{AB}(t)$.[18]

The general prescription for calculating observables within the CMD framework is simply to evaluate the classical observable using the centroid positions and momenta.[13] The correlation functions generated by CMD are accurate up to $\mathcal{O}(t^3)$[53; 54] if $\hat{A}$ and $\hat{B}$ are linear operators in terms of the position. If, on the other hand, $\hat{A}$ and $\hat{B}$ are general non-linear operators, then the approximated correlation function found from CMD is only accurate to $\mathcal{O}(1)$,[54] meaning that CMD cannot really be applied to the calculation of time correlation functions of highly non-linear operators with good confidence. In spite of this, CMD has been used to calculate correlation functions of non-linear operators to some success, such as in the shear viscosity of parahydrogen,[19] and would be expected to not be too bad of an approximation if the degree of non-linearity within the operators was small, or if the system was close to the classical limit.

One obstacle with the CMD method is the so-called "curvature problem", where in the presence of a repulsive region of a potential the ring polymers can extend in the degrees of freedom orthogonal to the gradient of the potential. This causes the mean force on the centroid mode found as the average of the forces on the beads to be lower than should be expected from where the centroid is physically located in space. This softening of repulsive regions in the centroid potential of mean force will be more apparent at lower temperatures where the ring polymers are more spread out and so the curvature is more apparent. The curvature problem is known to be a major cause in the failure of CMD to predict vibrational spectra at low temperatures, where peaks become artificially red-shifted.[55]

## 2.3 Ring Polymer Molecular Dynamics

Ring polymer molecular dynamics (RPMD)[18] is an approach that shares many similarities with CMD. Instead of using the centroid potential of mean force to propagate the position and momentum centroids classically, RPMD uses the "ring polymer Hamiltonian" of Eq. 2.10 directly to generate the dynamics for evaluating correlation functions. As such, RPMD relies on the assumption that the fictitious momenta introduced to sample phase space *do* contain enough information to at least approximate the quantum dynamics, when their associated masses are all chosen to be equal to the physical particle masses. The approximate quantum correlation functions calculated within RPMD for two position dependent operators $\hat{A}(\mathbf{x})$ and $\hat{B}(\mathbf{x})$ are given by[18]

$$C_{AB}(t) = \frac{\int d\mathbf{p}\, d\mathbf{x}\, e^{-\beta\mathcal{H}(\mathbf{p},\mathbf{x})} A_P(\mathbf{x}(0))\, B_P(\mathbf{x}(t))}{\int d\mathbf{p}\, d\mathbf{x}\, e^{-\beta\mathcal{H}(\mathbf{p},\mathbf{x})}}, \tag{2.41}$$

for $A_P(\mathbf{x}(0))$ and $B_P(\mathbf{x}(t))$ given by Eq. 2.23 and evaluated at the ring polymer positions at times 0 and $t$ respectively, and $\mathcal{H}(\mathbf{p},\mathbf{x})$ is the ring polymer Hamiltonian given in Eq. 2.10. These correlation functions again approximate the Kubo transformed quantum correlation function of Eq. 2.38, this time up to $\mathcal{O}(t^6)$ for operators which are linear in terms of position or momentum, and up to $\mathcal{O}(t^2)$ for general non-linear operators.[53; 54]

Whilst in ordinary RPMD these correlation functions are calculated within the microcanonical path integral ensemble, as $P$ increases the high-frequency normal modes become incredibly stiff, leading to non-ergodic sampling. It has been shown that attaching Langevin thermostats to the internal modes whilst leaving the centroid unthermostatted does not affect the quality of agreement of the RPMD correlation functions to the exact Kubo transformed correlation function up to the leading order error in $t$.[54] This thermostatted RPMD, or TRPMD, may be desirable to help improve ergodicity and the quality of sampling.

The accuracy to which RPMD approximates the true Kubo transformed correlation function may indicate that the assumption in using the fictitious momenta to evolve the Hamiltonian dynamics was not too drastic after all. In fact, it was found later that RPMD is related to a specific approximation of Matsubara dynamics[56], providing it some amount of theoretical justification.

RPMD and CMD have become popular methods for including nuclear quantum effects in dynamical properties in the condensed phase, particularly in the computation of transport properties and reaction rates.[22; 23; 57; 58] However, they are not without their limitations. RPMD, like CMD, fails to predict vibrational spectra accurately. The unphysical normal modes of the ring polymer interfere with the physical normal modes of the system, leading to spurious resonances appearing in the spectra.[54; 59] Whilst the short time accuracy of the correlation functions generated by RPMD are better than those from CMD, they both remain short time approximations and so neither should be expected to remain accurate over long timescales. They are also both best justified for correlation functions of operators which are linear in terms position or momentum, and will be less reliable if the correlation function of interest is non-linear in these, especially as quantum effects become more significant. RPMD has, however, been shown to be a reasonable approximation for non-linear operators in the specific problem of density fluctuations in orthodeuterium as the degree of non-linearity becomes small.[60]

# 3

# Classical methods for thermal conductivity

## 3.1 Introduction

Thermal transport in insulating crystalline solids occurs primarily due to lattice vibrations or "phonons" throughout the crystal.[61] Scattering of these phonons via anharmonic terms in the potential and irregularities in the lattice structure causes the thermal conductivity of the crystal to become finite.[61] As the temperature decreases, the thermal conductivity initially increases up to a maximum value, usually between 10 K and 30 K,[7; 62; 63] due to fewer phonons being scattered at lower temperatures, before decreasing to zero at zero temperature. The underlying reason for the vanishing thermal conductivity is due to the fact that the quantum mechanical heat capacity also vanishes as $T \to 0$ K.[62; 64] Therefore, in insulators - where nuclear motion is the dominant contributor to heat transport[61] - the maximum in the thermal conductivity is a clear indication of the presence of nuclear quantum effects, since a purely classical theory would predict that the heat capacity goes to a constant value as $T \to 0$ K and thus would be unable to account for this thermal conductivity maximum. In fact, the classical thermal conductivity is found to diverge as $T \to 0$ K.[65] In the vicinity of the peak in the thermal conductivity however, phonon scattering from defects and boundaries within the crystal become

important contributions to the thermal conductivity.[62; 66] These are difficult to include within computational simulations,[67] particularly in the context of molecular dynamics[68; 69] - and any prospective approximate quantum mechanical simulation inside this temperature range which neglected these mechanisms would likely be too simplified to be compared to experiment.[70]

Quantum mechanical effects may often be significant even at temperatures much greater than the position of the low temperature thermal conductivity maximum. A measure of the temperature below which quantum mechanical effects may start becoming important is the Debye temperature, $\Theta_D$. For instance, the Debye temperature of crystalline silicon is $\Theta_D = 695\,\mathrm{K}$[71] and whilst quantum mechanical effects do not necessarily persist significantly all the way up until $\Theta_D$,[72] quantum corrections to the thermal conductivity can be necessary even at ambient temperatures.[9; 65; 73] As an example, a small but noticeable quantum effect on the thermal conductivity of Stillinger-Weber silicon of 15 % was found by Turney *et al.*[27] at a temperature of 300 K using anharmonic lattice dynamics. Moreover, the same study found the quantum effect below 100 K to be very large, which is precisely the temperature regime in which superconductors and other cryoelectronic devices typically operate.[28]

The vast majority of interest in the computational simulation of the thermal conductivity has been applied to solids,[68; 74–78] owing to the great number of applications of the heat transfer of solids in engineering and materials development. However, thermal transport in solids is typically characterised by long phonon lifetimes, which results in requiring long simulation times in order to calculate the thermal conductivity.[74; 76] This is not ideal in the context of possible RPMD and CMD generalisations in two ways. The first being that they are short time approximations to the true (Kubo-transformed) quantum mechanical correlation functions and thus are less suitable the longer the correlation time is and the second is that the long simulation times will be compounded by the need to simulate multiple replicas.

We believe that it is best to first test any RPMD or CMD methods for quantum thermal conductivity calculation in regimes where we have most reason to believe it will work well, and then develop it as needed for more challenging systems afterwards. For this reason, we will focus on the liquid phase for the majority of this thesis, where the required simulation times are normally much shorter.[79] The thermal conductivity of most liquids displays a relatively simple temperature dependence, with a monotonic decrease as the temperature increases.[80] There are, however, a few exceptions - with notable examples being liquid parahydrogen[81] and liquid water.[82] This anomalous temperature dependence of the thermal conductivity, as well as the fact that both cases have previously been studied extensively by RPMD and CMD and display significant nuclear quantum effects, make them ideal test cases for applying potential methods for quantum thermal conductivity prediction.

Before developing any of these quantum methods, it is prudent to discuss the theory behind the classical methods for calculating the thermal conductivity that we wish to generalise. To do this, in this Chapter we will present the linearised equations of hydrodynamics and then describe how these may be used to derive the Green-Kubo relation[83] for the thermal conductivity, which has become the *de facto* method for calculating the thermal conductivity within molecular dynamics simulations. We will then discuss some previous attempted generalisations of the Green-Kubo method to approximate quantum dynamical methods and the reasons why this method may be ill-suited to a CMD or RPMD generalisation. Afterwards, we will briefly touch upon some of the other commonly used classical methods for computing the thermal conductivity and why generalising these may not be the best approach either, and also mention the anharmonic lattice dynamics method - which *can* calculate approximate quantum mechanical thermal conductivities but is limited in its scope. Finally, we will return to the linearised hydrodynamic equations and introduce a method based on calculating the thermal conductivity from equilibrium density fluctuations, which may be better suited for an extension to path integral simulations. In deriving both the Green-Kubo relation and the equations for the equilibrium density fluctuations from the hydrodynamic theory we will closely follow

the methods laid out by Hansen and McDonald[84] as well as that by Berne and Pecora.[85] Other helpful discussions may be found in Refs. [6; 86; 87].

## 3.2 The Linearised Hydrodynamic Equations

In order to derive the hydrodynamic equations which we will use to obtain our relations for the thermal conductivity, we must first introduce the concept of local variables. For a general system not at equilibrium, thermodynamic quantities such as the energy or pressure will vary throughout the system and with time. In the case of an extensive variable like the energy, we may define a local density $a(\mathbf{r}, t)$ associated with the thermodynamic observable $A(t)$ such that

$$A(t) = \int_V a(\mathbf{r}, t)\, d^3\mathbf{r}, \tag{3.1}$$

where the integral is over the entire volume $V$ of the system. For intensive variables like number density or temperature, we may also define a local version of the variable by taking it as the intensive variable evaluated over a subsystem of small volume around the point of interest. To make this definition we use the assumption of local thermodynamic equilibrium. That is, although the subsystem is small compared to the size of the macroscopic system, it is taken to be large enough and the intensive property is assumed to vary slowly enough in space and time that the subsystem can be assumed to be in a state of thermodynamic equilibrium itself. This means that we can use the same thermodynamic relations to define the local intensive property within the subsystem as one usually would to define the global variable in an equilibrium system.

To reduce the number of symbols to be introduced, we will often use the same symbol to also refer to the local version of the variable as the usual symbol used to refer to the macroscopic global thermodynamic variable. Additionally, we will often suppress the dependence of the local variable on position and time in the equations that follow to prevent the notation from becoming overly cumbersome. So, $T \equiv T(\mathbf{r}, t)$ would refer to the local temperature at a point $\mathbf{r}$ in the system at time $t$.

The definition of local thermodynamic quantities allows us to make stronger statements on the various conservation laws that apply to the system. For instance, not only should the energy be conserved over the whole system and its surroundings but it should also be locally conserved - that is that the rate of energy change within any subsystem of arbitrary volume $V$ must be equal to the negative of the rate at which energy flows out of the subsystem. This can be expressed mathematically by a continuity equation for the energy density $e \equiv e(\mathbf{r}, t)$ as

$$\int_V \frac{\partial e}{\partial t} d^3\mathbf{r} = -\oint \mathbf{J}^E \cdot d\mathbf{S} = -\int_V \nabla \cdot \mathbf{J}^E d^3\mathbf{r}, \tag{3.2}$$

where $\mathbf{J}^E$ is the energy flux, defined by the energy that flows through a unit area in a unit time, the surface integral is over the surface enclosing $V$ and the second equality results from the divergence theorem. Since this must hold for any $V$, we must therefore have that the two integrands are equal - so that

$$\frac{\partial e}{\partial t} = -\nabla \cdot \mathbf{J}^E. \tag{3.3}$$

In this Section, for simplicity we will restrict our discussion of the hydrodynamic theory to a monoatomic fluid. In this case, there are five independent locally conserved quantities - the energy density, the number density, $\rho$, and the three components of the local linear momentum, $\mathbf{p}$.[88] In the case of a molecular fluid the angular momentum is also locally conserved, and this must be additionally included to consider the system accurately.[6] For each of these, a continuity equation may be derived relating them to their corresponding fluxes analogously to what was already done for the energy density in Eq. 3.3. The other two continuity equations are: for the number density

$$\frac{\partial \rho}{\partial t} = -\nabla \cdot (\rho \mathbf{v}), \tag{3.4}$$

where $\mathbf{v} \equiv \mathbf{v}(\mathbf{r}, t)$ is the local velocity; and for the linear momentum

$$\frac{\partial \mathbf{p}}{\partial t} = -\nabla \cdot \mathbf{\Pi}, \tag{3.5}$$

where $\mathbf{\Pi} \equiv \mathbf{\Pi}(\mathbf{r}, t)$ is the momentum flux density tensor, defined by

$$\Pi_{\alpha\beta} = -\sigma_{\alpha\beta} + m\rho v_\alpha v_\beta, \tag{3.6}$$

where $\boldsymbol{\sigma}$ is the local stress tensor and can be further decomposed as $\sigma_{\alpha\beta} = -P\delta_{\alpha\beta} + \sigma'_{\alpha\beta}$, where $P$ is the local hydrostatic pressure and $\boldsymbol{\sigma}'$ is the viscous stress tensor - the contribution to the total stress tensor from viscous interactions. By considering various constraints on the fluid (ie. that $\sigma'_{\alpha\beta}$ must be identically zero if the velocity is constant in space) we may write an expression for the viscous stress tensor as[89]

$$\sigma'_{\alpha\beta} = \eta\left(\frac{\partial v_\alpha}{\partial r_\beta} + \frac{\partial v_\beta}{\partial r_\alpha}\right) - \left(\frac{2}{3}\eta - \zeta\right)\delta_{\alpha\beta}\nabla\cdot\mathbf{v}, \tag{3.7}$$

where $\eta$ is the shear viscosity and $\zeta$ is the bulk viscosity. The coefficients of viscosity, $\eta$ and $\zeta$, are known as transport coefficients - as is the thermal conductivity, $\kappa$. A Green-Kubo relation may be derived for each of the transport coefficients, including the relation given for the diffusion coefficient in Eq. 2.27, although we will focus on deriving the Green-Kubo relation for $\kappa$ specifically here. In general, transport coefficients will depend on both the temperature and pressure of the system. Since these vary with both $\mathbf{r}$ and $t$ in a non-equilibrium system - $\eta$, $\zeta$ and $\kappa$ will also be dependent on $\mathbf{r}$ and $t$.[89] However, since we will be assuming that the systems we are considering are "close" to equilibrium, where there are only small variations in the pressure and temperature throughout the fluid, we may make the approximation that the transport coefficients are independent of position and time.

Since the local momentum $\mathbf{p} = m\rho\mathbf{v}$, where $m$ is the particle mass, we can expand the partial derivative in Eq. 3.5 by the product rule and use Eq. 3.4 to obtain

$$\begin{aligned}\frac{\partial\mathbf{p}}{\partial t} &= m\rho\frac{\partial\mathbf{v}}{\partial t} + m\mathbf{v}\frac{\partial\rho}{\partial t}\\ &= m\rho\frac{\partial\mathbf{v}}{\partial t} - m\left(\nabla\cdot(\rho\mathbf{v})\right)\mathbf{v}\\ &= m\rho\frac{\partial\mathbf{v}}{\partial t} - m\left(\nabla\rho\cdot\mathbf{v}\right)\mathbf{v} - m\rho\left(\nabla\cdot\mathbf{v}\right)\mathbf{v}.\end{aligned} \tag{3.8}$$

Also taking the divergence of Eq. 3.6 and writing in vector form gives,

$$\begin{aligned}\nabla\cdot\boldsymbol{\Pi} =& \nabla P + m\left(\nabla\rho\cdot\mathbf{v}\right)\mathbf{v} + m\rho\left(\nabla\cdot\mathbf{v}\right)\mathbf{v} + m\rho\left(\mathbf{v}\cdot\nabla\right)\mathbf{v}\\ &- \eta\left[\nabla\left(\nabla\cdot\mathbf{v}\right) + \nabla^2\mathbf{v}\right] + \left(\frac{2}{3}\eta - \zeta\right)\nabla\left(\nabla\cdot\mathbf{v}\right),\end{aligned} \tag{3.9}$$

where $\nabla^2\mathbf{v}$ is the vector Laplacian of the local velocity. Substituting this into Eq. 3.5, and after the cancelling of terms Eq. 3.8 becomes,

$$m\rho\frac{\partial\mathbf{v}}{\partial t} = -\nabla P - m\rho\left(\mathbf{v}\cdot\nabla\right)\mathbf{v} + \left(\frac{1}{3}\eta + \zeta\right)\nabla\left(\nabla\cdot\mathbf{v}\right) + \eta\nabla^2\mathbf{v}, \tag{3.10}$$

which is the Navier-Stokes equation.

To proceed further we can place the Navier-Stokes equation in its linearised form by introducing a reference equilibrium system. We will denote the values that thermodynamic quantities would take in this reference system by a subscript $\square_0$ and the difference between the corresponding value in the real system and the reference value by a subscript $\square_1$. So, we may write the local density as $\rho = \rho_0 + \rho_1$, where $\rho_0$ is the number density at equilibrium, and also introduce similar expressions for the other local thermodynamic quantities. We note that Eq. 3.10 evaluated at the equilibrium variables must be zero, since there cannot be any velocity gradients at equilibrium, and we also choose a reference frame where the velocity of the fluid at equilibrium, $\mathbf{v}_0 = \mathbf{0}$. Since the deviations from equilibrium are taken to be small, we only retain terms which are linear in any combination of these equilibrium deviations. This causes the advection term $m\rho\left(\mathbf{v}\cdot\nabla\right)\mathbf{v}$ to disappear, since the only terms that do not contain $\mathbf{v}_0$ contain the expression $\left(\mathbf{v}_1\cdot\nabla\right)\mathbf{v}_1$, which is quadratic in the equilibrium deviations. With this, and after some more cancellation we arrive at the linearised form of the Navier-Stokes equation

$$m\rho_0\frac{\partial\mathbf{v}_1}{\partial t} = -\nabla P_1 + \left(\frac{1}{3}\eta + \zeta\right)\nabla\left(\nabla\cdot\mathbf{v}_1\right) + \eta\nabla^2\mathbf{v}_1. \tag{3.11}$$

For the case of an isotropic medium it is convenient to work with the divergence of the linearised Navier-Stokes equation,

$$m\rho_0\frac{\partial\varphi_1}{\partial t} + \nabla^2 P_1 = \left(\frac{4}{3}\eta + \zeta\right)\nabla^2\varphi_1 \tag{3.12}$$

where $\varphi_1 = \nabla\cdot\mathbf{v}_1$ and we have made use of the expression for the vector Laplacian

$$\nabla^2\mathbf{v}_1 = \nabla\left(\nabla\cdot\mathbf{v}_1\right) - \nabla\wedge\left(\nabla\wedge\mathbf{v}_1\right), \tag{3.13}$$

and the fact that the divergence of a curl is zero when evaluating the divergence of the $\nabla^2\mathbf{v}_1$ term.

We will also find it helpful for later purposes to additionally write Eq. 3.12 in terms of the local temperature and density deviations rather than the pressure deviation. To this end we may write

$$P_1 = \frac{1}{\rho_0 \chi_T}\rho_1 + \beta_V T_1, \tag{3.14}$$

where we have identified $(\partial P_0/\partial T_0)_{\rho_0} = \beta_V$, the thermal pressure coefficient, and $(\partial P_0/\partial \rho_0)_{T_0} = 1/\rho_0\chi_T$, where $\chi_T$ is the isothermal compressibility. For ease of notation later on, we can introduce the adiabatic speed of sound, $c_s$, which is related to $\chi_T$ by

$$c_s^2 = \frac{\gamma}{\rho_0 m \chi_T}, \tag{3.15}$$

where $\gamma = c_P/c_V$ with $c_P$ the heat capacity per particle at constant pressure and $c_V$ the heat capacity per particle at constant volume. We can also use the relation

$$\beta_V = \left(\frac{\partial P_0}{\partial T_0}\right)_{\rho_0} = -\left(\frac{\partial P_0}{\partial \rho_0}\right)_{T_0}\left(\frac{\partial \rho_0}{\partial T_0}\right)_{P_0} = \frac{\alpha}{\chi_T} = \frac{m\rho_0 c_s^2 \alpha}{\gamma}, \tag{3.16}$$

where we have identified the thermal expansion coefficient $\alpha = -\left(\partial\rho_0/\partial T_0\right)_{P_0}/\rho_0$ and used Eq. 3.15 to substitute for $\chi_T$.

Using these in Eq. 3.14 we have

$$P_1 = \frac{mc_s^2}{\gamma}\rho_1 + \frac{m\rho_0 c_s^2 \alpha}{\gamma}T_1, \tag{3.17}$$

and inserting this expression for $P_1$ into the linearised Navier-Stokes equation, Eq. 3.12, we reach the expression

$$m\rho_0\frac{\partial \varphi_1}{\partial t} + \frac{mc_s^2}{\gamma}\nabla^2\rho_1 + \frac{m\rho_0 c_s^2\alpha}{\gamma}\nabla^2 T_1 = \left(\frac{4}{3}\eta + \zeta\right)\nabla^2\varphi_1 \tag{3.18}$$

Together Eq. 3.12 and 3.18 represent the first of three equations which comprise the linearised hydrodynamic equations. To obtain the second we can simply place the continuity equation for the number density of Eq. 3.4 in its linearised form as

$$\frac{\partial \rho_1}{\partial t} = -\rho_0\varphi_1, \tag{3.19}$$

where we have again neglected terms which would be second order or higher in the differences from equilibrium.

To reach the final of the three linearised hydrodynamic equations we return to the energy flux defined by Eq. 3.3. We may find an expression for the energy flux by considering the different ways in which energy can flow through a surface within the fluid. Energy can travel via mass transport, by stresses imposed onto the surface or by heat transport.[6] We can express these three terms together as

$$\mathbf{J}^E = e\mathbf{v} - \boldsymbol{\sigma}\mathbf{v} + \mathbf{J}^Q, \tag{3.20}$$

where $\boldsymbol{\sigma}$ is the local stress tensor introduced earlier and $\mathbf{J}^Q$ is the heat flux, which measures the amount of the energy flux which is transferred as heat. This heat flux is related to the thermal conductivity, $\kappa$, by Fourier's Law

$$J^Q_\alpha = -\kappa_{\alpha\beta} \left(\nabla T\right)_\beta, \tag{3.21}$$

where in general the thermal conductivity is a second rank tensor, since the heat flux generated may not always be in the direction of the temperature gradient for an anisotropic material.[90; 91] However, for the isotropic monoatomic fluid we are considering here, the off-diagonal components of the thermal conductivity will all be zero and the diagonal components will all be equal - so we can define a scalar thermal conductivity by

$$\kappa = \frac{1}{3}\mathrm{Tr}\left[\boldsymbol{\kappa}\right], \tag{3.22}$$

such that

$$\mathbf{J}^Q = -\kappa\nabla T. \tag{3.23}$$

Using this, together with Eqs 3.3 and 3.20 we find that, after linearising with respect to the deviations from equilibrium and assuming that the thermal conductivity is constant within the system,

$$\frac{\partial e_1}{\partial t} = -\left(e_0 + P_0\right)\varphi_1 + \kappa\nabla^2 T_1, \tag{3.24}$$

where $e_0 = E_0/V$ is the energy density at equilibrium, and terms which arise from the viscous stress tensor do not contribute in the linearised approximation for

the same reason as the advection term in the linearised Navier-Stokes equation did not contribute. Then, using the continuity equation for the number density, Eq. 3.19, to substitute for $\nabla \cdot \mathbf{v}_1$ we reach

$$\frac{\partial e_1}{\partial t} = \frac{e_0 + P_0}{\rho_0} \frac{\partial \rho_1}{\partial t} + \kappa \nabla^2 T_1, \tag{3.25}$$

which is the linearised form of the energy transport equation.

In lieu of the above equation, we may introduce the quantity

$$q(\mathbf{r}, t) = e(\mathbf{r}, t) - \frac{e_0 + P_0}{\rho_0} \rho(\mathbf{r}, t), \tag{3.26}$$

so that referring to Eq. 3.25 we may write

$$\frac{\partial q_1}{\partial t} = \kappa \nabla^2 T_1. \tag{3.27}$$

We can elucidate the nature of $q$, since the differential for the total energy (with $dN = 0$) may be rearranged to give

$$TdS = d(eV) + PdV = V\left[de - \frac{e}{\rho} d\rho\right] - \frac{VP}{\rho} d\rho, \tag{3.28}$$

where we have used the relation $dV = -(V/\rho)\, d\rho$ applicable for fixed $N$. We can therefore see that $dq = TdS/V$ - so that fluctuations in $q$ can be associated with changes in the heat energy $TdS$ per unit volume. We can then expand the deviations in density and temperature in terms of the entropy and pressure as

$$\begin{aligned} T_1 &= \left(\frac{\partial T_0}{\partial S_0}\right)_P S_1 + \left(\frac{\partial T_0}{\partial P_0}\right)_S P_1 = \frac{T_0}{\rho_0 V_0 c_P} S_1 + \frac{\alpha T_0}{\rho_0 c_P} P_1 \\ &= \frac{1}{\rho_0 c_P} q_1 + \frac{\alpha T_0}{\rho_0 c_P} P_1, \end{aligned} \tag{3.29}$$

and

$$\rho_1 = -\frac{T_0 \beta_V \chi_T}{V_0 c_P} S_1 + \frac{\rho_0 \chi_T}{\gamma} P_1 = -\frac{\alpha}{c_P} q_1 + \frac{1}{m c_s^2} P_1, \tag{3.30}$$

where we have used some standard but lengthy thermodynamic manipulations to evaluate the required derivatives in the expressions for both $T_1$ and $\rho_1$. With this, we can write the energy transport equation as

$$\frac{\partial q_1}{\partial t} = D_T \nabla^2 q_1 + \alpha T_0 D_T \nabla^2 P_1, \tag{3.31}$$

with $D_T = \kappa/\rho_0 c_P$ being the thermal diffusivity.

As well as this, we will find it useful to also express the deviation in the heat energy density from Eq. 3.27 in terms of two other thermodynamic variables - this time choosing to do so in terms of the temperature and number density as

$$q_1 = \rho_0 c_V T_1 - \frac{\alpha m c_s^2 T_0}{\gamma}\rho_1, \tag{3.32}$$

which means Eq. 3.25 can also be written as, using Eq. 3.27,

$$\rho_0 c_V \frac{\partial T_1}{\partial t} = \frac{\alpha m c_s^2 T_0}{\gamma}\frac{\partial \rho_1}{\partial t} + \kappa \nabla^2 T_1. \tag{3.33}$$

Together Eqs 3.31 and 3.33 represent two equivalent forms of the energy transport equation - the final of the three linearised hydrodynamic equations which we will use to derive our relations for the thermal conductivity. We note that in the case that the local number density does not vary with time, $\partial\rho_1/\partial t = 0$, as is the case in a solid where mass transport is neglible, then the energy transport equation reduces to the heat equation

$$\frac{\partial T_1}{\partial t} = a\nabla^2 T_1, \tag{3.34}$$

with $a = \kappa/\rho_0 c_V$. Confusingly, both $a$ and $D_T$ are often referred to as the thermal diffusivity in the literature. Here, it should be clear from the context and from the symbol used which meaning is intended.

Finally, we will also need to write the number density continuity equation, Eq. 3.19, so that it is in the variables $q_1$ and $P_1$ rather than $\rho_1$. This can be easily achieved using Eq. 3.30 to yield

$$\frac{-\alpha}{c_P}\frac{\partial q_1}{\partial t} + \frac{1}{m c_s^2}\frac{\partial P_1}{\partial t} = -\rho_0 \varphi_1. \tag{3.35}$$

So, Eqs 3.18,3.19 and 3.33 provide the linearised hydrodynamic equations in terms of the divergence of the local velocity, temperature and density as the independent variables - which we will use to derive the expression for the thermal conductivity using the equilibrium density fluctuations in Section 3.4. With Eqs 3.12, 3.33 and 3.35 we also have these three equations expressed in terms of the divergence of the local velocity, pressure and heat density - which are the forms we will use to derive the Green-Kubo relation in the following Section.

## 3.3 The Green-Kubo relation

As mentioned previously, we will use the linearised hydrodynamic equations in the form of Eqs 3.12, 3.33 and 3.35 as our starting point for deriving the Green-Kubo relation for the thermal conductivity. By taking the Fourier transform in space and the Laplace transform in time we may transform these partial differential equations into a set of algebraic equations. We will adopt the notation

$$\tilde{f}(\mathbf{k},s)=\mathcal{L}\left\{\mathcal{F}\left\{f(\mathbf{r},t)\right\}\right\}=\int_0^\infty ds\, e^{-st}\int d^3\mathbf{r}\, e^{-i\mathbf{k}\cdot\mathbf{r}}f(\mathbf{r},t)\,, \tag{3.36}$$

where $\mathcal{L}\{\dots\}$ denotes a temporal Laplace transform and $\mathcal{F}\{\dots\}$ denotes the spatial three-dimensional Fourier transform, and we will also refer to just the spatial Fourier transform of $f$ as $f(\mathbf{k},t)$. Using the well known expressions for the Laplace transform of a derivative and the Fourier transform of a gradient and divergence

$$\mathcal{L}\left\{\frac{\partial f}{\partial t}\right\}=s\mathcal{L}\left\{f\right\}-f(t=0)\,, \tag{3.37}$$

as well as

$$\mathcal{F}\left\{\nabla f\right\}=i\mathbf{k}\mathcal{F}\left\{f\right\}, \tag{3.38}$$

and

$$\mathcal{F}\left\{\nabla\cdot\mathbf{f}\right\}=i\mathbf{k}\cdot\mathcal{F}\left\{\mathbf{f}\right\}, \tag{3.39}$$

the linearised hydrodynamic equations in Fourier-Laplace space may be written as, after some rearranging: the number density continuity equation

$$\frac{-\alpha mc_s^2 s}{c_P}\tilde{q}_1(\mathbf{k},s)+s\tilde{P}_1(\mathbf{k},s)+\rho_0 mc_s^2\tilde{\varphi}_1(\mathbf{k},s)=\frac{-\alpha mc_s^2}{c_P}q_1(\mathbf{k},0)+P_1(\mathbf{k},0)\,, \tag{3.40}$$

where, for clarity, the notation $f(\mathbf{k},0)$ indicates the spatial Fourier transform of $f$ evaluated at $t=0$, the Navier-Stokes equation

$$\left(s+bk^2\right)\tilde{\varphi}_1(\mathbf{k},s)-\frac{k^2}{m\rho_0}\tilde{P}_1(\mathbf{k},s)=\varphi_1(\mathbf{k},0)\,, \tag{3.41}$$

where $b=(4\eta/3+\zeta)/\rho_0 m$ is the longitudinal viscosity and $k=|\mathbf{k}|$, and the energy transport equation

$$\left(s+D_T k^2\right)\tilde{q}_1(\mathbf{k},s)+\alpha T_0 D_T k^2\tilde{P}_1(\mathbf{k},s)=q_1(\mathbf{k},0)\,. \tag{3.42}$$

Therefore, we can summarise the three equations above as a matrix equation via

$$\mathbf{M}\tilde{\boldsymbol{\psi}} = \mathbf{N}\boldsymbol{\psi}, \tag{3.43}$$

where

$$\mathbf{M} = \begin{pmatrix} s + D_T k^2 & \alpha T_0 D_T k^2 & 0 \\ \frac{-\alpha m c_s^2 s}{c_P} & s & m\rho_0 c_s^2 \\ 0 & \frac{-k^2}{m\rho_0} & s + bk^2 \end{pmatrix}, \tag{3.44}$$

$$\mathbf{N} = \begin{pmatrix} 1 & 0 & 0 \\ \frac{-\alpha m c_s^2}{c_P} & 1 & 0 \\ 0 & 0 & 1 \end{pmatrix}, \tag{3.45}$$

and

$$\tilde{\boldsymbol{\psi}} = \begin{pmatrix} \tilde{q}_1(k,s) \\ \tilde{P}_1(k,s) \\ \tilde{\varphi}_1(k,s) \end{pmatrix}, \qquad \boldsymbol{\psi} = \begin{pmatrix} q_1(k,0) \\ P_1(k,0) \\ \varphi_1(k,0) \end{pmatrix}, \tag{3.46}$$

where we have dropped the dependence on the direction of $\mathbf{k}$ since only its magnitude appears in Eqs 3.40, 3.41 and 3.42.

Upon inverting the matrix $\mathbf{M}$, we can write an expression for $\tilde{q}_1$ as

$$\tilde{q}_1(k,s) = A(k,s)\, q_1(k,0) + B(k,s)\, P_1(k,0) + C(k,s)\, \varphi_1(k,0), \tag{3.47}$$

where

$$A(k,s) = M_{11}^{-1} - \frac{\alpha m c_s^2}{c_P} M_{12}^{-1}, \tag{3.48}$$

in which $M_{ij}^{-1}$ denotes the $ij^{\text{th}}$ element of the inverse matrix of $\mathbf{M}$, and $B(k,s) = M_{12}^{-1}$ and $C(k,s) = M_{13}^{-1}$. Finally, we may take the inverse Laplace transform of both sides, and then multiply by $q_1(-k,0)$ and take the ensemble average. Noting that since $q_1 = T_0 S_1/V_0$, and that the entropy and pressure are thermodynamically uncorrelated variables[84], we have that $\langle q_1(-k,0)\, P_1(k,0)\rangle = 0$. Furthermore, the local heat density and the divergence of the local velocity have opposite parity under time reversal and therefore $\langle q_1(-k,0)\, \varphi_1(k,0)\rangle = 0$ also.[85] We then arrive at

$$\frac{\langle q_1(-k,0)\, q_1(k,t)\rangle}{\langle q_1(-k,0)\, q_1(k,0)\rangle} = \mathcal{L}^{-1}\{A(k,s)\}. \tag{3.49}$$

So, explicitly writing an expression for $A(k,s)$ by determining the inverse matrix coefficients $M_{11}^{-1}$ and $M_{12}^{-1}$,

$$A(k,s) = \frac{1}{D(k,s)}\left[s^2 + 2\Gamma k^2 s + (a - D_T) bk^4 + c_s^2 k^2\right], \tag{3.50}$$

where we made have used the identity $\alpha^2 = (\gamma - 1) c_P / m c_s^2 T_0$. We have also introduced the sound attenuation coefficient $\Gamma = [(\gamma - 1) D_T + b] / 2$ and $D(k, s)$, which is the determinant of the matrix $\mathbf{M}$, given by

$$D(k, s) = s^3 + (a + b) k^2 s^2 + \left( c_s^2 k^2 + abk^4 \right) s + D_T c_s^2 k^4. \tag{3.51}$$

In order to perform the inverse Laplace transform in Eq. 3.49, we need to know the location of the poles in $A(k, s)$ - or equivalently the roots of the cubic equation $D(k, s) = 0$. In the $k \to 0$ limit these roots will consist of a single real root, $s_0$, and a complex conjugate pair, $s_\pm$. We also note that the real part of all these roots must be negative, as otherwise the correlation function of the Fourier components of the heat density would contain an unphysical term which is exponentially increasing with time.

In principle, it is always possible to write down exact algebraic solutions for a cubic equation - but the expressions can become particularly unwieldy. For our purposes in deriving the Green-Kubo relation, it suffices to consider only the approximate roots of $D(k, s)$ which are applicable in the $k \to 0$ limit. There are numerous equivalent ways to come up with these roots, and the approach we will follow is that of Berne and Pecora.[85] It is observed experimentally that the coefficient related to the adiabatic speed of sound, $c_s k$, is typically orders of magnitude larger than the hydrodynamic parameters $ak^2$ and $bk^2$ for the values of $k$ which are commonly used in both light scattering experiments and also in molecular dynamics simulations. Therefore, we can treat $ak^2$ and $bk^2$ as perturbative terms and expand $s = s^{(0)} + s^{(1)} + \ldots$, where $s^{(n)}$ is $n^{\text{th}}$ order in the perturbation terms. Then, equating the zero-order terms we have

$$\left( s^{(0)} \right)^3 + c_s^2 k^2 s^{(0)} = 0, \tag{3.52}$$

which yields the zeroth order roots $s_0^{(0)} = 0$, $s_\pm^{(0)} = \pm i c_s k$. In order to find the corrections we equate terms that are first-order in the perturbation

$$3 \left( s^{(0)} \right)^2 s^{(1)} + (a + b) k^2 \left( s^{(0)} \right)^2 + c_s^2 k^2 s^{(1)} + D_T c_s^2 k^4 = 0, \tag{3.53}$$

and after substituting in the zeroth-order roots found earlier and rearranging we find that the approximate roots, accurate up to $\mathcal{O}(k^4)$, are $s_0 \approx -D_T k^2$ and $s_\pm \approx \pm i c_s k - \Gamma k^2$. With these, our approximate expression for $D(k,s)$ becomes

$$D(k,s) \approx (s-s_0)(s-s_+)(s-s_-) = \left(s + D_T k^2\right)\left(s^2 + 2\Gamma k^2 s + c_s^2 k^2\right), \quad (3.54)$$

where we have again neglected terms which are second order or higher in the small quantities $ak^2$ and $bk^2$. And thus referring to our expression for $A(k,s)$ from Eq. 3.50, noting that we can neglect the term $(a - D_T)bk^4$ as it is second order, we have in the $k \to 0$ limit

$$A(k,s) \approx \frac{s^2 + 2\Gamma k^2 s + c_s^2 k^2}{(s + D_T k^2)(s^2 + 2\Gamma k^2 s + c_s^2 k^2)} = \frac{1}{s + D_T k^2}. \quad (3.55)$$

From an analysis of thermodynamic fluctuations,[84] in the limit $k \to 0$ we can write $\langle q_1(-k,0)\, q_1(k,0)\rangle = N k_B T^2 c_P$, and so with all of this we may write Eq. 3.49 in a slightly different form

$$\lim_{k\to 0} \mathcal{L}\left\{\langle q_1(-k,0)\, q_1(k,t)\rangle\right\} = \lim_{k\to 0} \frac{N k_B T^2 c_P}{s + D_T k^2}. \quad (3.56)$$

Next, we can utilise an identity for time-correlation functions[84]

$$\langle \dot{A}(t)\, \dot{A}^*(0)\rangle = -\frac{d^2}{dt^2}\langle A(t)\, A^*(0)\rangle, \quad (3.57)$$

where the overdot indicates the time derivative of that quantity, so that we may write

$$\begin{aligned}\mathcal{L}\left\{\langle \dot{q}_1(-k,0)\, \dot{q}_1(k,t)\rangle\right\} &= -\mathcal{L}\left\{\frac{d^2}{dt^2}\langle q_1(-k,0)\, q_1(k,t)\right\} \\ &= -s^2 \mathcal{L}\left\{\langle q_1(-k,0)\, q_1(k,t)\rangle\right\} + s N k_B T^2 c_P, \end{aligned} \quad (3.58)$$

where we have used the fact that $d/dt\left[\langle q_1(-k,0)\, q_1(k,t)\rangle\right] = 0$ at $t = 0$,[84] and we have inserted the expression for $\langle q_1(-k,0)\, q_1(k,0)\rangle$ given earlier. Referring to equations 3.23 and 3.27, we see that in Fourier space we may write

$$\frac{\partial q_1(k,t)}{\partial t} = -i\mathbf{k}\cdot\mathbf{J}^Q(\mathbf{k},t) = -ikJ_x^Q(k,t), \quad (3.59)$$

where we have arbitrarily chosen the wavevector $\mathbf{k}$ to be oriented along the $x$ axis. Therefore,

$$\mathcal{L}\left\{\langle \dot{q}_1(-k,0)\, \dot{q}_1(k,t)\rangle\right\} = k^2 \mathcal{L}\left\{\langle J_x^Q(-k,0)\, J_x^Q(k,t)\rangle\right\}. \quad (3.60)$$

Combining this with equations 3.56 and 3.58 we arrive at

$$\frac{1}{Nk_BT^2c_P}\lim_{k\to 0}\int_0^\infty \langle J_x^Q\left(-k,0\right)J_x^Q\left(k,t\right)\rangle e^{-st}dt = \lim_{k\to 0}\frac{s}{k^2}\left(1-\frac{1}{1+D_Tk^2/s}\right), \tag{3.61}$$

and expanding the right-hand side as a Taylor series we can see that

$$\lim_{k\to 0}\frac{s}{k^2}\left(1-\frac{1}{1+D_Tk^2/s}\right) = \lim_{k\to 0}\frac{s}{k^2}\left(1-1+\frac{D_Tk^2}{s}+\mathcal{O}\left(k^4\right)\right) = D_T. \tag{3.62}$$

The Laplace parameter $s$ may be thought of as a complex frequency, since we may write it as $s = -i\omega + \epsilon$, where $\omega$ is real and represents a frequency and $\epsilon$ is an infinitesimal added to ensure convergence of the integral. We must therefore also take the low frequency $s \to 0$ limit in order to satisfy the assumption of local thermodynamic equilibrium, which requires averaging of local quantities over a sufficiently large timescale, but that the limit $s \to 0$ is understood to be taken *after* the limit $k \to 0$, since the reverse order would change the limiting behaviour of $A\left(k,s\right)$.[87] So putting this all together, we have an expression for the thermal conductivity

$$\begin{aligned}\kappa = \rho c_P D_T &= \frac{1}{Vk_BT^2}\lim_{s\to 0}\lim_{k\to 0}\int_0^\infty \langle J_x^Q\left(-k,0\right)J_x^Q\left(k,t\right)\rangle e^{-st}dt \\ &= \frac{1}{Vk_BT^2}\int_0^\infty \langle J_x^Q\left(0\right)J_x^Q\left(t\right)\rangle dt,\end{aligned} \tag{3.63}$$

where $J_x^Q\left(t\right)$ is now understood to imply the Fourier component of the local heat flux in the limit of zero wavevector. We also can see that since our choice of $\mathbf{k}$ to lie along the $x$ axis was entirely arbitrary, equivalent expressions for $\kappa$ could be derived where $\mathbf{k}$ lies along the $y$ or $z$ axes. So, we can average over these three quantities to yield

$$\kappa = \frac{1}{3Vk_BT^2}\int_0^\infty \langle \mathbf{J}^Q\left(0\right)\cdot\mathbf{J}^Q\left(t\right)\rangle dt, \tag{3.64}$$

which is the Green-Kubo relation for the thermal conductivity. Although we have derived this expression only in the case of a one component fluid, a similar expression may also be shown to apply to the solid phase as well.[88; 92] All that remains is to derive an expression for $\mathbf{J}^Q$ which may be calculated within an equilibrium molecular dynamics simulation,[93; 94] which will be the focus of the next subsection.

### 3.3.1 Formulation of the heat flux vector

In order to derive an expression for the Fourier components of the heat flux, $\mathbf{J}^{Q}(t)$, in the $k \to 0$ limit it is helpful to first consider the Fourier components of the energy flux vector, $\mathbf{J}^{E}(t)$, in the same limit. Taking the spatial Fourier transform of Eq. 3.3, with $\mathbf{k}$ again taken to be along the $x$ axis for convenience, we have that[95]

$$J_x^E(k,t) = \frac{i}{k}\frac{\partial}{\partial t}\int d^3\mathbf{r}\, e(\mathbf{r},t)\, e^{-ikx}. \tag{3.65}$$

An appropriate microscopic description of the energy density $e(\mathbf{r},t)$ is

$$e(\mathbf{r},t) = \sum_i \varepsilon_i \delta(\mathbf{r}-\mathbf{r}_i), \tag{3.66}$$

where the sum is over all particles in the system, $\mathbf{r}_i$ is the position vector of the $i^{\text{th}}$ particle and $\delta(\mathbf{r}-\mathbf{r}_i)$ is the Dirac delta function. The term $\varepsilon_i$ represents the site energy associated with the particle $i$ - it is somewhat ill-defined and the only restriction we will place on it for the time being is that the sum of the site energies is equal to the total energy of the system

$$\sum_i \varepsilon_i = E. \tag{3.67}$$

Inserting Eq. 3.66 into Eq. 3.65, we arrive at

$$J_x^E(k,t) = \frac{i}{k}\frac{\partial}{\partial t}\int d^3\mathbf{r}\sum_i \varepsilon_i\delta(\mathbf{r}-\mathbf{r}_i)\, e^{-ikx} = \frac{i}{k}\frac{\partial}{\partial t}\sum_i \varepsilon_i e^{-ikx_i}, \tag{3.68}$$

and, as we wish to take the $k \to 0$ limit of this equation, we can Taylor expand the right hand side to give

$$\begin{aligned}\lim_{k\to 0} J_x^E(k,t) &= \lim_{k\to 0}\frac{i}{k}\frac{\partial}{\partial t}\sum_i \varepsilon_i\left(1-ikx_i+\mathcal{O}\left(k^2\right)\right)\\ &= \lim_{k\to 0}\left[\frac{i}{k}\frac{\partial E}{\partial t}+\frac{\partial}{\partial t}\sum_i(\varepsilon_i x_i)+\mathcal{O}(k)\right]\\ &= \frac{\partial}{\partial t}\sum_i \varepsilon_i x_i,\end{aligned} \tag{3.69}$$

where we have used the constraint on the site energies represented by Eq. 3.67 in going from the first line above to the second, and the fact that the energy of the system is conserved in going from the second to the third. Again, since our

choice of the direction of $\mathbf{k}$ was completely arbitrary, similar expressions may be derived for the $y$ and $z$ components - and thus we have

$$\mathbf{J}^E(t) = \frac{\partial}{\partial t}\sum_i \varepsilon_i \mathbf{r}_i. \tag{3.70}$$

However, this expression is incompatible with periodic boundary conditions. To remedy this, we can use a procedure due to Irving and Kirkwood[93] to cast this equation in a different form. To do this, we need to assign a more precise definition to the site energy, $\varepsilon_i$. In this thesis, we will only be considering potentials which contain two-body and three-body interactions, and so we will likewise restrict our definition of the site energy so that it only contains two- and three-body terms - although generalisations to an arbitrary many-body potential are straightforward.[96] When dividing the potential energy of an interaction between the sites involved in that interaction, it has been observed that although the heat flux autocorrelation function may depend on the way in which the energy is divided, that the thermal conductivity calculated from its time integral does not.[74; 97–99] This has been shown to be due to a gauge invariance in the thermal conductivity definition.[88; 99] In this work we will always adopt the simple solution of dividing the energy of an interaction equally between all the atoms involved.

With this, we can define our site energy as

$$\varepsilon_i = \frac{1}{2}m|\mathbf{v}_i|^2 + \frac{1}{2}\sum_{j\neq i} u_2(r_{ij}) + \frac{1}{6}\sum_{j\neq i}\sum_{k\neq i,j} u_3(\mathbf{r}_i, \mathbf{r}_j, \mathbf{r}_k), \tag{3.71}$$

where $u_2(r_{ij})$ is the two-body interaction between the particles $i$ and $j$, and $u_3(\mathbf{r}_i, \mathbf{r}_j, \mathbf{r}_k)$ is similarly the three-body interaction between particles $i$, $j$, and $k$. In this case, we can compute the time derivative of $\varepsilon_i$ as

$$\frac{\partial \varepsilon_i}{\partial t} = \mathbf{F}_i \cdot \mathbf{v}_i + \frac{1}{2}\sum_{j\neq i}\sum_k \frac{\partial u_2(r_{ij})}{\partial \mathbf{r}_k}\cdot \mathbf{v}_k + \frac{1}{6}\sum_{j\neq i}\sum_{k\neq i,j}\sum_l \frac{\partial u_3(\mathbf{r}_i, \mathbf{r}_j, \mathbf{r}_k)}{\partial \mathbf{r}_l}\cdot \mathbf{v}_l, \tag{3.72}$$

where $\mathbf{F}_i$ is the total force acting on particle $i$ and we have made use of Newton's second law and the chain rule to evaluate the different derivatives. Since $\partial u_2(r_{ij})/\partial \mathbf{r}_k = -\mathbf{F}_{ij}\delta_{ik} - \mathbf{F}_{ji}\delta_{jk}$, where $\mathbf{F}_{ij}$ is the force contribution on $i$ due to its pair interaction with $j$, and $\partial u_3(\mathbf{r}_i, \mathbf{r}_j, \mathbf{r}_k)/\partial \mathbf{r}_l = -\mathbf{F}_{ijk}\delta_{il} - \mathbf{F}_{jik}\delta_{jl} - \mathbf{F}_{kij}\delta_{kl}$,

where $\mathbf{F}_{ijk}$ is the force contribution on $i$ due to the triplet interaction with $j$ and $k$, our expression for $\partial\varepsilon_i/\partial t$ can be written as

$$\frac{\partial \varepsilon_i}{\partial t} = \mathbf{F}_i \cdot \mathbf{v}_i - \frac{1}{2}\sum_{j\neq i}\left(\mathbf{F}_{ij}\cdot\mathbf{v}_i + \mathbf{F}_{ji}\cdot\mathbf{v}_j\right) - \frac{1}{6}\sum_{j\neq i}\sum_{k\neq i,j}\left(\mathbf{F}_{ijk}\cdot\mathbf{v}_i + \mathbf{F}_{jik}\cdot\mathbf{v}_j + \mathbf{F}_{kij}\cdot\mathbf{v}_k\right). \tag{3.73}$$

Noting that the total force on particle $i$ may be written as the sum of pair and triplet forces, $\mathbf{F}_i = \sum_{j\neq i}\mathbf{F}_{ij} + \sum_{j\neq i}\sum_{k\neq i,j}\mathbf{F}_{ijk}/2$, where the factor of $1/2$ must be included in the second summation to prevent double counting, we can reexpress this as

$$\frac{\partial \varepsilon_i}{\partial t} = \frac{1}{2}\sum_{j\neq i}\left(\mathbf{F}_{ij}\cdot\mathbf{v}_i - \mathbf{F}_{ji}\cdot\mathbf{v}_j\right) + \frac{1}{6}\sum_{j\neq i}\sum_{k\neq i,j}\left(2\mathbf{F}_{ijk}\cdot\mathbf{v}_i - \mathbf{F}_{jik}\cdot\mathbf{v}_j - \mathbf{F}_{kij}\cdot\mathbf{v}_k\right). \tag{3.74}$$

And so performing the derivative in our equation for the energy flux, Eq. 3.70, using the product rule we have, after swapping a couple of dummy indices

$$\mathbf{J}^E = \sum_i \varepsilon_i \mathbf{v}_i + \frac{1}{2}\sum_i\sum_{j\neq i}\left(\mathbf{F}_{ij}\cdot\mathbf{v}_i\right)\mathbf{r}_{ij} + \frac{1}{3}\sum_i\sum_{j\neq i}\sum_{k\neq i,j}\left(\mathbf{F}_{ijk}\cdot\mathbf{v}_i\right)\left(\mathbf{r}_{ij}+\mathbf{r}_{ik}\right), \tag{3.75}$$

where, for instance, $\mathbf{r}_{ij} = \mathbf{r}_i - \mathbf{r}_j$. It is helpful to write the final two terms above together as an outer product, so that

$$\mathbf{J}^E = \sum_i \varepsilon_i \mathbf{v}_i - \sum_i \boldsymbol{\sigma}_i \mathbf{v}_i, \tag{3.76}$$

with $\boldsymbol{\sigma}_i$ being the virial per atom microscopic stress tensor

$$\boldsymbol{\sigma}_i = -\frac{1}{2}\sum_{j\neq i}\mathbf{r}_{ij}\otimes\mathbf{F}_{ij} - \frac{1}{3}\sum_{j\neq i}\sum_{k\neq i,j}\left(\mathbf{r}_{ij}+\mathbf{r}_{ik}\right)\otimes\mathbf{F}_{ijk}. \tag{3.77}$$

For this reason, the first term in Eq. 3.76 is typically referred to as the convective heat flux, $\mathbf{J}_{\text{conv}}$, and the second term as the virial heat flux, $\mathbf{J}_{\text{vir}}$. The convective heat flux is typically negligible for solids where there is essentially no mass transport, and so is often neglected in this context.[100] However, for liquids it must be included.

Finally, we note that from Eq. 3.20, recalling that in this context we are referring to the zero wavevector Fourier components of that expression, we have in the linearised approximation

$$\mathbf{J}^E = \mathbf{J}^Q + (e_0 + P_0)\sum_i \mathbf{v}_i, \tag{3.78}$$

and since we conduct molecular dynamics simulations in a reference frame where $\sum_i \mathbf{v}_i = 0$ at every step for a one-component fluid, the second term on the right-hand side is zero at every simulation step. Our expression for the energy flux derived in Eq. 3.76 is therefore equivalent to the heat flux in this context, and so we can use this inside the Green-Kubo relation, Eq. 3.64, to evaluate the thermal conductivity. An analogous result equating the heat and energy flux vectors can also be shown to hold for the case of a molecular fluid.[101]

### 3.3.2 Applying the Green-Kubo relation in practice and other methods for thermal conductivity

In order to explain why the Green-Kubo method has become the most prominent approach for calculating the thermal conductivity within molecular dynamics simulations, it is necessary to first briefly discuss some of the alternative methods that one can use. There exist a wide variety of non-equilibrium methods for thermal conductivity prediction,[5; 102; 103] in which a temperature profile of some form is set up across the simulation and the thermal conductivity calculated from studying the relaxation back to equilibrium. However, the value of $\kappa$ calculated from these simulations is typically found to be dependent on the length(s) of the simulation cell in which the temperature profile was applied, resulting in needing very large simulations to converge $\kappa$ to its bulk value in the hydrodynamic limit. In fact, it is often not possible to reach system sizes large enough to reach the bulk thermal conductivity within reasonable computation times and so the thermal conductivity is calculated for several different system sizes and an extrapolation procedure is applied to estimate its value in the infinite system size limit.[104] As well as this, due to the limited system sizes accessible, the temperature gradients imposed by the non-equilibrium profile may become unphysically large - leading the assumptions of linear response into question.[105] The Green-Kubo procedure generally converges more rapidly with respect to system size,[76; 104] and for most systems it is not difficult to reach the bulk thermal conductivity - although some studies have found that very large system sizes are still required reach the bulk value in cases where the phonon

mean free path is large.[9] Also it is favourable that it is possible to use the Green-Kubo method within an equilibrium molecular dynamics simulation, since it is then easy to incorporate inside existing programs and one does not have to go through the trouble of ensuring that the non-equilibrium system is initialised properly.

However the Green-Kubo method is not without a couple of disadvantages. The first is that for several simulation approaches, *ab initio*[101; 105; 106] or machine learned potentials[107; 108] for instance, the heat flux vector may be difficult and computationally expensive to calculate. The second is that it is often found that the heat flux autocorrelation function contains a large amount of statistical noise. The variance in the computed integral increases with the simulation time, leading to drift - resulting in difficulty in assigning a "plateau" value to its integral.[74; 109] There are now several statistical methods which may help to alleviate this issue in certain circumstances,[88; 109] but often one still requires a large amount of statistical averaging in order to sufficiently converge the integrated thermal conductivity. For the systems we will be considering in this thesis, the site energy within the Green-Kubo relation is not difficult to define and the heat flux autocorrelation function decays over a reasonable timescale so that neither of these issues will prove to be a significant problem.

Finally we should briefly discuss an existing method that *can* calculate the quantum thermal conductivity for certain systems - anharmonic lattice dynamics.[26; 27; 100] This is based on calculating the harmonic phonon frequencies from the dynamical matrix, correcting with cubic and quartic terms using perturbation theory and calculating the thermal conductivity using the Boltzmann Transport Equation. As it is a lattice model, this method is only applicable to crystalline solids and cannot be used to calculate the quantum thermal conductivity for liquids or amorphous materials. Furthermore, since anharmonic effects are only included perturbatively, the approach suffers at high temperature where anharmonicity becomes increasingly significant[26] and also for highly anharmonic potentials. This makes it an interesting point of comparison for any path integral approach for quantum thermal conductivity calculation, where anharmonic effects are included

up to all orders. However, as mentioned earlier, we believe that solids present a more challenging problem for path integral based calculations of the quantum thermal conductivity and we will leave any possible comparison with anharmonic lattice dynamics for solid systems to future work. We will, however, briefly explore whether the methods we present for the thermal conductivity determination in classical liquids at the end of this Chapter can be extended to also apply to classical crystalline solids in Chapter 6.

### 3.3.3 Quantum generalisations of the Green-Kubo method

As mentioned previously, the Green-Kubo relation for the thermal conductivity is just one of many Green-Kubo relations for the different transport coefficients. In addition, analogous quantum mechanical expressions for each may also be derived by considering the linear response of the Hamiltonian to an external perturbation.[52; 83] The corresponding quantum mechanical expression for the thermal conductivity is given by

$$\kappa = \frac{1}{3Vk_BT^2}\int_0^\infty dt\left[\frac{1}{\beta\hbar}\int_0^{\beta\hbar} d\tau\langle\hat{\mathbf{J}}\left(-i\tau\right)\cdot\hat{\mathbf{J}}\left(t\right)\rangle\right], \tag{3.79}$$

where $\hat{\mathbf{J}}\left(t\right)$ is the time evolved Heisenberg operator $\hat{\mathbf{J}}\left(t\right) = e^{i\hat{H}t/\hbar}\hat{\mathbf{J}}e^{-i\hat{H}t/\hbar}$ and the time derivative in the classical formula for the heat flux, Eq. 3.70, is replaced by a commutator as

$$\hat{\mathbf{J}} = \frac{1}{2}\sum_i \frac{i}{\hbar}\left[\hat{H}, \hat{E}_i\hat{\mathbf{r}}_i + \hat{\mathbf{r}}_i\hat{E}_i\right]. \tag{3.80}$$

Numerous attempts have been made to generalise the classical Green-Kubo calculation within the molecular dynamics framework to incorporate nuclear quantum effects. The first two we shall discuss here are a series of studies on Silvera-Goldman liquid parahydrogen[110] - the first by Yonetani and Kinugawa[19] using the CMD approximation, and the second by Liu *et al.*[25] using the linearised semiclassical initial value representation (LSC-IVR) approximation.[111; 112] Liquid parahydrogen is an especially useful "toy" system for testing methods which attempt to include nuclear quantum effects since essentially all of the hydrogen molecules

lie in the spherically symmetric $J = 0$ rotational state, and thus the system is well-described by a simple pair potential - of which the Silvera-Goldman potential is the best established. As well as this, due to its applications as a fuel source, a wealth of experimental measurements of the thermal conductivity have been made from the triple point ($\approx 13.8\,\mathrm{K}$) up to the critical point ($\approx 33.1\,\mathrm{K}$) along the liquid-vapour saturation line for which to compare results with. Moreover, nuclear quantum effects are significant due to the presence of light nuclei (if one attempts to do a classical Silvera-Goldman simulation at one of the state points on the saturation line then a bubble will form inside the simulation[22]), but identical particle exchange effects may be neglected. The results found by these two studies, as well as the relevant experimental results from Roder and Diller[81] are summarised in Fig. 3.1.[113]

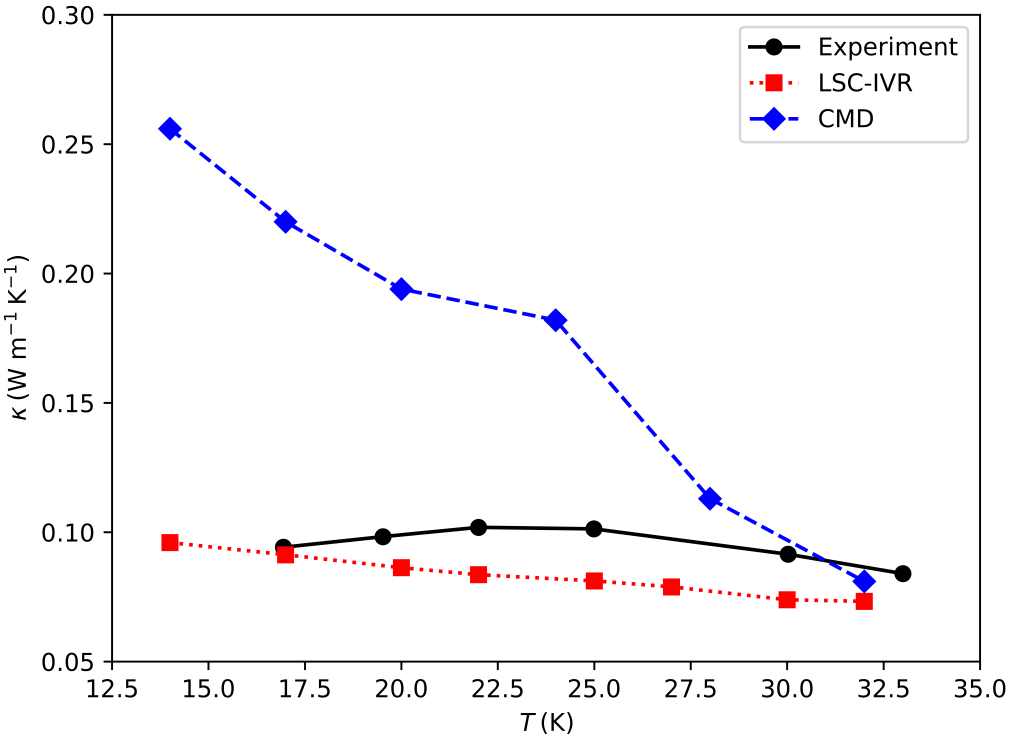



**Figure 3.1:** A comparison of CMD[19] and LSC-IVR[25] calculations of the thermal conductivity of liquid Silvera-Goldman parahydrogen along the liquid-vapour saturation line. Also shown are the corresponding experimental measurements.[81; 113]

The experimental measurements deserve some comment. A peak in the thermal

conductivity is observed close to 22K, before it begins to decrease as the temperature is lowered further. It is unclear if this peak occurs for the same reason as in low-temperature crystalline solids due to the vanishing quantum heat capacity - since a peak also appears in the thermal conductivity of solid parahydrogen at a much lower temperature of 2 K[114] - or whether other effects such as some change in the structure of the fluid at low temperatures play a role. Nevertheless, the presence of the peak is clearly an important feature in the true temperature dependence of the thermal conductivity of liquid parahydrogen, and being able to reproduce it may be considered an important baseline for any approximate method aiming to include quantum mechanical effects in the nuclear motion.

The CMD approximation to the heat flux uses the same formula as in the classical case, Eq. 3.70, with the classical positions and momenta in the definition of the heat flux and site energy replaced with the positions and momenta of the centroid variable as it evolves on the centroid potential of mean force. As can be seen in Fig. 3.1, the CMD approximation completely fails to account for the peak, and with the diverging thermal conductivity as $T \to 0$ is in fact more reminiscent of a classical thermal conductivity calculation than a quantum mechanical one. In some sense this is not surprising, since the quantum mechanical heat flux given by Eq. 3.80 is a highly non-linear operator in terms of $\mathbf{r}$ and $\mathbf{p}$ and so the CMD approximation to it is under no guarantee to be accurate. Indeed, the CMD approximation to $\hat{\mathbf{J}}$ can be shown to not even give the correct value of the Kubo-transformed heat flux autocorrelation function of Eq. 3.79 at time $t = 0$.[113]

On the other hand, the LSC-IVR approximation does treat the quantum heat flux vector so that the autocorrelation function is calculated correctly at time $t = 0$.[25] However, there are numerous approximations which must be made in order to evaluate the required operators and to propagate the dynamics which means that the approximation suffers as the simulation progresses.[115] Although the quantitative agreement with experiment is much better than in the CMD case (the LSC-IVR results are within 20% of the experimental values at all of

the state points), LSC-IVR still predicts a monotonic increase in the thermal conductivity as the temperature decreases.

Another study to mention is the RPMD calculations of Luo *et al.*[116] on an ordered phase of ice. They attempt to generalise the Green-Kubo method to RPMD by making the rather *ad hoc* assumption that the heat flux may be calculated within the RPMD framework by evaluating the classical heat flux formula using the centroid positions and momenta of the ring polymers - i.e. the same as the CMD approximation to $\hat{\mathbf{J}}$, although calculated within the full PIMD ensemble rather than that defined by the centroid potential of mean force. Although their results do not show much disagreement from the predictions of anharmonic lattice dynamics, they do not compare to any experimental results and the approximation in their definition of $\hat{\mathbf{J}}$ is lacking in theoretical justification - and so testing on more than one system is required to see if their approach really holds water. Moreover, it seems to us to be difficult to devise a theoretically justified estimator for the heat flux that is appropriate for use in RPMD but that is also computationally efficient and statistically well-behaved due to the complex form of said heat flux operator.

So, it appears from the liquid parahydrogen results and in particular the high non-linearity of the heat flux operator, that generalisation of the classical Green-Kubo method to path integral based approximate quantum dynamical methods like CMD or RPMD is not the best approach. Therefore, for the time being we will move onto discussing other classical methods which might be more suited to a CMD or RPMD generalisation. However, we will find in later Chapters that the Green-Kubo method will prove a useful tool in finding the quantum thermal conductivity using path integral methods.

## 3.4 Thermal conductivity from density fluctuations

In order to find a classical method for calculation of the thermal conductivity in molecular dynamics simulations that may be better suited to an adaptation within either the RPMD or CMD frameworks, we return to the linearised hydrodynamic

equations presented in Section 3.2. To summarise the results found in that Section, the three linearised hydrodynamic equations are, expressed in terms of the number density fluctuations, $\rho_1$, and the local temperature fluctuations, $T_1$, as the independent variables: the continuity equation for the number density

$$\frac{\partial \rho_1}{\partial t} = -\rho_0 \varphi_1, \tag{3.81}$$

the divergence of the Navier-Stokes equation

$$m\rho_0 \frac{\partial \varphi_1}{\partial t} + \frac{mc_s^2}{\gamma}\nabla^2 \rho_1 + \frac{m\rho_0 c_s^2 \alpha}{\gamma}\nabla^2 T_1 = \left(\frac{4}{3}\eta + \zeta\right)\nabla^2 \varphi_1, \tag{3.82}$$

and the energy transport equation

$$\rho_0 c_V \frac{\partial T_1}{\partial t} = \frac{mc_s^2 \alpha T_0}{\gamma}\frac{\partial \rho_1}{\partial t} + \kappa \nabla^2 T_1. \tag{3.83}$$

Analogously to the derivation of the Green-Kubo relation in Section 3.3, we can convert these into a set of algebraic equations by taking the spatial Fourier transform and the temporal Laplace transform to give, after some rearranging of terms,

$$s\tilde{\rho}_1(\mathbf{k}, s) + \rho_0 \tilde{\varphi}_1(\mathbf{k}, s) = \rho_1(\mathbf{k}, 0), \tag{3.84}$$

for the continuity equation, where the definitions of $\tilde{f}(\mathbf{k}, s)$ and $f(\mathbf{k}, 0)$ are the same as in Section 3.3,

$$\left(s + bk^2\right)\tilde{\varphi}_1(\mathbf{k}, s) - \frac{c_s^2 k^2}{\gamma \rho_0}\tilde{\rho}_1(\mathbf{k}, s) - \frac{c_s^2 \alpha k^2}{\gamma}\tilde{T}_1(\mathbf{k}, s) = \varphi_1(\mathbf{k}, 0), \tag{3.85}$$

for the divergence of the Navier-Stokes equation and

$$\left(s + ak^2\right)\tilde{T}_1(\mathbf{k}, s) - \frac{mc_s^2 \alpha T_0 s}{\gamma \rho_0 c_V}\tilde{\rho}_1(\mathbf{k}, s) = T_1(\mathbf{k}, 0) - \frac{mc_s^2 \alpha T_0}{\gamma \rho_0 c_V}\rho_1(\mathbf{k}, 0), \tag{3.86}$$

for the energy transport equation. Again, writing these as the matrix equation yields

$$\mathbf{M}\tilde{\boldsymbol{\psi}} = \mathbf{N}\boldsymbol{\psi}, \tag{3.87}$$

where in this case

$$\mathbf{M} = \begin{pmatrix} s & 0 & \rho_0 \\ \frac{-mc_s^2 \alpha T_0 s}{\gamma \rho_0 c_V} & s + ak^2 & 0 \\ \frac{-c_s^2 k^2}{\gamma \rho_0} & \frac{-c_s^2 \alpha k^2}{\gamma} & s + bk^2 \end{pmatrix}, \tag{3.88}$$

$$\mathbf{N} = \begin{pmatrix} 1 & 0 & 0 \\ \frac{-mc_s^2\alpha T_0}{\gamma\rho_0 c_V} & 1 & 0 \\ 0 & 0 & 1 \end{pmatrix}, \tag{3.89}$$

and

$$\tilde{\boldsymbol{\psi}} = \begin{pmatrix} \tilde{\rho}_1(k,s) \\ \tilde{T}_1(k,s) \\ \tilde{\varphi}_1(k,s) \end{pmatrix}, \qquad \boldsymbol{\psi} = \begin{pmatrix} \rho_1(k,0) \\ T_1(k,0) \\ \varphi_1(k,0) \end{pmatrix}. \tag{3.90}$$

Inverting the matrix $\mathbf{M}$ allows us to obtain the following equation for the Fourier-Laplace transform of the local number density

$$\tilde{\rho}_1(k,s) = A(k,s)\,\rho_1(k,0) + B(k,s)\,T_1(k,0) + C(k,s)\,\varphi_1(k,0), \tag{3.91}$$

where

$$A(k,s) = M_{11}^{-1} - \frac{mc_s^2\alpha T_0}{\gamma\rho_0 c_V} M_{12}^{-1}, \tag{3.92}$$

and $B(k,s) = M_{12}^{-1}$ and $C(k,s) = M_{13}^{-1}$.

Similarly to the entropy and the pressure, the local density and temperature are also thermodynamically independent variables[84] and therefore multiplying both sides by $\rho_1(-k,0)$ and taking the ensemble average will remove the temperature dependence since $\langle \rho_1(-k,0)\,T_1(k,0)\rangle = 0$. The local number density and the divergence of the local velocity also have opposite parity under time reversal so that $\langle \rho_1(-k,0)\,\varphi_1(k,0)\rangle = 0$ as well.[85] We also note that since the density and temperature are uniform in the equilibrium reference system, if we choose the wavevector, $k$, and the system length, $L$, to be along the $x$ axis such that the system contains an integer number of wavelengths in this direction, then the spatial Fourier transforms of $\rho_0$ and $T_0$ will be zero. Therefore, since $\rho = \rho_0 + \rho_1$, we are free to replace the Fourier and Fourier-Laplace transforms of the deviations $\rho_1$ and $T_1$ with the corresponding transforms of the overall local variables, $\rho$ and $T$. Upon taking the inverse Laplace transform we are then left with

$$\frac{F(k,t)}{F(k,0)} = \frac{\langle \rho(-k,0)\,\rho(k,t)\rangle}{\langle \rho(-k,0)\,\rho(k,0)\rangle} = \frac{1}{2\pi i}\int_{c-i\infty}^{c+i\infty} e^{st} A(k,s)\,ds, \tag{3.93}$$

where $c$ is a point on the real axis which is greater than the real part of any of the poles of $A(k,s)$. We have also identified the intermediate scattering function,

$$F(\mathbf{k},t) = \frac{1}{N}\langle \rho(-\mathbf{k},0)\,\rho(\mathbf{k},t)\rangle = \frac{1}{N}\left\langle \sum_{ij} e^{i\mathbf{k}\cdot[\mathbf{r}_j(t)-\mathbf{r}_i(0)]} \right\rangle, \tag{3.94}$$

which is a well-known function due to its importance in light and neutron scattering.[85; 117]

Determining the form of $A(k,s)$ by computing the inverse matrix elements $M_{11}^{-1}$ and $M_{12}^{-1}$ we find

$$A(k,s) = \frac{n(k,s)}{D(k,s)}, \tag{3.95}$$

where $n(k,s)$ is given by

$$n(k,s) = s^2 + (a+b)k^2 s + abk^4 + \frac{\gamma - 1}{\gamma} c_s^2 k^2, \tag{3.96}$$

and $D(k,s)$ is the determinant of $\mathbf{M}$ and is equal to

$$D(k,s) = s^3 + (a+b)k^2 s^2 + \left(c_s^2 k^2 + abk^4\right) s + \frac{ac_s^2 k^4}{\gamma}. \tag{3.97}$$

So, again analogously to our derivation of the Green-Kubo relation, the poles of $A(k,s)$ are at the roots of the cubic equation $D(k,s) = 0$ and consist of one real root, $s_0$, and a complex conjugate pair, $s_\pm$. Since the real part of all of these roots must be negative, we may form a contour integral by closing the contour with a large semicircle in the left-hand side of the complex plane to evaluate the inverse Laplace transform - where the integral goes to zero on the large semicircle due to Jordan's Lemma. Then, by Cauchy's Residue Theorem the desired integral is just the sum of the residues of the three enclosed poles

$$\frac{F(k,t)}{F(k,0)} = \frac{n(k,s_0)\, e^{s_0 t}}{(s_0 - s_+)(s_0 - s_-)} + \frac{n(k,s_+)\, e^{s_+ t}}{(s_+ - s_0)(s_+ - s_-)} + \frac{n(k,s_-)\, e^{s_- t}}{(s_- - s_0)(s_- - s_+)}. \tag{3.98}$$

Mountain[117] first derived this equation for the intermediate scattering function in the context of light scattering, but a few studies since have taken to using this equation a tool for calculating the thermal conductivity in molecular dynamics simulations - via computation of $F(k,t)$ during the simulation and then fitting to an appropriate functional form to obtain an estimate of $\kappa$ (which we recall that the hydrodynamic parameter $a = \kappa/\rho_0 c_V$ is related to). The first attempt at this which we are aware of was by Schoen *et al.*[118], studying a simple Lennard-Jones fluid and it has recently been rediscovered by Cheng and Frenkel[107] who applied it in

the context of machine-learned and non-pairwise additive potentials - for which the calculation of the heat flux vector in the Green-Kubo relation is difficult. All three of these considered approximate solutions to the roots of $D(k,s)$ in the $k \to 0$ limit, similar to the approximate roots found in the derivation of the Green-Kubo relation in Section 3.3. At the very least, the form of Eq. 3.98 which results from using these approximate roots gives us some insight on the behaviour of the intermediate scattering function in the hydrodynamic limit - and so we will present the derivation for $F(k,t)$ that results from these approximate roots here. However, we will see later on that in the context of using Eq. 3.98 as a tool to fit simulation data to that the approximate roots are not necessarily needed.

Since the determinant $D(k,s)$ found in Eq. 3.97 is identical to that in Eq. 3.51, the approximate roots are in fact the same as those found in the Green-Kubo case - $s_0 \approx -D_T k^2$ and $s_\pm \approx \pm i c_s k - \Gamma k^2$. Inserting these into Eq. 3.98 we obtain

$$\begin{aligned}\frac{n(k,s_0)}{(s_0-s_+)(s_0-s_-)} &\approx \frac{(a-D_T)(b-D_T)k^4 + \frac{\gamma-1}{\gamma}c_s^2k^2}{(\Gamma-D_T)^2k^4 + c_s^2k^2} \\ &= \frac{\gamma-1}{\gamma} + \mathcal{O}\left(k^2\right), \end{aligned} \tag{3.99}$$

$$\begin{aligned}\frac{n(k,s_+)}{(s_+-s_-)(s_+-s_0)} &\approx \frac{(\Gamma-a)(\Gamma-b)k^4 + ic_sD_Tk^3 - \frac{c_s^2}{\gamma}k^2}{2ic_sk^3(D_T-\Gamma) - 2c_s^2k^2} \\ &= \frac{\frac{1}{2\gamma} - \frac{iD_T}{2c_s}k + \mathcal{O}(k^2)}{1 - \frac{i}{c_s}(D_T-\Gamma)k} \\ &= \frac{1}{2\gamma} + \frac{i}{2\gamma c_s}\left[(1-\gamma)D_T - \Gamma\right]k + \mathcal{O}\left(k^2\right), \end{aligned} \tag{3.100}$$

and

$$\begin{aligned}\frac{n(k,s_-)}{(s_--s_+)(s_--s_0)} &= \left(\frac{n(k,s_+)}{(s_+-s_-)(s_+-s_0)}\right)^* \\ &\approx \frac{1}{2\gamma} - \frac{i}{2\gamma c_s}\left[(1-\gamma)D_T - \Gamma\right]k + \mathcal{O}\left(k^2\right), \end{aligned} \tag{3.101}$$

where $(\dots)^*$ signifies the complex conjugate. Neglecting the terms in these equations which are $\mathcal{O}(k^2)$ and greater, Eq. 3.98 becomes

$$\frac{F(k,t)}{F(k,0)} \approx \frac{\gamma-1}{\gamma}e^{-D_Tk^2t} + \frac{1}{\gamma}e^{-\Gamma k^2t}\left[\cos(c_skt) + d(k)\sin(c_skt)\right], \tag{3.102}$$

where the function $d(k)$ is

$$d(k) = \frac{k}{c_s}\left[(\gamma - 1) D_T + \Gamma\right], \tag{3.103}$$

which is the form derived by Berne[85] and used by Schoen *et al.*[118] The intermediate scattering function, normalised by its $t = 0$ value, therefore contains a decaying thermal diffusion component of fraction $1 - 1/\gamma$ and decay time determined by the thermal diffusivity $D_T$ and an oscillating sound wave component of fraction $1/\gamma$ that decays according to the sound attenuation coefficient $\Gamma$. Mountain's original derivation,[117] as well as the fitting functions used by Cheng and Frenkel,[107] additionally neglected the $d(k)$ term in Eq. 3.102. However this is clearly incomplete, since then the approximate form for $F(k,t)$ does not satisfy the condition

$$\left.\frac{dF(k,t)}{dt}\right|_{t=0} = 0, \tag{3.104}$$

which must be true for all autocorrelation functions.[84] When the $d(k)$ term is included however, then the approximate form for $F(k,t)$ does satisfy this condition.

Fitting the intermediate scattering function calculated from a molecular dynamics simulation to this functional form would then allow us to determine the four unknown hydrodynamic parameters, $a$, $b$, $\gamma$ and $c_s$ - or equivalently $D_T$ and $\Gamma$ instead of $a$ and $b$. We will stick to $a$ and $b$ as our parameters of choice in this thesis even if they do not explicitly appear in Eq. 3.102 as it is written, since these are the "true" hydrodynamic parameters present in Eq. 3.98. But fitting to four unknown parameters is not ideal, and thankfully in this case it is also avoidable since $\gamma$ and $c_s$ are static equilibrium properties which may be computed independently and straightforwardly by other methods, either in the same simulation or a separate one. Perhaps the simplest approach to calculating $c_s$ and $\gamma$ is to use their definitions in terms of the thermodynamic derivatives of the total energy, $E$, and the pressure, $P$,[107] where

$$c_V = \frac{1}{N}\left(\frac{\partial E}{\partial T}\right)_\rho, \tag{3.105}$$

$$c_P - c_V = -\frac{T}{\rho^2}\left(\frac{\partial P}{\partial T}\right)_\rho^2 \left(\frac{\partial P}{\partial \rho}\right)_T^{-1}, \tag{3.106}$$

which together allow for determination of $c_P$ and so also $\gamma = c_P/c_V$, and

$$c_s^2 = -\frac{\gamma}{m}\left(\frac{\partial P}{\partial \rho}\right)_T, \tag{3.107}$$

for the adiabatic speed of sound. The average energy and pressure may be computed easily within an $NVT$ molecular dynamics simulation, both within classical molecular dynamics and path-integral molecular dynamics. By calculating the values of $E$ and $P$ at a set of volumes and temperatures surrounding the state point of interest then one can evaluate the thermodynamic derivatives in Eqs 3.105, 3.106 and 3.107 by finite difference and obtain an estimate for $c_s$ and $\gamma$. Using these values in Eq. 3.102 means we only need to fit to the two remaining unknown parameters, $a$ and $b$.

Considering that our assumptions of local thermodynamic equilibrium are only valid in the $k \to 0$ limit, one may be lead to believe that the approximate $\mathcal{O}(k)$ solution represented by Eq. 3.102 would be sufficient to model the simulation data accurately. However, in real simulations the smallest available value of $k$ is $2\pi/L$, where $L$ is the largest dimension of the simulation box. One is therefore limited by the system sizes accessible within reasonable computational time, and this results in having to apply Eq. 3.102 to systems which are as close to the hydrodynamic limit as possible, but that are not necessarily in the hydrodynamic limit. This case represents the field of *generalised hydrodynamics*,[119; 120] which we will not discuss in detail here other than to say that we can model the unknown dynamical parameters $a$ (or equivalently $D_T$) and $b$ as being functions of $k$. The functions $a(k)$ and $b(k)$ must go to their bulk values, $a$ and $b$, as $k \to 0$. Without any information on the form of these functions, the procedure one takes to extract $a$ or $D_T$ is to compute $a(k)$ or $D_T(k)$ for a set of values of $k$ which are as small as is possible, and then perform some sort of extrapolation procedure to find the $k \to 0$ limit of these functions and to obtain the bulk value. Various extrapolation methods are available, and the approach we will use here is a linear fit of $1/a(k)$ against $k$ to find the value of $a(k)$ at $k = 0$, since this extrapolation scheme is also used for calculating the

bulk thermal conductivity within the context of a well-established non-equilibrium method[5; 104] and in the system size dependence of the diffusion constant.[22]

Returning to our expression for $D(k,s)$, Eq. 3.97, we note that since it is always possible to write closed form solutions for a cubic equation that one may solve for the roots exactly and then use these in the equation for $F(k,t)$, Eq. 3.98. This has the disadvantage that the resulting expression for $F(k,t)$ is more opaque and that the exact roots may be difficult to work with algebraically - but if the aim is to use the equation as a model to fit data to then using the exact roots will be no more complicated than using the approximate roots after an appropriate fitting routine has been implemented. Additionally, since the equation for $F(k,t)$ then contains terms to all orders in $k$ it is possible that the values of $a(k)$ will have a smaller $k$ dependence than they would if the approximate roots were used, and this is something that we will test when applying our fits of $F(k,t)$ to real simulation data.

The quantum mechanical analogue of the classical intermediate scattering function is still a non-linear operator in terms of position due to the presence of the $e^{i\mathbf{k}\cdot\mathbf{r}}$ terms. In our paper[113] we stated that that since $e^{i\mathbf{k}\cdot\mathbf{r}} \sim 1 + i\mathbf{k}\cdot\mathbf{r}$ as $k \to 0$ that the operator does become approximately linear in the hydrodynamic limit. This is not strictly true in practice, as in order to calculate the intermediate scattering function in the $k \to 0$ limit one must also take the limit as $L \to \infty$. Therefore, whilst $F(k,t)$ does become a linear operator in the local sense, it does not necessarily become linear when computed as the sum over an increasingly large simulation box. However, the self part of the intermediate scattering function

$$F_{\text{self}}(k,t) = \frac{1}{N}\left\langle \sum_i e^{i\mathbf{k}\cdot[\mathbf{r}_i(t)-\mathbf{r}_i(0)]} \right\rangle, \tag{3.108}$$

has been previously calculated using RPMD[60; 121] and CMD[20] and the approximation was found to be successful in the $k \to 0$ limit. Therefore, it is possible that the RPMD/CMD estimates of the full intermediate scattering function may perform better than they did for the heat flux in the Green-Kubo relation, and we will see later on that this is indeed the case.

### 3.4.1 Thermal conductivity from local temperature fluctuations

Returning to the hydrodynamic matrix equation of Eq. 3.87, it is also possible to derive a relation for the autocorrelation function of the Fourier components of the local temperature in a similar fashion to how Eq. 3.98 was derived. After inverting the matrix $\mathbf{M}$ in Eq. 3.87, multiplying both sides by $T_1(-k,0)$ and taking the ensemble average we have, remembering that the Fourier components of the temperature and density are instantaneously uncorrelated and that the $T_1$ and $\varphi_1$ have opposite parity under time reversal,

$$C_{TT}(k,t) = \frac{\langle T(-k,0)\,T(k,t)\rangle}{\langle T(-k,0)\,T(k,0)\rangle} = \mathcal{L}^{-1}\left\{\frac{C(k,s)}{D(k,s)}\right\}, \tag{3.109}$$

where the function $C(k,s)$ is given by

$$C(k,s) = s\left(s + bk^2\right) + \frac{c_s^2 k^2}{\gamma}. \tag{3.110}$$

Performing the inverse Laplace transform as before we find that

$$C_{TT}(k,t) = \frac{C(k,s_0)\,e^{s_0 t}}{(s_0-s_+)(s_0-s_-)} + \frac{C(k,s_+)\,e^{s_+ t}}{(s_+-s_0)(s_+-s_-)} + \frac{C(k,s_-)\,e^{s_- t}}{(s_--s_0)(s_--s_+)}, \tag{3.111}$$

where $s_0$, $s_+$ and $s_-$ are the same roots as in Eq. 3.98. Eq. 3.111 may already be used as a fitting model, but we can gain greater insight into its form by using the approximate roots $s_0 \approx -D_T k^2$ and $s_\pm \approx \pm i c_s k - \Gamma k^2$. Then we have that

$$\begin{aligned}\frac{C(k,s_0)}{(s_0-s_+)(s_0-s_-)} &= \frac{\frac{c_s^2 k^2}{\gamma} + \left(D_T^2 - D_T b\right)k^4}{c_s^2 k^2 + \left(\Gamma - D_T\right)^2 k^4} \\ &= \frac{1}{\gamma} + \mathcal{O}\left(k^2\right),\end{aligned} \tag{3.112}$$

$$\begin{aligned}\frac{C(k,s_+)}{(s_+-s_0)(s_+-s_-)} &= \frac{\frac{1-\gamma}{\gamma}c_s^2 k^2 + i\left(b-2\Gamma\right)c_s k^3 + \left(\Gamma^2 - \Gamma b\right)k^4}{2ic_s k^3\left(D_T-\Gamma\right) - 2c_s^2 k^2} \\ &= \frac{\frac{\gamma-1}{2\gamma} + \frac{i}{2c_s}\left(2\Gamma - b\right)k + \mathcal{O}\left(k^2\right)}{1 - \frac{i}{c_s}\left(D_T-\Gamma\right)k} \\ &= \frac{\gamma-1}{2\gamma} + \frac{i\left(\gamma-1\right)}{2\gamma c_s}\left[\left(\gamma+1\right)D_T - \Gamma\right]k + \mathcal{O}\left(k^2\right),\end{aligned} \tag{3.113}$$

where in the last line we have used the identity $2\Gamma - b = (\gamma - 1) D_T$ to simplify some terms, and finally

$$\frac{C(k, s_-)}{(s_- - s_0)(s_- - s_+)} = \frac{\gamma - 1}{2\gamma} - \frac{i(\gamma - 1)}{2\gamma c_s} [(\gamma + 1) D_T - \Gamma] k + \mathcal{O}\left(k^2\right), \quad (3.114)$$

from taking the complex conjugate of Eq. 3.113. Using these inside of our expression for $C_{TT}(k, t)$, and neglecting terms which are $\mathcal{O}(k^2)$ and higher, we obtain

$$C_{TT}(k, t) = \frac{1}{\gamma} e^{-D_T k^2 t} + \frac{\gamma - 1}{\gamma} e^{-\Gamma k^2 t} [\cos(c_s k t) + f(k) \sin(c_s k t)], \quad (3.115)$$

where in this case the function $f(k)$ is given by

$$f(k) = \frac{k}{c_s} [\Gamma - (\gamma + 1) D_T]. \quad (3.116)$$

So, Eq. 3.115 shares many similarities with Eq. 3.102 but with the relative proportion of the thermal decay and sound wave terms switched. We note that in this case, even with the $f(k)$ correction the time derivative of $C_{TT}(k, t)$ at $t = 0$ is non-zero but is instead equal to $-ak^2$. Eq. 3.115 represents an alternative to Eq. 3.102 available for when $\gamma$ is close to unity, since in this case the fraction of the signal dependent on the thermal diffusivity in the intermediate scattering function becomes very small.

In practice, the local temperature is more difficult to define than the local density within a molecular dynamics simulation. This will be discussed in greater detail when we apply a generalisation of Eq. 3.111 to simulation data obtained from solids in Chapter 6.

# 4

# Thermal conductivity of quantum liquids

## 4.1 Introduction

As a starting point to calculate the quantum mechanical thermal conductivity using path-integral based methods, we focus on the liquid phase - where the simulation times required will likely be shorter and the mechanisms for heat transfer are less complex. In this Chapter we will develop a methodology to obtain a CMD estimate of the thermal conductivity that is more in line with experimental values, choosing first to focus on the case of parahydrogen. We will begin by describing a method to precompute the centroid potential of mean force applicable to liquids which are described by a pair potential, which reduces the computational cost of performing our CMD calculations considerably. We then use the hydrodynamic equation for the intermediate scattering function, Eq. 3.98, as a fitting model to obtain the CMD thermal diffusivity, $a_{\mathrm{CMD}}$. We show that when this is combined with the constant volume heat capacity calculated using PIMD, $c_{V,\mathrm{PIMD}}$, that one obtains a thermal conductivity $\kappa = a_{\mathrm{CMD}}\rho c_{V,\mathrm{PIMD}}$ which is much closer to experimental values than previous studies. We use this as a motivation to develop a more efficient method to calculate the thermal conductivity using CMD, by devising a scaling to "fix" the CMD generalisation of the Green-Kubo relation. We then apply this across a wide range of temperatures from the triple point to the critical

point close to the saturation line, and find good agreement with experimental data. Finally, we also apply this methodology to the case of liquid helium, and show that it works just as well for that.

## 4.2 Silvera-Goldman parahydrogen

Molecular hydrogen, $H_2$, exists in one of two states based on the alignment of the two nuclear spins - ortho (aligned) and para (opposite). Although liquid hydrogen generally consists of a mixture of these two states, highly concentrated solutions of the lower energy parahydrogen state may be prepared through the use of a catalytic procedure.[122] The properties of liquid hydrogen, including the thermal conductivity, have been studied extensively experimentally due to its applications as a fuel source and in nuclear physics.[123] Parahydrogen has also been of interest recently to enhance the signals in nuclear magnetic resonance (NMR) and magnetic resonance imaging (MRI) applications.[124]

Theoretically, parahydrogen is useful in that it is a liquid where nuclear quantum effects play a significant role in the dynamics but identical particle exchange effects are small even close to the triple point, $T_t = 13.8\,\mathrm{K}$.[22] Further, in parahydrogen rotational states with odd values of $J$ are forbidden due to the Pauli exclusion principle. The rotational temperature of hydrogen is $\theta_{\mathrm{rot}} \approx 87.6\,\mathrm{K}$, so the thermal population of the first excited $J = 2$ state will be exceedingly small, even close to the critical temperature of $T_c = 33.1\,\mathrm{K}$.[22] We can therefore approximate that the system lies solely in the spherically symmetric $J = 0$ rotational state, which may be modelled using a simple pair potential.

We describe the interactions between parahydrogen molecules using the potential due to Silvera and Goldman,[110] where the pair energy between two molecules at a separation $r$ is given by

$$u(r) = \exp\left(\alpha - \beta r - \gamma r^2\right) - \left[\frac{C_6}{r^6} + \frac{C_8}{r^8} - \frac{C_9}{r^9} + \frac{C_{10}}{r^{10}}\right] f(r), \tag{4.1}$$

where

$$f(r) = \begin{cases} \exp\left[-\left(\frac{r_0}{r} - 1\right)^2\right], & r \leq r_0 \\ 1, & r > r_0. \end{cases} \tag{4.2}$$

The various parameters for the Silvera-Goldman potential are provided in Table 4.1 below. In this potential the first exponential term models the hard wall close range repulsion between hydrogen molecules, and the $C_6$, $C_8$ and $C_{10}$ terms incorporate dispersion interactions. The $C_9$ term is added to include a pairwise approximation of three-body effects into the potential. The Silvera-Goldman potential has been found to predict the values of many properties of parahydrogen relatively accurately when used in conjunction with PIMD, CMD or RPMD.[20; 22]

| | |
|---|---|
| $\alpha$ | 1.713 |
| $C_6$ | 12.14 |
| $\beta$ | 1.5671 |
| $C_8$ | 215.2 |
| $\gamma$ | 0.00993 |
| $C_9$ | 143.1 |
| $r_0$ | 8.32 |
| $C_{10}$ | 4813.9 |

**Table 4.1:** Parameters for the Silvera-Goldman potential, given in atomic units.

All simulations in this Section were performed using a timestep of 2 fs, which was found to be sufficient to conserve both the total centroid energy in our CMD calculations and the ring polymer Hamiltonian in our PIMD simulations. We truncate and shift the interactions at a cutoff radius of $r_c = 15\, a_0$ and use periodic boundary conditions throughout. All $NVT$ PIMD simulations were performed using the PILE-G thermostatting procedure, where Langevin thermostats are attached to each internal mode of the ring polymers and a stochastic velocity rescaling thermostat is applied to the centroid.[40] For the CMD and classical simulations we used the stochastic velocity rescaling thermostat proposed by Bussi *et al.*[125] We used $P = 128$ ring polymer beads for all PIMD simulations presented in this Section.

### 4.2.1 The CMD potential of mean force

Despite the fact that liquids present a more straightforward case to calculate the thermal conductivity than solids, we still anticipate that large system sizes will be necessary to approximately simulate the hydrodynamic limit. It is therefore advisable to devise ways in which one can alleviate the additional computational

expense of performing path integral simulations, which we may recall require in principle $P$ times the effort of classical simulations, where $P$ is the number of path integral beads needed. In this subsection we will present a method to precompute the centroid potential of mean force (CPMF), tailored to the specific case of a pair potential in an isotropic liquid, which reduces the computational cost of CMD calculations to the same as the classical case. The approach shares many similarities with the "fast-CMD" approach used by Hone *et al.*[21] except that we make use of additional simplifications applicable to the aforementioned special case we are considering here.

The approach which we use is incredibly simple - first, we make the approximation that the centroid potential of mean force is pairwise additive. This is not generally true, but it seems reasonable to assume that many body effects in the centroid potential of mean force will be small if the underlying classical potential is also pairwise additive (recent developments on precomputation of the centroid potential of mean force have been done by machine learning the potential using a neural network,[126–128] in which case many body effects are included automatically). Then, at each configuration generated by a PIMD trajectory one may calculate the centroid component of the pair force on ring polymer $i$ due to the presence of ring polymer $j$ as

$$\mathbf{F}_{ij}^{(c)} = \frac{1}{P}\sum_{k=1}^{P}\mathbf{F}_{ij}^{(k)} = -\frac{1}{P}\sum_{k=1}^{P}\frac{\mathbf{r}_{ij}^{(k)}}{r_{ij}^{(k)}}\frac{du\left(r_{ij}^{(k)}\right)}{dr_{ij}^{(k)}}, \tag{4.3}$$

where $\mathbf{F}_{ij}^{(k)}$ is the force from the classical potential $u\left(r_{ij}^{(k)}\right)$ on the $k^{\text{th}}$ bead of ring polymer $i$ due to the presence of the $k^{\text{th}}$ bead of ring polymer $j$ and $\mathbf{r}_{ij}^{(k)} = \mathbf{r}_{i}^{(k)} - \mathbf{r}_{j}^{(k)}$ is the separation vector between the $k^{\text{th}}$ beads of the ring polymers. As the magnitude of the pairwise approximation to the centroid mean force must only be a function of the separation of the centroids, $r_{ij}^{(c)} = |\mathbf{r}_{ij}^{(c)}|$, where $\mathbf{r}_{ij}^{(c)} = \mathbf{r}_{i}^{(c)} - \mathbf{r}_{j}^{(c)}$ is the separation vector between the centroids of ring polymers $i$ and $j$, we may calculate the projection of $\mathbf{F}_{ij}^{(c)}$ along the centroid-centroid separation vector using

$$f_{ij}^{(c)}\left(r_{ij}^{(c)}\right) = \frac{\mathbf{r}_{ij}^{(c)}\cdot\mathbf{F}_{ij}^{(c)}}{r_{ij}^{(c)}} = -\frac{1}{P}\sum_{k=1}^{P}\frac{\mathbf{r}_{ij}^{(c)}\cdot\mathbf{r}_{ij}^{(k)}}{r_{ij}^{(c)}r_{ij}^{(k)}}\frac{du\left(r_{ij}^{(k)}\right)}{dr_{ij}^{(k)}}. \tag{4.4}$$

We may then obtain the pairwise approximation to the centroid potential of mean force, $u^{(c)}(r)$, by integrating the average of the centroid mean force as

$$u^{(c)}(r) = \int_r^\infty dr_{ij}^{(c)} \left\langle f^{(c)}\left(r_{ij}^{(c)}\right)\right\rangle, \tag{4.5}$$

and we may also use the same cutoff radius, $r_c$, for $u^{(c)}(r)$ as for the classical pair potential $u(r)$, meaning can replace the upper limit of the integral in Eq. 4.5 with $r_c$ - which is equivalent to truncating and shifting the CPMF at the chosen cutoff. Therefore, $u^{(c)}(r)$ may be calculated from a PIMD simulation which only requires small system sizes. Furthermore, due to the large number of centroid pairs ($\mathcal{O}(N^2)$) at each snapshot of the PIMD trajectory, the statistical errors in $f^{(c)}\left(r_{ij}^{(c)}\right)$ become small even after a short simulation and one only needs to simulate for a relatively short time to obtain $u^{(c)}(r)$. So, whilst one does still need to perform a full PIMD simulation at each thermodynamic state point to obtain $u^{(c)}(r)$, this may be achieved without too significant of a computational expense - and once $u^{(c)}(r)$ has been found it may then be applied to larger systems requiring longer simulation times with the same effort as for a classical molecular dynamics simulation. This provides a significant saving in computational expense over the conventional partially adiabatic CMD algorithm, not only because it requires a factor of $P$ fewer force evaluations to propagate the dynamics but also because we do not need to integrate over the rapid fluctuations of the internal modes of the ring polymers, so we may use the same timestep as we would in a classical simulation. We will therefore use CMD rather than RPMD in our calculations, since with the precomputation of the CPMF then CMD is a lot more efficient than RPMD.

For the purposes of this subsection we choose to focus on the CPMFs for two state points in detail, and show that various static and dynamical properties calculated from them are consistent with other studies. The first state point is at a temperature of 14 K and a molar volume of 25.6 $\mathrm{cm^3\,mol^{-1}}$, close to the triple point, and the second is at a temperature of 25 K and a molar volume of 31.7 $\mathrm{cm^3\,mol^{-1}}$. Both of these state points are in the liquid phase close to the liquid-vapour saturation line of the Silvera-Goldman potential. We choose to focus on these two state points in

particular because they have been used in a wide variety of previous investigations of Silvera-Goldman parahydrogen using PIMD, RPMD and CMD.[21; 22]

In practice, we compute the CPMF from a set of PIMD simulations as follows. First, the system is initialised on a face centred cubic lattice of $4 \times 4 \times 4$ unit cells ($N = 256$ molecules) at the chosen density, and then allowed to melt by running in the path integral $NVT$ ensemble for an equilibration period of 100ps. After equilibration, the simulation was then run for a further 100ps in order to calculate the centroid potential of mean force. At each timestep, the separation vector between each pair of centroids was calculated and, if its magnitude was less than $r_c$, placed in one of a set of histogram bins of width $0.01\,a_0$ arranged from zero up to the cutoff radius. A neighbour list scheme for the centroids could have been used to reduce the number of centroid separation vectors which need to be computed at every timestep, however for the small systems we are considering here the simulations are already fast enough that we did not implement one in this case. For long range potentials where $r_c$ is larger then this would be advisable. The value of $f_{ij}^{(c)}$ was accumulated within each histogram bin and the average value computed over the simulation which was then used to integrate $u^{(c)}(r)$ using the midpoint rule. This gives us the value of $u^{(c)}(r)$ at a grid of points which may then be fitted to a cubic spline to convert the grid into a smoothly varying potential with which one may compute forces and so use to propagate the centroid dynamics in a CMD simulation.

The CPMFs computed via this method at the 14 K and 25 K state points are shown as an example in Fig. 4.1, as well as the classical Silvera-Goldman potential for a reference. The first thing to note about the CPMFs is that since the centroid constrained path integral ensemble which defines the CPMF is different at different temperatures and densities, the resulting CPMF will also vary with temperature and density. The main features of the CPMFs are that the potential well is shifted to larger separation and becomes shallower, which may be rationalised by referring to the effects of zero point energy and ring polymer swelling - and these effects become more pronounced at lower temperatures where quantum mechanical effects are more significant. As the temperature increases, the CPMF

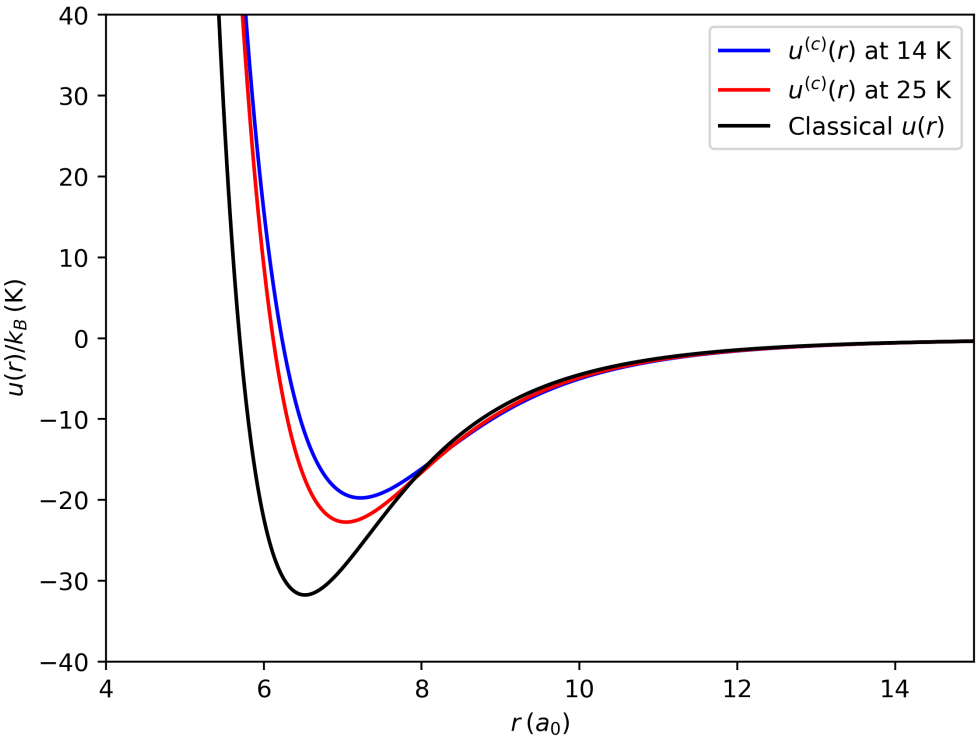



**Figure 4.1:** Centroid potentials of mean force calculated at the 25 K and 14 K state points. The classical Silvera-Goldman potential is also shown for reference.

more closely approximates the classical Silvera-Goldman potential since CMD reduces to classical mechanics in the high temperature limit. The CPMFs are also observed to be more repulsive at short separations and more attractive at large separations than the classical potential. At very short $r$ we do not attain any information on the centroid mean force from our PIMD simulation since the probability of finding two centroids so close together rapidly approaches zero. To prevent any unforeseen effects in the rare event that molecules penetrate into this region during our CMD simulations we add an exponentially repulsive term to the CPMF in the region where we do not obtain sufficient information on $f^{(c)}(r)$ from our short PIMD simulation. For Silvera-Goldman parahydrogen the CPMF is already highly repulsive in this region, so any inaccuracies which arise from adding this term should have a negligible effect on the dynamics.

The approach we have detailed here for the precomputation of the CPMF

is simple to apply to systems in the liquid phase, where the PIMD centroid radial distribution function (RDF) is non-zero for all separations above some minimum value, and thus one has information on the average centroid force over the whole range of centroid separations which are relevant for the dynamics - making integration of this average centroid force to obtain the CPMF straightforward. This is obviously not the case for solids, where the PIMD centroid radial distribution function goes to zero for centroid separations which are in between the different coordination shells of the solid structure. Therefore, one obtains no information on the centroid mean force within the troughs of the PIMD centroid radial distribution function, and so Eq. 4.5 cannot be used to integrate the CPMF through these regions with the data obtained from a PIMD simulation. An alternative in these situations would be to fit the CPMF in the regions where it can be integrated from Eq. 4.5 to some appropriate functional form, perhaps based on the underlying classical potential with adjustable parameters, and use this to extrapolate the CPMF over the separations where it cannot be integrated using Eq. 4.5. One could also use techniques such as iterative Boltzmann inversion[129–131] to provide additional corrections to the CPMF if the extrapolation procedure yields radial distribution functions which are still not in agreement with the PIMD centroid radial distribution function - although this method will be best applied to situations where the differences between the two radial distribution functions is small. Nevertheless, it seems likely that extrapolating the CPMF through the regions where it cannot be obtained accurately would give a good baseline, and any corrections that may still be necessary will be small enough for a technique like iterative Boltzmann inversion to be able to rectify.

In order to test how accurate our CPMFs were at capturing the properties of the system, we calculated the radial distribution functions, $g(r)$, at both the 25 K and the 14 K state points and compared them with the radial distribution function of the centroids, $g^{(c)}(r)$, calculated from a PIMD simulation at the same state points. These radial distribution functions could have been calculated using the conventional "histogram binning" method in a manner similar to the way in which the values of

$f^{(c)}(r)$ were calculated from a PIMD simulation earlier. However, in our simulations we used the force based estimator developed by Borgis *et al.*,[132; 133] which gives a smaller variance in the computed $g(r)$ and thus allows us to obtain converged results in a much shorter simulation time.[132] In this approach $g(r)$ is calculated as

$$g(r) = \frac{\beta}{4\pi N\rho} \left\langle \sum_{i \neq j} \frac{1}{2r_{ij}^3} (\mathbf{F}_j - \mathbf{F}_i) \cdot \mathbf{r}_{ij}\, \theta(r - r_{ij}) \right\rangle, \tag{4.6}$$

where $\mathbf{F}_i$ is the total force acting on the molecule $i$ and $\theta(r - r_{ij})$ is the Heaviside step function. Due to the presence of $\theta(r - r_{ij})$ every pair of molecules with separation $r_{ij}$ less than $r$ contribute to the radial distribution function at the point $r$. When using Eq. 4.6 to calculate the PIMD centroid RDF all force and position vectors are simply replaced by the corresponding centroid force and position vectors. This is in contrast to the histogram binning approach to computing the radial distribution function

$$g(r) = \frac{1}{4\pi r^2 N\rho} \left\langle \sum_{i \neq j} \delta(r_{ij} - r) \right\rangle, \tag{4.7}$$

where only pairs of molecules with separations $r_{ij}$ that fall inside a particular histogram bin contribute to the radial distribution function in that bin. The greater number of contributions at each separation are likely part of the reason why the force based estimator of Eq. 4.6 gives better statistics.[133]

The CMD calculations were performed using the same system size, timestep and potential cutoff radius as the PIMD simulations used to calculate the CPMF that were detailed earlier. These are shown for the 25 K state point in Fig. 4.2 and the 14 K state point in Fig. 4.3. Also shown in both Figures are the radial distribution functions which one would obtain by performing purely classical molecular dynamics on the Silvera-Goldman potential at these state points. The CMD and centroid PIMD RDFs show almost perfect agreement at both state points, and a similar observation was found, although not shown here, at the other state points considered in this Chapter. This provides confidence that the pairwise approximation to the CPMF made earlier was justified and that our effective classical potentials include the relevant nuclear quantum effects accurately. The purely classical $g(r)$ is distinctly different to both the centroid PIMD and CMD $g(r)$, showing that nuclear quantum

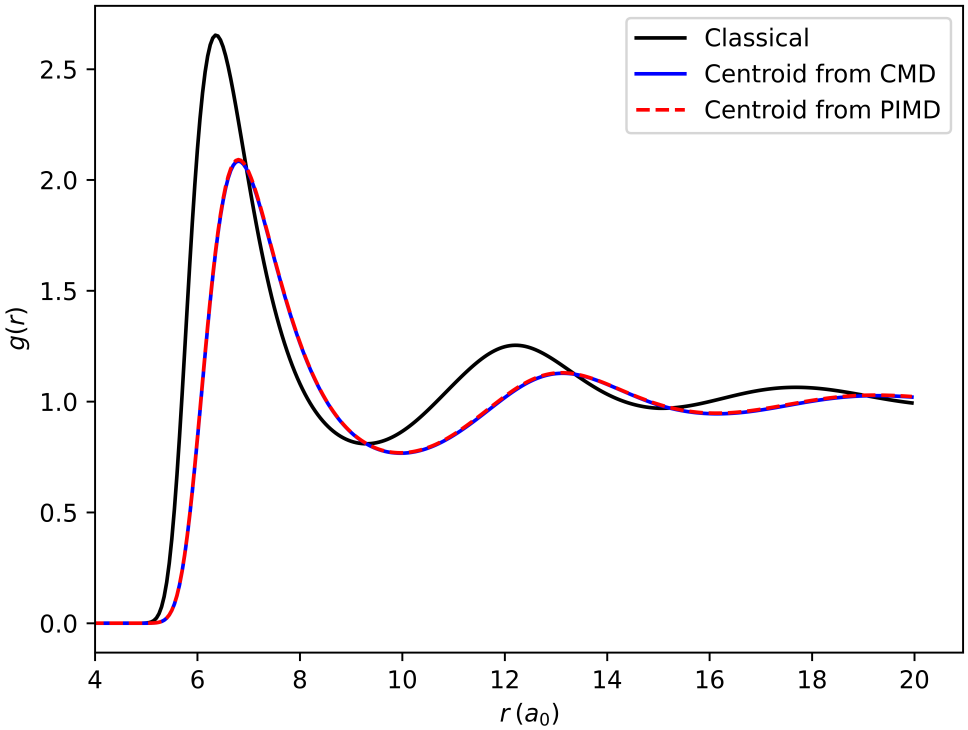



**Figure 4.2:** Various radial distribution functions calculated at $T = 25.0\,\mathrm{K}$ and molar volume $V = 31.7\,\mathrm{cm}^3\,\mathrm{mol}^{-1}$.

effects play a significant role at these state points. In fact, although the quantum mechanical simulations lie in the liquid phase close to the saturated vapour line of the quantum thermodynamic phase diagram - nuclear quantum effects are large enough such that in the classical simulations these lie within the liquid-vapour coexistence region of the corresponding classical thermodynamic phase diagram. As such, when performing a classical molecular dynamics simulation at these state points a bubble will spontaneously form within the simulation.[22] This means that purely classical simulations are not even in the same phase as the CMD or PIMD simulations - and so it does not make sense to compare the thermal conductivity or other quantities calculated at the state points considered in this Section from classical molecular dynamics with those from CMD, and we will not attempt to do so here.

As an additional check, to confirm that our CPMFs were also capturing the quantum dynamics adequately we computed the (Kubo-transformed) velocity

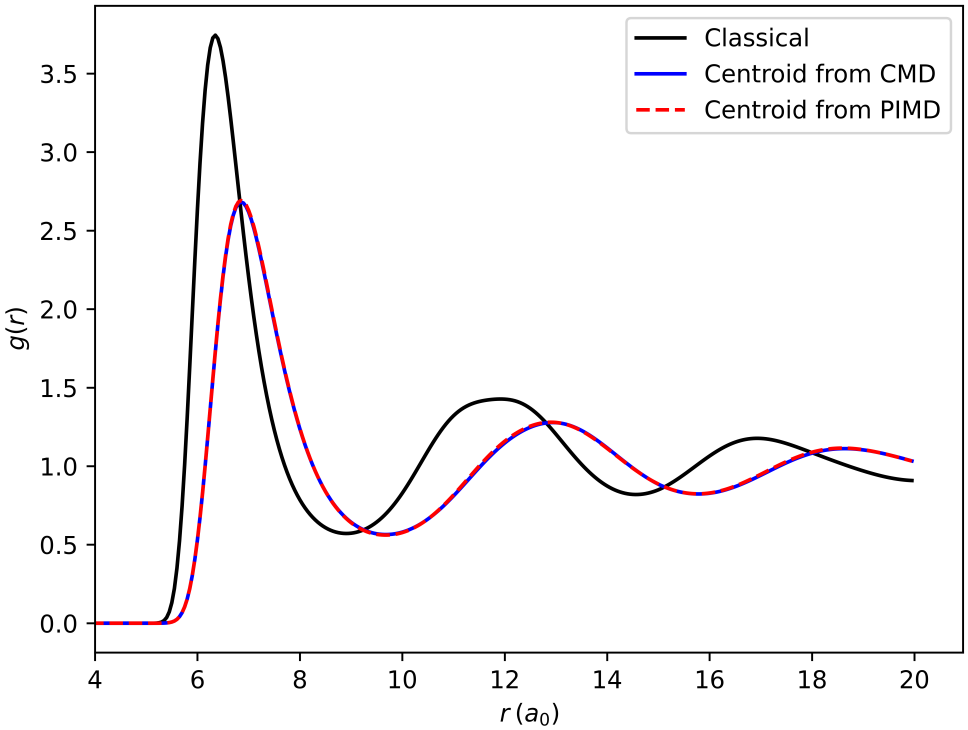



**Figure 4.3:** Various radial distribution functions calculated at $T = 14.0\,\mathrm{K}$ and molar volume $V = 25.6\,\mathrm{cm}^3\,\mathrm{mol}^{-1}$.

autocorrelation functions at the 14 K and the 25 K state points. In order to calculate these autocorrelation functions, we used an $NVT$ equilibration period of 1 ns before running 20 consecutive $NVE$ trajectories of length 4 ps with a resampling of the momenta from the Boltzmann distribution in between each. The average velocity autocorrelation function over the different $NVE$ trajectories was then calculated up to a correlation time of 2 ps. This was then repeated 50 times from independent starting configurations to obtain an estimate of the uncertainty in the computed autocorrelation function.

The CMD velocity autocorrelation functions are shown in Fig. 4.4 and Fig. 4.5 for the 25 K and the 14 K state points, respectively. Both look very similar to previously obtained results from Miller and Manolopoulos using RPMD[22] and from Yonetani and Kinugawa using CMD.[19] The diffusion constants calculated from these autocorrelation functions using Eq. 2.27 are $1.487 \pm 0.004\,\text{Å}^2\,\text{ps}^{-1}$ at

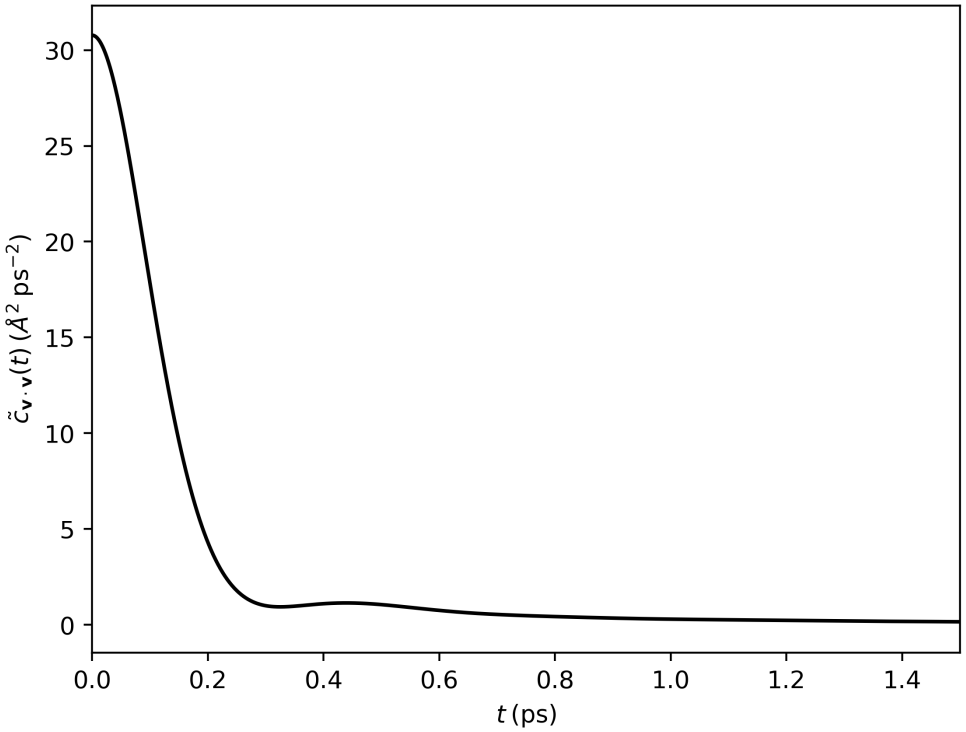



**Figure 4.4:** The CMD velocity autocorrelation function calculated at $T = 25.0\,\mathrm{K}$ and molar volume $V = 31.7\,\mathrm{cm}^3\,\mathrm{mol}^{-1}$.

the 25 K state point and $0.302 \pm 0.002$ Å$^2$ ps$^{-1}$ at the 14 K state point. These are both slightly lower than the experimental diffusion constants of 1.6 Å$^2$ ps$^{-1}$ and 0.4 Å$^2$ ps$^{-1}$ at the 25 K and the 14 K state points, respectively.[134] This is in part due to the fact that we have neglected finite size effects in our calculations. As pointed out by Miller and Manolopoulos,[22] calculating the velocity autocorrelation function for small system sizes leads to an underestimate of the diffusion constant - and by performing simulations on progressively larger systems and extrapolating the diffusion constant to infinite system size they found diffusion constants using RPMD which were more in line with the experimental values. Nevertheless, both of our diffusion constants are consistent with those calculated by Hone *et al.*[21] for slightly smaller system sizes ($N = 216$ molecules) of $0.30 \pm 0.03$ Å$^2$ ps$^{-1}$ at the $T = 14$ K state point and $1.50 \pm 0.09$ Å$^2$ ps$^{-1}$ at the $T = 25$ K state point using a force-matching algorithm to precompute the CPMF with $P = 28$ path integral beads. They also

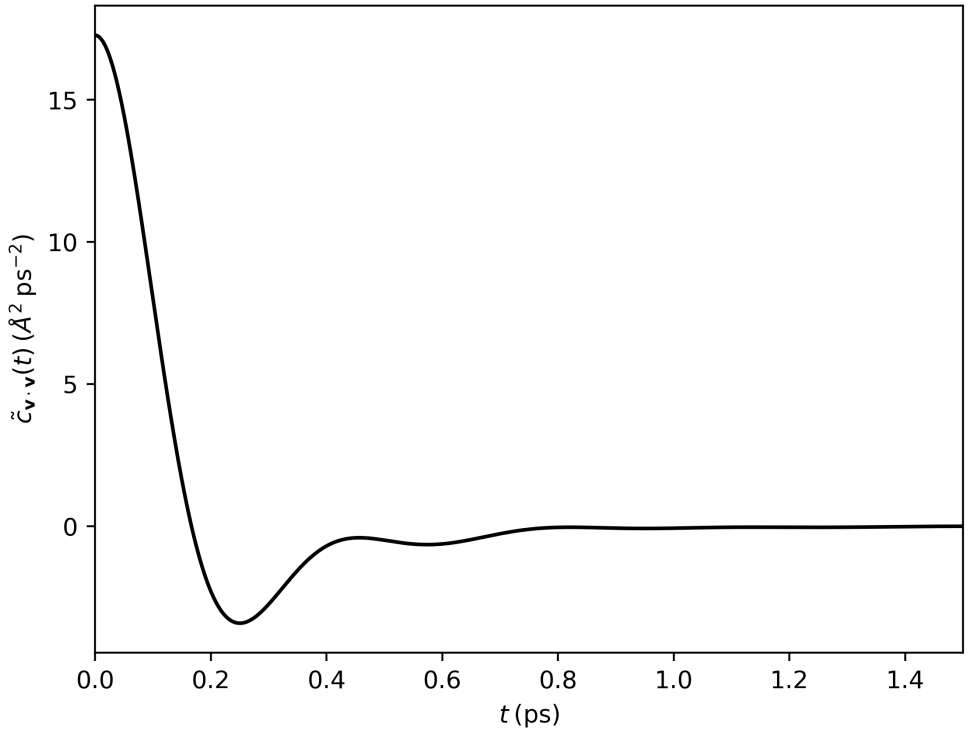



**Figure 4.5:** The CMD velocity autocorrelation function calculated at $T = 14.0\,\mathrm{K}$ and molar volume $V = 25.6\,\mathrm{cm}^3\,\mathrm{mol}^{-1}$.

found comparable values of $0.35 \pm 0.05\,\mathrm{Å}^2\,\mathrm{ps}^{-1}$ and $1.52 \pm 0.08\,\mathrm{Å}^2\,\mathrm{ps}^{-1}$ using the adiabatic CMD algorithm ($N = 180$ molecules with $P = 48$ beads) at the 14 K and the 25 K state points respectively. So, satisfied that our CMD implementation is in agreement with previously used applications of CMD, and since the calculation of diffusion constants is not the primary focus of this thesis, we will not attempt to perform any sort of infinite size extrapolation on our results here.

Finally, we may also make use of the fact that the standard form of the quantum mechanical velocity autocorrelation function, $c_{\mathbf{v}\cdot\mathbf{v}}(t)$, at time $t = 0$ is proportional to the average kinetic energy per molecule, $\langle\mathcal{K}\rangle$, of the system via

$$c_{\mathbf{v}\cdot\mathbf{v}}(0) = \frac{2}{m}\langle\mathcal{K}\rangle, \tag{4.8}$$

where $\langle\mathcal{K}\rangle$ may be calculated efficiently within a PIMD simulation using the centroid virial kinetic energy estimator, Eq. 2.25. As discussed by Braams *et al.*,[135] by

analysing the relationship between the standard form of the quantum mechanical autocorrelation function and its Kubo transform - that is the inverse Fourier transform of Eq. 2.28 - one may also obtain a sum-rule relating the value of the standard form of the quantum correlation function at $t = 0$ to its Kubo transform. Using this we may write that

$$c_{\mathbf{v}\cdot\mathbf{v}}(0) = \tilde{c}_{\mathbf{v}\cdot\mathbf{v}}(0) + \int_0^\infty \frac{2}{1 - e^{2\pi t/\beta\hbar}} \frac{d\tilde{c}_{\mathbf{v}\cdot\mathbf{v}}(t)}{dt} dt, \tag{4.9}$$

where $\tilde{c}_{\mathbf{v}\cdot\mathbf{v}}(t)$ is the Kubo transform of $c_{\mathbf{v}\cdot\mathbf{v}}(t)$, and we may recall is the correlation function that is approximated by a CMD simulation. Therefore, one may use Eq. 4.9 to assess how accurately CMD is approximating the dynamics by comparing the estimate of the quantum kinetic energy computed using it together with Eq. 4.8, and the quantum kinetic energy calculated exactly by PIMD.

The values of $c_{\mathbf{v}\cdot\mathbf{v}}(0)$ calculated from the CMD velocity autocorrelation function and from PIMD at various state points are shown in Table 4.2, as are the previously calculated values using RPMD by Miller and Manolopoulos with a smaller number of path integral beads - $P = 24$ at the 25 K and $P = 48$ at the 14 K state points.[22] We see that CMD slightly underestimates the PIMD value of $\langle \mathcal{K} \rangle$, whereas RPMD gives a slight overestimate. In both cases, however, the predicted values of $\langle \mathcal{K} \rangle$ are a great deal closer to the PIMD values than the corresponding classical values of $\langle \mathcal{K} \rangle_{\mathrm{cl}} = 3k_B T/2$. Therefore, whilst neither the CMD nor the RPMD approximations to the quantum dynamics are exact, they clearly incorporate enough of the nuclear quantum effects to provide a decent approximation.

| | $\langle \mathcal{K} \rangle / k_B$ (K) | | | |
|---|---|---|---|---|
| $T$ (K) | CMD[a.] | RPMD[b.] | PIMD[a.] | Classical |
| 14.0 | 60.4 | 67.6 | 63.8 | 21 |
| 25.0 | 61.3 | 64.2 | 62.3 | 37.5 |

**Table 4.2:** Various estimates of the kinetic energies per molecule for $N = 256$ molecules at the 14 K and $V_{\mathrm{mol}} = 25.6\,\mathrm{cm}^3\,\mathrm{mol}^{-1}$ and the 25 K and $V_{\mathrm{mol}} = 31.7\,\mathrm{cm}^3\,\mathrm{mol}^{-1}$ state points. The superscript [a.] refers to the present calculations with $P = 128$ and [b.] refers to calculations with $P = 48$ at $T = 14$ K and with $P = 24$ at $T = 25$ K from Ref. [22].

### 4.2.2 Equilibrium density fluctuations

With the effective classical potentials of mean force in hand, we may now use them to compute the thermal diffusivity from the equilibrium density fluctuations, where we use Eq. 3.98 as our starting point. In the case of CMD, we may interpret this as applying to the Kubo-transformed quantum intermediate scattering function

$$\tilde{F}(k,t) = \frac{1}{N\beta\hbar}\int_0^{\beta\hbar} \langle \hat{\rho}(-\mathbf{k}, i\tau)\, \hat{\rho}(\mathbf{k},t)\rangle \, d\tau, \tag{4.10}$$

where $\hat{\rho}(\mathbf{k},t)$ is the Fourier component of the density operator

$$\hat{\rho}(\mathbf{k},t) = \sum_{i=1}^{N} e^{i\mathbf{k}\cdot\hat{\mathbf{r}}_i(t)}, \tag{4.11}$$

and as in the classical case for an isotropic system $\tilde{F}(k,t)$ is independent of the direction of $\mathbf{k}$. We recall that the CMD approximation to a Kubo-transformed quantum correlation function is simply the classical correlation function evaluated at the centroid positions and momenta - or in other words Eq. 3.94 evaluated on the CPMF using classical dynamics.

The previous investigations into the quantum thermal conductivity by Yonetani and Kinugawa[19] using the CMD Green-Kubo relation and Liu *et al.*[25] using LSC-IVR mentioned in Chapter 3 were both performed at state points close to the liquid-vapour saturation line of the Silvera-Goldman potential, including the two state points analysed in the previous subsection.[136] These state points differ slightly from the experimental state points reported close to the saturation line by Roder and Diller,[81] since the Silvera-Goldman potential is not an exact description of the interaction between parahydrogen molecules. In this subsection and in the one following we choose to perform our simulations at the same state points used by Roder and Diller in their experimental measurements which were close to the saturation line rather than the theoretical state points close to the saturation line of the model Silvera-Goldman potential. This is to remove any effects that small variations in temperature or density may have on the calculated thermal conductivity. In addition we also choose to conduct simulations at the theoretical state point of $T = 14\,\mathrm{K}$ and $\rho = 25.6\,\mathrm{cm}^3\,\mathrm{mol}^{-1}$, which was also used in the previous

subsection. This state point was not included in Roder and Diller's experiments, who did not consider any temperatures below 17 K,[81] but is included here so that we may probe the low temperature behaviour of the thermal conductivity as the triple point is approached in greater detail.

Since all of the experimental state points along the saturation line paint a similar picture, we will focus on just the $T = 22.001$ K and $\rho_m = 69.066\,\mathrm{kg\,m^{-3}}$ state point, where $\rho_m$ in this case refers to the mass density rather than the number density. This state point is close to the experimental observed peak in the thermal conductivity. In the following subsection we will present a more efficient way to compute the thermal conductivity using CMD, which will be more conducive for an investigation over the entire temperature range.

As the first order of business we calculated the CMD values of the constant volume and constant pressure heat capacities, $c_V$ and $c_P$, respectively, as well as the adiabatic speed of sound, $c_s$, by finite difference, using the thermodynamic derivatives given in Eqs 3.105 - 3.107 to obtain independently calculated values of $\gamma$ and $c_s$ to use in our fitting procedure. This involves calculating the total energy, $E$, and pressure, $p$, on a grid of temperatures and densities which are displaced around the state point at which the CPMF was calculated. In this Chapter and the next, we will switch to using a lowercase $p$ to refer to the pressure to avoid confusion with the number of path integral beads, $P$. Although we know that the true CPMF will differ as one varies the temperature and density, the correct way to calculate the CMD estimates of $\gamma$ and $c_s$ using Eqs 3.105 - 3.107 is to calculate $E$ and $p$ at each grid point *without* allowing the CPMF to change. This is because CMD is nothing more than classical molecular dynamics on an effective potential, and so to calculate the values of $\gamma$ and $c_s$ which are consistent with the fit of the intermediate scattering function calculated from CMD we must compute them exactly as we would in a classical simulation via finite difference - which is without allowing the potential to change at the different state points.

We choose to calculate $E$ and $p$ at five temperatures evenly spaced around each state point with a 5% variation in temperature for each one, and five densities

also evenly spaced with a 1% variation in each. These spacings were found to give both the energy and pressure with sufficiently small uncertainty to obtain a good estimate of the derivatives from finite difference. All together, this means that we require nine sets of simulations at each state point to evaluate the necessary derivatives - but since these are classical simulations and that the calculation of the energy and the pressure do not need particularly long or large simulations to achieve good statistics compared to the intermediate scattering function simulations detailed earlier, this is not too large of an issue.

Both the energy and pressure variation with temperature were found to exhibit a linear dependence over this temperature range, and thus a simple weighted linear least squares fit was used to estimate the derivatives at the state point. The pressure dependence on density showed a slight non-linear behaviour however, and was instead fitted to a quadratic. Additionally, there are known long-range corrections to the energy and pressure applicable to truncating and shifting the potential at the cutoff, $r_c$, based on assuming a value of $g(r) = 1$ at separations $r > r_c$.[30] Based on the observation that the CPMFs shown in Fig. 4.1 become equivalent to the classical Silvera-Goldman potential at large separations, we make the approximation that the long range corrections we apply to our CPMFs can be taken as the same as the long range corrections for the original Silvera-Goldman potential. For the Silvera-Goldman potential, the long-range corrections to the energy, $E_{\text{l.c.}}$, and pressure, $p_{\text{l.c}}$, are given by, where we have neglected the exponential repulsive term in the potential as it is negligible at a cutoff radius of 15 $a_0$

$$E_{\text{l.c.}} = -2\pi\rho N \left( \frac{C_6}{3r^3} + \frac{C_8}{5r^5} - \frac{C_9}{6r^6} + \frac{C_{10}}{7r^7} \right), \tag{4.12}$$

and

$$p_{\text{l.c.}} = \frac{1}{V} \left[ E_{\text{l.c.}} - \frac{2\pi\rho N}{3} \left( \frac{C_6}{r^3} + \frac{C_8}{r^5} - \frac{C_9}{r^6} + \frac{C_{10}}{r^7} \right) \right]. \tag{4.13}$$

Both $E_{\text{l.c}}$ and $p_{\text{l.c}}$ are seen to be independent of temperature at this level of approximation, and thus adding the long-range corrections does not affect the estimated values of $(\partial E/\partial T)_\rho$ or $(\partial p/\partial T)_\rho$. In contrast, the long-range correction

to the pressure does depend on the density, and so this must be added at each grid point in order to obtain the estimate of $(\partial p/\partial \rho)_T$.

The CMD values of $c_V$, $c_P$, $\gamma$ and $c_s$ were calculated from 50 independent simulations of $N = 256$ molecules at each grid point, where after an equilibration period of 1 ns the energy and pressure were sampled at every time step in the $NVT$ ensemble also for a further time period of 1 ns. For comparison, we also calculate these properties using PIMD with $P = 128$ beads. In principle, $c_V$ and $c_P$ may both be calculated using a scaled coordinates estimator developed by Yamamoto.[44; 137] However, we also choose to calculate the PIMD values by finite difference of the relevant thermodynamic derivatives, analogously to the way we computed them using CMD. This is because we found that Yamamoto estimators converged more slowly with respect to the number of path integral beads used in our simulations and gave a larger uncertainty when compared with a finite difference procedure over the same computation time. A similar observation was made by Musil *et al.* when calculating the PIMD constant pressure heat capacity of metal organic frameworks.[137] A finite difference procedure also has the advantage that the thermodynamic derivatives necessary to compute $c_V$ and $c_P$ also allow us to find $c_s$, which we are not aware of any efficient path integral estimators for, without performing any additional simulations. The PIMD simulations were carried out using the same equilibration and sampling periods as the CMD calculations mentioned previously, but for a smaller system size of $N = 108$ molecules and only over 10 independent simulations at each grid point for computational efficiency. In the PIMD simulations the energy was calculated using the centroid virial estimator for the kinetic energy, Eq. 2.25, and the potential energy from

$$\mathcal{V} = \frac{1}{P} \sum_{k=0}^{P-1} V\left(\mathbf{x}^{(k)}\right), \tag{4.14}$$

where $V\left(\mathbf{x}^{(k)}\right)$ refers in this case to the Silvera-Goldman potential evaluated over the $k^{\text{th}}$ beads of the ring polymers. The pressure was calculated also using a centroid virial estimator of the form

$$p = \frac{2T_{\text{CV}}}{3V} + \frac{1}{3PV} \sum_{k=0}^{P-1} \sum_{i=0}^{N} \sum_{j>i}^{N} \mathbf{r}_{ij}^{(k)} \cdot \mathbf{F}_{ij}^{(k)}, \tag{4.15}$$

where $T_{CV}$ refers to the centroid virial kinetic energy calculated using Eq. 2.25. The average values of $c_V$, $c_P$, $\gamma$ and $c_s$ obtained from these procedures at the $T = 22.001$K state point from CMD and their estimated uncertainties are summarised in Table 4.3, as are the corresponding values found from PIMD.

| | $c_V$ $(k_B)$ | $c_P$ $(k_B)$ | $\gamma$ | $c_s$ $\left(\text{Å ps}^{-1}\right)$ |
|---|---|---|---|---|
| CMD | $2.3803 \pm 0.0005$ | $4.822 \pm 0.004$ | $2.0259 \pm 0.0017$ | $12.140 \pm 0.007$ |
| PIMD | $1.439 \pm 0.004$ | $2.40 \pm 0.04$ | $1.67 \pm 0.03$ | $10.8 \pm 0.2$ |

**Table 4.3:** Parameters calculated via finite difference from CMD and PIMD at $T = 22.001$ K and $\rho_m = 69.066\,\text{kg m}^{-3}$.

As may be seen from Table 4.3, the thermodynamic derivatives predicted by CMD on the fixed CPMF do not agree with the PIMD thermodynamic derivatives all that well. In particular, CMD gives a rather poor estimate of the PIMD constant volume and constant pressure heat capacities, which disagree by 65% and 101%, respectively. The predicted values of $c_s$ differ by 12% and by 21% for $\gamma$. Interestingly, the ratio $c_s^2/\gamma$ only disagrees by 3% between CMD and PIMD. We believe this to be a result of the fact that this ratio is determined by the value of $\partial^2 \tilde{F}(k,t)/\partial t^2$ at $t = 0$ in our hydrodynamic model - and since this derivative is a short time dynamical property it may be expected to be found more accurately using CMD.

If the CPMF was allowed to vary at each density and temperature then presumably the resulting CMD estimates would be a lot closer to the PIMD estimates. Of course, since PIMD is exact in the infinite bead limit and CMD is only approximate, the values calculated by PIMD should be taken as a better representation of the true quantum mechanical properties of the system. But the "true" quantum mechanical properties are actually not what we require in this case - what we want are the values of $c_s$ and $\gamma$ which allow us to fit the data obtained from the CMD calculation of $\tilde{F}(k,t)$. In fact, these differences indicate that the procedure used to calculate the CMD estimates of $\gamma$ and $c_s$ detailed earlier by not allowing the CPMF to change was the correct one, as using the PIMD estimates would not yield as convincing of a fit to $\tilde{F}(k,t)$ as those to be shown later. These values can also be used as a check on the accuracy of our CMD simulations. Given that we

know that CMD is inaccurate by up to 21% for some of the properties used in the fit of $\tilde{F}(k,t)$, we may use this as a rough indication that the thermal diffusivity computed by CMD from our fits may also be similarly inaccurate. Of course, things are not so simplistic in reality - the CMD estimate of $c_V$ shows that CMD can give a much poorer estimate of some properties than it does others. However, using the difference in the PIMD and CMD values of $\gamma$ and $c_s$ as a guideline for the inaccuracy in $a$ seems sensible, as all three parameters may be found from CMD in the same fit.

For our CMD calculations of $\tilde{F}(k,t)$, we choose to initialise the system on an elongated $60 \times 4 \times 4$ set of face-centred cubic unit cells ($N = 3840$ molecules) and allow the system to melt and equilibrate in the $NVT$ ensemble for $1 \times 10^6$ time steps. A small cross-section size of $4 \times 4$ unit cells was used to facilitate longer simulation times, but some testing using a $6 \times 6$ unit cell cross-section indicated that a $4 \times 4$ cross-section was sufficient to produce converged results of the fitted thermal diffusivity with respect to the cross-section dimensions.

After equilibration, 60 $NVE$ trajectories of length 320 ps were run, with the momenta being resampled from the Boltzmann distribution between each one. The cosine and sine Fourier components of the density were calculated at each step for the 4 smallest $k$-vectors which fit an integer number of wavelengths across the long dimension of the simulation box. These were then used to find the intermediate scattering function, which was computed up to a correlation time of 160 ps, and averaged over the 60 different $NVE$ trajectories. This process was then repeated 300 times from independent configurations to further improve the statistics. Such a long correlation time and large number of simulations was found to be necessary to obtain a reliable fit to $\tilde{F}(k,t)$ for the smallest $k$-vector used in our simulations and to achieve good statistics in the different correlation functions, respectively. The average (Kubo-transformed) intermediate scattering function normalised by its $t = 0$ value which is calculated by this procedure, as well as the fits to Eq. 3.98 by a non-linear least squares scheme are shown for the 4 smallest $k$-vectors in Fig. 4.6. We also considered fits to the approximate hydrodynamic solution represented by Eq. 3.102, both with and without including the $d(k)$ correction term. Both of

the fits to the two approximate solutions looked almost indistinguishable from the fits shown in Fig. 4.6, apart from that the approximate solution without the $d(k)$ correction term gives an ever so slightly worse fit due to being unable to satisfy the constraint that $d\tilde{F}(k,t)/dt = 0$ at $t = 0$, and so they are not shown here.

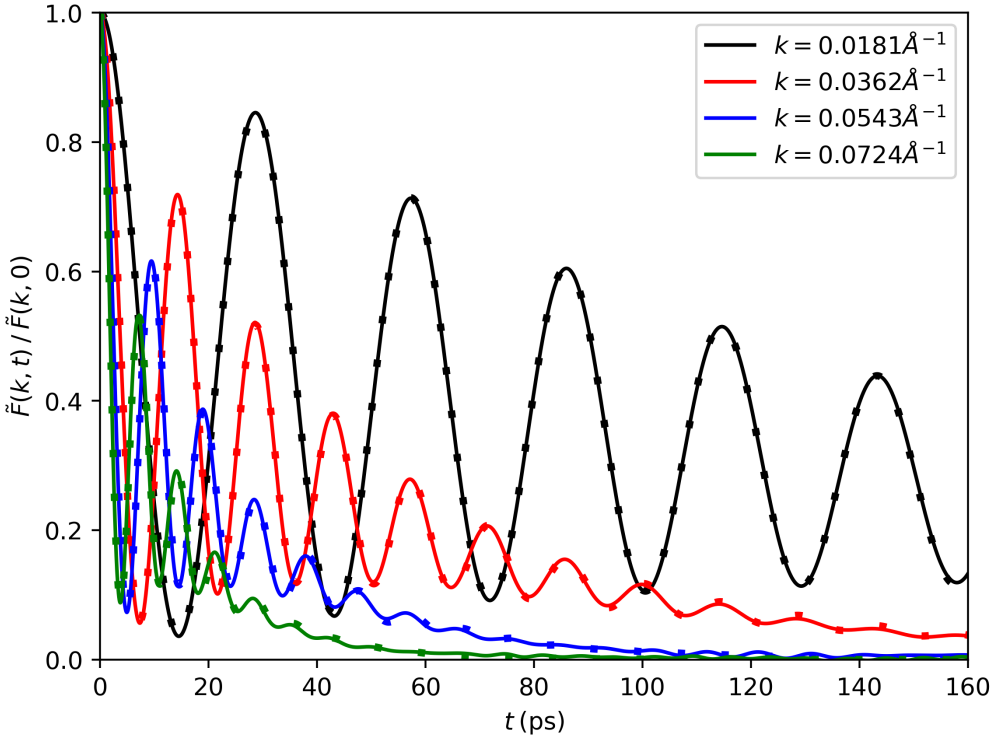



**Figure 4.6:** Intermediate scattering functions calculated at $T = 22.001$ K and $\rho_m = 69.066\,\text{kg}\,\text{m}^{-3}$. Lines show the simulated data and dots show the different fits to $\tilde{F}(k,t)$ using Eq. 3.98.

For each value of $k$, the 300 independent simulations were partitioned into 6 sets of 50 simulations a piece, and the CMD thermal diffusivity, $a_{\text{CMD}}(k)$, determined by independently fitting Eq. 3.98 to the average of $\tilde{F}(k,t)$ from each set. This partitioning was done so that the $\tilde{F}(k,t)$ from each of the sets was sufficiently well averaged to provide a good fit. The mean value of $a_{\text{CMD}}(k)$ and its standard error were then calculated for each value of $k$ across these sets. The bulk value of the thermal diffusivity was found by plotting $k$ against $1/a_{\text{CMD}}(k)$ and using a weighted linear least squares fit to extrapolate to $k = 0$. We compare the extrapolation to

infinite system size at the $T = 22.001$ K state point, both in the case that $\tilde{F}(k,t)$ is fitted to the exact solution of the inverse Laplace transform, Eq. 3.98, in Fig. 4.7 and to the approximate solutions of Eq. 3.102 in Fig. 4.8. Also shown in the Figures are the predicted intercepts and their associated uncertainties from the least squares fits. The intercepts are then taken as the reciprocal of the bulk value of the thermal diffusivity, $1/a_{\mathrm{CMD}}$. The values of the $a_{\mathrm{CMD}}(k)$ used in Fig. 4.8 were found analogously to those in the exact hydrodynamic extrapolation shown in Fig. 4.7, by calculating the average value of $a_{\mathrm{CMD}} = \gamma_{\mathrm{CMD}} D_{T,\mathrm{CMD}}(k)$ obtained from fits to Eq. 3.102 with and without the $d(k)$ correction term, where we recall that $D_{T,\mathrm{CMD}} = \kappa_{\mathrm{CMD}}/\rho c_{P,\mathrm{CMD}}$ is the quantity calculated from the fits to Eq. 3.102 and $\gamma_{\mathrm{CMD}} = c_{P,\mathrm{CMD}}/c_{V,\mathrm{CMD}}$. The fits where the $d(k)$ term was neglected, similar to the fitting procedure used by Cheng and Frenkel,[107] were found to give the same value of $a_{\mathrm{CMD}}(k)$ as the fits when the $d(k)$ was included at each of the values of $k$ considered here despite giving a qualitatively worse fit to the simulated data. Therefore we have only shown the extrapolation procedure for the approximate solution with the $d(k)$ term included in Fig. 4.8.

From these Figures, we may see that fitting to the exact hydrodynamic solution or to the approximate solution provide values of the extrapolated bulk thermal diffusivity which are consistent with each other. However, in this case it is clear that fitting to the "exact" solution provides a much less pronounced system size dependence than fitting to either of the approximate solutions. In fact the $k$-dependence of $a_{\mathrm{CMD}}(k)$ from the fits to the exact solution is so slight in this case that there is less than a 2% variation in the $k$-dependent thermal conductivity between the largest and smallest values of $k$ used in our calculations, which is within the error bars of all of the points and of the extrapolated intercept. We could, therefore, have simply used the value of $a_{\mathrm{CMD}}(k)$ calculated at the largest value of $k$, foregoing the extrapolation procedure entirely, and still obtained a similar result - which in this instance would be equivalent to using a system which is a factor of four times smaller. One cannot know that the system size dependence would be so small without actually performing the simulations however. Given the much larger

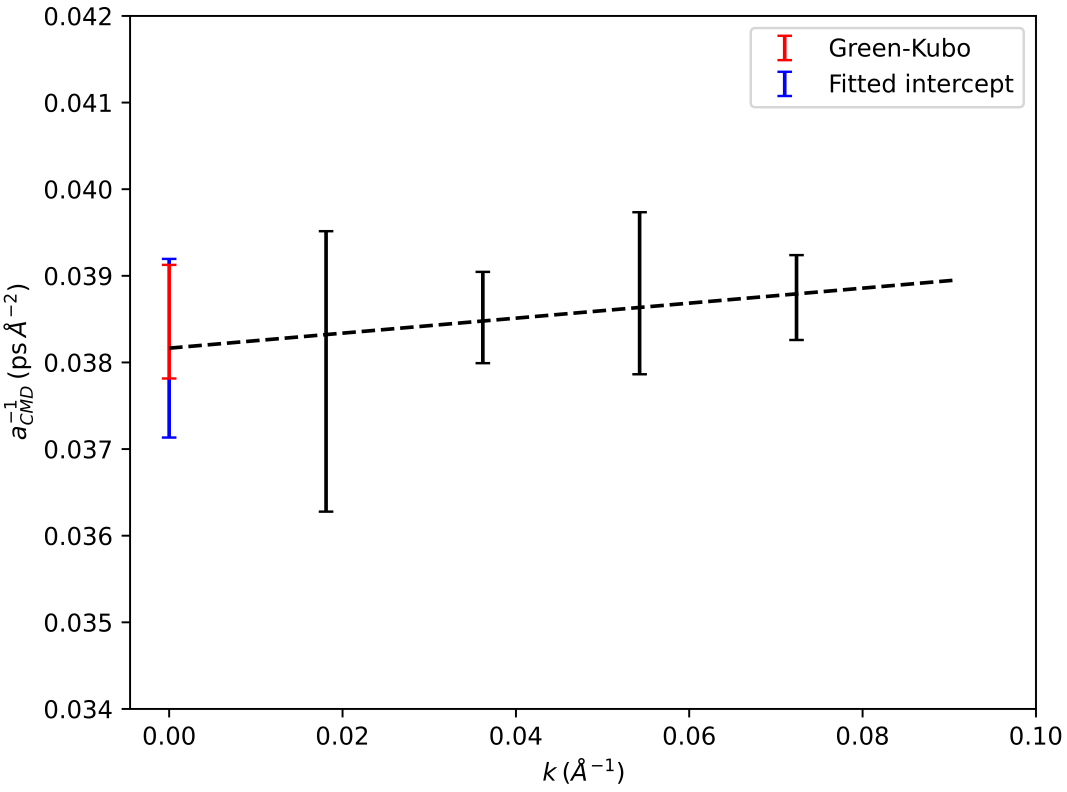



**Figure 4.7:** Extrapolation of the $k$-dependent thermal diffusivity to infinite system size, when $\tilde{F}(k,t)/\tilde{F}(k,0)$ is fitted to the exact solution of the hydrodynamic equation, Eq. 3.98. The red errorbars labelled "Green-Kubo" denote the value of $1/a_{\mathrm{CMD}}$ and its uncertainty that were calculated from the method to be described in the next subsection. All errorbars in this Figure denote one standard error in the mean.

system size dependence observed by Cheng and Frenkel[107] when fitting to the approximate solution for $F(k,t)$ in some of their classical simulations it seems best practice to at least check the system size dependence by performing some slightly larger simulations even when using the exact hydrodynamic solution in cases where the system size dependence might reasonably assumed to be small. It remains to be seen if the essentially zero $k$-dependence on the thermal conductivity is limited to the special case of a simple liquid such as parahydrogen or if this observation is reproduced more generally when fitting to the exact solution of the hydrodynamic model. The data from Fig. 4.7 at least indicates that fitting to Eq. 3.98 rather than Eq. 3.102 leads to a less severe extrapolation and thus a more convincing estimate of the bulk thermal conductivity, providing the potential benefit of being able to

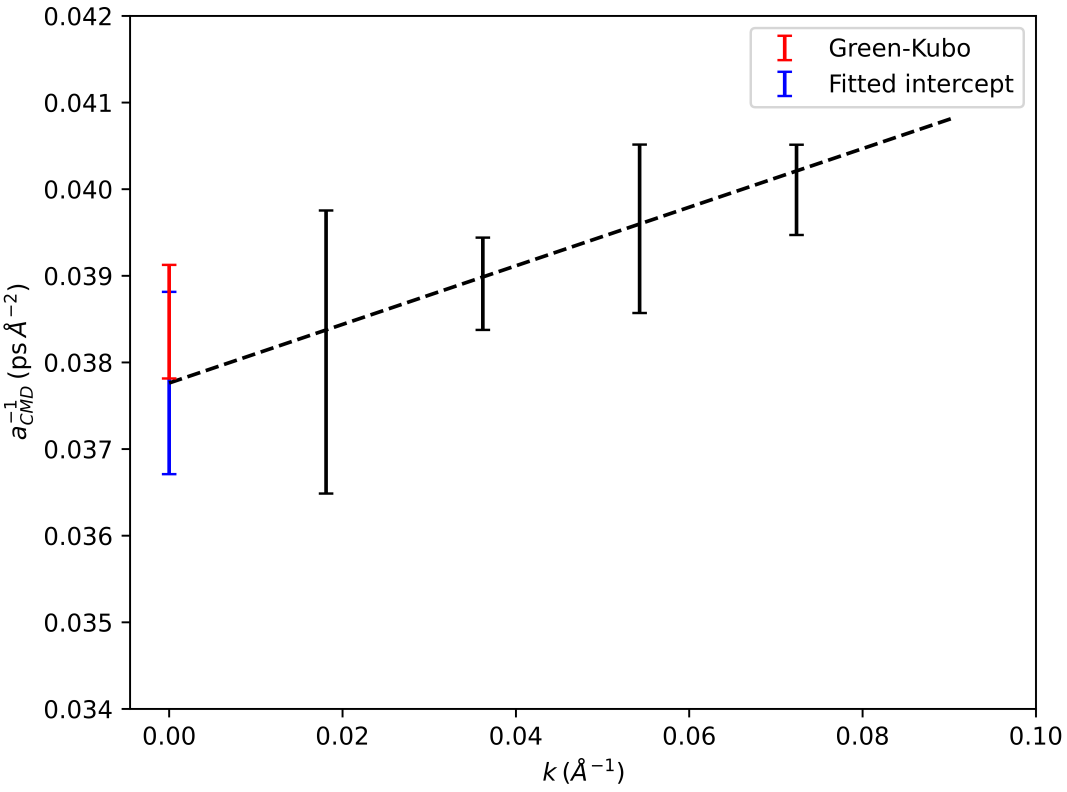



**Figure 4.8:** Extrapolation of the $k$-dependent thermal diffusivity to infinite system size, when $\tilde{F}(k,t)/\tilde{F}(k,0)$ is fitted to the approximate solution of the hydrodynamic equation, Eq. 3.102. The red errorbars labelled "Green-Kubo" denote the value of $1/a_{\mathrm{CMD}}$ and its uncertainty that were calculated from the method to be described in the next subsection. All errorbars in this Figure denote one standard error in the mean.

get away with using smaller system sizes in the calculations for some systems.

The extrapolated bulk value of the thermal diffusivity is then found from the intercept of Figure 4.7 to be $26.2 \pm 0.7$ Å$^2$ ps$^{-1}$. When this is combined with the constant volume heat capacity calculated by PIMD, we obtain a thermal conductivity of $0.107 \pm 0.003$ W (m K)$^{-1}$, which is in close agreement with the experimental thermal conductivity of 0.1019 W (m K)$^{-1}$ found at this state point by Roder and Diller.[81] A 5% inaccuracy in the calculated thermal conductivity is fairly impressive considering the 12% and 21% differences in the CMD and PIMD estimates of $c_s$ and $\gamma$ which were mentioned earlier. We note that if one would have used $c_{V,\mathrm{CMD}}$ in place of $c_{V,\mathrm{PIMD}}$ in the calculation of $\kappa$ then one would have obtained a value of $0.178 \pm 0.005$ W (m K)$^{-1}$, which is more in line with the

CMD Green-Kubo results of Yonetani and Kinugawa.[19] This suggests that the problem with the CMD generalisation of the Green-Kubo relation for the thermal conductivity is not due to the CMD estimate of the thermal diffusivity - which appears to be calculated relatively accurately by CMD. We will use this observation to develop a more efficient method to calculate the quantum thermal conductivity using CMD in the following subsection.

### 4.2.3 Returning to the Green-Kubo relation

The agreement of the CMD thermal diffusivity calculated from the decay of the equilibrium density fluctuations with experiment indicates that CMD *can* be used as a reliable way to calculate the thermal conductivity when combined with an appropriate quantum mechanical heat capacity. However, the requirement to use large system sizes to approximate the hydrodynamic limit as well as the need for long simulation times and good statistics to accurately fit the intermediate scattering function means that this is still a relatively computationally inefficient method - even with the speed-up from precomputation of the centroid potential of mean force. The results by Yonetani and Kinugawa, although not in agreement with experiment, showed that converged values of the thermal conductivity could be obtained from the CMD generalisation of the Green-Kubo relation with an order of magnitude fewer molecules and two orders of magnitude shorter correlation time[19] than the results presented in the previous subsection, and a similar observation was made in our testing.

In essence, CMD is simply classical molecular dynamics on an effective potential which incorporates nuclear quantum effects. Since the estimates of the thermal conductivity calculated using two equivalent methods within the classical molecular dynamics framework should be in agreement with each other, this raises an interesting suggestion to "fix" the CMD generalisation of the Green-Kubo thermal conductivity. The CMD Green-Kubo estimate of the thermal diffusivity is $a_{\mathrm{CMD}} = \kappa_{\mathrm{CMD}}/\rho c_{V,\mathrm{CMD}}$, where $\kappa_{\mathrm{CMD}}$ is the thermal conductivity calculated from the CMD generalisation of the Green-Kubo thermal conductivity and $c_{V,\mathrm{CMD}}$ is the

classical constant volume specific heat capacity calculated on the centroid potential of mean force. This should be equivalent to the CMD thermal diffusivity calculated via equilibrium density fluctuations. Then, combining the CMD estimate of the thermal diffusivity with the quantum mechanical heat capacity calculated using PIMD, $c_{V,\mathrm{PIMD}}$, we have that our estimate of the quantum mechanical thermal conductivity is $\kappa_{\mathrm{scaled}} = a_{\mathrm{CMD}}\rho c_{V,\mathrm{PIMD}} = \kappa_{\mathrm{CMD}} c_{V,\mathrm{PIMD}}/c_{V,\mathrm{CMD}}$ - which implies that the CMD Green-Kubo thermal conductivity may be corrected by a simple scaling by the ratio of the PIMD and the CMD constant volume heat capacities. The problem with the CMD Green-Kubo estimate of the thermal conductivity therefore appears to be due to the inaccurate CMD estimate of the heat capacity. The poor CMD estimate of the heat capacity is not surprising, since CMD is only classical molecular dynamics on an effective potential the CMD heat capacity will go to the classical equipartition limit of $3k_B$ per molecule as the temperature approaches zero - whereas the true quantum mechanical heat capacity goes to zero in the same limit.

We emphasise that this is *not* the same as simply scaling the thermal conductivity calculated from the Green-Kubo relation in a purely classical molecular dynamics simulation by the ratio of the quantum and classical constant volume heat capacities, since the CMD estimates of the Green-Kubo thermal conductivity and the constant volume heat capacity contain nuclear quantum effects within the centroid potential of mean force. This is particularly evident for the case of Silvera-Goldman parahydrogen, where the classical heat capacity and Green-Kubo thermal conductivity estimates are clearly very different from their CMD counterparts by virtue of being in a different phase.

A simple scaling of the classical Green-Kubo thermal conductivity by the ratio of the quantum and classical heat capacities has been utilised as a scheme to attempt to incorporate quantum mechanical corrections to classical simulations in several previous studies.[9; 73] Whilst this scaling was found to often improve the estimate of the thermal conductivity in comparison to experiment, it has been shown by Turney *et al.*[27] that this approach is incomplete for solids, where the thermal conductivity can be broken down into contributions from each of the phonon modes.

The contribution from each phonon depends on the phonon specific heat capacity, $c_{\mathrm{ph}}$, the phonon group velocity, $v_g$, and the phonon relaxation time, $\tau$. What we are proposing is to scale the thermal conductivity globally by the ratio of the overall quantum and classical specific heat capacities of the system, which is not the same as scaling the individual phonon contributions by the ratio of the quantum and classical heat capacities of that phonon mode. This seems sensible for liquids, where heat is transferred without the long-range vibrations present in the ordered lattice structure of solids. However, in light of the observations of Turney *et al.* it seems likely that for solids one would need to find a way to calculate the heat capacities of each phonon via both PIMD for the quantum heat capacity and via CMD for the effective classical heat capacity in order to scale the phonon contributions to the thermal conductivity appropriately. We still anticipate that scaling the classical thermal conductivity by the quantum to classical specific heat capacity ratio might provide a good approximation for many liquid systems, particularly if nuclear quantum effects in the CMD thermal conductivity and CMD heat capacity are expected to be small. We will see that this indeed can be the case when we study the thermal conductivity of liquid water in the following Chapter.

To calculate the CMD thermal conductivity from the Green-Kubo relation we use a much smaller system size of $6 \times 6 \times 6$ face-centred cubic unit cells. After an equilibration period of $5 \times 10^5$ time steps in the $NVT$ ensemble the thermostat was switched off and an $NVE$ trajectory of length 1.25 ns was run. The heat flux autocorrelation was then calculated from this $NVE$ trajectory up to a correlation time of 2 ps and the thermal conductivity was found by integrating Eq. 3.64 using the trapezium rule. This whole process was repeated across 50 independent simulations to obtain an estimate of the average heat flux autocorrelation function and its uncertainty.

The average heat flux autocorrelation function, scaled by the prefactor $1/3Vk_BT^2$, for the $T = 22.001\,\mathrm{K}$ state point is shown in Fig. 4.9. From Fig. 4.9 we can see that the heat flux autocorrelation function decays to zero by about 1.5 ps, making it clear that this is a much more efficient approach than the $0.96\,\mu$s simulations used to find

the thermal diffusivity using the intermediate scattering function in the previous subsection. The heat flux autocorrelation function also shows a simple form, with negligible statistical noise in the long time tail. This makes specification of the thermal conductivity by direct integration straightforward in this case. The value of the thermal conductivity obtained by integrating the heat flux autocorrelation function in Fig. 4.9 is $0.176 \pm 0.003\,\mathrm{W\,(m\,K)^{-1}}$, which when combined with the density and CMD constant volume heat capacity yields a CMD thermal diffusivity of $a_{\mathrm{CMD}} = 26.0 \pm 0.5\,\mathrm{\AA^2\,ps^{-1}}$. As expected, this is consistent with the CMD thermal diffusivity of $26.2 \pm 0.7\,\mathrm{\AA^2\,ps^{-1}}$ we found from fitting the intermediate scattering function to the hydrodynamic model at this state point in the previous subsection.

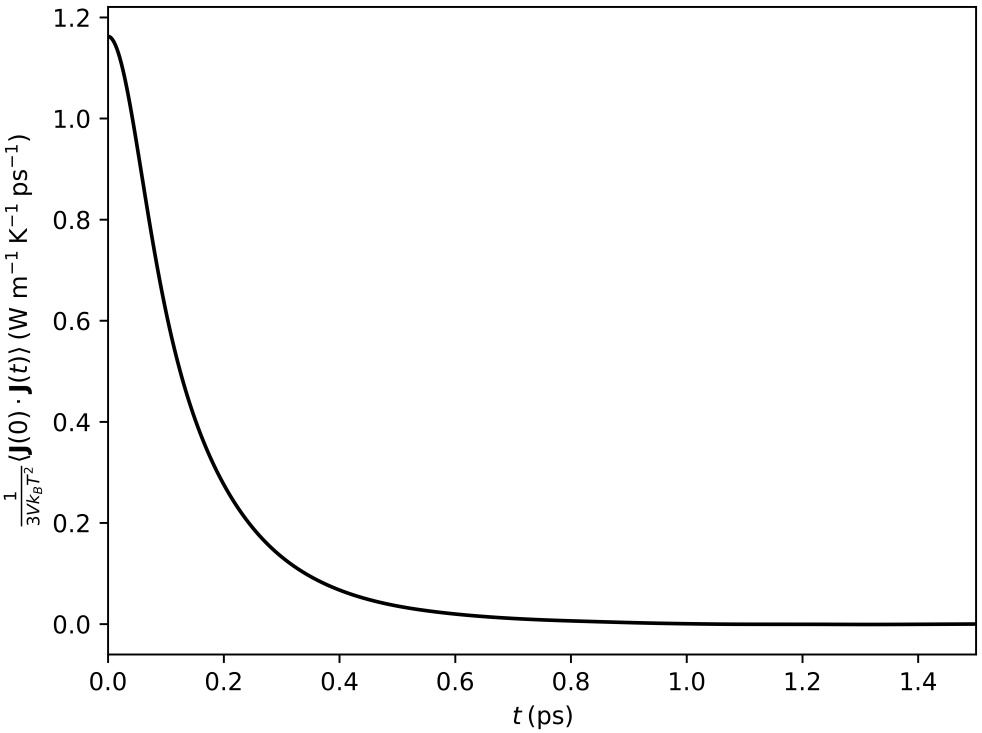



**Figure 4.9:** The CMD Green-Kubo heat flux autocorrelation function calculated at $T = 22.001\,\mathrm{K}$ and $\rho_m = 69.066\,\mathrm{kg\,m^{-3}}$, scaled by the prefactor $1/3Vk_BT^2$.

The values of the unscaled CMD thermal conductivities, as well as their corresponding scaled values at six state points along the experimental saturation line are summarised in Table 4.4 and plotted in Figure 4.10, as are the experimental

| $T$ (K) | $\rho_m$ ($\mathrm{kg\,m^{-3}}$) | $\kappa_{\mathrm{CMD}}$ ($\mathrm{W\,m^{-1}\,K^{-1}}$) | $c_{V,\mathrm{CMD}}$ ($k_B$) | $c_{V,\mathrm{PIMD}}$ ($k_B$) | $\kappa_{\mathrm{scaled}}$ ($\mathrm{W\,m^{-1}\,K^{-1}}$) | $\kappa_{\mathrm{Expt.}}$ ($\mathrm{W\,m^{-1}\,K^{-1}}$) |
|---|---|---|---|---|---|---|
| 14.0 | 78.755 | 0.249 (5) | 2.991 (9) | 1.18 (2) | 0.098 (2) | |
| 16.942 | 74.556 | 0.209 (3) | 2.703 (6) | 1.307 (3) | 0.101 (2) | 0.0942 |
| 19.522 | 71.799 | 0.190 (3) | 2.522 (4) | 1.404 (3) | 0.106 (2) | 0.0983 |
| 22.001 | 69.066 | 0.176 (3) | 2.377 (4) | 1.439 (4) | 0.106 (2) | 0.1019 |
| 24.990 | 64.916 | 0.151 (3) | 2.228 (5) | 1.495 (7) | 0.101 (2) | 0.1013 |
| 30.026 | 56.361 | 0.119 (2) | 2.068 (5) | 1.535 (3) | 0.088 (2) | 0.0915 |
| 33.001 | 45.900 | 0.091 (1) | 2.004 (6) | 1.563 (4) | 0.071 (1) | 0.0840 |

**Table 4.4:** Values of the CMD Green-Kubo thermal conductivities, the CMD and PIMD constant volume heat capacities and the corresponding scaled thermal conductivities, as well as experimental measurements by Roder and Diller[81] at six state points close to the saturation line of liquid parahydrogen. Also included are the computational results obtained at $T = 14.0\,\mathrm{K}$ and $\rho_m = 78.755\,\mathrm{kg\,m^3}$ (a molar volume of $25.6\,\mathrm{cm^3\,mol^{-1}}$) close to the triple point, which was not included in Roder and Diller's experiments.

thermal conductivities measured at these state points by Roder and Diller.[81] As mentioned previously, we have also included the state point of $T = 14.0\,\mathrm{K}$ and $\rho_m = 78.755\,\mathrm{kg\,m^{-3}}$ in our theoretical simulations to examine the low temperature behaviour of the thermal conductivity more closely. From this Figure we can see that scaling the CMD Green-Kubo thermal conductivity by the ratio of the quantum and classical constant volume specific heat capacities drastically improves the agreement with experiment. Moreover, the previous monotonic decrease in the thermal conductivity as the temperature is increased is replaced with a temperature dependence that successfully reproduces the experimentally observed peak in the thermal conductivity, which is also predicted to occur at approximately the same temperature as in experiment. The scaled CMD Green-Kubo thermal conductivities are within 20% of the experimental values across the whole temperature range, with the agreement becoming slightly worse at higher temperatures as the critical point is approached. Given the approximations inherent to CMD, as well as the fact that the uncertainties in Roder and Diller's measurements are unspecified, we believe this to be a very promising result - especially compared to the qualitatively wrong temperature dependence predicted by previous studies.[19; 25]

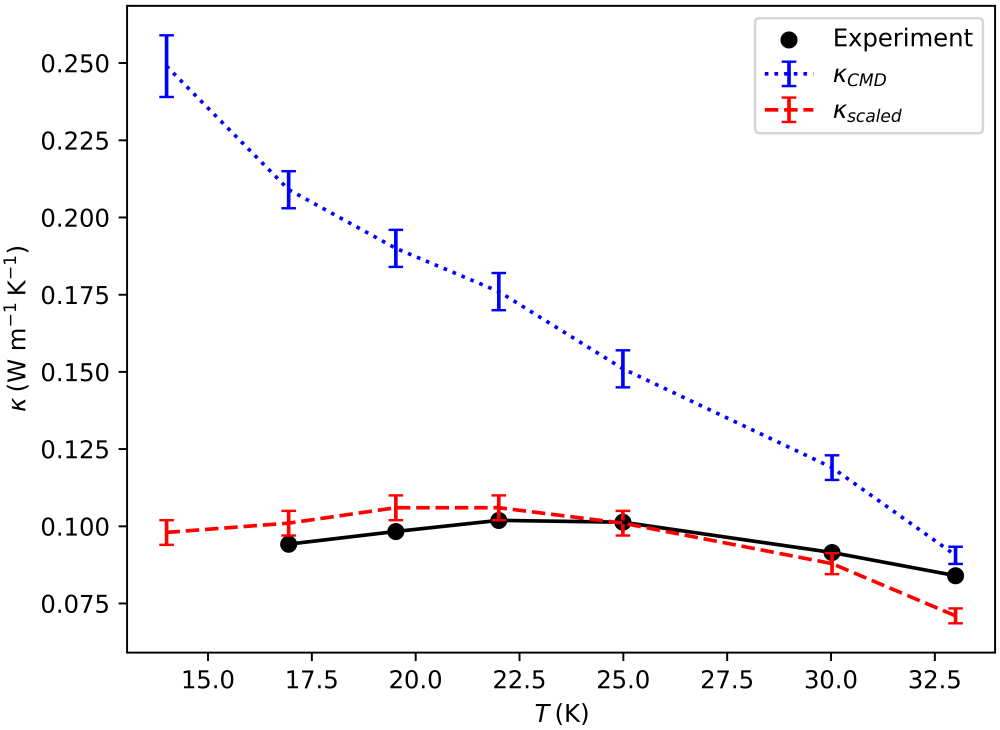



**Figure 4.10:** CMD Green-Kubo thermal conductivities and their corresponding scaled versions calculated at a variety of state points along the saturation line for liquid parahydrogen, compared to the experimental measurements of Roder and Diller[81] at these state points. Also included is the theoretical state point of $T = 14.0\,\mathrm{K}$ and $\rho_m = 78.755\,\mathrm{kg\,m^{-3}}$.

## 4.3 Normal liquid helium

In order to validate that our findings in the previous section are applicable to more systems than just liquid parahydrogen, we turn to another liquid where nuclear quantum effects are known to play a prominent role - liquid helium. The triple point of $^4$He is at $T = 5.2\,\mathrm{K}$ and it undergoes a superfluid transition at $T = 2.2\,\mathrm{K}$, leaving us with a narrow temperature range to probe the role of nuclear quantum effects in the liquid phase before quantum mechanical exchange effects (which PIMD and CMD are unable to account for) become significant close to the superfluid transition. For this reason, we choose to focus on the small temperature range of $T = 3\,\mathrm{K}$ to $T = 4\,\mathrm{K}$. Nevertheless, there still exists a good deal of experimental data along the saturation line within this for us to compare our simulated results to. We choose to

focus on four state points within this temperature range, and compare our results to the experimental measurements of Donnelly and Barenghi[138] at these state points.

We use the highly accurate HFD-B2 pair potential developed by Aziz *et al.*[139], in which the interaction between He atoms are described by

$$u(r) = A\exp\left(-\alpha r + \beta r^2\right) - \left[\frac{C_6}{r^6} + \frac{C_8}{r^8} + \frac{C_{10}}{r^{10}}\right] f(r), \tag{4.16}$$

and where the function $f(r)$ is given by

$$f(r) = \begin{cases} \exp\left[-\left(\frac{r_0}{r} - 1\right)^2\right], & r \leq r_0 \\ 1, & r > r_0. \end{cases} \tag{4.17}$$

We use a cutoff radius of $r_c = 15\,a_0$ and a timestep of 1.2 fs in all simulations using the HFD-B2 potential shown in this subsection. The various parameters for the HFD-B2 potential are given in Table 4.5 below.

| | |
|---|---|
| $A$ | 6.659321 |
| $\alpha$ | 1.912736 |
| $\beta$ | $-6.009413 \times 10^{-2}$ |
| $C_6$ | 1.461 |
| $C_8$ | 14.11 |
| $C_{10}$ | 183.5 |
| $r_0$ | 7.931565 |

**Table 4.5:** Parameters for the HFD-B2 potential, given in atomic units.

The CPMFs calculated at the $T = 3\,\mathrm{K}$ and the $T = 4\,\mathrm{K}$ state points, and also the classical HFD-B2 potential, are shown in Figure 4.11. The qualitative behaviours of the CPMFs are similar to those for parahydrogen shown in the previous Section, although here the shallowing and shift in position of the potential well occur to a much greater degree. At very short separations however, the CPMF stops increasing as rapidly and eventually becomes less repulsive than the classical potential. This effect is more severe at the lower temperature $T = 3\,\mathrm{K}$ state point. This crossover occurs in a region where we still have data on the CPMF from Eq. 4.5 - i.e. before the PIMD centroid radial distribution function goes to zero. We believe this to be a manifestation of the curvature effect - in the region where the classical potential is highly repulsive the two ring polymers may arrange themselves by expanding in the

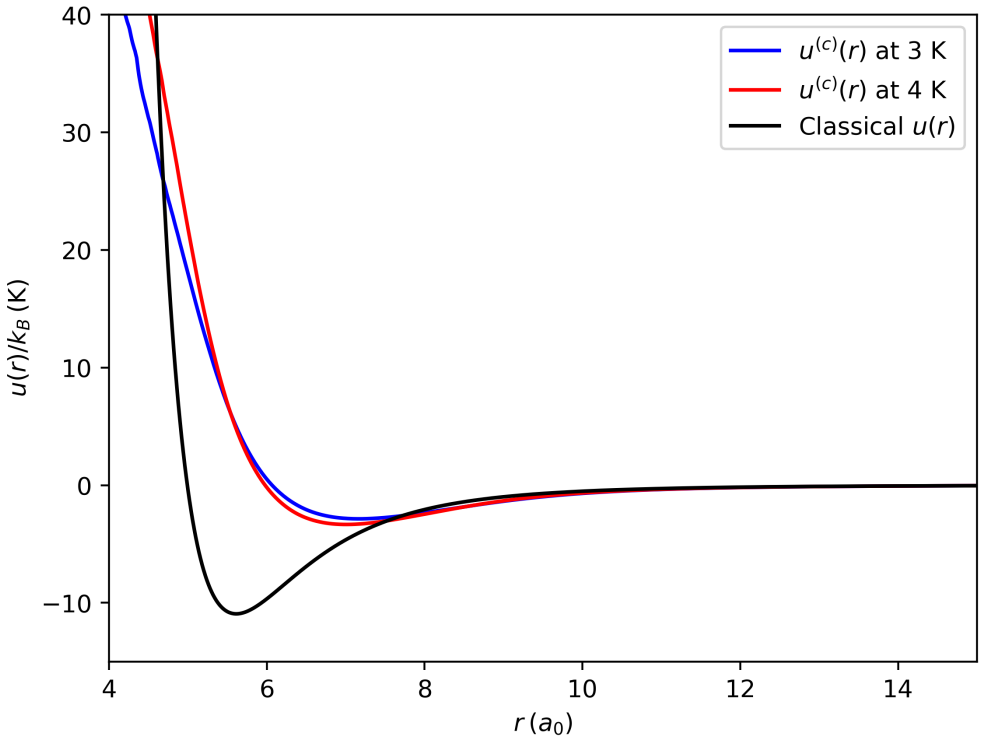



**Figure 4.11:** Centroid potentials of mean force calculated at both the $T = 3\,\mathrm{K}$ and $\rho_m = 141.23\,\mathrm{kg\,m^{-3}}$ and the $T = 4\,\mathrm{K}$ and $\rho_m = 128.97\,\mathrm{kg\,m^{-3}}$ state points. The classical HFD-B2 potential is also shown for reference.

directions orthogonal to the vector separating their centroids. Then, each pair of beads which interact with each other via the classical potential are positioned such that they are further apart than the centroids, and thus the actual forces on the beads are less repulsive than they would be if the beads did not splay out and were located close to the centroid. Since this effect is only relevant at separations where the CPMF is already highly repulsive, these regions will only be visited rarely in a simulation and thus inaccuracies in the potential in this region is not expected to have a significant effect on the dynamics. To prevent any unforeseen effects due to the forces not being repulsive enough in the unlikely event that two molecules do become close enough together to enter this region of the CPMF, we replace the short $r$ region of the calculated CPMF with an exponential fit to the repulsive region of the CPMF where the curvature problem is not significant.

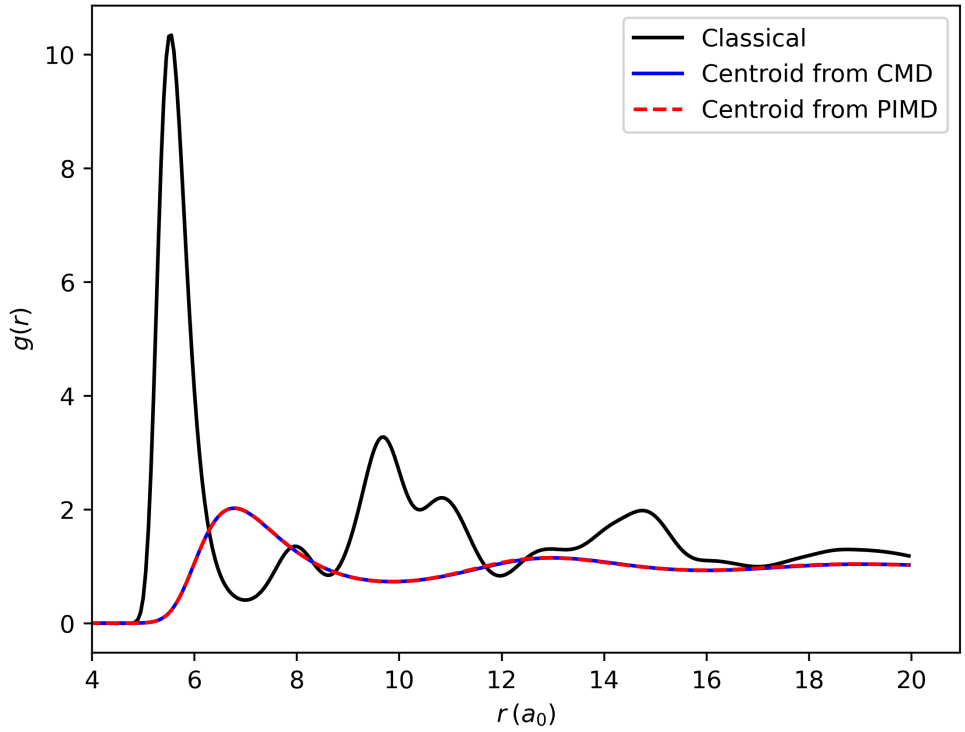



**Figure 4.12:** Various radial distribution functions for HFD-B2 $^4$He calculated at $T = 3.00\,\mathrm{K}$ and $\rho_m = 141.23\,\mathrm{kg\,m^{-3}}$.

The various radial distribution functions calculated for the $T = 3\,\mathrm{K}$ and $T = 4\,\mathrm{K}$ state points are shown in Figs 4.12 and 4.13, respectively. The classical radial distribution functions show, as in the case of liquid parahydrogen, that purely classical HFD-B2 He does not lie in the liquid phase of the classical phase diagram at either of these state points. Instead, both are in the solid-vapour coexistence region. So, for much the same reasons as for parahydrogen in the previous Section we will not be comparing any of the thermal conductivities calculated from CMD with HFD-B2 He with those from classical molecular dynamics.

The scaled Green-Kubo thermal conductivities at four thermodynamic state points close to the saturation line are provided in Table 4.6, as are their unscaled counterparts. The PIMD heat capacity calculations were performed using $P = 512$ path integral beads, where such a large number was found to be necessary to sufficiently converge the energy using the Trotter discretisation. With the benefit

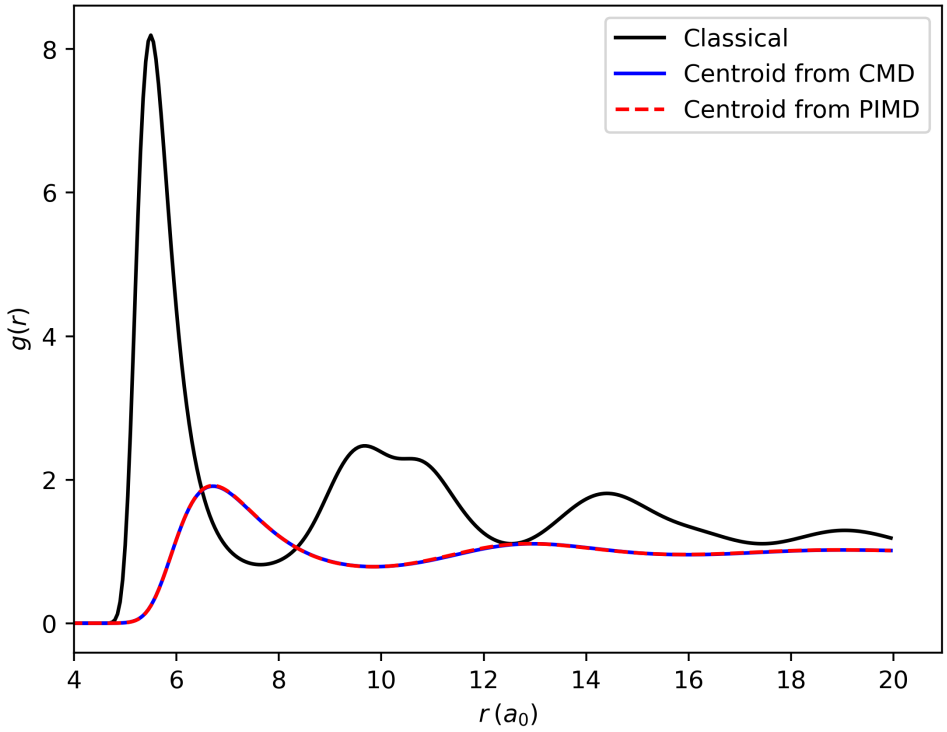



**Figure 4.13:** Various radial distribution functions for HFD-B2 $^4$He calculated at $T = 4.00\,\mathrm{K}$ and $\rho_m = 128.97\,\mathrm{kg\,m^{-3}}$.

| $T$ (K) | $\rho_m$ ($\mathrm{kg\,m^{-3}}$) | $\kappa_{\mathrm{CMD}}$ ($\mathrm{W\,m^{-1}\,K^{-1}}$) | $c_{V,\mathrm{CMD}}$ ($k_B$) | $c_{V,\mathrm{PIMD}}$ ($k_B$) | $\kappa_{\mathrm{scaled}}$ ($\mathrm{W\,m^{-1}\,K^{-1}}$) | $\kappa_{\mathrm{Expt.}}$ ($\mathrm{W\,m^{-1}\,K^{-1}}$) |
|---|---|---|---|---|---|---|
| 3.00 | 141.23 | 0.0446 (7) | 2.470 (2) | 0.898 (10) | 0.0162 (3) | 0.01717 |
| 3.30 | 138.34 | 0.0424 (5) | 2.383 (2) | 0.967 (11) | 0.0172 (3) | 0.01815 |
| 3.65 | 134.17 | 0.0381 (5) | 2.293 (1) | 1.068 (10) | 0.0177 (3) | 0.01902 |
| 4.00 | 128.97 | 0.0357 (7) | 2.217 (3) | 1.120 (11) | 0.0180 (4) | 0.01985 |

**Table 4.6:** Values of the CMD Green-Kubo thermal conductivities, the CMD and PIMD constant volume heat capacities and the corresponding scaled thermal conductivities, as well as experimental measurements by Donnelly and Barenghi[138] at four state points close to the saturation line of liquid $^4$He. The calculations for $\kappa_{\mathrm{CMD}}$ and $c_{V,\mathrm{CMD}}$ were performed by William Moore.

of hindsight, it would probably be advantageous to use an alternative discretisation scheme, such as the Suzuki-Chin discretisation,[48; 50] for faster convergence with respect to the number of beads used. The precomputation of the CPMFs used for the calculation of the CMD data in Table 4.6, as well as the actual calculation of the CMD Green-Kubo thermal conductivities, $\kappa_{\mathrm{CMD}}$, and the CMD heat capacities,

$c_{V,\mathrm{CMD}}$, presented in this Table were performed by William Moore using an edited code provided by the author of this thesis.

These are compared to the experimental values at the same state points in Fig. 4.14. Again, we see that scaling by the ratio of the quantum to classical heat capacities does a good job at bringing the CMD Green-Kubo thermal conductivities closer to experiment - being within 10% of the experimental values across the whole of the temperature range considered. Moreover, the scaled thermal conductivities are found to increase with increasing temperature, in agreement with the experimental temperature dependence. This is in contrast with the unscaled thermal conductivities, which have the opposite temperature dependence. The previous CMD results by Imaoka and Kinugawa[24] also predicted this incorrect temperature dependence, as did the LSC-IVR results by Liu *et al.*[25] As far as we are aware, this is the first theoretical study to capture the temperature dependence of the thermal conductivity of liquid helium correctly.

After applying our method for calculating the quantum thermal conductivity to the two "go-to" examples for simple liquids where significant nuclear quantum effects are present, it is desirable to now apply our approach to a more complicated system. To this end, we move on to the case of liquid water - which we will discuss in the next Chapter.

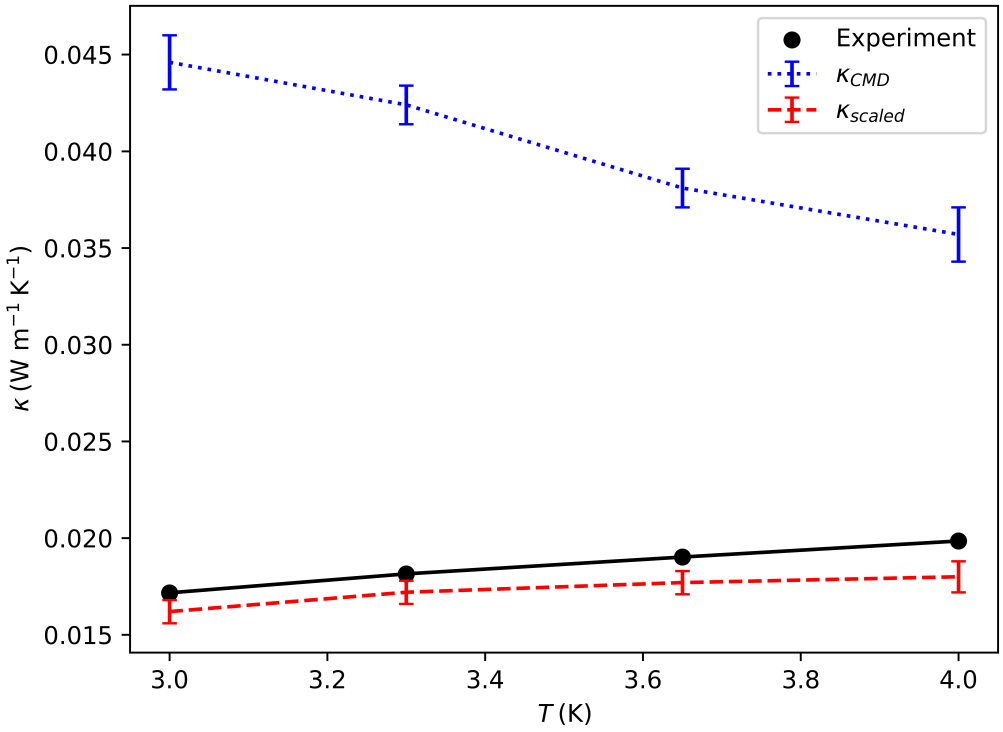



**Figure 4.14:** CMD Green-Kubo thermal conductivities and their corresponding scaled versions calculated at a variety of state points along the saturation line for liquid $^4$He, and compared to the experimental measurements of Donnelly and Barenghi[138] at these state points. The calculations of $\kappa_{\mathrm{CMD}}$ and of the $c_{V,\mathrm{CMD}}$ used in the scaling $\kappa_{\mathrm{scaled}} = c_{V,\mathrm{PIMD}}\kappa_{\mathrm{CMD}}/c_{V,\mathrm{CMD}}$ were performed by William Moore.

# 5

# Thermal conductivity of liquid water

## 5.1 Introduction

As mentioned in Chapter 3, the temperature dependence of the thermal conductivity of liquids generally displays a monotonic decrease as the temperature increases. This primarily occurs due to the decreasing density, so that the average distance between molecules increases and thus heat is transferred through the liquid less efficiently. Liquid water is one of the few substances which presents an exception to this rule - and although the density increases upon melting (contrary to most other liquids), this only occurs within a small temperature range close to the melting point whilst the thermal conductivity continues to increase over a much larger temperature range - up to a maximum close to 400 K.[140] The reason that the thermal conductivity has this anomalous temperature trend is instead likely due to changes in the arrangement of the hydrogen bond network which characterises the liquid structure as the temperature rises. Since hydrogen bonding in theoretical water models is known to require the inclusion of nuclear quantum effects in order to be described correctly,[33] this makes liquid water an appealing system to further test the methods for the calculation of the quantum mechanical thermal conductivity developed in the previous Chapter. Water also has an abnormally high thermal conductivity when compared to other molecular liquids, which together with the

fact that liquid water is one of the most commonly used fluids for heat regulation within engineering applications makes accurate prediction of its thermal conductivity interesting from both a theoretical and an industrial viewpoint.

Nevertheless, liquid water presents a difficult system to model accurately - even without allowing for nuclear quantum effects in the dynamics. A host of potentials have been developed to describe the interactions present in water, with varying degrees of complexity and computational cost. Amongst the most elaborate are many-body potentials found from training a neural network on *ab initio* calculations[141] as well as polarisable models,[142] but due to the appetite for modelling water in large scale simulations, comparatively much simpler pairwise additive potentials remain commonly used. The most popular of these include the extended simple point charge (SPC/E) water model[143] and reparameterisations of the "transferable interatomic potential" (TIP) family - TIP3P, TIP4P and TIP4P/2005 to name a few.[144; 145] These are generally rigid models, where the intramolecular bond length, $r_{\mathrm{OH,\,eq}}$, and bond angle, $\theta_{\mathrm{eq}}$, are held fixed throughout the simulation. Taking the simplicity of these models into account, they typically perform better than one might expect when used in molecular dynamics simulations. However, none of these provide a general potential which is able to calculate all properties with reasonable accuracy,[146] and they may not be applicable to more elaborate simulation environments than bulk-phase liquid water.[147] Flexible versions of each of these potentials have been proposed to enhance their accuracy and extend their viability,[148; 149] but in many cases they do not perform noticeably better than their rigid counterparts.[147]

One feature of classical water models is that they frequently actually give worse agreement with experiment after nuclear quantum effects are included via a path integral simulation.[23; 32; 150] This is because these models have been developed by tuning the parameters within the potential until they give predictions which are consistent with various experimental properties in classical molecular dynamics, and thus will to some extent already include the quantum mechanical effects present in these properties in an effective manner. Therefore, when one uses path integrals to

include nuclear quantum effects in the simulation there is an overcounting of the quantum effects, resulting in less accurate predictions of the true dynamics.[32]

Hence, from the perspective of calculating the properties of liquid water with the inclusion of nuclear quantum effects it is desirable to use a potential which has been parameterised specifically to give accurate results when used in a path integral simulation rather than in one with classical nuclei. Thankfully, several potentials have been proposed to allow for this.[32; 151; 152] Here, we will favour the q-TIP4P/F model since it is fully flexible, and has been parameterised to give the correct radial distribution functions and density at pressures of $p = 1$ atm. using PIMD, the correct diffusion constant using RPMD and the correct vibrational spectrum using partially adiabatic CMD at a temperature of 298 K.[32]

In this Chapter, we will apply the methodology discussed in the previous Chapter to calculate the quantum thermal conductivity of the q-TIP4P/F water model at six state points along the saturation line from 300 K to 550 K, comparing both to previous classical simulations using the SPC/E model by Lee[153] and also to experimental results at the same state points. We will use precomputed CPMFs at each of the state points generated by Dr. Joseph Lawrence using iterative Boltzmann inversion to calculate the CMD Green-Kubo thermal conductivity, and scale them by the ratio of the quantum to CMD constant volume heat capacities. We find that although the precomputed CPMFs produce radial distribution functions consistent with the PIMD centroid distributions, neither the scaled nor the unscaled CMD thermal conductivities perform better than the classical SPC/E results - with the unscaled thermal conductivities overestimating the experimental results and the scaled thermal conductivities underestimating them. We will also for comparison calculate the Green-Kubo thermal conductivities from purely classical molecular dynamics at these state points and scale these by the ratio of the quantum to classical constant volume heat capacities. We find that these are very close to the corresponding CMD scaled and unscaled thermal conductivities at all of the state points considered, indicating that nuclear quantum effects play a very minor

role in the CMD thermal diffusivity within this temperature range (although they do have a large effect on the heat capacity).

## 5.2 The q-TIP4P/F model

Within the q-TIP4P/F model the intramolecular interactions are comprised of two bond terms and an angle term

$$U_{\text{intra}} = \sum_i \left[ u_{\text{bond}}\left(r_{i,\text{OH}_1}\right) + u_{\text{bond}}\left(r_{i,\text{OH}_2}\right) + u_{\text{angle}}\left(\theta_i\right) \right], \tag{5.1}$$

where $r_{i,\text{OH}_1}$ and $r_{i,\text{OH}_2}$ are the O-H bond lengths and $\theta_i$ is the H-O-H bond angle within the $i^{\text{th}}$ water molecule. The bond terms are given by the first three non-zero terms in the Taylor expansion of a Morse potential

$$u_{\text{bond}}\left(r\right) = D_r \left[ \alpha_r^2 \left(r - r_{\text{eq}}\right)^2 - \alpha_r^3 \left(r - r_{\text{eq}}\right)^3 + \frac{7}{12}\alpha_r^4 \left(r - r_{\text{eq}}\right)^4 \right], \tag{5.2}$$

and the angle terms are given by a harmonic potential

$$u_{\text{angle}}\left(\theta\right) = \frac{1}{2} k_\theta \left(\theta - \theta_{\text{eq}}\right)^2. \tag{5.3}$$

The intermolecular interactions are described by a Lennard-Jones type interaction between the oxygen sites

$$u_{\text{LJ}}\left(r\right) = 4\varepsilon \left[ \left(\frac{\sigma}{r}\right)^{12} - \left(\frac{\sigma}{r}\right)^{6} \right], \tag{5.4}$$

and these interactions are computed up to a cutoff radius of $r_{c,\text{LJ}} = 9\text{Å}$. Additionally, charge sites are placed at the two hydrogen atoms with charge $q_M/2$ as well as at a virtual site located at

$$\mathbf{r}_{i,\text{M}} = \gamma \mathbf{r}_{i,\text{O}} + \frac{1}{2}\left(1 - \gamma\right)\left(\mathbf{r}_{i,\text{H}_1} - \mathbf{r}_{i,\text{H}_2}\right), \tag{5.5}$$

with charge $-q_M$ within each molecule $i$. The negative charge is placed here rather than at the position of the oxygen atom to give a more realistic description of the charge distribution around the molecule. The Coulomb interactions, given in atomic units, may be written as

$$U_{\text{Coul}} = \sum_{i>j} \sum_{A,B} \frac{q_{i,A} q_{j,B}}{r_{iAjB}} \tag{5.6}$$

where here, and in the rest of the Chapter, we adopt the convention that the indices $i$ and $j$ label the different molecules in the system whereas the uppercase indices $A$ and $B$ label the interacting charge sites within said molecule, and $r_{iAjB} = |\mathbf{r}_{i,A} - \mathbf{r}_{j,B}|$. In this case, $A$ and $B$ belong to the set $\{\mathbf{r}_{i,\mathrm{M}}, \mathbf{r}_{i,\mathrm{H}_1}, \mathbf{r}_{i,\mathrm{H}_2}\}$ for a given molecule $i$. When the need arises, we will use a lowercase $a$ and $b$ to refer to the set of the physical atomic locations within the molecule, $\{\mathbf{r}_{i,\mathrm{O}}, \mathbf{r}_{i,\mathrm{H}_1}, \mathbf{r}_{i,\mathrm{H}_2}\}$.

Due to the long-range nature of the Coulombic interactions they cannot be truncated using a simple spherical cutoff. Therefore we use the well-established Ewald summation method to split the charge interactions into a contribution which may be calculated efficiently in real space with a short truncation cutoff and a term which is computed in reciprocal space. The real space electrostatic interactions are calculated from

$$U_{\text{Ew, real}} = \sum_{i>j} \sum_{A,B} \frac{q_{i,A} q_{j,B}}{r_{iAjB}} \operatorname{erfc}(\alpha r_{iAjB}), \tag{5.7}$$

where $\operatorname{erfc}(x)$ is the complementary error function and $\alpha$ is a parameter which may be tuned to balance the relative convergence of the real space and the reciprocal space sums. Here we choose to use the value $\alpha = 2.6\,(\rho/V)^{1/6}$, where $\rho$ is the number density and $V$ is the volume of the simulation box, so that the time spent evaluating the two summations are roughly equal.

The reciprocal space interactions are computed as a sum over reciprocal lattice vectors, $\mathbf{k}$, using

$$U_{\text{Ew, recip.}} = \frac{2\pi}{V} \sum_{\mathbf{k}\neq\mathbf{0}} \frac{\exp(-k^2/4\alpha^2)}{k^2} \sum_{i,A,j,B} q_{i,A} q_{j,B} \exp(i\mathbf{k}\cdot\mathbf{r}_{iAjB}), \tag{5.8}$$

where $k = |\mathbf{k}|$ is the magnitude of the reciprocal lattice vector and the sums run over all the charges in the system. Since the intramolecular electrostatic interactions must be excluded from the overall energy and yet are included in the reciprocal space portion of the Ewald sum a correction must be added to the real space sum of the form

$$U_{\text{Ew, intra}} = \sum_{i} \sum_{A\neq B} \frac{q_{i,A} q_{j,B}}{r_{iAjB}} \operatorname{erf}(\alpha r_{iAjB}), \tag{5.9}$$

where erf $(x)$ is the error function. Finally, the atomic self energy calculated in the reciprocal space sum must also be subtracted from

$$U_{\text{Ew, self}} = \frac{-\alpha}{\sqrt{\pi}} \sum_{i,A} q_{i,A}^2. \tag{5.10}$$

The forces calculated on the virtual site from this procedure are distributed onto the physical atoms within each molecule using the chain rule.

An efficient implementation of the Ewald sum method scales as $N^{3/2}$, meaning this is by far the most expensive part of the force evaluation.[154] More sophisticated alternatives exist - such as the Particle-Particle-Particle Mesh (PPPM) method, which scales as $N \log N$.[155] However, as we will mostly be concerned with relatively small system sizes ($N \approx 256$ molecules) in this work, we opted to use the standard Ewald sum method for the simulations in this Chapter due to its relative simplicity to implement. The various parameters present in the q-TIP4P/F potential are provided in Table 5.1 below.

| | |
|---|---|
| $D_r$ | 0.1850 |
| $\alpha_r$ | 1.210 |
| $r_{\text{eq}}$ | 1.780 |
| $k_\theta$ | 0.140 |
| $\theta_{\text{eq}}$ | 1.874 |
| $\varepsilon$ | $2.951 \times 10^{-4}$ |
| $\sigma$ | 5.9695 |
| $\gamma$ | 0.73612 |
| $q_M$ | 1.128 |

**Table 5.1:** Parameters for the q-TIP4P/F potential, given in atomic units or radians where applicable.

Unless stated otherwise, all results presented in this Chapter were calculated using $N = 256$ molecules and the dynamics propagated using a timestep of 0.2 fs. Temperature control in the $NVT$ ensemble was achieved using a stochastic velocity rescaling thermostat[125] for the classical and CMD simulations and the PILE-G thermostat[40] for the PIMD simulations. Periodic boundary conditions were used throughout.

## 5.3 Quantum mechanical heat capacities

Due to the need to treat the long range Coulomb interactions the liquid water simulations are significantly more computationally expensive than either the liquid parahydrogen or the liquid helium simulations discussed in the previous Chapter, even with an efficient implementation of an Ewald sum exploiting the symmetries of the cubic simulation cell. Hence, it is especially desirable here to make our path integral calculations as efficient as possible. As a result, we switch to using the Suzuki-Chin propagator to evolve the path integral dynamics.[48] When using this propagator, the forces used to update the momenta in the "B" portion of the integrator splitting are no longer the forces from the classical potential evaluated at the bead positions, as they were in Eq. 2.20, but now also include an additional term involving the Hessian. Evaluating the Hessian is obviously undesirable in the already expensive force computation, so to avoid this we follow the symmetric finite difference scheme proposed by Kapil *et al.*[50]

Using this, the Suzuki-Chin forces on the $k^{\text{th}}$ bead of the ring polymer associated with the $i^{\text{th}}$ particle are approximated by

$$\mathbf{F}^{(k)}_{\text{SC},i} = w_k \mathbf{F}^{(k)}_i \left(\mathbf{x}^{(k)}\right) - \frac{w_k d_k}{\varepsilon_{\text{SC}} \delta \omega_P^2} \left[\mathbf{F}^{(k)}_i \left(\mathbf{x}^{(k)} + d\mathbf{x}^{(k)}\right) - \mathbf{F}^{(k)}_i \left(\mathbf{x}^{(k)} - d\mathbf{x}^{(k)}\right)\right], \quad (5.11)$$

in which $\omega_P = 1/\beta\hbar$ and $w_k$ and $d_k$ are weighting parameters that take different values depending on whether $k$ is odd or even. When $k$ is odd we have $w_k = 4/3$ and $d_k = 1/12$, and in the case that $k$ is even we have $w_k = 2/3$ and $d_k = 0$. $\mathbf{F}^{(k)}_i \left(\mathbf{x}^{(k)}\right)$ denotes the classical force $-\partial U \left(\mathbf{x}^{(k)}\right) / \partial \mathbf{x}^{(k)}_i$, where $U \left(\mathbf{x}^{(k)}\right)$ is the q-TIP4P/F potential evaluated at the positions $\mathbf{x}^{(k)}$. The finite difference displacements $d\mathbf{x}^{(k)}$ are given by $d\mathbf{x}^{(k)} = \varepsilon_{\text{SC}} \delta \mathbf{F}^{(k)}_i \left(\mathbf{x}^{(k)}\right) / m_i$, where $m_i$ is the mass of the $i^{\text{th}}$ atom. $\delta$ is given by

$$\delta^{-2} = \frac{1}{NP} \sum_i \frac{|\mathbf{F}^{(k)}_i|^2}{m_i^2} \quad (5.12)$$

and $\varepsilon_{\text{SC}}$ is a tolerance parameter which we set to $10^{-5}$ in all the Suzuki-Chin simulations presented in this Chapter. We note that there is a change of sign in

Eq. 5.11 compared to the equation originally given in Ref. [50], which we believe to be due to a typographic error in that paper.

Since $d_k$ is zero for the even beads, the displaced forces need only be evaluated for the case where $k$ is odd. This formulation of the Suzuki-Chin propagator therefore requires twice as many force evaluations as the Trotter propagator used previously in this thesis. However, the Suzuki-Chin propagator converges to the true quantum partition function as $\mathcal{O}\left(\beta_P^4\right)$, compared to $\mathcal{O}\left(\beta_P^2\right)$ when the Trotter propagator is used. So, for systems where one can use fewer than half as many beads with Suzuki-Chin then this represents a speed-up over the conventional Trotter propagator.

In order to compute the energy of the system when using the Suzuki-Chin propagator one must use different estimators than one would when using the Trotter propagator. Within the Suzuki-Chin scheme there are several classes of estimators which one can use to compute for thermodynamic quantities,[50] and here we will favour the "operator" form due to its simplicity to implement. These make use of the fact that only the coordinates of the even beads sample the correct distribution of positions, and so the estimators for the kinetic and potential energies in the Trotter formulation given in Eqs 2.25 and 4.14 can simply be adapted so that the sums only run over the even beads. The potential energy is calculated using

$$V^{\mathrm{SC}} = \frac{2}{P} \sum_{k \in \mathrm{even}} U\left(\mathbf{x}^{(k)}\right), \tag{5.13}$$

and the Suzuki-Chin kinetic energy is found using

$$T^{\mathrm{SC}} = \frac{3N}{2\beta} + \frac{1}{P} \sum_{k \in \mathrm{even}} \left(\mathbf{x}^{(k)} - \mathbf{x}_c\right) \cdot \mathbf{F}^{(k)}. \tag{5.14}$$

The PIMD per molecule heat capacity was calculated using a finite difference approximation to $c_V = (1/N)\left(\partial E/\partial T\right)_\rho$ at six state points along the saturation line of liquid water, over a wide temperature range from 300 K to 550 K. For each temperature $T$, we computed the total energy at five different temperatures along an evenly spaced grid from $0.9\,T$ to $1.1\,T$. The system was equilibrated in the $NVT$ ensemble for a time period of 100 ps and then the Suzuki-Chin energy was computed at each step using Eqs 5.13 and 5.14 for a further 100 ps. This was then repeated

over five independent trajectories to give an estimate of the average energy and its standard error at each of the grid points. A value of $P = 32$ ring polymer beads was found to be sufficient to converge the heat capacity at 300 K, the lowest temperature considered here, and this value of $P$ was used at the other temperatures as well. The PIMD heat capacity, $c_{V,\,\mathrm{PIMD}}$, and its uncertainty was then found from the gradient of a weighted linear least squares fit through these five data points. The resulting constant volume heat capacities and their standard errors at each of the six thermodynamic state points considered in this Chapter are summarised in Table 5.2 below, as are the experimental values, $c_{V,\,\mathrm{Expt.}}$, taken from the NIST website.[140]

| $T$ (K) | $\rho_m$ (g cm$^{-3}$) | $c_{V,\,\mathrm{PIMD}}$ ($k_B$) | $c_{V,\,\mathrm{Class.}}$ ($k_B$) | $c_{V,\,\mathrm{CMD}}$ ($k_B$) | $c_{V,\,\mathrm{Expt.}}$ ($k_B$) |
|---|---|---|---|---|---|
| 300 | 0.9965 | 8.3 (1) | 13.82 (8) | 13.55 (7) | 8.950 |
| 350 | 0.9737 | 7.87 (9) | 12.65 (7) | 12.59 (6) | 8.427 |
| 400 | 0.9375 | 7.55 (6) | 11.60 (4) | 11.73 (3) | 7.870 |
| 450 | 0.8903 | 7.07 (5) | 10.86 (2) | 10.96 (3) | 7.384 |
| 500 | 0.8313 | 6.80 (4) | 10.23 (2) | 10.35 (2) | 6.989 |
| 550 | 0.7558 | 6.56 (4) | 9.83 (2) | 9.97 (2) | 6.698 |

**Table 5.2:** Constant volume heat capacities per molecule calculated using PIMD, CMD and classical molecular dynamics as well as the corresponding experimental heat capacities at six state points along the saturation curve of liquid water. The experimental values were taken from Ref. [140]. The CPMFs used in the calculation of $c_{V,\mathrm{CMD}}$ were computed by Dr. Joseph Lawrence.

Also included in Table 5.2 are the constant volume heat capacities per molecule calculated from classical molecular dynamics from the fluctuations of the total energy in the $NVT$ ensemble as

$$c_{V,\,\mathrm{Class.}} = \frac{\langle E^2 \rangle - \langle E \rangle^2}{N k_B T^2}, \tag{5.15}$$

where $E$ is the total energy of the system and $\langle \dots \rangle$ denotes a canonical ensemble average. These heat capacities were calculated in the same set of simulations as the classical Green-Kubo thermal conductivities to be discussed in Section 5.5. Additionally, the constant volume heat capacities calculated from CMD, $c_{V,\,\mathrm{CMD}}$, are also provided. These were calculated in a similar manner using the approximate CPMFs computed by Dr. Joseph Lawrence to be discussed in the following Section. From these results it is clear that the inclusion of nuclear quantum effects in

the q-TIP4P/F potential greatly improves the prediction of the heat capacity compared to the classical or the CMD simulations, which consistently overestimate the experimental results by around 50%. The agreement with experiment is still not perfect, with the PIMD simulations systematically underestimating the experimental heat capacity and being up to 8% different at 300 K. Somewhat surprisingly, the agreement of $c_{V,\mathrm{PIMD}}$ with experiment is a lot closer at the higher temperatures than it is near to the temperatures at which the potential was originally parameterised. However, given that the q-TIP4P/F is still a somewhat simplistic description of liquid water even whilst considering nuclear quantum effects, the agreement with experiment is reasonable across the whole temperature range studied here. There is not any significant difference between $c_{V,\,\mathrm{Class.}}$ and $c_{V,\,\mathrm{CMD}}$ at any of the state points considered.

## 5.4 Centroid potentials of mean force

Due to liquid water being a molecular system we cannot adequately approximate the centroid potential of mean force as a single set of spherically symmetric pairwise additive interactions, as we did for the comparatively simpler models used for liquid parahydrogen and liquid helium in the previous Chapter. However, the added complexity of the q-TIP4P/F potential and the requirement to use an Ewald summation to compute the charge interactions means that these calculations are already fairly expensive, and thus resorting to a typical implementation of partially adiabatic CMD, with the need for a full path integral simulation and a smaller time step, is especially undesirable. Development of a process for calculating the centroid potentials of mean force and the actual computation of these potentials was done by Dr. Joseph Lawrence, and then the potentials were sent to the author of this thesis for the calculation of the thermal conductivity. Due to the importance of these potentials for the results to be presented later in this Chapter, it is useful to provide a description of the method in which they were computed here.

The CPMF was chosen to be approximated using a set of pairwise additive correction terms to the classical q-TIP4P/F potential, $u_{ab}(r)$, where $a, b \in \{\mathrm{O}, \mathrm{H}\}$

differentiate the *intermolecular* oxygen-oxygen, oxygen-hydrogen and hydrogen-hydrogen interactions. The intramolecular bond potentials were modelled by a quartic function

$$u_{\text{bond}}^{\text{CMD}}(r) = k_2 (r - r_{\text{eq}})^2 + k_3 (r - r_{\text{eq}})^3 + k_4 (r - r_{\text{eq}})^4 , \tag{5.16}$$

and the intramolecular angle potential as a harmonic function of the bond angle

$$u_{\text{angle}}^{\text{CMD}}(\theta) = \frac{1}{2} k_\theta (\theta - \theta_{\text{eq}})^2 . \tag{5.17}$$

This choice of intramolecular potentials is of the same form as the original q-TIP4P/F intramolecular potentials, Eq.s 5.2 and 5.3, so this effectively represents a reparameterisation of the intramolecular portion of the q-TIP4P/F potential. Whilst restricting the intramolecular part of our approximate CPMF to the above forms and neglecting the intermolecular many-body contributions to the true CPMF is clearly an approximation, it has the advantage of being straightforward and efficient to include in a molecular dynamics simulation.

Our aim in determining the form of the $u_{ab}(r)$ and the parameters in the intramolecular CMD potentials is to devise an approximate CPMF that reproduces the structural information contained within the centroid intermolecular radial distribution functions between species $a$ and $b$, $g_{ab}^{c}(r)$, as well as the intramolecular centroid bond length and angle distributions, $g_{\text{bond}}^{c}(r)$ and $g_{\text{angle}}^{c}(\theta)$ respectively, which are calculated from PIMD. For this purpose we adopt the iterative Boltzmann inversion technique,[130; 131] where a trial potential is systematically improved upon until the radial and angular distribution functions generated by it are consistent with those from a more accurate (and usually more expensive) reference calculation - in this case the PIMD centroid distributions - to within some small tolerance.

At each stage of the iterative process the intermolecular correction potentials are updated using

$$u_{ab}^{(i+1)}(r) = u_{ab}^{(i)}(r) + \frac{1}{\beta} \log \frac{g_{ab}^{\text{c}}(r) + \varepsilon g_{ab}^{\max}(r)}{g_{ab}^{(i)}(r) + \varepsilon g_{ab}^{\max}(r)}, \tag{5.18}$$

where the initial trial intermolecular correction, $u_{ab}^{(0)}$, is set to zero and $g_{ab}^{(i)}(r)$ is the intermolecular radial distribution function between species $a$ and $b$ calculated

using the current set of approximate intermolecular and intramolecular correction potentials together with the underlying q-TIP4P/F potential. The term $\varepsilon g_{ab}^{\max}(r)$, where $g_{ab}^{\max}(r)$ is the maximum value of either $g_{ab}^{(i)}(r)$ or $g_{ab}^{c}(r)$ over the range of separations considered and $\varepsilon$ is a tolerance parameter, is a modification added to the usual iterative Boltzmann inversion scheme to prevent the correction potentials from changing too significantly in regions where one does not obtain sufficient information from the RDF calculation. Here the value of $\varepsilon = 1$ was chosen in all cases. This modification was found to allow for more reliable iteration in cases where the RDF goes close to zero, for example in between the first two intermolecular coordination shells of the oxygen-hydrogen RDF shown in Fig. 5.2.

An analogous equation to Eq. 5.18 is used to update the intramolecular bond and angle potentials using the corresponding intramolecular bond or angle distribution functions. The only difference is that after each iteration step the intramolecular potentials plus the current correction terms (which are again initially set to zero) are fitted to the functional forms defined by Eqs 5.16 and 5.17 for the bond and angle potentials respectively, and it is these fitted functions which are then used in the following iteration step.

The theoretical basis for iterative Boltzmann inversion relies on the observation that for a pairwise additive potential there is a one-to-one correspondence between the potential and the radial distribution function generated by it.[130; 156] However, this argument does not translate to a molecular system like liquid water,[157] and it has been observed that even for purely pairwise additive one-component systems that two very different potentials can produce radial distribution functions which are indistinguishable from each other to within the statistical errors of the simulation.[158; 159] Moreover, iterative Boltzmann inversion can converge very slowly in cases where multiple different potentials need to be corrected simultaneously, so that it may not be feasible to exactly reproduce the centroid distribution functions within a reasonable number of iterations.[160] Nevertheless, iterative Boltzmann inversion has been applied to a wide variety of problems in coarse-graining simulations with good success,[131; 161; 162] and if the correct

quantum position distributions can be estimated well enough then it is hopeful that the resulting approximate CPMFs will contain enough information for dynamics calculations as well.

The CPMFs at each state point were found by applying the process outlined earlier to the three intermolecular corrections and both of the intramolecular potentials simultaneously at each iteration step. Since, for example, the distribution function $g_{ab}^{(i)}(r)$ depends not only on the current iteration of the potential associated with it, $u_{ab}^{(i)}(r)$, but also on the potentials between the other species, the convergence of the iterative process is not always straightforward. One of the distribution functions may converge to the target distribution function quickly initially, but then further convergence may slow or even reverse slightly as corrections in other areas of the overall potential take place. A total of 20 iterative Boltzmann inversions were performed at each of the state points. All of the classical and PIMD centroid distribution functions were computed using $N = 216$ water molecules and the PIMD simulations used $P = 32$ ring polymer beads in each case.

The CMD intramolecular parameters found from this procedure at the $T = 300\,\mathrm{K}$ and $\rho_m = 0.9965\,\mathrm{g\,cm^{-3}}$ state point as an example are shown in Table 5.3 below, as are the corresponding intramolecular parameters for the purely classical q-TIP4P/F potential. For ease of comparison the parameters for the classical q-TIP4P/F O-H bond potential, Eq. 5.2, have been converted to the form used in the fitting procedure for the centroid potential of mean force, Eq. 5.16. So, for the classical potential we have that $k_2 = D_r\alpha_r^2$, $k_3 = -D_r\alpha_r^3$ and that $k_4 = 7D_r\alpha_r^4/12$. From this Table we may see that the inclusion of nuclear quantum effects produces a small increase in both the equilibrium O-H bond length and H-O-H bond angle of the isolated water molecule. Whilst there is only a relatively minor change in the magnitude of these properties in going from the classical to the CMD potentials, it is known that even small changes in the intramolecular geometry can have marked effects on the predicted properties of the system.[163]

As a check on both the implementation of the liquid water centroid potentials of mean force and to assess their accuracy in incorporating the nuclear quantum

| | CMD | Classical |
|---|---|---|
| $r_{\mathrm{eq}}$ | 1.7824 | 1.780 |
| $k_2$ | 0.2354 | 0.2709 |
| $k_3$ | −0.1811 | −0.3277 |
| $k_4$ | 0.03396 | 0.2313 |
| $\theta_{\mathrm{eq}}$ | 1.87925 | 1.874 |
| $k_\theta$ | 0.13537 | 0.140 |

**Table 5.3:** Intramolecular parameters for the CMD potentials of mean force at the $T = 300\,\mathrm{K}$, $\rho_m = 0.9965\,\mathrm{g\,cm^{-3}}$ state point and the classical q-TIP4P/F potential, both given in atomic units or radians where applicable.

effects, we calculated the radial distribution functions for the oxygen-oxygen, $g_{\mathrm{OO}}(r)$, oxygen-hydrogen, $g_{\mathrm{OH}}(r)$, and hydrogen-hydrogen, $g_{\mathrm{HH}}(r)$, pairs at the $T = 300\,\mathrm{K}$ and $\rho_m = 0.9965\,\mathrm{g\,cm^{-3}}$ state point both classically and using our CPMFs. We also calculated the corresponding PIMD centroid radial distribution functions at the same state point using $P = 32$ path integral beads and the Suzuki-Chin propagator. It is important to recall from Section 5.3 that when using this propagator only the even beads of the ring polymer sample the correct quantum mechanical distribution of positions,[50; 164] and therefore this must be accounted for when calculating the PIMD centroid radial distribution functions. For this reason the centroid position and the centroid force in the force based estimator of Eq. 4.6 are replaced with

$$\mathbf{x}_c^{\mathrm{SC}} = \frac{2}{P} \sum_{k \in \mathrm{even}} \mathbf{x}^{(k)}, \tag{5.19}$$

and

$$\mathbf{F}_c^{\mathrm{SC}} = \frac{2}{P} \sum_{k \in \mathrm{even}} \frac{\partial U\left(\mathbf{x}^{(k)}\right)}{\partial \mathbf{x}^{(k)}}, \tag{5.20}$$

respectively. All calculations were performed using an equilibration period of 100 ps in the relevant $NVT$ ensemble. After the equilibration period the radial distribution functions were accumulated over a sampling period of 100 ps and the entire process averaged over 50 independent simulations for the classical and the CMD calculations, and 20 independent simulations for the PIMD calculations.

The resulting oxygen-oxygen radial distribution functions, $g_{\mathrm{OO}}(r)$, are shown as an example in Fig. 5.1 below. There is only a very small difference between any of the three radial distribution functions, with the CMD and PIMD centroid RDFs

showing closer agreement with each other and containing slightly less structure than the classical RDF - consistent with the hydrogen bond network being broken up by quantum mechanical fluctuations within the system.

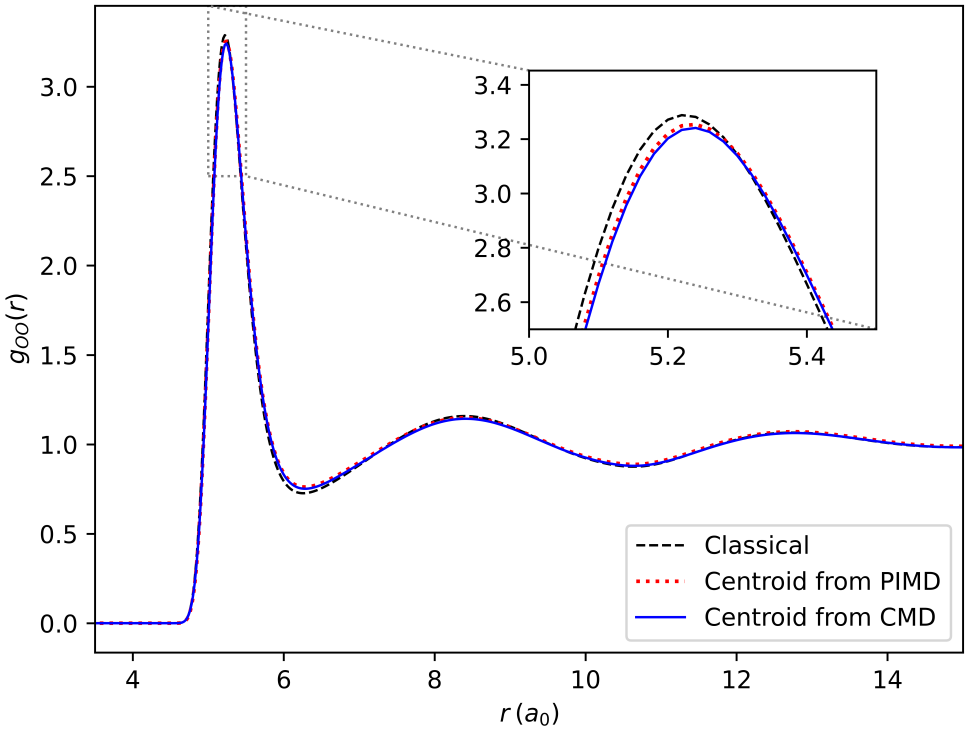



**Figure 5.1:** The classical oxygen-oxygen radial distribution function for the q-TIP4P/F potential at $T = 300$ K and $\rho_m = 0.9965$ g cm$^{-3}$. Also shown are the centroid radial distribution functions calculated with both PIMD and CMD using our approximate CPMFs. The inset shows a magnification of the first coordination peak. The approximate CPMFs used in the CMD calculation were determined by Dr. Joseph Lawrence.

The oxygen-hydrogen and hydrogen-hydrogen radial distribution functions are also shown in Figs 5.2 and 5.3 respectively. They tell a very similar story to the oxygen-oxygen RDFs shown in Fig. 5.1. For the most part, the CPMFs generated by iterative Boltzmann inversion do well at correcting the slight inaccuracies in the classical RDFs compared to those from the PIMD centroids, including in the intramolecular region. This is particularly true in the case of the hydrogen-hydrogen RDF, $g_{\mathrm{HH}}(r)$, where there is very close agreement between the CMD centroid and the PIMD centroid RDFs across the whole range of separations considered. That is not

to say that the CPMFs are perfect, however. The shape of the intramolecular peak in the oxygen-hydrogen RDF, $g_{\mathrm{OH}}(r)$, is certainly better accounted for in the CMD centroid RDF than in the classical case, but it is still slightly too high when compared to the PIMD centroid RDF. Moreover, the first intermolecular coordination peak close to $3.5a_0$ in the CMD centroid RDF is actually underestimated compared to that from the PIMD centroids, whilst the classical RDF shows almost perfect agreement with the PIMD centroid RDF in the same region. These small inaccuracies in the CMD centroid RDF are likely an artefact of using the iterative Boltzmann inversion technique to generate the CPMFs. Even after 20 iterations the CPMFs cannot reproduce the correct quantum mechanical structure generated from the PIMD centroids exactly. However, we should emphasise that on the whole the agreement of the CMD centroid and the PIMD centroid RDFs is very good, and we can be satisfied that our approximate CPMFs can capture much of the role that nuclear quantum effects play in the liquid structure.

## 5.5 Green-Kubo thermal conductivity

Having determined the form of the different approximate centroid potentials of mean force for each of the state points considered in this Chapter, we now move on to test how well they capture the role of nuclear quantum effects on the dynamics of the system. For this purpose we move directly towards calculating the thermal conductivity, which we will again do using the equilibrium Green-Kubo method together with the scaling by the ratio of the PIMD to CMD constant volume heat capacities developed in the previous Chapter.

In addition, we investigate how good an approximation one can obtain by simply scaling the classical Green-Kubo thermal conductivity by the ratio of the PIMD and classical constant volume heat capacities, as this could potentially remove the requirement to calculate the centroid potential of mean force altogether. Obtaining the centroid potential of mean force is more involved in the case of water than it was for liquid parahydrogen or liquid helium, and so it would be useful if one could

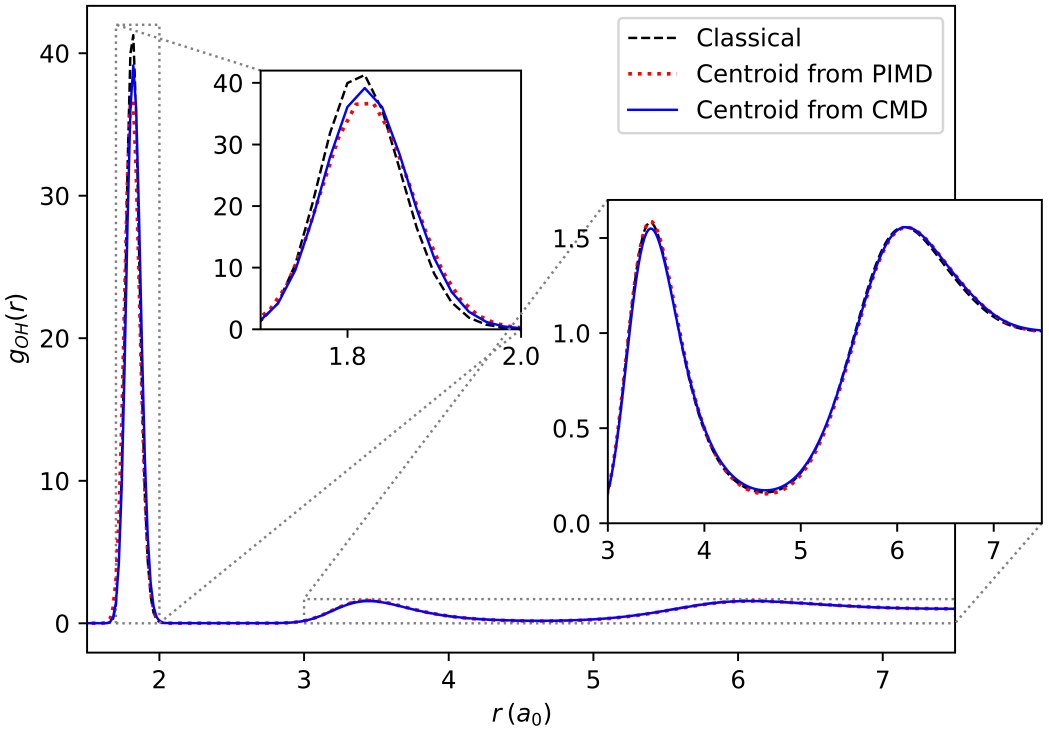



**Figure 5.2:** The classical oxygen-hydrogen radial distribution function for the q-TIP4P/F potential at $T = 300$ K and $\rho_m = 0.9965$ g cm$^{-3}$. Also shown are the centroid radial distribution functions calculated with both PIMD and CMD using our approximate CPMFs. The insets show magnifications of the intramolecular and intermolecular regions. The approximate CPMFs used in the CMD calculation were determined by Dr. Joseph Lawrence.

bypass this and obtain a reasonable estimate of the quantum thermal conductivity simply by scaling the classical Green-Kubo thermal conductivity.

The thermal conductivity of liquid water has been previously studied using molecular dynamics by a variety of different models and methods.[165–167] We choose to use as a comparison the results of Lee,[153; 168] who calculated the classical Green-Kubo thermal conductivity of the SPC/E model of water over a wide temperature range on the saturation line between 300 K and 550 K. Their results qualitatively reproduced the experimentally observed maximum in the thermal conductivity close to 400 K. The results showed relatively poor quantitative agreement with experiment however, with an overestimation of the thermal conductivity by 26% at 400 K. Here, we focus on the six high temperature state points between 300 K

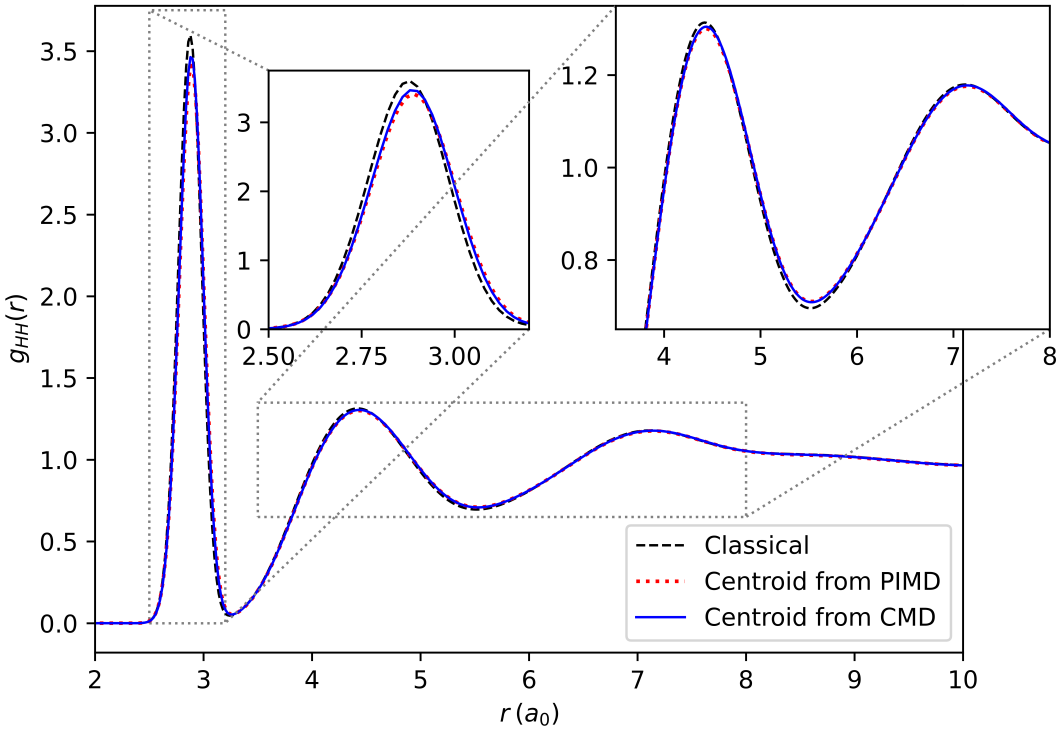



**Figure 5.3:** The classical hydrogen-hydrogen radial distribution function for the q-TIP4P/F potential at $T = 300\,\mathrm{K}$ and $\rho_m = 0.9965\,\mathrm{g\,cm^{-3}}$. Also shown are the centroid radial distribution functions calculated with both PIMD and CMD using our approximate CPMFs. The insets show magnifications of the intramolecular and intermolecular regions. The approximate CPMFs used in the CMD calculation were determined by Dr. Joseph Lawrence.

and 550 K used by Lee,[153] which are the same state points as used to calculate the values of $c_{V,\mathrm{PIMD}}$ given in Table 5.2 earlier, using both the classical q-TIP4P/F potential and the CPMFs calculated by Dr. Joseph Lawrence at these state points.

For a molecular system, two different formulations of the heat flux vector are commonly used.[169; 170] We choose to calculate the heat flux in the *atomic representation*, where the site energy of each atom in a molecule is calculated independently and used together with the velocity of the respective atom in Eq. 3.70 to compute the overall heat flux vector. This is in contrast to the *molecular representation*, in which each molecule is instead treated as a distinct "site". The site energy of each molecule is calculated, and then Eq. 3.70 is used by summing over all of the molecules together with the centre-of-mass positions and velocities

of that molecule. Although the different divisions of the site energy within each molecule may yield differently appearing heat flux autocorrelation functions, it can be shown that the integrated thermal conductivity from Eq. 3.64 is independent of which representation is used.[169] We choose to calculate the heat flux in the atomic representation since the contributions arising from the Coulomb interactions in an Ewald summation scheme are more straightforward to include.[171]

The calculation of the contribution of the Coulomb interactions to the heat flux vector is complicated by the presence of the virtual charge sites in the q-TIP4P/F potential, meaning that the previously derived expressions for the heat flux cannot be used "out of the box" for this contribution. To show this, we consider a simplified system where the only interactions present are the electrostatic interactions within the q-TIP4P/F potential. The result carries over to the full q-TIP4P/F potential since the contributions to the heat flux from different parts of the potential are straightforwardly additive.

If we denote the heat flux generated from this simplified system as $\mathbf{J}^{\mathrm{coul}}$, then we may write

$$\mathbf{J}^{\mathrm{coul}} = \frac{d}{dt} \sum_{i,a} \varepsilon_{i,a} \mathbf{r}_{i,a}, \tag{5.21}$$

where $\varepsilon_{i,a}$ is the site energy of atom $a$ in molecule $i$. We recall that the lowercase indices $a$ and $b$ refer to a sum over the atomic positions in each molecule only, so that the virtual site is not included explicitly in the summation. Instead, we distribute the electrostatic energy originating from the virtual site of each molecule onto the sites of the physical atoms in that molecule with weight given by the coefficients used in determining the virtual site position in Eq. 5.5 - so that

$$\varepsilon_{i,a} = \frac{1}{2} m_a |\mathbf{v}_{i,a}|^2 + U_{i,a} + c_a U_{i,\mathrm{M}}, \tag{5.22}$$

in which $c_{\mathrm{O}} = \gamma$ and $c_{\mathrm{H}_1} = c_{\mathrm{H}_2} = (1-\gamma)/2$ and $m_a$ is the mass of atom $a$. $U_{i,a}$ denotes the contribution to the electrostatic potential energy from atom $a$ in molecule $i$, and $U_{i,\mathrm{M}}$ that from the virtual site. Since the oxygen atoms do not participate explicitly in the charge interactions, then $U_{i,\mathrm{O}} = 0$.

The convective contribution to the Coulombic heat flux can then be found straightforwardly as

$$\begin{aligned}\mathbf{J}_{\text{conv}} &= \sum_{i,a} \varepsilon_{i,a}\mathbf{v}_{i,a} \\ &= \sum_{i,a}\left(\frac{1}{2}m_a|\mathbf{v}_{i,a}|^2 + U_{i,a}\right)\mathbf{v}_{i,a} + \sum_i U_{i,\text{M}}\mathbf{v}_{i,\text{M}},\end{aligned} \tag{5.23}$$

where $\mathbf{v}_{i,\text{M}} = \sum_a c_a \mathbf{v}_{i,a}$ is the "velocity" of the virtual site. So, for the purposes of calculating the convective heat flux, our choice of distributing the energy contribution from the virtual site onto the real atomic sites is entirely equivalent to treating the virtual site as an additional massless atom with its own site energy and velocity given by the weighted contribution of the real atomic velocities - which was the way in which the virtual site was treated in the earlier work by Luo and Yu.[116]

The Coulombic contribution to the virial heat flux, $\mathbf{J}_{\text{vir}}$, is where the difficulty arises. We have that

$$\mathbf{J}_{\text{vir}} = \sum_{i,a} \frac{d\varepsilon_{i,a}}{dt}\mathbf{r}_{i,a}, \tag{5.24}$$

where

$$\frac{d\varepsilon_{i,a}}{dt} = \mathbf{F}_{i,a}^{\text{tot}} \cdot \mathbf{v}_{i,a} + \frac{dU_{i,a}}{dt} + c_a\frac{dU_{i,\text{M}}}{dt}, \tag{5.25}$$

and $\mathbf{F}_{i,a}^{\text{tot}}$ is the total force on atom $a$ in molecule $i$, including any force which is distributed onto it from the virtual site. In order to find expressions for $dU_{i,a}/dt$ and $dU_{i,a}/dt$ we utilise the chain rule together with a complete set of independent positions to write

$$\frac{dU_{i,a}}{dt} = \sum_{j,B}\frac{dU_{i,a}}{d\mathbf{r}_{j,B}} \cdot \mathbf{v}_{j,B}, \tag{5.26}$$

and a similar expression holds for $dU_{i,\text{M}}/dt$. We recall that the uppercase indices $A$ and $B$ refer to the sites which *participate* in the charge interactions rather than the physical atomic positions. The choice to expand the site potentials in terms of this set of vectors was done so that the resulting derivatives are easily expressible in terms of the forces which are calculated within the simulation. We also note that

since $U_{i,\mathrm{O}} = 0$ that we can use the notation $U_{i,A}$ to encompass all of the non-zero site potentials in Eq. 5.26 and $U_{i,\mathrm{M}}$ without loss of generality.

We can then write that

$$U_{i,A} = \frac{1}{2}\sum_{j,B} u\left(r_{iAjB}\right), \tag{5.27}$$

where $u\left(r_{iAjB}\right)$ is the pair interaction between site $A$ in molecule $i$ and the site $B$ in molecule $j$ and $r_{iAjB} = |\mathbf{r}_{i,A} - \mathbf{r}_{j,B}|$. We note that the case where $i = j$ and $A = B$ should be excluded from the summation. Then, since $du\left(r_{iAjB}\right)/d\mathbf{r}_{i,A} = -\mathbf{F}_{iAjB}$, the pair force on site $A$ in molecule $i$ due to the presence of site $B$ in molecule $j$, we can re-express the derivative in Eq. 5.26 as $dU_{i,A}/d\mathbf{r}_{j,B} = -1/2\left(\mathbf{F}_{jBiA} + \sum_{k,C}\mathbf{F}_{iAkC}\delta_{iAjB}\right)$ and so our expression for $dU_{i,A}/dt$ becomes

$$\begin{aligned}\frac{dU_{i,A}}{dt} &= -\frac{1}{2}\sum_{j,B}\left(\mathbf{F}_{jBiA}\cdot\mathbf{v}_{j,B} + \sum_{k,C}\mathbf{F}_{iAkC}\cdot\mathbf{v}_{i,A}\delta_{iAjB}\right)\\ &= -\frac{1}{2}\sum_{j,B}\left(\mathbf{F}_{jBiA}\cdot\mathbf{v}_{j,B} + \mathbf{F}_{iAjB}\cdot\mathbf{v}_{i,A}\right),\end{aligned} \tag{5.28}$$

after interchanging some dummy indices in the second line.

Furthermore, we can decompose the total force which acts on each atom as

$$\mathbf{F}_{i,a}^{\mathrm{tot}} = \mathbf{F}_{i,a} + c_a\mathbf{F}_{i,\mathrm{M}}, \tag{5.29}$$

where $\mathbf{F}_{i,a}$ is the force that originates from the Coulomb interactions involving the physical atom $a$ (again so that $\mathbf{F}_{i,\mathrm{O}} = 0$), and $c_a\mathbf{F}_{i,M}$ is the Coulomb force which is distributed onto atom $a$ from the virtual site. We then write out the total virial heat flux as a sum over all molecules, $i$, via

$$\begin{aligned}\mathbf{J}_{\mathrm{vir}} = \sum_i \Big[&c_{\mathrm{O}}\left(\mathbf{F}_{i,\mathrm{M}}\cdot\mathbf{v}_{i,\mathrm{O}}\right)\mathbf{r}_{i,\mathrm{O}} + \left(\mathbf{F}_{i,\mathrm{H}_1}\cdot\mathbf{v}_{i,\mathrm{H}_1}\right)\mathbf{r}_{i,\mathrm{H}_1} + c_{\mathrm{H}}\left(\mathbf{F}_{i,\mathrm{M}}\cdot\mathbf{v}_{i,\mathrm{H}_1}\right)\mathbf{r}_{i,\mathrm{H}_1}\\ &+ \left(\mathbf{F}_{i,\mathrm{H}_2}\cdot\mathbf{v}_{i,\mathrm{H}_2}\right)\mathbf{r}_{i,\mathrm{H}_2} + c_{\mathrm{H}}\left(\mathbf{F}_{i,\mathrm{M}}\cdot\mathbf{v}_{i,\mathrm{H}_2}\right)\mathbf{r}_{i,\mathrm{H}_2} - \frac{1}{2}\sum_{j,\mathrm{B}}\Big\{c_{\mathrm{O}}\left(\mathbf{F}_{j\mathrm{B}i\mathrm{M}}\cdot\mathbf{v}_{j,\mathrm{B}}\right)\mathbf{r}_{i,\mathrm{O}}\\ &+ c_{\mathrm{O}}\left(\mathbf{F}_{i\mathrm{M}j\mathrm{B}}\cdot\mathbf{v}_{i\mathrm{M}}\right)\mathbf{r}_{i,\mathrm{O}} + \left(\mathbf{F}_{j\mathrm{B}i\mathrm{H}_1}\cdot\mathbf{v}_{j,\mathrm{B}}\right)\mathbf{r}_{i,\mathrm{H}_1} + \left(\mathbf{F}_{i\mathrm{H}_1j\mathrm{B}}\cdot\mathbf{v}_{i\mathrm{H}_1}\right)\mathbf{r}_{i,\mathrm{H}_1}\\ &+ c_{\mathrm{H}}\left(\mathbf{F}_{j\mathrm{B}i\mathrm{M}}\cdot\mathbf{v}_{j,\mathrm{B}}\right)\mathbf{r}_{i,\mathrm{H}_1} + c_{\mathrm{H}}\left(\mathbf{F}_{i\mathrm{M}j\mathrm{B}}\cdot\mathbf{v}_{i\mathrm{M}}\right)\mathbf{r}_{i,\mathrm{H}_1} + \left(\mathbf{F}_{j\mathrm{B}i\mathrm{H}_2}\cdot\mathbf{v}_{j,\mathrm{B}}\right)\mathbf{r}_{i,\mathrm{H}_2}\\ &+ \left(\mathbf{F}_{i\mathrm{H}_2j\mathrm{B}}\cdot\mathbf{v}_{i\mathrm{H}_2}\right)\mathbf{r}_{i,\mathrm{H}_2} + c_{\mathrm{H}}\left(\mathbf{F}_{j\mathrm{B}i\mathrm{M}}\cdot\mathbf{v}_{j,\mathrm{B}}\right)\mathbf{r}_{i,\mathrm{H}_2} + c_{\mathrm{H}}\left(\mathbf{F}_{i\mathrm{M}j\mathrm{B}}\cdot\mathbf{v}_{i\mathrm{M}}\right)\mathbf{r}_{i,\mathrm{H}_2}\Big\}\Big],\end{aligned} \tag{5.30}$$

which, after grouping terms which include $(\mathbf{F}_{j\mathrm{B}i\mathrm{M}} \cdot \mathbf{v}_{j,\mathrm{B}})$ and $(\mathbf{F}_{i\mathrm{M}j\mathrm{B}} \cdot \mathbf{v}_{i,\mathrm{M}})$, may be written slightly more succinctly as

$$\begin{aligned}\mathbf{J}_{\mathrm{vir}} = \sum_i \big[ & c_{\mathrm{O}} \left(\mathbf{F}_{i,\mathrm{M}} \cdot \mathbf{v}_{i,\mathrm{O}}\right) \mathbf{r}_{i,\mathrm{O}} + \left(\mathbf{F}_{i,\mathrm{H}_1} \cdot \mathbf{v}_{i,\mathrm{H}_1}\right) \mathbf{r}_{i,\mathrm{H}_1} + c_{\mathrm{H}} \left(\mathbf{F}_{i,\mathrm{M}} \cdot \mathbf{v}_{i,\mathrm{H}_1}\right) \mathbf{r}_{i,\mathrm{H}_1} \\ & + \left(\mathbf{F}_{i,\mathrm{H}_2} \cdot \mathbf{v}_{i,\mathrm{H}_2}\right) \mathbf{r}_{i,\mathrm{H}_2} + c_{\mathrm{H}} \left(\mathbf{F}_{i,\mathrm{M}} \cdot \mathbf{v}_{i,\mathrm{H}_2}\right) \mathbf{r}_{i,\mathrm{H}_2} \big] \\ & - \frac{1}{2} \sum_{i,j,\mathrm{A},\mathrm{B}} \left[ \left(\mathbf{F}_{j\mathrm{B}i\mathrm{A}} \cdot \mathbf{v}_{j,\mathrm{B}}\right) \mathbf{r}_{i,\mathrm{A}} + \left(\mathbf{F}_{i\mathrm{A}j\mathrm{B}} \cdot \mathbf{v}_{i,\mathrm{A}}\right) \mathbf{r}_{i,\mathrm{A}} \right]. \end{aligned} \tag{5.31}$$

In order to proceed further, we add and subtract $\sum_i \left(\mathbf{F}_{i,\mathrm{M}} \cdot \mathbf{v}_{i,\mathrm{M}}\right) \mathbf{r}_{i,\mathrm{M}}$ to Eq. 5.31, and upon expanding $\mathbf{F}_{i,\mathrm{A}}$ into pair force contributions as $\sum_{j,\mathrm{B}} \mathbf{F}_{i\mathrm{A}j\mathrm{B}}$ we may rewrite our expression for $\mathbf{J}_{\mathrm{vir}}$ as

$$\begin{aligned}\mathbf{J}_{\mathrm{vir}} = & \frac{1}{2} \sum_{i,j,\mathrm{A},\mathrm{B}} \left[ \left(\mathbf{F}_{i\mathrm{A}j\mathrm{B}} \cdot \mathbf{v}_{i,\mathrm{A}}\right) \mathbf{r}_{i,\mathrm{A}} - \left(\mathbf{F}_{j\mathrm{B}i\mathrm{A}} \cdot \mathbf{v}_{j,\mathrm{B}}\right) \mathbf{r}_{i,\mathrm{A}} \right] \\ & + \sum_i \left[ \sum_a \left\{ c_a \left(\mathbf{F}_{i,\mathrm{M}} \cdot \mathbf{v}_{i,a}\right) \mathbf{r}_{i,a} \right\} - \left(\mathbf{F}_{i,\mathrm{M}} \cdot \mathbf{v}_{i,\mathrm{M}}\right) \mathbf{r}_{i,\mathrm{M}} \right], \end{aligned} \tag{5.32}$$

which after interchanging some dummy indices in the first summation becomes

$$\begin{aligned}\mathbf{J}_{\mathrm{vir}} &= \frac{1}{2} \sum_{i,j,\mathrm{A},\mathrm{B}} \left(\mathbf{F}_{i\mathrm{A}j\mathrm{B}} \cdot \mathbf{v}_{i,\mathrm{A}}\right) \mathbf{r}_{i\mathrm{A}j\mathrm{B}} + \mathbf{J}_{\mathrm{corr}} \\ &= -\sum_{i,\mathrm{A}} \boldsymbol{\sigma}_{i,\mathrm{A}} \mathbf{v}_{i,\mathrm{A}} + \mathbf{J}_{\mathrm{corr}}, \end{aligned} \tag{5.33}$$

where $\boldsymbol{\sigma}_{i,\mathrm{A}}$ is the per-site virial stress tensor for site A in molecule $i$ and $\mathbf{J}_{\mathrm{corr}}$ is a correction term to the Coulombic virial heat flux due to the presence of the virtual charge sites. The first term is the way in which one would usually calculate the virial heat flux if there were no virtual sites present, or by treating the virtual site as its own distinct "site" for the purposes of computing the virial heat flux.

The correction term is given by

$$\mathbf{J}_{\mathrm{corr}} = \sum_i \left[ \sum_a \left\{ c_a \left(\mathbf{F}_{i,\mathrm{M}} \cdot \mathbf{v}_{i,a}\right) \mathbf{r}_{i,a} \right\} - \left(\mathbf{F}_{i,\mathrm{M}} \cdot \mathbf{v}_{i,\mathrm{M}}\right) \mathbf{r}_{i,\mathrm{M}} \right], \tag{5.34}$$

which after expanding $\mathbf{v}_{i,\mathrm{M}} = \sum_a c_a \mathbf{v}_{i,a}$ becomes

$$\mathbf{J}_{\mathrm{corr}} = \sum_{i,a} c_a \left(\mathbf{F}_{i,\mathrm{M}} \cdot \mathbf{v}_{i,a}\right) \left(\mathbf{r}_{i,a} - \mathbf{r}_{i,\mathrm{M}}\right), \tag{5.35}$$

where we expand $\mathbf{v}_{i,\mathrm{M}}$ rather than $\mathbf{r}_{i,\mathrm{M}}$ so that the resulting expression is compatible with periodic boundary conditions. Our final expression for the virtual site correction

to the heat flux is equivalent to that found by Luo and Yu in their study on the RPMD thermal conductivity of q-TIP4P/F ice.[116]

Since in reality the Coulombic energy and forces are calculated using an Ewald summation procedure, for the reciprocal space contribution we use a form of the per-site virial stress tensor applicable to the sum over $k$-space vectors[171]

$$\sigma_{i,\mathrm{A}}^{\alpha\beta} = -\frac{2\pi}{V}\sum_{\mathbf{k}\neq\mathbf{0}}\frac{\exp\left(k^2/4\alpha^2\right)}{k^2}\left[\delta_{\alpha\beta} - 2\left(\frac{1}{k^2}+\frac{1}{4\alpha^2}\right)k_\alpha k_\beta\right] q_i \sum_j q_j \exp\left(i\mathbf{k}\cdot\mathbf{r}_{ij}\right), \tag{5.36}$$

where the indices $\alpha$ and $\beta$ label the Cartesian components. The components of $\boldsymbol{\sigma}_{i,\mathrm{A}}$ may be computed easily during the reciprocal space portion of the force evaluation. As the $\mathbf{J}_{\mathrm{corr}}$ only involves the total electrostatic force on the virtual site and not any pairwise terms, the correction term can be determined using Eq. 5.35 without any modifications at the end of the computation of the forces in the system.

We computed the classical and CMD Green-Kubo thermal conductivities, $\kappa_{\mathrm{Class.}}$ and $\kappa_{\mathrm{CMD}}$ respectively, for each of the chosen state points. These simulations were equilibrated for a total of 100 ps in the $NVT$ ensemble. Afterwards, we continued to evolve the system in the $NVT$ ensemble for a further 100 ps to determine the relevant constant volume heat capacities, $c_{V,\mathrm{Class.}}$ and $c_{V,\mathrm{CMD}}$, using Eq. 5.15. Finally, the thermostat was switched off and 50 successive $NVE$ trajectories of length 4 ps were run with a resampling of the momenta from the Boltzmann distribution in between each one. The heat flux vector was calculated at each step and its autocorrelation function found from each of the trajectories up to a correlation time of 2 ps. These autocorrelation functions were then averaged over all of the different $NVE$ trajectories and integrated to obtain the Green-Kubo thermal conductivity using Eq. 3.64. The only difference between the classical and the CMD calculations were in the potentials used in the simulations. This was then repeated over 50 independent starting configurations at each of the state points to obtain an estimate of the average values of the heat capacity and the thermal conductivity and the associated uncertainty in these quantities.

A key feature of the computed heat flux autocorrelation functions at all of the state points are large high frequency oscillations, which are a consequence of

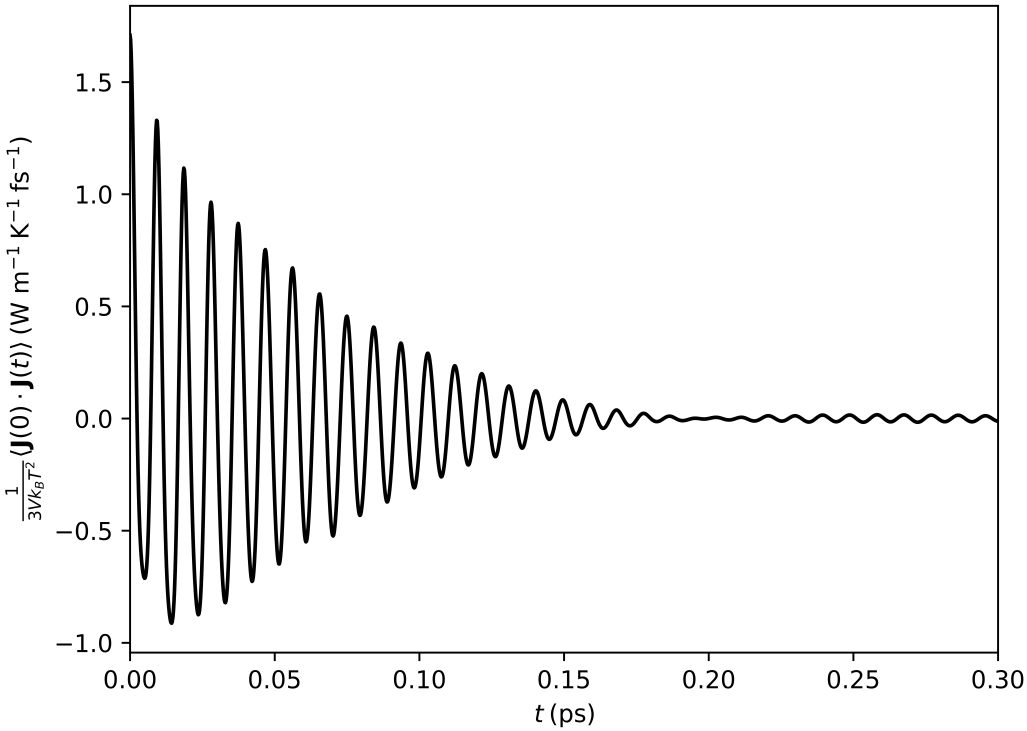



**Figure 5.4:** The classical heat flux autocorrelation function calculated using the q-TIP4P/F potential and the $T = 300\,\mathrm{K}$ and $\rho_m = 0.9965\,\mathrm{g\,cm^{-3}}$ state point, scaled by the prefactor $1/3Vk_BT^2$. The correlation function was calculated up to 2 ps but only the first 0.3 ps are shown here in order to display the initial decay in greater detail.

using a flexible water model.[166] These oscillations persist over a long timescale compared to the overall decay time of the autocorrelation function and eventually become dominated by statistical noise, which at some of the state points caused its accumulated time integral to begin to drift at long times and hence the thermal conductivity from Eq. 3.64 became more difficult to specify. For this reason, we choose to truncate the time integration at 0.25 ps at each of the state points - which was found to be long enough for the time integral to be properly accumulated but before the noise began to significantly contaminate the signal in all six cases. As many of the classical heat flux autocorrelation functions look very similar, we show just two examples here - at the $T = 300\,\mathrm{K}$ and $\rho_m = 0.9965\,\mathrm{g\,cm^{-3}}$ state point in Fig. 5.4 and at the higher temperature $T = 500\,\mathrm{K}$ and $\rho_m = 0.8313\,\mathrm{g\,cm^{-3}}$ state point in Fig. 5.5. The CMD heat flux autocorrelation functions were almost

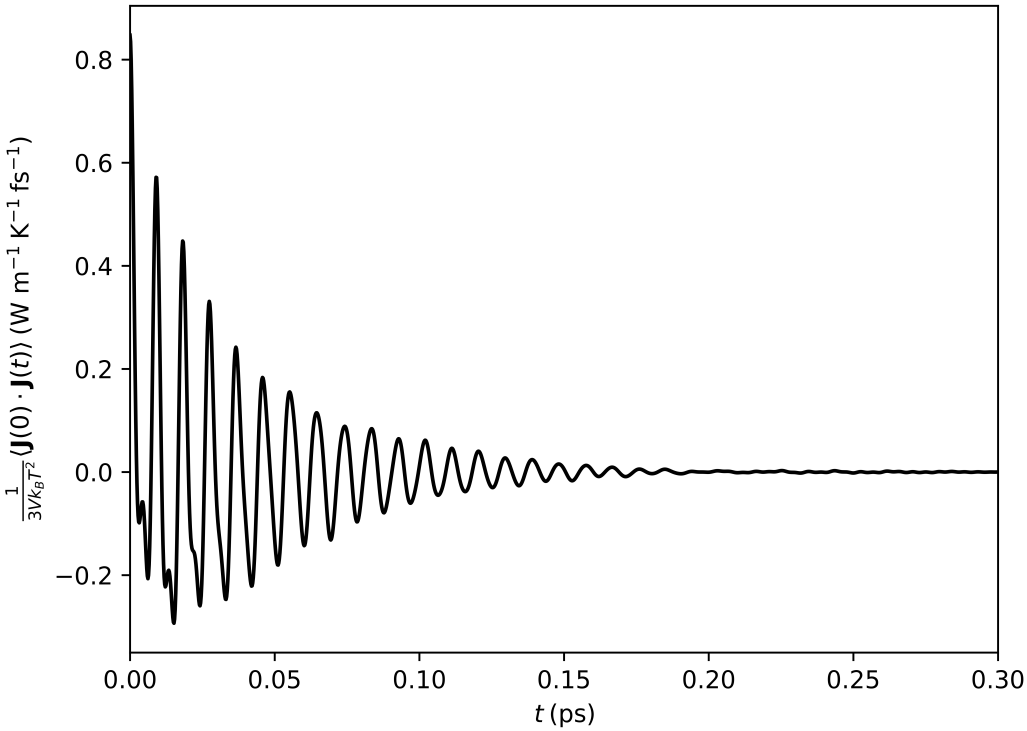



**Figure 5.5:** The classical heat flux autocorrelation function calculated using the q-TIP4P/F potential and the $T = 500\,\mathrm{K}$ and $\rho_m = 0.8313\,\mathrm{g\,cm^{-3}}$ state point, scaled by the prefactor $1/3Vk_BT^2$. The autocorrelation function was calculated up to 2 ps but only the first 0.3 ps are shown here in order to display the initial decay in greater detail.

indistinguishable from the classical heat flux autocorrelation functions at all of the state points. We also show an example of the running time integral of the heat flux autocorrelation function,

$$\kappa(\tau) = \frac{1}{3Vk_BT^2}\int_0^\tau \langle \mathbf{J}(0)\cdot\mathbf{J}(t)\rangle dt, \tag{5.37}$$

for the $T = 500\,\mathrm{K}$ and $\rho_m = 0.8313\,\mathrm{g\,cm^{-3}}$ state point in Fig. 5.6 as the long time drift is more apparent here. It is possible that choosing 0.25 ps as the cutoff point for the integration introduces a small systematic error in the final thermal conductivities due to a potential positive or negative long time tail of the autocorrelation function which is lost within the statistical noise. Significantly more lengthy simulations would be necessary to tame the fluctuations in order to check for this, however.

The classical and CMD Green-Kubo thermal conductivities, $\kappa_{\mathrm{Class.}}$ and $\kappa_{\mathrm{CMD}}$

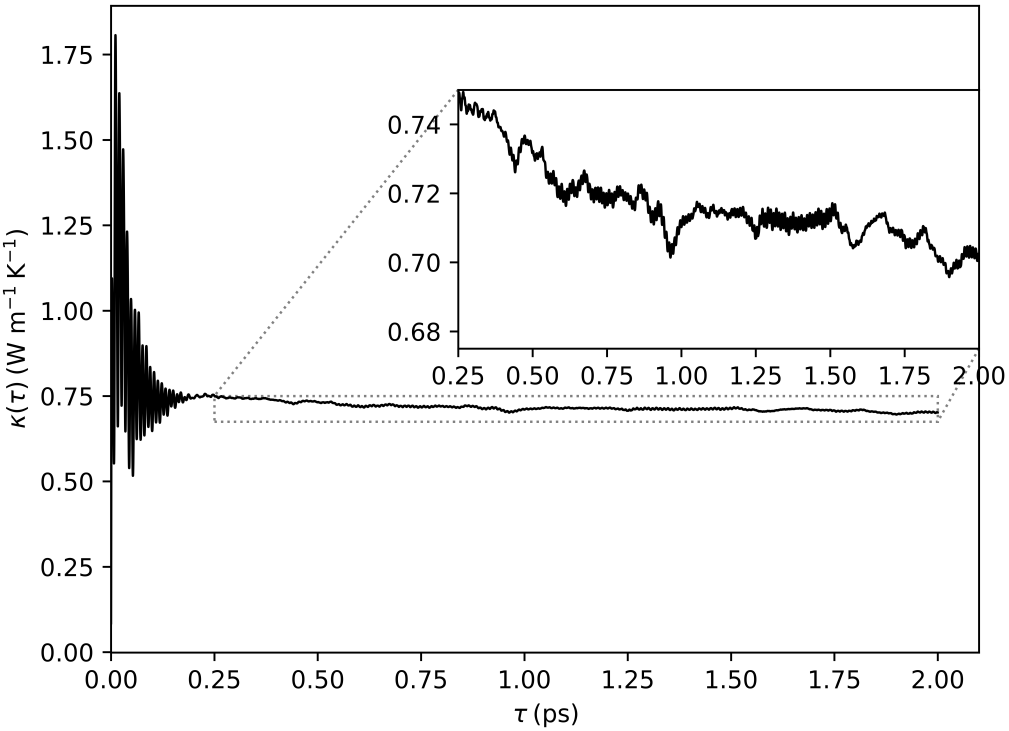



**Figure 5.6:** Running time integral of the classical heat flux autocorrelation function for the q-TIP4P/F potential at $T = 500\,\mathrm{K}$ and $\rho_m = 0.8313\,\mathrm{g\,cm^{-3}}$. The inset shows a magnification of the statistical noise and drift in the integral at long times. Due to this, the integration was truncated at 0.25 ps when determining the thermal conductivity.

| $T$ (K) | $\rho_m$ ($\mathrm{g\,cm^{-3}}$) | $\kappa_{\mathrm{Class.}}$ ($\mathrm{W\,m^{-1}\,K^{-1}}$) | $\kappa_{\mathrm{CMD}}$ ($\mathrm{W\,m^{-1}\,K^{-1}}$) | $\kappa_{\mathrm{Class.,\,scal.}}$ ($\mathrm{W\,m^{-1}\,K^{-1}}$) | $\kappa_{\mathrm{CMD,\,scal.}}$ ($\mathrm{W\,m^{-1}\,K^{-1}}$) | $\kappa_{\mathrm{Expt.}}$ ($\mathrm{W\,m^{-1}\,K^{-1}}$) |
|---|---|---|---|---|---|---|
| 300 | 0.9965 | 0.909 (5) | 0.880 (8) | 0.547 (6) | 0.540 (7) | 0.610 |
| 350 | 0.9737 | 0.864 (7) | 0.872 (9) | 0.538 (8) | 0.545 (9) | 0.668 |
| 400 | 0.9375 | 0.847 (7) | 0.851 (7) | 0.551 (7) | 0.548 (6) | 0.684 |
| 450 | 0.8903 | 0.812 (7) | 0.796 (8) | 0.529 (6) | 0.513 (6) | 0.675 |
| 500 | 0.8313 | 0.751 (7) | 0.740 (7) | 0.499 (6) | 0.486 (5) | 0.644 |
| 550 | 0.7558 | 0.658 (7) | 0.651 (6) | 0.439 (5) | 0.428 (5) | 0.586 |

**Table 5.4:** Green-Kubo thermal conductivities calculated both classically and with CMD at six state points along the saturation line of liquid water. Also provided are the corresponding "scaled" thermal conductivities for each. Experimental thermal conductivities at the same state points were taken from Ref. [140]. The CPMFs used in the calculations for $\kappa_{\mathrm{CMD}}$ and the values of $c_{V,\mathrm{CMD}}$ use in the scaling $\kappa_{\mathrm{CMD,\,scal.}} = c_{V,\mathrm{PIMD}}\kappa_{\mathrm{CMD}}/c_{V,\mathrm{CMD}}$ were computed by Dr. Joseph Lawrence.

respectively, at the six state points as well as their standard error are provided in Table 5.4. Also provided are the corresponding results after scaling by the relevant

ratio of the constant volume heat capacities, $\kappa_{\text{Class., scal.}} = \kappa_{\text{Class.}} c_{V,\,\text{PIMD}}/c_{V,\,\text{Class.}}$ and $\kappa_{\text{CMD, scal.}} = \kappa_{\text{CMD}} c_{V,\,\text{PIMD}}/c_{V,\,\text{CMD}}$. The experimental thermal conductivities from the NIST website[140] are also given at these state points for comparison. The temperature dependence of the unscaled classical and CMD Green-Kubo thermal conductivities is plotted in Fig. 5.7, together with the experimental values and the previous Green-Kubo results from the SPC/E water model found by Lee.[153] The scaled classical and CMD Green-Kubo thermal conductivities are compared to experiment in Fig. 5.8.

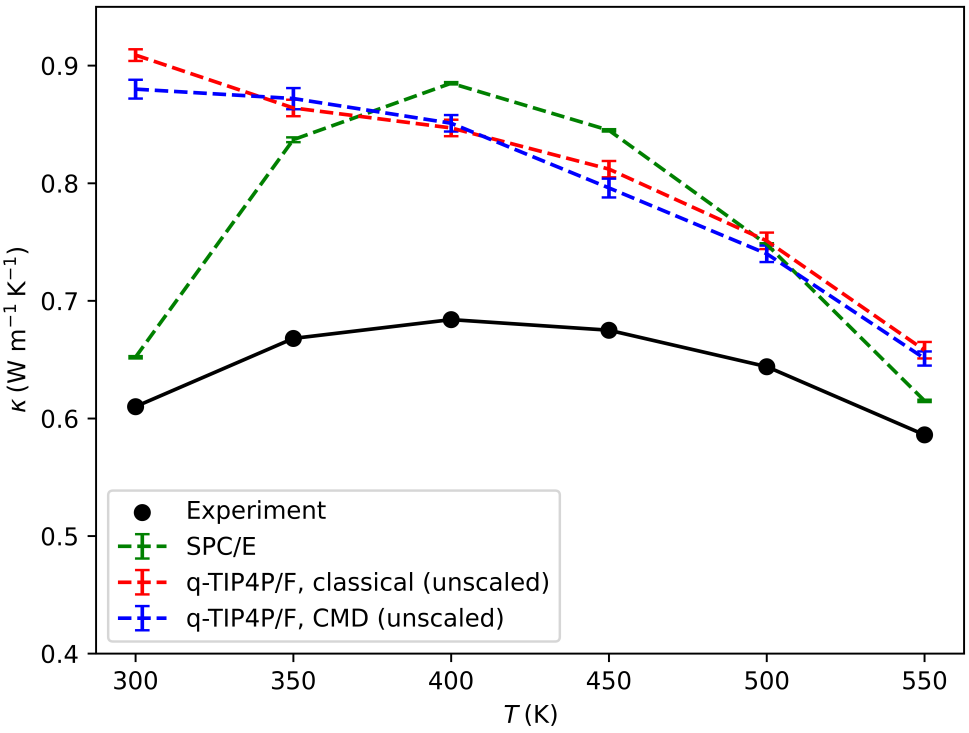



**Figure 5.7:** Classical and CMD unscaled thermal conductivities calculated with the q-TIP4P/F potential at six state points along the saturation line of liquid water. Also shown are previous results for the SPC/E water model by Lee[153] as well as experimental measurements[140] at the same state points. The CPMFs used in the calculation of the CMD thermal conductivities were computed by Dr. Joseph Lawrence.

Interestingly, using the centroid potentials of mean force does not seem to noticeably affect the Green-Kubo thermal conductivity or constant volume heat capacity compared to the classical results even at the lowest temperature considered.

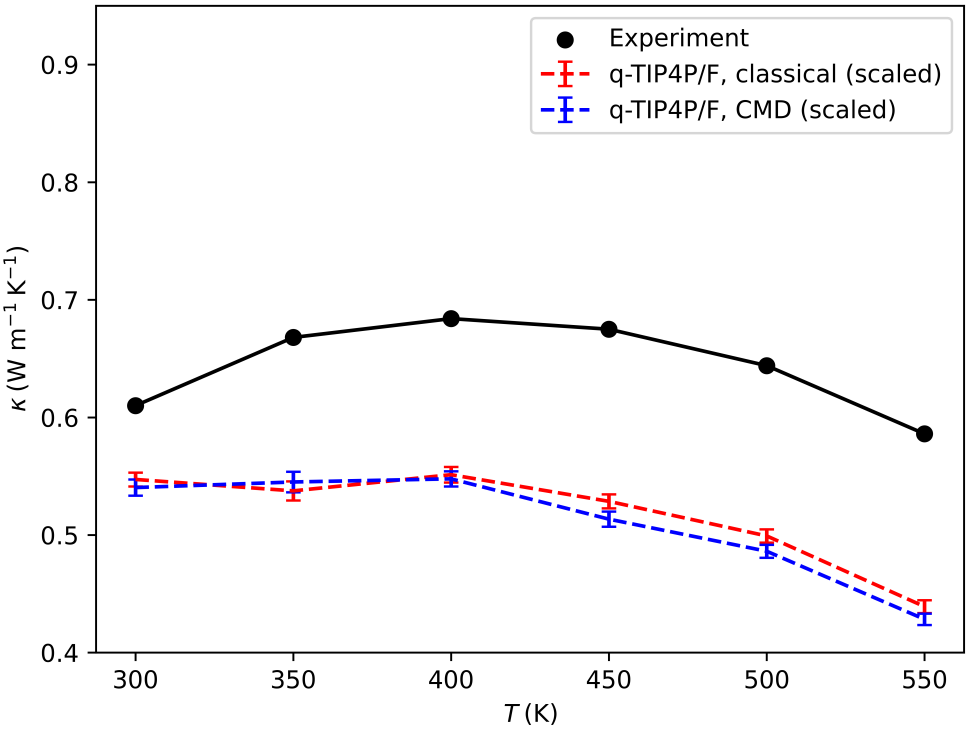



**Figure 5.8:** Classical and CMD scaled thermal conductivities calculated with the q-TIP4P/F potential at six state points along the saturation line of liquid water. Also shown are experimental measurements[140] at the same state points. The CPMFs used for the calculation of the CMD thermal conductivities and the CMD constant volume heat capacities used in the scaling were computed by Dr. Joseph Lawrence.

As such, there is no significant difference between the CMD and the classical thermal conductivities both with and without the heat capacity scaling. Therefore, in this case one can simply scale the classical thermal conductivities and still obtain results similar to those found using CMD. The range of systems that this observation applies to remains to be seen, but for cases where nuclear quantum effects are expected to be minor then it is likely a reasonable approximation to make. Together with the fact that calculation of the centroid potentials of mean force becomes more unwieldy as the complexity of the system increases makes the option of scaling the classical Green-Kubo thermal conductivities particularly useful, even if it does introduce an error in the final scaled thermal conductivities.

However, this will not be a sensible route to take for every system which one

might wish to study. For the liquid parahydrogen and the liquid helium systems shown in the previous Chapter the classical Green-Kubo thermal conductivities clearly *will* be very different from the CMD Green-Kubo thermal conductivities by virtue of the fact that the classical simulations do not even predict the system to be in the same phase as the CMD simulations - which was exactly the reason why scaling the classical thermal conductivities was not considered as an option in that Chapter. Therefore, whilst scaling the classical thermal conductivities may be useful as an approximation for the quantum mechanical thermal conductivity in cases where using the centroid potential of mean force is impractical as well as when nuclear quantum effects are expected to not be too significant, its validity should be considered on a case by case basis.

A previous study on q-TIP4P/F water using RPMD found a relatively minor quantum effect of 15% on the diffusion constant at a similar state point of $T = 298\,\mathrm{K}$ and $\rho_m = 0.997\,\mathrm{g\,cm^{-3}}$ using $N = 216$ molecules.[23] In a sense it is therefore unsurprising that the difference in the thermal conductivities and heat capacities in going from a classical simulation to CMD is so slight. In that case the difference was attributed to a competition of different quantum effects within the system - with the diffusion in the system being slowed by an increase in the average O-H bond length (making the intermolecular electrostatic interactions stronger) but enhanced by the hydrogen bond network becoming more disordered due to quantum fluctuations.[23] Although the mechanisms for heat transfer are more involved than they are for mass transfer, it is possible that a similar mechanism of competing quantum effects also explains why the diffusion of heat energy through the system is hardly changed by the introduction of nuclear quantum effects. Eltareb *et al.*[172] also found that the inclusion of nuclear quantum effects within the q-TIP4P/F potential had only a negligible effect on several static and dynamic properties for temperatures above 270 K. The relatively small change between the classical and CMD results is obviously contrasted by the comparatively much larger difference in the classical and PIMD constant volume heat capacities (and as a result also

between the scaled and unscaled thermal conductivities), indicating that nuclear quantum effects still do play a large role in certain properties for this system.

The fact that the CMD and the classical thermal conductivities are so similar for this system may be rationalised by the fact that the classical and the PIMD centroid RDFs shown in Figs. 5.1, 5.2 and 5.3 show only relatively small differences. Presumably, a much larger effect would be observed if one were to use the true PIMD estimate of the quantum radial distribution functions generated by the average of the bead positions, but this would not allow us to construct the centroid potentials of mean force required by CMD which requires the positions of the centroids and not of the beads.

The unscaled classical and CMD q-TIP4P/F calculations significantly overestimate the thermal conductivity at lower temperatures, by up to 50 % close to 300 K. However, if we exclude the $T = 300$ K state point then the q-TIP4P/F thermal conductivities perform similarly to the SPC/E results of Lee[153] - with the disagreement with experiment ranging from 30% at $T = 350$ K down to 10% at $T = 550$ K. The qualitative appearance of the unscaled q-TIP4P/F thermal conductivities is noticeably worse, with the computed values appearing to monotonically decrease with increasing temperature and there being no significant evidence for a maximum in either of the unscaled q-TIP4P/F thermal conductivities within this temperature range. After the heat capacity scaling the q-TIP4P/F thermal conductivities switch from consistently overestimating the experimental thermal conductivity to underestimating it. The agreement with the experimental values is similar to in the unscaled case, with there now being a 12% disagreement at low temperatures increasing to a 27% disagreement at high temperatures. There does appear to be some evidence of a slight peak appearing in the thermal conductivity between 350 K and 450 K however, so the qualitative temperature dependence seems to be modestly better than it was in the unscaled case.

Although the scaled q-TIP4P/F CMD thermal conductivities do not compare noticeably better with experiment than previous classical water models, they do not compare noticeably worse either. Since the q-TIP4P/F potential is still a

fairly unsophisticated model for the interactions within liquid water and CMD is only an approximate quantum dynamical method, an error of up to 27% at high temperatures far from where the potential was originally parameterised is not unexpected. It will be interesting to investigate how well scaling the CMD thermal conductivity performs with a more accurate water model, such as MBPol[141] - which we leave as a potential avenue for future work.

# 6

# Thermal conductivity of classical solids

## 6.1 Introduction

The approach outlined in Section 3.4 for predicting the thermal conductivity from simulations has, as far as we are aware of, only previously been applied to the liquid phase.[107; 118–120] It would be desirable for the method we developed for the calculation of quantum thermal conductivities of liquids in Chapter 4 based on the equilibrium density fluctuation method to also be applicable to the calculation of the quantum thermal conductivity of solids, at least in principle.

Therefore, in this Chapter we present the changes from the hydrodynamic theory presented in Chapter 3 which are necessary in order to describe the hydrodynamics of solids. We then apply the hydrodynamic model for the equilibrium density fluctuations in solids to extract the thermal diffusivity by fitting to the data obtained from classical molecular dynamics simulations, applied to case of Lennard-Jones argon. We find that, at temperatures of $T = 20\,\mathrm{K}$ and below, the fraction of the thermal diffusion component in the signal becomes too small to obtain a reliable estimate of the thermal diffusivity from the fits. Instead, we show that here it is possible to find the thermal diffusivity from the hydrodynamic model of the equilibrium local temperature fluctuations instead. In both cases we compare

the predicted thermal conductivities to those found from the Green-Kubo method, and find that they agree to within 13% in all cases.

## 6.2 Hydrodynamic theory of solids

The theory developed in Chapter 3 must be adapted somewhat before it can be applied to solids. This is because the hydrodynamics of solids differs from that of liquids in two main respects. The first is that solids are characterised by strong bonds between neighbouring atoms. Therefore, as the local structure of the solid is deformed additional stresses are induced within the system. In the case of a crystalline solid these stresses may be accounted for by considering the strains generated by the local displacements, $\mathbf{u}$, from the equilibrium lattice structure[173]

$$u_i = x_i - x_i^0, \tag{6.1}$$

in which $x_i$ is the coordinate of the $i^{\text{th}}$ degree of freedom and $x_i^0$ is its location within the equilibrium lattice structure. We can then construct the symmetrised strains

$$u_{ij} = \frac{1}{2}\left(\frac{\partial u_i}{\partial x_j} + \frac{\partial u_j}{\partial x_i}\right), \tag{6.2}$$

and, assuming that deformations of the system are elastic, we may write down an expression for the components of the stress which are generated by these strains,

$$\sigma_{ij} = C_{ijkl} u_{kl}, \tag{6.3}$$

where $C_{ijkl}$ are the moduli of elasticity and the indices each run over the three coordinate axes of the system.[173] The $C_{ijkl}$ become a fourth rank tensor in order to be able to relate the longitudinal and shear stresses to the longitudinal and shear strains present in a solid structure. These stresses must then be added to the overall stress tensor given for liquids in Eq. 3.7.

The second difference relates to the special case of a crystalline solid, which we will be focussing on in this Chapter. Due to the long-range order present in these structures, we can no longer reasonably assume that the system is isotropic - as we did for liquids in Section 3.4. Therefore, the adaptation of the linearised hydrodynamic

equations of solids in Fourier-Laplace space will be dependent on the orientation of the wavevector, $\mathbf{k}$, relative to the crystallographic axes of the system. The viscosity coefficients present in a liquid, $\eta$ and $\zeta$, generalise to the fourth rank tensor $\eta_{ijkl}$ and generate local internal stresses through the relation $\sigma_{ij} = \eta_{ijkl} v_{kl}$ where

$$v_{ij} = \frac{1}{2}\left(\frac{\partial v_i}{\partial x_j} + \frac{\partial v_j}{\partial x_i}\right), \tag{6.4}$$

where $v_i$ is the $i^{\text{th}}$ component of the local velocity for a similar reason to the $C_{ijkl}$ being described by a fourth rank tensor in solids.[173] The thermal conductivity, $\kappa_{ij}$, and the coefficient of thermal expansion, $\alpha_{ij}$, also become second rank tensors in order to relate the heat flux or the expansion generated by temperature gradients along different directions of the anisotropic medium.[173]

There are 21 independent components of the elasticity and viscosity tensors in a general crystalline solid of triclinic symmetry, as well as six independent components of the thermal conductivity and thermal expansion tensors.[174; 175] Deriving the linearised hydrodynamic equations for a crystalline solid with arbitrary symmetry is therefore a daunting task, and one which is outside the scope of this thesis. However, the problem is greatly simplified if one restricts the analysis to cubic crystals, where the number of independent elasticity and viscosity coefficients are each reduced to three, and the thermal conductivity and thermal expansion tensors each to only one - so that they may be treated as in the isotropic case with $\kappa = \mathrm{Tr}\left[\boldsymbol{\kappa}\right]/3$ and $\alpha = \mathrm{Tr}\left[\boldsymbol{\alpha}\right]/3 = -\left(\partial\rho/\partial T\right)_P/\rho$.[173] Further simplification can also be achieved through a judicious choice of the direction of $\mathbf{k}$. In this Chapter we will only consider the case where $\mathbf{k}$ is oriented along the [100] crystallographic direction, which we will always take to be the $x$ axis of our system. As well as simplifying the hydrodynamic equations this has the additional advantage that the Fourier components of the local density and temperature along this wavevector are trivial to calculate in a molecular dynamics simulation.

With this choice of wavevector orientation, the linearised hydrodynamic equations in Fourier-Laplace space for a one-component crystal of cubic symmetry with particle mass $m$ were derived by Fleming and Cohen[175] and found to separate

into longitudinal and transverse components. As Fleming and Cohen wanted their equations to describe the hydrodynamics of real crystals, where the presence of defects within the lattice has a significant effect on the thermal diffusion and the sound wave propagation, they included the vacancy concentration as an additional variable and introduced new transport coefficients related to the diffusion of these vacancies through the system.[175] Since we will be considering idealised perfect lattices in our simulations, we shall set the vacancy concentration and the transport coefficients associated with the vacancies to zero.

With these considerations, the Fourier-Laplace transforms of the linearised hydrodynamic equations become, taking the local number density, temperature, and velocity as the independent variables

$$s\tilde{\rho}_1(k,s) + ik\rho_0\tilde{v}_{1,x}(k,s) = \rho_1(k,0), \tag{6.5}$$

$$\left(s + \frac{\kappa}{\rho_0 c_V}k^2\right)\tilde{T}_1(k,s) - \frac{\alpha m c_s^2 T_0 s}{\gamma\rho_0 c_V}\tilde{\rho}_1(k,s) = T_1(k,0) - \frac{\alpha m c_s^2 T_0}{\gamma\rho_0 c_V}\rho_1(k,0), \tag{6.6}$$

and

$$\left(s + \frac{\eta_{11}}{m\rho_0}k^2\right)\tilde{v}_{1,x}(k,s) + \left(\frac{C_{11}}{m\rho_0^2} + \frac{1-\gamma}{\gamma\rho_0}c_s^2\right)ik\tilde{\rho}_1(k,s) + \frac{i\alpha c_s^2 k}{\gamma}\tilde{T}_1(k,s) = v_{1,x}(k,0), \tag{6.7}$$

in which $k = |\mathbf{k}| = k_x$, $\eta_{11} = \eta_{xxxx} = \eta_{yyyy} = \eta_{zzzz}$, and $C_{11} = C_{xxxx} = C_{yyyy} = C_{zzzz}$. The parameters $\alpha$, $c_s$ and $\gamma$ have the same definitions in terms of the thermodynamic derivatives as they did in Chapter 3. Whilst we will continue to refer to $c_s$ as the adiabatic speed of sound, it no longer bears any concrete relation to the sound speed through the anisotropic crystal - which will depend on the direction of propagation of the sound wave through the crystal and on whether the wave is transverse or longitudinal. The notations $\tilde{f}(k,s)$ and $f(k,0)$ also have the same meaning as they did in Chapter 3 - as the spatial Fourier transform and the temporal Laplace transform of $f(\mathbf{r},t)$ and the spatial Fourier transform of $f(\mathbf{r},t)$ evaluated at $t = 0$ respectively. We have also reused the convention that a subscript $\square_0$ refers to the value that a local quantity takes in the equilibrium reference system and that a subscript $\square_1$ describes the difference between its values in the "true" non-equilibrium

system and in this equilibrium reference system, and we choose a reference frame such that the components of the velocity at equilibrium are zero. The equations involving the transverse components of the local velocity have not been written here, since they do not couple to the local density or to the local temperature.[175]

The number density continuity equation, Eq. 6.5, and the energy transport equation, Eq. 6.6, remain unchanged from their forms in liquids given in Eqs 3.84 and 3.86 respectively (we have chosen to express Eq. 6.5 in terms of the longitudinal component of $\mathbf{v}_1$ as an independent variable rather than its divergence $\varphi_1 = \nabla \cdot \mathbf{v}_1$ so that we may isolate the longitudinal equations from the transverse equations in an anisotropic medium). The generalisation of the Navier-Stokes equation, Eq. 6.7, is also very similar to the corresponding equation for liquids, Eq. 3.85, except for an extra term of $C_{11}/m\rho_0^2 - c_s^2/\rho_0$ which is coupled to the density fluctuations.

Writing these three equations together as a matrix equation we have that

$$\mathbf{M}\tilde{\boldsymbol{\psi}} = \mathbf{N}\boldsymbol{\psi}, \tag{6.8}$$

where in this case

$$\mathbf{M} = \begin{pmatrix} s & 0 & ik\rho_0 \\ \frac{-mc_s^2\alpha T_0 s}{\gamma\rho_0 c_V} & s + ak^2 & 0 \\ \left(c_L^2 - \frac{\gamma-1}{\gamma}c_s^2\right)\frac{ik}{\rho_0} & \frac{ic_s^2\alpha k}{\gamma} & s + bk^2 \end{pmatrix}, \tag{6.9}$$

in which the hydrodynamic parameters $a$ and $b$ are now given by $a = \kappa/\rho_0 c_V$ and $b = \eta_{11}/m\rho_0$, and we have introduced the longitudinal speed of sound $c_L^2 = C_{11}/m\rho_0$. The matrix $\mathbf{N}$ and the vectors $\tilde{\boldsymbol{\psi}}$ and $\boldsymbol{\psi}$ are

$$\mathbf{N} = \begin{pmatrix} 1 & 0 & 0 \\ \frac{-mc_s^2\alpha T_0}{\gamma\rho_0 c_V} & 1 & 0 \\ 0 & 0 & 1 \end{pmatrix}, \tag{6.10}$$

and

$$\tilde{\boldsymbol{\psi}} = \begin{pmatrix} \tilde{\rho}_1(k,s) \\ \tilde{T}_1(k,s) \\ \tilde{v}_{1,x}(k,s) \end{pmatrix}, \qquad \boldsymbol{\psi} = \begin{pmatrix} \rho_1(k,0) \\ T_1(k,0) \\ v_{1,x}(k,0) \end{pmatrix}. \tag{6.11}$$

In this case we find that the determinant of $\mathbf{M}$ is

$$D(k,s) = s^3 + (a+b)k^2 s^2 + \left(c_L^2 k^2 + abk^4\right)s + \left(c_L^2 + \frac{1-\gamma}{\gamma}c_s^2\right)ak^4, \tag{6.12}$$

where we have made use of the thermodynamic relation $\alpha^2 = \frac{(\gamma-1)c_P}{mc_s^2 T_0}$.

Inverting $\mathbf{M}$ and performing an inverse Laplace transform allows us to write an expression for $\rho_1(k,t)$ as

$$\rho_1(k,t) = \mathcal{L}^{-1}\left\{\frac{A(k,s)}{D(k,s)}\right\}\rho_1(k,0) + \mathcal{L}^{-1}\left\{\frac{B(k,s)}{D(k,s)}\right\}T_1(k,0) + \mathcal{L}^{-1}\left\{\frac{C(k,s)}{D(k,s)}\right\}v_{1,x}(k,0), \tag{6.13}$$

where the functions $A(k,s)$, $B(k,s)$ and $C(k,s)$ are determined by the matrix product of $\mathbf{M}^{-1}$ and $\mathbf{N}$. After multiplying both sides of Eq. 6.13 by $\rho_1(-k,0)$ and taking the ensemble average we find

$$\frac{\langle \rho_1(k,t)\,\rho_1(-k,0)\rangle}{\langle \rho_1(k,0)\,\rho_1(-k,0)\rangle} = \mathcal{L}^{-1}\left\{\frac{A(k,s)}{D(k,s)}\right\}. \tag{6.14}$$

Here we have again used the facts that since $\rho_1$ and $v_{1,x}$ have opposite parity under time reversal the ensemble average $\langle \rho_1(-k,0)\,v_{1,x}(k,0)\rangle = 0$[85] and that since the temperature and the density are thermodynamically uncorrelated variables $\langle \rho_1(-k,0)\,T_1(k,0)\rangle = 0$ also.[84] By restricting our choices of $k$ so that an integer number of wavelengths, $n$, fit along the $x$ axis of the system we may again make the identification that the intermediate scattering function, $F(k,t)$, is equal to the ensemble average of the $n^{\text{th}}$ Fourier component of the density fluctuation (since the $n \neq 0$ Fourier components of the density in the equilibrium system are zero) to arrive at

$$\frac{F(k,t)}{F(k,0)} = \mathcal{L}^{-1}\left\{\frac{A(k,s)}{D(k,s)}\right\}. \tag{6.15}$$

Therefore, only the function $A(k,s)$ needs to be determined from inverting the matrix $\mathbf{M}$ in order to analyse the behaviour of the equilibrium density fluctuations.

Performing the inverse Laplace transform in Eq. 6.15 allows us to write

$$\frac{F(k,t)}{F(k,0)} = \frac{A(k,s_0)\,e^{s_0 t}}{(s_0-s_+)(s_0-s_-)} + \frac{A(k,s_+)\,e^{s_+ t}}{(s_+-s_0)(s_+-s_-)} + \frac{A(k,s_-)\,e^{s_- t}}{(s_--s_0)(s_--s_+)}, \tag{6.16}$$

where $s_0$, $s_+$ and $s_-$ are the roots of the cubic equation $D(k,s) = 0$. The function $A(k,s)$ may be found explicitly by determining elements of the inverse matrix $\mathbf{M}^{-1}$ and is given by

$$A(k,s) = s^2 + (a+b)\,k^2 s + abk^4 + \frac{\gamma-1}{\gamma}c_s^2 k^2. \tag{6.17}$$

We note that this formula for $A(k,s)$ is exactly the same as the corresponding equation given for liquids in Eq. 3.92, and so the only difference between the hydrodynamic equations for the density fluctuations in liquids and in solids arises from the different roots of $D(k,s)$. Since these roots will still comprise of one real negative root and a complex conjugate pair with a negative real part, the form of $F(k,t)$ found from Eq. 6.16 will be similar to that found for liquids - with an exponentially decaying thermal diffusion term coupled to an oscillating sound wave term. However, since the roots are no longer the same the exponential decay constants, the oscillating frequency, and the relative proportions of the thermal and sound wave components will be different.

While Eq. 6.16 is already sufficient for use as a fitting model to extract the hydrodynamic parameters $a$ and $b$, it is illustrative to again derive an approximate solution valid for small values of $k$ to give better insight into the time dependent behaviour of $F(k,t)$. Treating $ak^2$ and $bk^2$ as perturbative terms, the zeroth order roots, $s^{(0)}$, are given by the solutions to the equation

$$\left(s^{(0)}\right)^3 + c_L^2 k^2 s^{(0)} = 0, \tag{6.18}$$

which yields the solutions as $s_0^{(0)} = 0$ and $s_\pm^{(0)} = \pm i c_L k$. The first order corrections to these roots, $s^{(1)}$, are then the solutions of

$$3\left(s^{(0)}\right)^2 s^{(1)} + (a+b)\,k^2\left(s^{(0)}\right)^2 + c_L^2 k^2 s^{(1)} + \left(\frac{1-\gamma}{\gamma}c_s^2 + c_L^2\right) a k^4 = 0, \tag{6.19}$$

when $s^{(0)}$ is substituted by the corresponding zeroth order root, $s_0^{(0)}$ and $s_\pm^{(0)}$, which were found earlier. When $s^{(0)} = s_0^{(0)} = 0$ we find

$$s_0^{(1)} = -\left[(1-\gamma)\,\frac{c_s^2}{c_L^2} + \gamma\right] D_T k^2, \tag{6.20}$$

where as before the thermal diffusivity $D_T = \kappa/\rho_0 c_P = a/\gamma$, which motivates us to define an "effective" thermal diffusivity, $D_T^{\text{eff}}$, by

$$D_T^{\text{eff}} = \left[(1-\gamma)\,\frac{c_s^2}{c_L^2} + \gamma\right] D_T, \tag{6.21}$$

so that the approximate root associated with the thermal diffusive term becomes $s_0 \approx -D_T^{\text{eff}} k^2$. As noted by Fleming and Cohen, one may consider this effective

thermal diffusivity to be the ratio of thermal conductivity and the heat capacity at constant "longitudinal pressure" - the pressure generated by the longitudinal components of the internal stress.[175]

In the cases where $s^{(0)} = s_{\pm}^{(0)}$ we find that

$$s_{\pm}^{(1)} = \frac{1}{2}\left[D_T^{\text{eff}} - (a+b)\right]k^2, \tag{6.22}$$

which again allows us to define an "effective" sound attenuation coefficient by

$$\Gamma^{\text{eff}} = \frac{1}{2}\left[a + b - D_T^{\text{eff}}\right], \tag{6.23}$$

so that the approximate roots up to first order in the perturbative terms are $s_{\pm} \approx \pm ic_L k - \Gamma^{\text{eff}} k^2$.

Having determined approximate solutions for the three roots, we then use these in the formula for the intermediate scattering function found earlier, Eq. 6.16, and neglecting terms which are second order or higher in the perturbative terms we find after some lengthy algebra

$$\begin{aligned}\frac{F(k,t)}{F(k,0)} = {} & \frac{\gamma-1}{\gamma}\frac{c_s^2}{c_L^2}e^{-D_T^{\text{eff}}k^2t} + \left(1 - \frac{\gamma-1}{\gamma}\frac{c_s^2}{c_L^2}\right)e^{-\Gamma^{\text{eff}}k^2t}\cos(c_L k t) \\ & - \frac{k}{c_L}\left[\left(1 - \frac{\gamma-1}{\gamma}\frac{c_s^2}{c_L^2}\right)\left(D_T^{\text{eff}} - \Gamma^{\text{eff}}\right) - D_T^{\text{eff}}\right]e^{-\Gamma^{\text{eff}}k^2t}\sin(c_L k t).\end{aligned} \tag{6.24}$$

Inspection of the above formula also allows us to define another "effective" parameter

$$\gamma^{\text{eff}} = \frac{\gamma c_L^2}{\gamma(c_L^2 - c_s^2) + c_s^2}, \tag{6.25}$$

so that Eq. 6.24 may be rewritten as

$$\frac{F(k,t)}{F(k,0)} = \frac{\gamma^{\text{eff}}-1}{\gamma^{\text{eff}}}e^{-D_T^{\text{eff}}k^2t} + \frac{1}{\gamma^{\text{eff}}}e^{-\Gamma^{\text{eff}}k^2t}\left[\cos(c_L k t) + d(k)\sin(c_L k t)\right], \tag{6.26}$$

where the $d(k)$ correction term is given by

$$d(k) = \frac{k}{c_L}\left(\gamma^{\text{eff}} D_T^{\text{eff}} + \Gamma^{\text{eff}} - D_T^{\text{eff}}\right). \tag{6.27}$$

The final approximate solution for $F(k,t)$ for solids valid in the $k \to 0$ limit is then found to be in exactly the same form as the formula for liquids provided

by Eq. 3.102, but with the definitions of the parameters altered, as expected. The frequency of the oscillating sound wave component is now the longitudinal speed of sound rather than the adiabatic speed of sound, and the thermal diffusivity and the sound attenuation coefficient in the exponential decay constants of the thermal and sound wave components have been altered to the "effective" formulae given by Eqs 6.21 and 6.23 respectively.

So we again have two options by which we can extract the thermal diffusivity from fitting the intermediate scattering function data obtained from a molecular dynamics simulation, similar to the procedures we used to fit the CMD intermediate scattering functions of liquid parahydrogen in Section 4.2. Either we can fit directly to the exact solution of the inverse Laplace transform given in Eq. 6.16 or fit to the approximate form of Eq. 6.26 using the formulae for the "effective" parameters given by Eqs 6.21, 6.23 and 6.25. We will refer to fitting directly to Eq. 6.16 as the "exact" fitting model and fitting to Eq. 6.24 via the formulae for the "effective" parameters as the "approximate" fitting model. Whilst the exact model provided a greatly reduced system size dependence in the fitted value of $a$ when applied to liquid parahydrogen, we still need to determine whether this remains to be true when applied to other systems - especially when we expect the system size dependence to be more pronounced in solids than in liquids.

In both cases the values of the adiabatic speed of sound, $c_s$, and the ratio of the constant volume and constant pressure heat capacities, $\gamma$, may be found independently from their definitions in terms of thermodynamic derivatives, meaning that there are three unknown parameters which must be obtained from the fitting model - the hydrodynamic parameters $a$ and $b$, as well as the longitudinal speed of sound, $c_L$. When fitting the intermediate scattering function data obtained from our simulations we observed that the frequency of the oscillating component may be found rather accurately and consistently. Since $c_L$ determines this frequency in the approximate solution (and thus also is the only unknown parameter which will have a significant effect on this frequency in the exact solution as well), introducing $c_L$ as an extra free parameter to the fitting model did not introduce much in the

way of additional variability in the estimates of the other two fitted parameters, $a$ and $b$. A similar observation was made by Cheng and Frenkel in their study on obtaining the thermal conductivity from the equilibrium density fluctuations of liquids.[107] For this reason, and the fact that the elastic constant $C_{11}$ is more difficult to calculate from an independent method than $c_s$ or $\gamma$,[176; 177] we left $c_L$ as a parameter to be obtained from the fitting model in each of these two cases.

## 6.3 Application to Lennard-Jones argon

To investigate the viability of determining the thermal conductivity by fitting the intermediate scattering function obtained for solids to an appropriate functional form, we choose to work with argon as our application of choice. We use this system for several reasons - the first of which is that it is a one component crystal of cubic symmetry. As well as this, in alternative methods for extracting the thermal conductivity which exhibit a significant dependence on the size of the system used in the simulations, while the system size dependence is more pronounced for solid argon than it is for the liquid example using the equilibrium density fluctuations shown in Chapter 4, it is not as severe as it can be in many other crystalline solids.[74; 104; 178]

The interactions in argon may be described to a good approximation with a simple Lennard-Jones pair potential,

$$u_2\left(r_{ij}\right) = 4\varepsilon\left[\left(\frac{\sigma}{r_{ij}}\right)^{12} - \left(\frac{\sigma}{r_{ij}}\right)^{6}\right], \tag{6.28}$$

where $\varepsilon$ and $\sigma$ are the Lennard-Jones energy and length scales, respectively. We use the parameters $\sigma = 3.40$ Å, $\varepsilon/k_B = 120.96$ K and we truncate the interactions at a cutoff radius of $r_c = 3.1\sigma$. A timestep of $dt = 5$ fs and periodic boundary conditions were used throughout. When conducting simulations in the $NVT$ ensemble we again used a stochastic velocity rescaling thermostat.[125] We initially attempted to reproduce the Green-Kubo results of McGaughey and Kaviany[76] for the thermal conductivity of Lennard-Jones argon at zero external pressure for a total of eight state points over a wide temperature range from 10 K to 80 K. Whilst for the most part our results were in good agreement with theirs, we did find some significant

differences at a couple of the state points, perhaps due to smaller system sizes and simulation times being used in their calculations, and so we will present our own Green-Kubo results in the following subsection.

### 6.3.1 Thermal conductivity from the Green-Kubo relation

At each of the eight state points we initialised on a face centred cubic lattice consisting of a set of $6 \times 6 \times 6$ unit cells ($N = 864$ atoms), using the zero pressure densities computed by McGaughey and Kaviany[76] These densities are consistent to the experimental densities of solid argon to within 2%.[179] The system was equilibrated in the $NVT$ ensemble for a time period of 2.5ns, and then the thermostat was switched off and the momenta resampled from the Boltzmann distribution before evolving the simulation in the $NVE$ ensemble for a further 10 ns. The heat flux vector was computed at every time step using Eq. 3.76 with the three-body terms set to zero. The heat flux autocorrelation function (HFACF) was then calculated by averaging over time differences in the trajectory up to a maximum correlation time of 250 ps, and the procedure was repeated using 100 independent trajectories to obtain the average heat flux autocorrelation function and an estimate of its error. The only exception to this was the $T = 10$ K and $\rho_m = 1820\,\mathrm{kg\,m^{-3}}$ state point, where the HFACF was computed up to a maximum correlation time of 500 ps since it had not decayed completely to zero by 250 ps.

The average HFACF at the $T = 10\,\mathrm{K}$ and $\rho_m = 1820\,\mathrm{kg\,m^{-3}}$ state point is shown in Fig. 6.1, showing the characteristic two stage decay of a crystalline solid.[74; 76] There is an initial very fast decay over the first picosecond which is followed by a slower decay over a much longer timescale. These decays have been attributed to being due to short wavelength and long wavelength phonons, respectively.[76] For this reason, the Green-Kubo HFACF in solids is often approximated by fitting to the sum of two exponential decays.[72; 76; 180] However, it has been found that fitting the slowly decaying long wavelength component to an exponential is not always sufficient to determine the integral when compared to direct numerical integration,[74] and to fit this component accurately it may also be necessary to

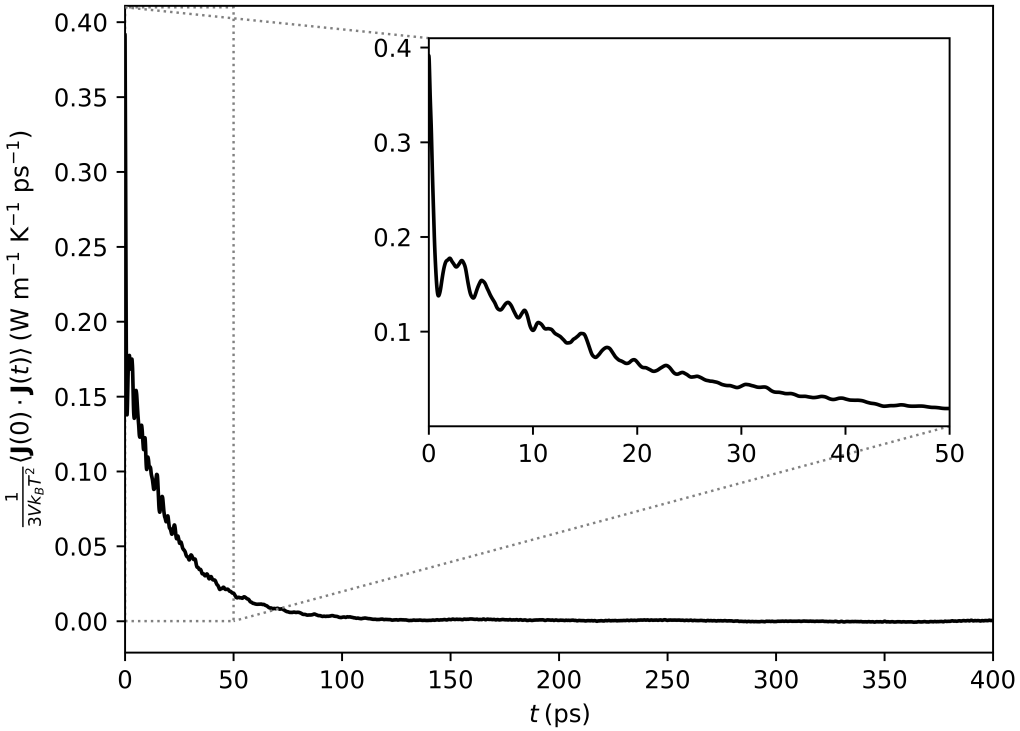



**Figure 6.1:** The heat flux autocorrelation function computed for Lennard-Jones argon at $T = 10\,\mathrm{K}$ and $\rho_m = 1820\,\mathrm{kg\,m^{-3}}$. The inset shows the initial rapid decay in the autocorrelation function in greater detail. The autocorrelation function was found not to reach zero until close to 300 ps. Although we only show the first 400 ps here, the heat flux autocorrelation was computed up to a maximum time difference of 500 ps in this case.

use an additional exponential decay in the fit.[98; 181] To avoid any difficulties or ambiguities due to exponential fits not fitting the data sufficiently, we choose to obtain the thermal conductivity by direct integration of the HFACF at all of the state points considered here. Although the running-time integral of the HFACF,

$$\kappa(\tau) = \frac{1}{3Vk_BT^2}\int_0^\tau \langle \mathbf{J}(0)\cdot\mathbf{J}(t)\rangle dt, \tag{6.29}$$

is observed to drift somewhat as the integration time is increased, this drift is found to be relatively minor and in each case a "plateau region" of the integral may be identified where $\kappa(\tau)$ varies only slightly ($\approx \pm 1\%$) over a large time period ($> 100\,\mathrm{ps}$). Due to this, we find that we can take the value of $\kappa(\tau)$ evaluated when $\tau$ is the maximum correlation time of the computed HFACF without introducing much error. This is likely due to the relatively large amount of statistical averaging

performed in computing the HFACFs. An example of the running time integral of the HFACF is shown for the $T = 10\,\mathrm{K}$ and $\rho_m = 1820\,\mathrm{kg\,m^{-3}}$ state point in Fig. 6.2.

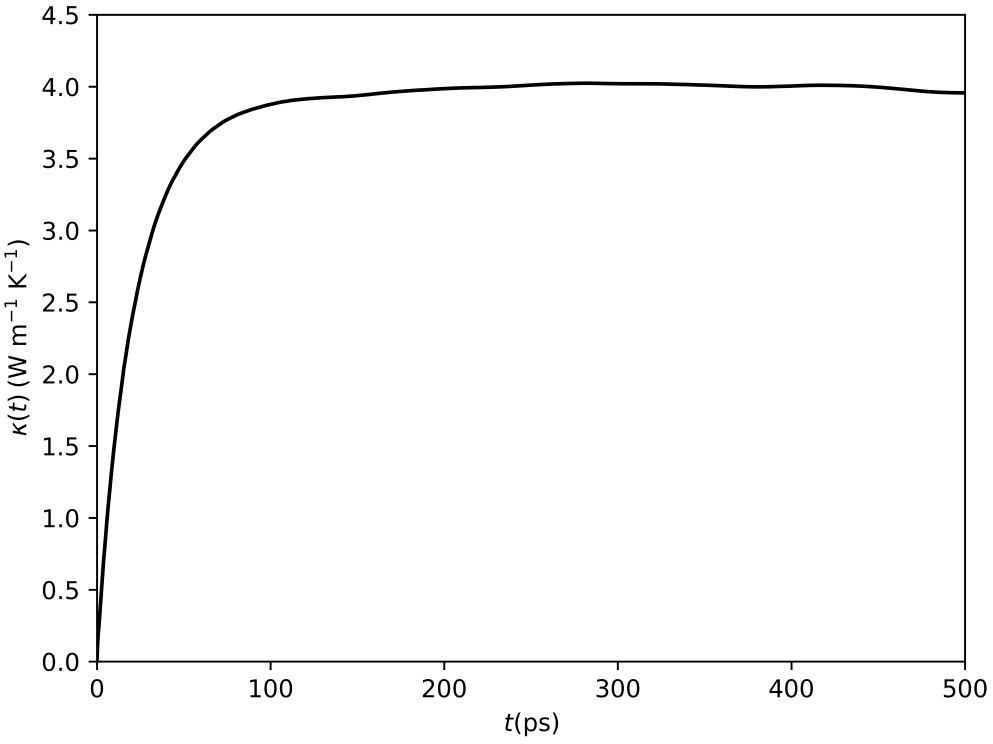



**Figure 6.2:** Running time integral of the heat flux autocorrelation function, $\kappa(t)$ computed for Lennard-Jones argon at $T = 10\,\mathrm{K}$ and $\rho_m = 1820\,\mathrm{kg\,m^{-3}}$. The value of $\kappa(t)$ varies only between $\pm 1\%$ of its final value between $t = 250\,\mathrm{ps}$ and $t = 500\,\mathrm{ps}$.

As the temperature increases the long wavelength component is observed to decay faster whilst the decay time of the short wavelength component is found to remain roughly constant. This is consistent with the findings of McGaughey and Kaviany[76] For example, at $T = 30\,\mathrm{K}$ the HFACF takes close to 30 ps to decay to zero whilst it takes only approximately 12 ps at the $T = 70\,\mathrm{K}$ state point. Other than the faster decay of the long wavelength component there is very little difference between the appearance of the HFACFs at the different state points. The calculated values of $\kappa$ found from direct integration of the HFACF at each state point are summarised in Table 6.1 below. We also performed some simulations for a larger system size of $10 \times 10 \times 10$ unit cells ($N = 4000$ atoms),

and the Green-Kubo thermal conductivities were found to be the same to within our estimated uncertainties at each of the state points.

| $T$ (K) | $\rho_m$ (kg m$^{-3}$) | $\kappa$ $\left(\mathrm{W\,m^{-1}\,K^{-1}}\right)$ |
|---|---|---|
| 10 | 1820 | 3.99 (2) |
| 20 | 1801 | 1.60 (3) |
| 30 | 1780 | 0.98 (2) |
| 40 | 1756 | 0.62 (1) |
| 50 | 1729 | 0.435 (8) |
| 60 | 1701 | 0.331 (6) |
| 70 | 1671 | 0.262 (5) |
| 80 | 1639 | 0.216 (4) |

**Table 6.1:** Thermal conductivities calculated from the Green-Kubo relation by direct integration for solid Lennard-Jones argon at each of eight state points considered in this Chapter. Standard errors in the mean for the last digit are given in parentheses.

Whilst for the most part there is good agreement between our thermal conductivities and those found by McGaughey and Kaviany,[76] there are some differences - particularly at the intermediate temperatures between 30 K and 50 K. For example, McGaughey and Kaviany give thermal conductivities of $\kappa = 0.902\,\mathrm{W\,m^{-1}\,K^{-1}}$ and $\kappa = 0.574\,\mathrm{W\,m^{-1}\,K^{-1}}$ at the $T = 30\,\mathrm{K}$ and $T = 40\,\mathrm{K}$ state points, respectively.[76] These are both $\approx 8\%$ different from the results we have presented in Table 6.1 and lie significantly outside of our estimated errors. We also see similar discrepancies with their results at the $T = 80\,\mathrm{K}$ state point. We believe that these differences are likely due to the fact that McGaughey and Kaviany only considered relatively small system sizes ($N = 256$) and only provided the thermal conductivities calculated from fitting the HFACF to the sum of two exponentials rather than by direct integration, without providing much in the way of estimates of the errors in their calculations.[76] We will therefore use the Green-Kubo thermal conductivities that we calculated in Table 6.1 rather than those of McGaughey and Kaviany when comparing to the thermal conductivities found from fitting the intermediate scattering functions to the hydrodynamic models in the following subsection.

### 6.3.2 Equilibrium density fluctuations

As our first port of call we calculated the constant volume and constant pressure heat capacities per atom, $c_V$ and $c_P$ respectively, as well as the adiabatic speed of sound, $c_s$, from the thermodynamic derivatives given by Eqs 3.105 to 3.107 at each of the eight thermodynamic state points in Table 6.1. In order to calculate $(\partial E/\partial T)_\rho$ and $(\partial p/\partial T)_\rho$ by finite difference we considered five temperatures equally spaced around each of the state points with the density held constant and a 5% variation in temperature between each point. We also calculated $(\partial p/\partial \rho)_T$ by considering five densities equally spaced around the state point with the temperature held constant and a 1% difference in density between each. At each of the different combinations of temperature and density the average total energy, $E$, and pressure, $p$, as well as their uncertainties were calculated from a total of 25 independent simulations. Each of these simulations were initialised on a face centred cubic lattice consisting of $6 \times 6 \times 6$ unit cells ($N = 864$ atoms) and equilibrated in the $NVT$ ensemble for a time period of 2.5 ns after which the total energy and pressure of the system was sampled at each step for a further 2.5 ns. The thermodynamic derivatives $(\partial E/\partial T)_\rho$ and $(\partial p/\partial T)_\rho$ were then estimated from a linear least squares fit through the data points which were at constant density, and $(\partial p/\partial \rho)_T$ estimated from a quadratic fit through the data points which were at constant temperature. The values of $c_V$, $c_P$, $\gamma$ and $c_s$ and the uncertainties in each which were obtained from this procedure are summarised in Table 6.2.

From Table 6.2 we can immediately see an issue with this approach for determining the thermal diffusivity at low temperatures. As the temperature decreases, we find that $\gamma \to 1$ and therefore the relative weight of the thermal diffusive component of the intermediate scattering function goes to zero (as $\gamma \to 1$, $\gamma^{\text{eff}} \to 1$ also). The fraction of the signal which depends most on $a$, the parameter in which we are most interested in here, therefore becomes very small and hence $a$ becomes more difficult to determine accurately from the fit. The observation that $\gamma \to 1$ is generally true for solids as $T \to 0$, and moreover $\gamma$ may be as small as 1.05 at room temperature for many typical solids.[182] Therefore, whilst in the specific case of Lennard-Jones

| $T$ (K) | $\rho_m$ (kg m$^{-3}$) | $c_V$ ($k_B$) | $c_P$ ($k_B$) | $\gamma$ | $c_s$ (Å ps$^{-1}$) |
|---|---|---|---|---|---|
| 10 | 1820 | 2.90 (7) | 2.99 (7) | 1.03 (3) | 12.7 (2) |
| 20 | 1801 | 2.83 (6) | 3.03 (6) | 1.07 (3) | 12.5 (2) |
| 30 | 1780 | 2.90 (7) | 3.23 (7) | 1.12 (4) | 12.3 (2) |
| 40 | 1756 | 2.88 (8) | 3.36 (8) | 1.17 (4) | 12.0 (2) |
| 50 | 1729 | 2.83 (7) | 3.47 (8) | 1.23 (4) | 11.6 (2) |
| 60 | 1701 | 2.85 (6) | 3.75 (7) | 1.31 (4) | 11.1 (2) |
| 70 | 1671 | 2.80 (7) | 3.92 (9) | 1.40 (5) | 10.9 (2) |
| 80 | 1639 | 2.64 (6) | 3.97 (8) | 1.51 (4) | 10.5 (2) |

**Table 6.2:** Values of properties estimated from the thermodynamic derivatives evaluated using finite difference for Lennard-Jones argon. The values of $\gamma$ and $c_s$ given here were used directly in the application of the "exact" and "approximate" fitting models to the intermediate scattering function data to be shown later in this Section. Estimated uncertainties in the last digit are shown in parentheses.

argon the values of $\gamma$ are large enough to have a reasonable fraction of the thermal diffusion component above $\approx 30$ K, determining $a$ from fits to the intermediate scattering function of solids will not be a viable approach in a large number of systems. Thankfully, the hydrodynamic theory discussed in Section 6.2 suggests an alternative approach which is better suited for thermal diffusivity prediction in the case where $\gamma \to 1$, which we will present in Section 6.4.

We initialised our systems on a face centred cubic lattice set up in a cuboidal geometry with a $6 \times 6$ unit cell cross-section. We considered five long-axis lengths between 24 and 120 unit cells and calculated the intermediate scattering function for the smallest value of $k$ which could fit a whole wavelength along the long axis of the system for each. The system was equilibrated in the $NVT$ ensemble for a time period of 2.5 ns at each long axis length and then 25 successive $NVE$ trajectories of length 750 ps were run with a resampling of the momenta from the Boltzmann distribution between each one. The intermediate scattering function for the smallest wavevector which fit a whole wavelength along the long axis of the system was calculated up to a correlation time of 375 ps and averaged over the 25 $NVE$ trajectories. This was repeated over a total of 250 independent simulations at each length. An example of the average intermediate scattering function at the

$T = 50\,\mathrm{K}$ and $\rho_m = 1729\,\mathrm{kg\,m^{-3}}$ state point for a long axis length of 120 unit cells using the "exact" fitting procedure is shown in Fig. 6.3 below.

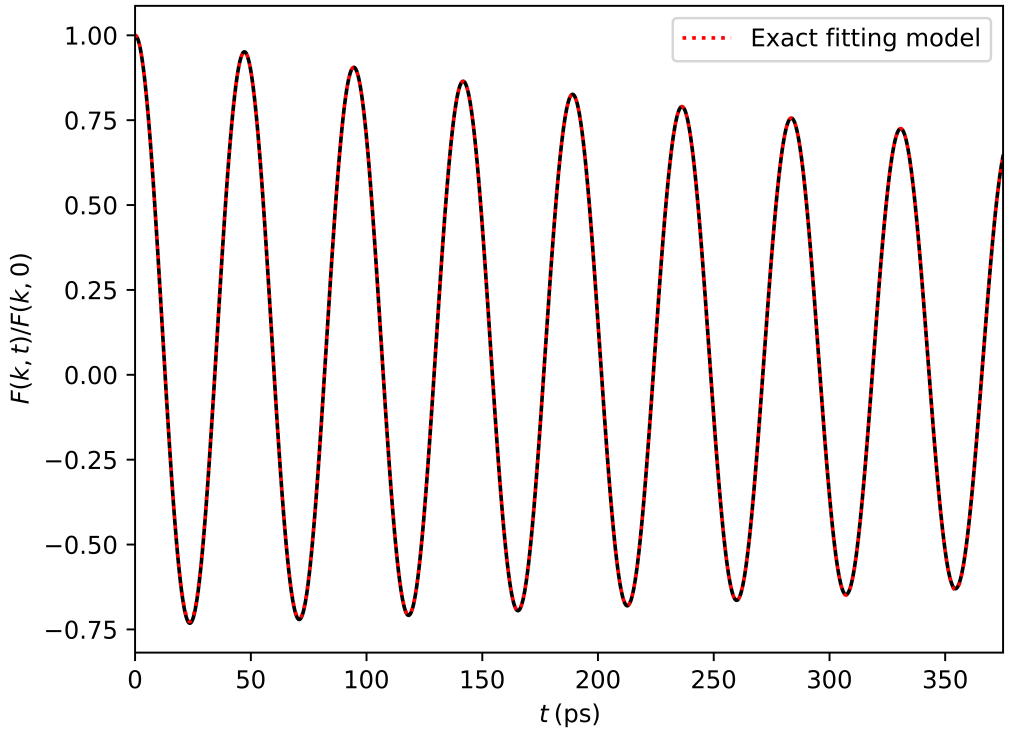



**Figure 6.3:** The intermediate scattering function obtained at $T = 50\,\mathrm{K}$ and $\rho_m = 1729\,\mathrm{kg\,m^{-3}}$ for a system of $120 \times 6 \times 6$ unit cells with $k$ taken to fit exactly one wavelength along the long axis of the system (solid black line). Also shown is the fit to Eq. 6.16 (dotted red line) using the independently calculated values of $c_s$ and $\gamma$ provided in Table 6.2.

From inspection of Fig. 6.3 we can see that that the hydrodynamic model developed for the density fluctuations in Section 6.2 provides a good description of the data obtained from our simulations. Whilst the values of the fitted parameters sometimes differed slightly between the different fitting models, the fits from the two models were found to be qualitatively indistinguishable from each other and thus we only show the fit to the "exact" fitting model here. A similar quality of fit was also seen at the other lengths and at the other state points. As the temperature was decreased we observed that the fraction of the thermal diffusion component decreased, consistent with the trend found for the independently calculated values

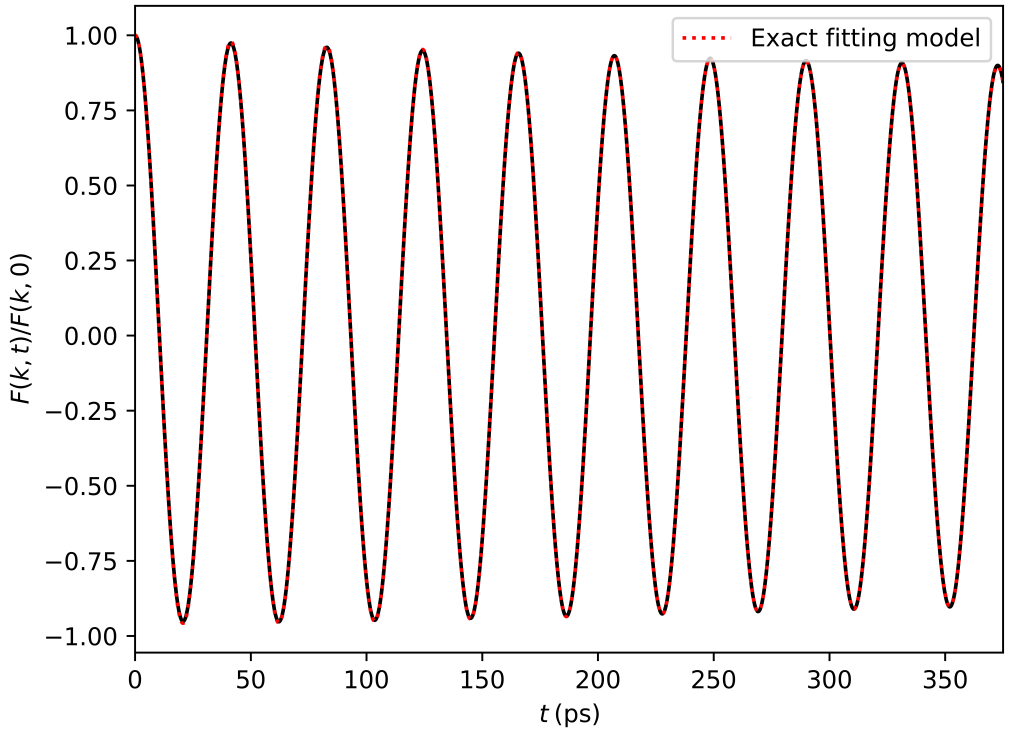



**Figure 6.4:** The intermediate scattering function obtained at $T = 10\,\mathrm{K}$ and $\rho_m = 1820\,\mathrm{kg\,m^{-3}}$ for a system of $120 \times 6 \times 6$ unit cells with $k$ taken to fit exactly one wavelength along the long axis of the system (solid black line), showing a negligible thermal diffusion component. Also shown is the fit to Eq. 6.16 (dotted red line) using the independently calculated values of $c_s$ and $\gamma$ provided in Table 6.2.

of $\gamma$ in Table 6.2, and that the frequency of the sound wave component increased. At temperatures of 10 K and 20 K, as expected from the data in Table 6.2, we found that the intermediate scattering function showed almost no noticeable thermal diffusion component. This is evidenced by the data and fit to the "exact" model shown for a long axis length of 120 unit cells at $T = 10\,\mathrm{K}$ and $\rho_m = 1820\,\mathrm{kg\,m^{-3}}$ in Fig. 6.4 - where the intermediate scattering function has only decayed by $\approx 10\%$ of its initial value after 375 ps.

The 250 simulations were then split evenly into 5 sets and we separately fit the average intermediate scattering simulation of each set to the three fitting models. This gave us five independent estimates of $a\,(k)$ at each length for each fitting model, allowing us to obtain an estimate of the average value and its uncertainty. These

were converted into the corresponding length dependent thermal conductivities using $\kappa(k) = \rho c_V a(k)$. We then plotted $1/\kappa(k)$ against $k$ at each temperature and used a weighted linear least squares fit to extrapolate $\kappa(k)$ to its value in the hydrodynamic limit, at $k = 0$. An example of this extrapolation at the $T = 70\,\mathrm{K}$ and $\rho_m = 1671\,\mathrm{kg\,m^{-3}}$ state point is shown in Fig. 6.5 using both of the "exact" and the "approximate" fitting models, as well as the intercepts and their uncertainties predicted by the weighted least squares fit. Also shown is the corresponding value of $1/\kappa(0)$ and its uncertainty which would be expected from the Green-Kubo thermal conductivity provided at this state point in Table 6.1. Here, we see that the "exact" and "approximate" fitting models do give extrapolated thermal conductivities which are consistent with the thermal conductivity calculated from the Green-Kubo calculation to within our estimated uncertainties. We also see very little variation in the length dependent thermal conductivities at each of the values of $k$ between the two fitting models, with the values of $\kappa(k)$ becoming almost indistinguishable from each other as $k \to 0$.

Whilst we see that both of the fitting models do show a fairly good linear dependence of $1/\kappa(k)$ against $k$ which extrapolates to a value at the hydrodynamic limit in agreement with the Green-Kubo thermal conductivity in this case, we emphasise that despite the lengthy simulations conducted (a total of 6250 $NVE$ trajectories for a cumulative $4.5\,\mu\mathrm{s}$ of simulation time at each value of $k$) that there is still a good deal of uncertainty in the intermediate scattering functions. This is compounded by the fact that the values of $\gamma$ and $c_s$ given in Table 6.2 have a much larger uncertainty than those given for liquid parahydrogen in Table 4.3. This makes the linear extrapolation scheme less convincing in some cases, as shown by the plot of $1/\kappa(k)$ against $k$ for the $T = 80\,\mathrm{K}$ and $\rho_m = 1639\,\mathrm{kg\,m^{-3}}$ state point in Fig. 6.6. Although once again the length dependent thermal conductivities predicted by the two fitting models are in good agreement with each other and appear to show a linear dependence of $1/\kappa(k)$ on $k$, they now extrapolate to a value which is significantly less than that predicted by the Green-Kubo method. We tried to improve the results by conducting additional simulations but it was clear that

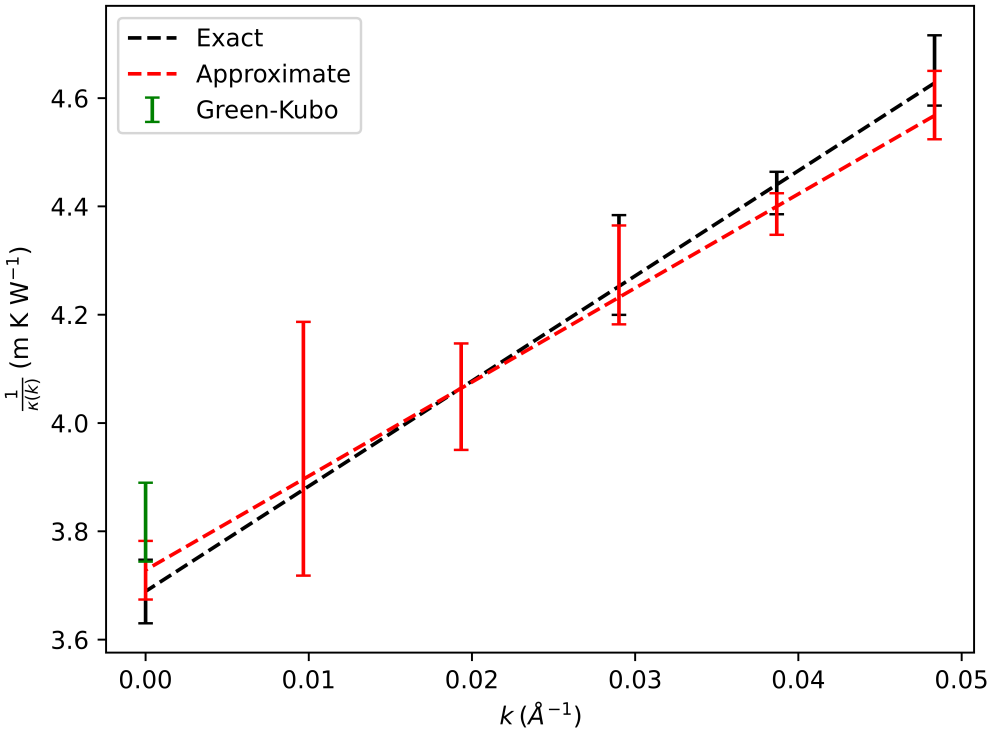



**Figure 6.5:** The length dependent thermal conductivities and their associated uncertainties found from fitting to each of the fitting models described in Section 6.2 at the $T = 70\,\mathrm{K}$ and $\rho_m = 1671\,\mathrm{kg\,m^{-3}}$ state point. The weighted linear least squares fits used in the extrapolation to $k = 0$ in each case are shown as dotted lines. The errorbars shown at $k = 0$ are the intercept and its uncertainty which were predicted from these least squares fits. The green errorbar labelled "Green-Kubo" is the value of $1/\kappa$ and its uncertainty which one would find using the Green-Kubo thermal conductivity calculated at this state point from Table 6.1.

any improvement would be slow and arduous to complete, especially considering that the simulations detailed here are already over an order of magnitude more expensive than the Green-Kubo calculations described in subsection 6.3.1.

Nevertheless, we were able to extrapolate the thermal conductivity to the hydrodynamic limit for each of the state points at temperatures of 30 K and above. Below $T = 30\,\mathrm{K}$ we found that $\gamma$ was too close to 1 to give a reasonable extrapolation of $1/\kappa\,(k)$ against $k$ for the reasons mentioned earlier. The resulting thermal conductivities extrapolated using the "exact" fitting model, $\kappa_{\mathrm{exact}}$, and the "approximate" fitting model, $\kappa_{\mathrm{approx.}}$, as well as their uncertainties are summarised in Table 6.3

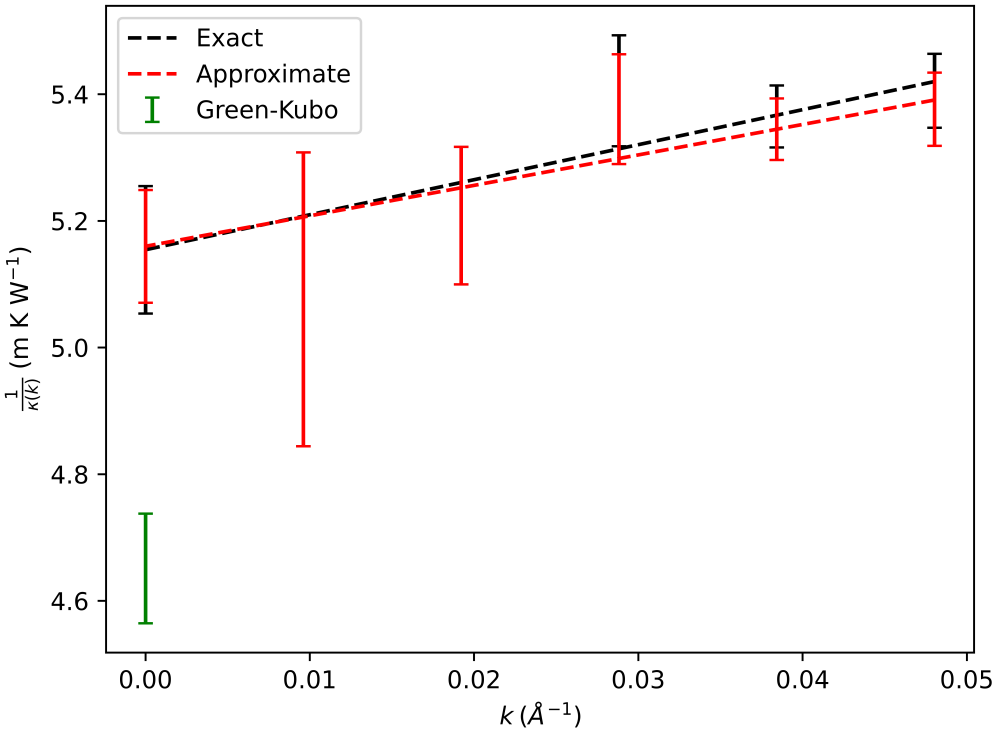



**Figure 6.6:** The length dependent thermal conductivities and their associated uncertainties found from fitting to each of the three fitting models described in Section 6.2 at the $T = 80\,\mathrm{K}$ and $\rho_m = 1639\,\mathrm{kg\,m^{-3}}$ state point. The weighted linear least squares fits used in the extrapolation to $k = 0$ in each case are shown as dotted lines. The errorbars shown at $k = 0$ are the intercept and its uncertainty which were predicted from these least squares fits. The green errorbar labelled "Green-Kubo" is the value of $1/\kappa$ and its uncertainty which one would find using the Green-Kubo thermal conductivity calculated at this state point from Table 6.1.

below. Also given are the corresponding Green-Kubo thermal conductivities, $\kappa_{\mathrm{GK}}$, at each state point from Table 6.1. From inspection of Table 6.3 we see that both fitting models give thermal conductivities that agree with the corresponding Green-Kubo thermal conductivities to within 10% at each of the state points.

The values of $1/\kappa\,(k)$ found using the "exact" fitting model are plotted against $k$ for all of these state points in Fig. 6.7, showing the weighted linear least squares fits used. We can see that, apart from the state point at $T = 80\,\mathrm{K}$, the slope of the linear extrapolations is found to be largely independent of temperature. However, we note that as we are extrapolating $1/\kappa\,(k)$ and that $\kappa\,(k)$ increases at lower

| $T$ (K) | $\rho_m$ ($\mathrm{kg\,m^{-3}}$) | $\kappa_{\mathrm{exact}}$ ($\mathrm{W\,m^{-1}\,K^{-1}}$) | $\kappa_{\mathrm{approx.}}$ ($\mathrm{W\,m^{-1}\,K^{-1}}$) | $\kappa_{\mathrm{GK}}$ ($\mathrm{W\,m^{-1}\,K^{-1}}$) |
|---|---|---|---|---|
| 30 | 1780 | 1.04 (5) | 0.98 (3) | 0.98 (2) |
| 40 | 1756 | 0.68 (3) | 0.66 (2) | 0.62 (1) |
| 50 | 1729 | 0.444 (9) | 0.441 (8) | 0.435 (8) |
| 60 | 1701 | 0.350 (9) | 0.346 (8) | 0.331 (6) |
| 70 | 1671 | 0.271 (4) | 0.268 (4) | 0.262 (5) |
| 80 | 1639 | 0.194 (4) | 0.194 (3) | 0.215 (4) |

**Table 6.3:** Thermal conductivities extrapolated to $k = 0$ when the intermediate scattering functions are fitted to Eq. 6.16 ($\kappa_{\mathrm{exact}}$) or to Eq. 6.26 ($\kappa_{\mathrm{approx.}}$). Also shown for reference are the Green-Kubo thermal conductivities found at these state points from Table 6.1. Estimated uncertainties in the last digit are shown in parentheses.

temperatures, the rate of change of $\kappa(k)$ with $k$ is increasing as the temperature decreases. The less negative slope found at the $T = 80\,\mathrm{K}$ state point may be indicative of inaccurate estimates of $\kappa(k)$ from the fits and might explain why the extrapolated bulk thermal conductivity is in less good agreement with the Green-Kubo thermal conductivity here.

We also see from Table 6.3 that the extrapolated thermal conductivities using the "exact" and the "approximate" models are in good agreement with each other. This is consistent with the observations made about Figs 6.5 and 6.6 that these fitting procedures gave largely the same estimated values for $\kappa(k)$, especially as $k \to 0$. So whilst for liquid parahydrogen we found that fitting to the exact solution of the inverse Laplace transform gave a more favourable system size dependence than fitting to the approximate solution, we do not find any evidence here that this is also true for the case of solid Lennard-Jones argon. In fact, we find that fitting to the approximate solution of Eq. 6.26 gives results that tend to be in slightly better agreement with the Green-Kubo thermal conductivity than fitting to the exact solution of Eq. 6.16, although the difference is not large enough to be significant. It is also found that apart from the state point at $T = 80\,\mathrm{K}$ that the extrapolated thermal conductivities tend to slightly overestimate the thermal conductivity when compared to the Green-Kubo method.

Finally, we also investigated the values of the elastic constant $C_{11}$ which one would expect using the longitudinal speed of sounds, $c_L$, which we found from our fits

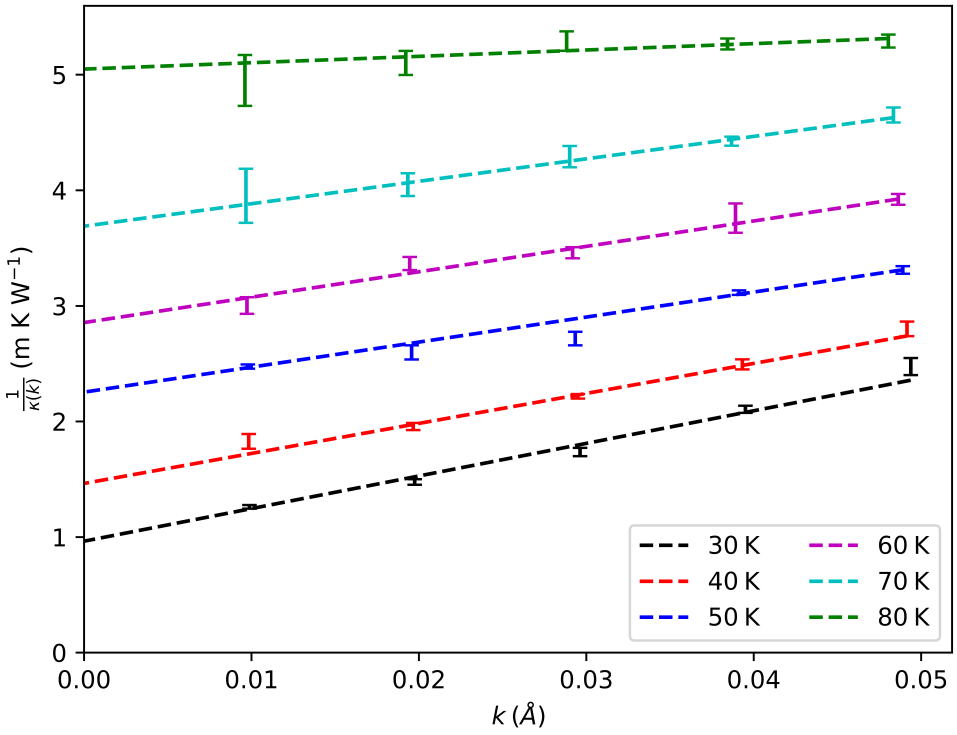



**Figure 6.7:** The length dependent thermal conductivities and their associated uncertainties found from fitting the intermediate scattering function to Eq. 6.16 using the independently calculated values of $c_s$ and $\gamma$ from Table 6.2 at each of the state points from $T = 30\,\mathrm{K}$ to $T = 80\,\mathrm{K}$. The weighted linear least squares fits used in the extrapolation to $k = 0$ in each case are shown as dotted lines. At the $T = 10\,\mathrm{K}$ and $T = 20\,\mathrm{K}$ state points the fraction of the thermal diffusion component in the intermediate scattering function was found to be too small to obtain a reliable estimate of $a$.

to the "exact" model. Here we found that the values of $c_L(k)$ displayed essentially no dependence on $k$ (there was less than a 2% variation in $c_L(k)$ between the smallest and largest values of $k$ used at each of the state points), so we take the $c_L(k)$ obtained from the smallest values of $k$ we used as its value in the hydrodynamic limit, $c_L$. These are provided in Table 6.4 below, as well as the values of $C_{11} = m\rho_0 c_L^2$ predicted from them. Also included are the experimental measurements of $C_{11,\mathrm{expt.}}$ obtained for an argon single crystal by Keeler and Batchelder.[183] The values of $C_{11,\mathrm{expt.}}$ presented in Table 6.4 at temperatures of $T = 10\,\mathrm{K}$ and $T = 80\,\mathrm{K}$ were obtained by extrapolation of their measurements between $T = 16\,\mathrm{K}$ and $T = 77\,\mathrm{K}$.[183]

From Table 6.4 we may observe that although there is one the whole a good

| $T$ (K) | $\rho_m$ (kg m$^{-3}$) | $c_L$ (Å ps$^{-1}$) | $C_{11}$ ($10^9$ N m$^{-2}$) | $C_{11,\text{expt.}}$ ($10^9$ N m$^{-2}$) |
|---|---|---|---|---|
| 10 | 1820 | 15.253 | 4.235 | 4.342 |
| 20 | 1801 | 14.927 | 4.013 | 4.204 |
| 30 | 1780 | 14.543 | 3.765 | 4.004 |
| 40 | 1756 | 14.097 | 3.489 | 3.766 |
| 50 | 1729 | 13.597 | 3.197 | 3.507 |
| 60 | 1701 | 13.100 | 2.919 | 3.240 |
| 70 | 1671 | 12.576 | 2.643 | 2.972 |
| 80 | 1639 | 12.023 | 2.369 | 2.702 |

**Table 6.4:** Values of the longitudinal speed of sound, $c_L$, calculated from the average of separate fits to Eq. 6.16 from the five independent sets of data for a system size of $120 \times 6 \times 6$ unit cells. The standard error in the mean in the last digit across these five sets is shown in parentheses. Also provided are the values of the elastic constant $C_{11}$ which would be predicted using this value of $c_L$ as well as the corresponding experimental measurements given at these temperatures, $C_{11,\text{expt.}}$ by Keeler and Batchelder[183]. The experimental measurements at 10 K and 80 K were obtained by extrapolation of the measured sound velocities between 16 K and 77 K.[183]

agreement between our predicted values of $C_{11}$ and experiment, we find that we systematically underestimate the experimental results. The values of $C_{11}$ at $T = 10$K are within 3% of experiment, but this agreement gradually worsens as one decreases the temperature. At a temperature of $T = 80$ K our predicted value of $C_{11}$ is close to 13% smaller than the experimental value.

So, whilst there are likely issues with sufficient convergence of the intermediate scattering function and also of the independently calculated values of $c_s$ and $\gamma$ - which will need a very large amount of computational resources to begin to alleviate - it does appear that we can find the thermal conductivity from fitting the intermediate scattering function of Lennard-Jones argon to the hydrodynamic models of Eqs 6.16 and 6.26 with reasonable accuracy at temperatures above $T = 30$ K. At temperatures of $T = 20$ K and below, as mentioned previously we find that the fraction of the intermediate scattering function which depends most sensitively on the thermal conductivity becomes small and we must turn to an alternative approach from the hydrodynamic theory - which we will discuss in the following Section.

## 6.4 Temperature fluctuations

Returning to the hydrodynamic matrix equation given in Eq. 6.8, similarly to how we derived an expression for the autocorrelation of the Fourier components of the local density in the hydrodynamic limit, we may also derive an expression for the Fourier components of the local temperature in this same limit. From a very similar argument to those used in the derivation of Eq. 6.14 we find that, provided $k$ is chosen such that an integer number of wavelengths fit inside the simulation box, the autocorrelation function of the Fourier components of the local temperature, $C_{TT}(k,t) = \langle T_1(k,t)\, T_1(-k,0)\rangle$, may be written as

$$\frac{C_{TT}(k,t)}{C_{TT}(k,0)} = \mathcal{L}^{-1}\left\{\frac{B(k,s)}{D(k,s)}\right\}, \tag{6.30}$$

where the function $B(k,s)$ is given by

$$B(k,s) = s^2 + bk^2 s + \left(\frac{1-\gamma}{\gamma}c_s^2 + c_L^2\right)k^2, \tag{6.31}$$

and $D(k,s)$ is the determinant of the hydrodynamic matrix $\mathbf{M}$ and is given by Eq. 6.12.

Performing the inverse Laplace transform in Eq. 6.30 yields

$$\frac{C_{TT}(k,t)}{C_{TT}(k,0)} = \frac{B(k,s_0)\,e^{s_0 t}}{(s_0-s_+)(s_0-s_-)} + \frac{B(k,s_+)\,e^{s_+ t}}{(s_+-s_0)(s_+-s_-)} + \frac{B(k,s_-)\,e^{s_- t}}{(s_--s_0)(s_--s_+)}, \tag{6.32}$$

where, as before, $s_0$, $s_+$ and $s_-$ are the roots to the cubic equation $D(k,s) = 0$. Whilst one can already use Eq. 6.32 as a fitting model, for the same reasons as discussed earlier in the context of the density fluctuations it is again useful to derive an approximation to Eq. 6.32 using the first order perturbative roots derived in Section 6.2. By substituting in these approximate roots to Eq. 6.32 and only retaining terms up to first order in the small quantities $ak^2$ and $bk^2$ we find that

$$\frac{C_{TT}(k,t)}{C_{TT}(k,0)} \approx \frac{1}{\gamma^{\text{eff}}}e^{-D_T^{\text{eff}}k^2 t} + \frac{\gamma^{\text{eff}}-1}{\gamma^{\text{eff}}}e^{-\Gamma^{\text{eff}}k^2 t}\left[\cos(c_L k t) + f(k)\sin(c_L k t)\right], \tag{6.33}$$

where the definitions of $\gamma^{\text{eff}}$, $D_T^{\text{eff}}$ and $\Gamma^{\text{eff}}$ are the same as in Section 6.2. In this case the function $f(k)$ is given by

$$f(k) = \frac{k}{c_L}\left[\Gamma^{\text{eff}} - \left(\gamma^{\text{eff}}+1\right)D_T^{\text{eff}}\right]. \tag{6.34}$$

Both of Eqs 6.33 and 6.34 are very similar to the expressions derived for the autocorrelation function of the Fourier components of the local temperature of liquids in Section 3.4.1, but with $\gamma$, $D_T$ and $\Gamma$ replaced by their corresponding "effective" variables and with $c_s$ replaced by $c_L$.

Therefore, again we find that the approximate expression for the autocorrelation function of the Fourier components of the local temperature in solids given in Eq. 6.33 shares many similarities with the corresponding approximate expression for the autocorrelation function of the Fourier components of the local density given in Eq. 6.26. Both contain an exponentially decaying thermal diffusion term and an oscillating sound wave term, but the relative proportions of these two components are switched between the two approximate expressions. Therefore, when $\gamma \to 1$ at low temperatures and the fraction of the intermediate scattering function which is dependent on the thermal diffusivity becomes small, the fraction of the corresponding component in $C_{TT}(k,t)$ will become large. In light of this observation we aim to determine whether finding the thermal conductivity by fitting the values of $C_{TT}(k,t)$ obtained from molecular dynamics simulations to an appropriate functional form is a viable approach in systems where $\gamma \approx 1$, as is the case in many room temperature solids[182] and in Lennard-Jones argon as $T \to 0$.

The function $C_{TT}(k,t)$ is more difficult to work with than $F(k,t)$ due to issues in defining a local temperature, $T(\mathbf{r},t)$, within the context of a molecular dynamics simulation. One could naively take the local temperature to be related to the instantaneous kinetic energy of each of the particles in the system via

$$T(\mathbf{r},t) = \sum_i \frac{|\mathbf{p}_i(t)|^2}{3m_i k_B} \delta(\mathbf{r} - \mathbf{r}_i(t)), \tag{6.35}$$

where $|\mathbf{p}_i(t)|^2$ is the squared magnitude of the momentum vector of particle $i$ at time $t$. However, one finds that due to rapid interconversion of the local kinetic and potential energies that one must average the local temperature given in Eq. 6.35 over a sufficiently long time window to remove these fluctuations and obtain local thermal equilibrium.[184] Further, one must also average $T(\mathbf{r},t)$ over a large enough spatial region of the system to ensure local thermal equilibrium and to

remove the effects that density fluctuations may have on the fluctuations of the local kinetic energy. As we are only interested in the Fourier components of the local temperature when $\mathbf{k}$ is taken along the $x$ axis here, one must average the instantaneous temperature of Eq. 6.35 over all particles within a region of space from $x = x_i - \Delta x$ to $x = x_i + \Delta x$ for a set of bins with width $2\Delta x$. The average local temperature of each of these bins is then assigned to the centre of the bin, at $x = x_i$, in addition to the temporal averaging mentioned previously.

Whilst the local temperature may be defined in this manner, we found that the temporal averaging increased the time interval between which the correlation function $C_{TT}(k,t)$ could be evaluated to such a degree that it contained too few points to accurately describe the sound wave oscillations, especially at the larger values of $k$ used in the extrapolation. Further, it is unclear *a priori* exactly what amount of spatial and temporal averaging is required to achieve local thermodynamic equilibrium and whether this has any unforeseen effects on the computation of the correlation function $C_{TT}(k,t)$.

Thankfully, there is a better option than using the local instantaneous temperature as defined by a spatially and temporally averaged version of Eq. 6.35, which was originally derived by Schofield.[185] The local energy of the system may be written as $E(\mathbf{r},t) = \rho(\mathbf{r},t)\, e(\mathbf{r},t)$, where $\rho(\mathbf{r},t)$ is the local number density and $e(\mathbf{r},t)$ is the local energy per particle. Then we may find an expression for the spatial Fourier transform of the fluctuations in the local energy, denoting the values at equilibrium with a subscript $\square_0$ and the fluctuations from equilibrium with a subscript $\square_1$,

$$E_1(\mathbf{k},t) = e_0\rho_1(\mathbf{k},t) + \rho_0 e_1(\mathbf{k},t), \tag{6.36}$$

where $e_0$ and $\rho_0$ are the average energy per particle and number density at equilibrium respectively and we have kept only terms which are linear in the fluctuations from equilibrium. We then argue that the fluctuations described by $e_1(\mathbf{k},t)$ must be proportional to the fluctuations in the local temperature, $T_1(\mathbf{k},t)$. So, after some rearranging we arrive at

$$T_1(\mathbf{k},t) \propto E_1(\mathbf{k},t) - e_0\rho_1(\mathbf{k},t). \tag{6.37}$$

where after multiplying both sides by $\rho_1(-\mathbf{k},t)$ and taking the ensemble average we find, using the fact that the temperature and density fluctuations are thermodynamically independent ($\langle\rho_1(-\mathbf{k},t)\,T_1(\mathbf{k},t)\rangle = 0$)[84; 85; 185] and some rearranging of terms

$$e_0 = \frac{\langle\rho_1(-\mathbf{k},t)\,E_1(\mathbf{k},t)\rangle}{\langle\rho_1(-\mathbf{k},t)\,\rho_1(\mathbf{k},t)\rangle}. \tag{6.38}$$

Then, since the average energy per particle in the equilibrium reference system, $e_0$, must be independent of time we may replace the ensemble average of the product of the fluctuations on the right hand side of Eq. 6.38 with their $t = 0$ values. Also, to tidy up some of the notation we will denote the following correlation functions by $C_{EE}(\mathbf{k},t) = \langle E_1(-\mathbf{k},0)\,E_1(\mathbf{k},t)\rangle$, $C_{E\rho}(\mathbf{k},t) = \langle\rho_1(-\mathbf{k},0)\,E_1(\mathbf{k},t)\rangle = \langle E_1(-\mathbf{k},0)\,\rho_1(\mathbf{k},t)\rangle$ and $C_{\rho\rho}(\mathbf{k},t) = \langle\rho_1(-\mathbf{k},0)\,\rho_1(\mathbf{k},t)\rangle$. With these we may re-express Eq. 6.37 as

$$T_1(\mathbf{k},t) \propto E_1(\mathbf{k},t) - \frac{C_{E\rho}(\mathbf{k},0)}{C_{\rho\rho}(\mathbf{k},0)}\rho_1(\mathbf{k},t)\,. \tag{6.39}$$

Using Eq. 6.39 we can then find a relation for $C_{TT}(\mathbf{k},t) = \langle T_1(-\mathbf{k},0)\,T_1(\mathbf{k},t)\rangle$ via

$$C_{TT}(\mathbf{k},t) \propto C_{EE}(\mathbf{k},t) - 2\frac{C_{E\rho}(\mathbf{k},0)}{C_{\rho\rho}(\mathbf{k},0)}C_{E\rho}(\mathbf{k},t) + \left(\frac{C_{E\rho}(\mathbf{k},0)}{C_{\rho\rho}(\mathbf{k},0)}\right)^2 C_{\rho\rho}(\mathbf{k},t)\,, \tag{6.40}$$

where we have used the fact that since these correlation functions are real, $C_{AB}(\mathbf{k},t) = C_{AB}(-\mathbf{k},t)$. So, dividing Eq. 6.40 by its value at $t = 0$ we find

$$\frac{C_{TT}(\mathbf{k},t)}{C_{TT}(\mathbf{k},0)} = \frac{C_{EE}(\mathbf{k},t) - 2\frac{C_{E\rho}(\mathbf{k},0)}{C_{\rho\rho}(\mathbf{k},0)}C_{E\rho}(\mathbf{k},t) + \left(\frac{C_{E\rho}(\mathbf{k},0)}{C_{\rho\rho}(\mathbf{k},0)}\right)^2 C_{\rho\rho}(\mathbf{k},t)}{C_{EE}(\mathbf{k},0) - \frac{C_{E\rho}(\mathbf{k},0)^2}{C_{\rho\rho}(\mathbf{k},0)}}. \tag{6.41}$$

Our final expression for $C_{TT}(\mathbf{k},t)$ is equivalent to the expressions for $T_1(\mathbf{k},t)$ derived by Schofield,[186; 187] and to those used by Bertolini and Tani[119] as well as de Schepper *et al.*[120] in their studies on the generalised hydrodynamics of liquid water and liquid argon, respectively.

Remembering that since we always choose our wavevector $\mathbf{k}$ such that an integer number of wavelengths fit exactly along the long axis of our system, we may replace the fluctuations from equilibrium, $\rho_1(\mathbf{k},t)$ and $E_1(\mathbf{k},t)$, in the

definitions of $C_{EE}(\mathbf{k},t)$, $C_{E\rho}(\mathbf{k},t)$ and $C_{\rho\rho}(\mathbf{k},t)$ given earlier with their overall local values, $\rho(\mathbf{k},t)$ and $E(\mathbf{k},t)$, where in real space $\rho(\mathbf{r},t)=\rho_0+\rho_1(\mathbf{r},t)$, for example. Therefore, in order to compute the correlation function of the Fourier components of the local temperature we can instead calculate the correlation functions of the Fourier components of the local energy and number density, $C_{EE}(\mathbf{k},t)$ and $C_{\rho\rho}(\mathbf{k},t)$ respectively, as well as their cross correlation, $C_{E\rho}(\mathbf{k},t)$. The local energy and the local number density are much easier to define in the context of a molecular dynamics simulation than the local temperature, and in fact we have already done so. If we make the identification that the Fourier components of the local number density are

$$\rho(\mathbf{k},t)=\sum_{i=1}^{N}\delta(\mathbf{r}-\mathbf{r}_i)\,e^{i\mathbf{k}\cdot\mathbf{r}}, \tag{6.42}$$

where $N$ is the number of particles in the system, then we may relate $C_{\rho\rho}(\mathbf{k},t)$ to the intermediate scattering function $F(\mathbf{k},t)$ given in Eq. 3.94. Similarly we can define the Fourier components of the local energy using

$$E(\mathbf{k},t)=\sum_{i=1}^{N}\varepsilon_i\delta(\mathbf{r}-\mathbf{r}_i)\,e^{i\mathbf{k}\cdot\mathbf{r}}, \tag{6.43}$$

where $\varepsilon_i$ is the site energy of the $i^{\text{th}}$ atom and may be defined in the same way as the site energy in the Green-Kubo relation.

In order to test whether is feasible to find the thermal conductivity by fitting the values of $C_{TT}(k,t)/C_{TT}(k,t)$ found using Eq. 6.41 to the exact solution of the inverse Laplace transform from the hydrodynamic theory given in Eq. 6.32, we consider only the low temperature state point of $T=10\,\text{K}$ and $\rho_m=1820\,\text{kg m}^{-3}$ where $\gamma\approx 1$, and leave a more robust investigation to future work.

We initialised our simulations on a face centred cubic lattice consisting of $120\times 6\times 6$ unit cells ($N=17280$ atoms) and equilibrated in the $NVT$ ensemble for a time period of 2.5 ns. After this, 25 successive $NVE$ trajectories of length 750 ps were run and the Fourier components of the local number density and energy were calculated every five timesteps, using Eqs 6.42 and 6.43 respectively, for the five smallest wavevectors which fit an integer number of wavelengths along the long axis of the system. Using these, the correlation functions $C_{\rho\rho}(k,t)$, $C_{E\rho}(k,t)$

and $C_{\rho\rho}(k,t)$ were calculated up to a maximum correlation time of 375 ps for each of these values of $k$, and averaged over the 25 $NVE$ trajectories. This was then repeated over a total of 300 independent simulations. The average of the three correlations over all the simulations were then used to find $C_{TT}(k,t)/C_{TT}(k,0)$ using Eq. 6.41, and fit to the exact solution of the inverse Laplace transform from the hydrodynamic theory given by Eq. 6.32 using the independently calculated values of $c_s$ and $\gamma$ given in Table 6.2. This is shown for the smallest wavevector considered here, $k = 0.0099$ Å$^{-1}$, in Fig. 6.8 below.

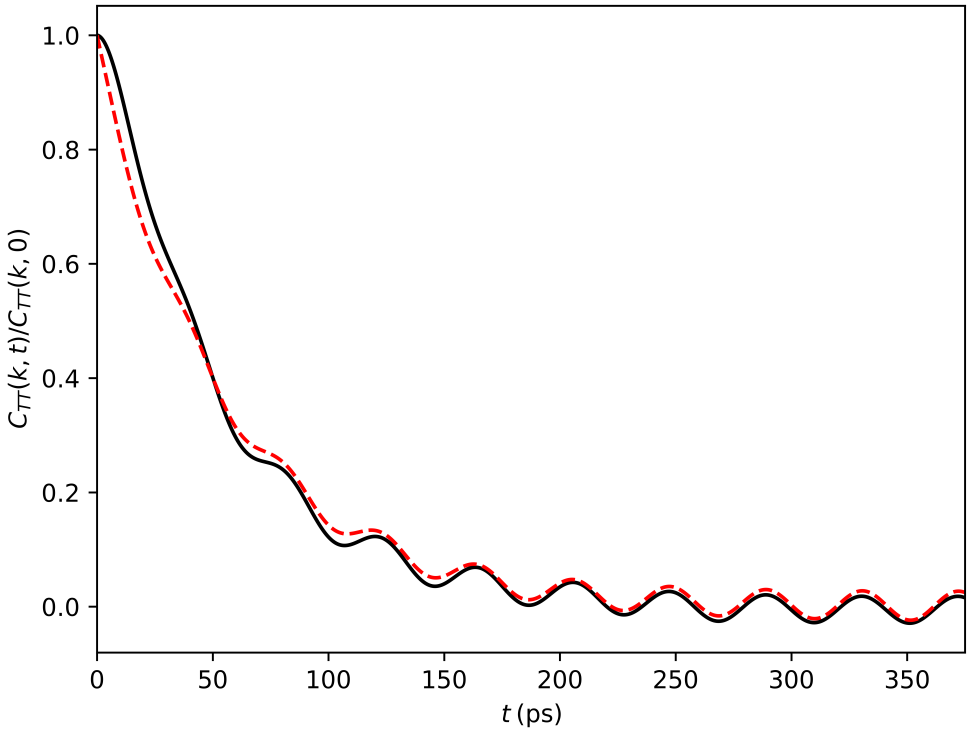



**Figure 6.8:** Values of $C_{TT}(k,t)$ normalised by its $t = 0$ value calculated for $k = 0.0099$ Å at the $T = 10$ K and $\rho_m = 1820$ kg m$^{-3}$ state point. Solid black lines show the values computed from our simulations using Eq. 6.41 and dashed red lines show the fit to the hydrodynamic model using the exact solution to the inverse Laplace transform given by Eq. 6.32. The values of $c_s$ and $\gamma$ calculated independently for this state point provided in Table 6.2 were used directly in the fitting procedure.

From inspection of Fig. 6.8 we see that the hydrodynamic model of Eq. 6.32 gives a good description of the decay of the local temperature fluctuations, with the fitted data able to capture the correct frequency of the oscillating component

and the correct proportion of the exponentially decaying thermal diffusion term. However the overall quality of the fit is slightly worse than those shown for the density fluctuations in Figs 6.3 and 6.4, especially at short times. We believe this is related to the fact that the approximate solution given by Eq. 6.33 does not satisfy the constraint that $dC_{TT}(k,t)/dt = 0$ at $t = 0$ even with the $f(k)$ correction term, and that this appears to carry over to the exact solution given by Eq. 6.32 as well. As a result, the fitting model cannot adequately capture the initial short time decay of $C_{TT}(k,t)$. In light of this, it appears some adaptations to the hydrodynamic theory may be necessary if one wishes to describe the short time decay of the temperature fluctuations accurately.

However, despite these short time inaccuracies in the fits to the $C_{TT}(k,t)$ we obtained from our simulations, the overall quality of the fit is still rather good and it seems likely that the values of $a(k)$ found from the fits will be at least a reasonable estimate of the $k$ dependent thermal diffusivity. To investigate this, we partitioned our data from the 300 independent simulations into 5 sets of 60 simulations each, and independently fit the $C_{TT}(k,t)$ obtained from each set to Eq. 6.32 for each of the 5 wavevectors considered. This gave us 5 independent estimates of the value of $a(k)$ and its uncertainty at each value of $k$, which we then converted into the corresponding $k$ dependent thermal conductivity $\kappa(k) = \rho_0 c_V a(k)$. We then plotted $1/\kappa(k)$ against $k$ and used a weighted linear least squares fit to extrapolate the thermal conductivity to the hydrodynamic limit at $k = 0$. The extrapolation used is shown in Fig. 6.9 below.

From the extrapolation to $k = 0$ we predict of value of the thermal conductivity in the hydrodynamic limit of $\kappa = 4.50 \pm 0.19\,\mathrm{W\,(m\,K)^{-1}}$, which is within 13% of the Green-Kubo thermal conductivity of $\kappa = 3.99 \pm 0.02\,\mathrm{W\,(m\,K)}$ found at this state point. This level of disagreement with the Green-Kubo thermal conductivities is comparable to the disagreement between the Green-Kubo thermal conductivities and the thermal conductivities found from the equilibrium density fluctuations given in Table 6.3. We note that even at the smallest value of $k$ considered here the value of $\kappa(k)$ predicted from the fits to Eq. 6.32 is still less than half of

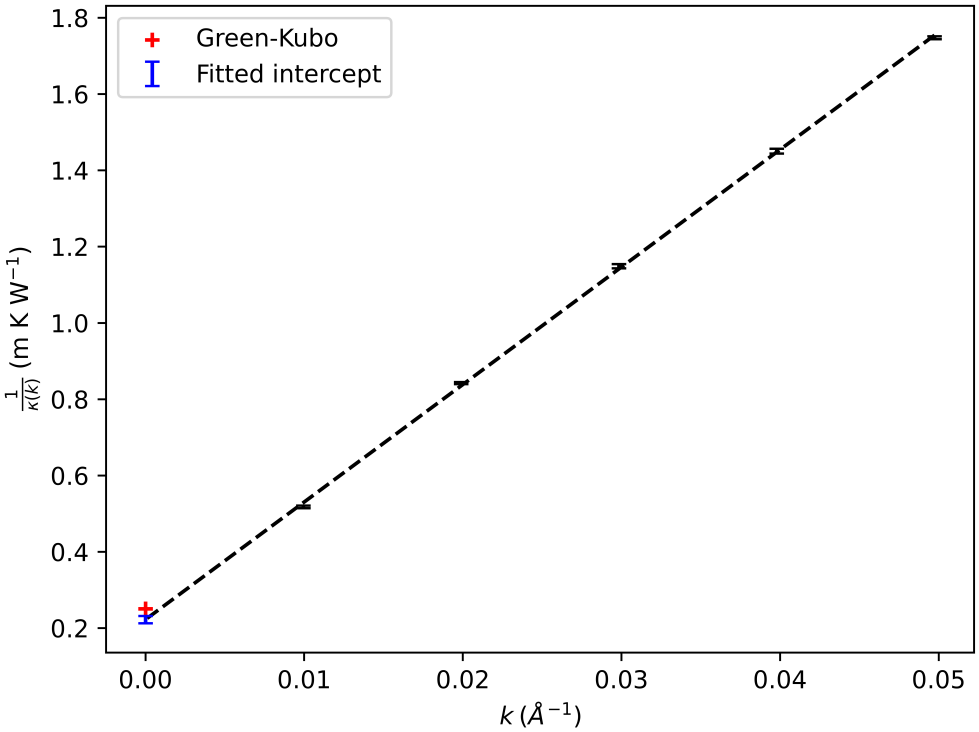



**Figure 6.9:** The extrapolation of $1/\kappa\,(k)$ against $k$ used to extract the value of the predicted thermal conductivity in the hydrodynamic limit. Black errorbars show the values of $1/\kappa\,(k)$ predicted from our fits to $C_{TT}\,(k,t)$ and the dashed black lines show the weighted linear least squares fit through these points. The predicted intercept and its estimated uncertainty from this fit is shown as a blue errorbar. Also shown as a red marker is the value of $1/\kappa$ which would be expected from the Green-Kubo thermal conductivity calculated for this state point from Table 6.1. The estimated uncertainty in the Green-Kubo value is less than the size of the marker.

the value of the extrapolated thermal conductivity at $k = 0$. Hence, it may be desirable to consider even smaller values of $k$ (larger system sizes) to obtain a better extrapolation of $1/\kappa\,(k)$. However, simulations at larger system sizes are not only more computationally expensive due to the increased number of atoms. $C_{TT}\,(k,t)$ will also decay more slowly at small values of $k$ and thus the correlation functions must be computed for a longer time period. Therefore, we leave any investigation of this matter to future work.

Despite the fact that we were not able to achieve agreement with the thermal conductivity predicted from the hydrodynamic theory of the equilibrium density

fluctuations and those from the Green-Kubo method to within the estimated uncertainties at most of the state points (perhaps due to insufficient convergence of the correlation functions and the independently calculated values of $c_s$ and $\gamma$, as well as potential issues with the extrapolation scheme used), the agreement is mostly acceptable over the temperature range from $T = 30\,\mathrm{K}$ to $T = 80\,\mathrm{K}$, with a maximum disagreement of less than 10%. Therefore, it seems reasonable to suggest that the generalisation of the calculation of the thermal diffusivity, $a$, from the decay of the equilibrium density fluctuations on the centroid potential of mean force would also give an acceptable estimate of the CMD thermal diffusivity. Then, as CMD is just classical molecular dynamics on an effective potential the arguments made in Chapter 4 should still hold and one should be able to calculate a CMD estimate of the thermal conductivity by scaling the CMD Green-Kubo thermal conductivity by the ratio of PIMD and CMD constant volume heat capacities. Although we found that the fraction of the thermal diffusion component was too small to reliably find an estimate of the thermal diffusivity at temperatures of $T = 20\,\mathrm{K}$ due to $\gamma$ approaching unity, it also seems likely from the preliminary results presented in this Section that one may instead find the thermal diffusivity from the hydrodynamic theory for the equilibrium local temperature fluctuations. Since both the relations for the equilibrium density fluctuations, Eq. 6.16, and for the equilibrium local temperature fluctuations, Eq. 6.32, are derived from the same underlying hydrodynamic theory, it would be expected that finding the thermal diffusivity from the equilibrium density fluctuations would be possible as $\gamma \to 1$ if one were able to converge the intermediate scattering function perfectly accurately, although this is unlikely to be possible to achieve in practice. Therefore it may be expected that scaling the CMD Green-Kubo thermal conductivities would also be a viable approach even as $\gamma \to 1$.

However, there are reasons to believe that if we were to do this the results would not be as useful as they were for liquid parahydrogen in Chapter 4. The classical Green-Kubo thermal conductivities found for Lennard-Jones argon by molecular dynamics agree well with experiment even down to 10 K.[63; 76] The Debye temperature of argon is 85 K[76; 188], and the estimated quantum heat

capacity found from the harmonic approximation is less than one fifth of the classical heat capacity at 10 K.[70] This would suggest that one would need to find a CMD Green-Kubo thermal conductivity which is approximately five times larger than the classical Green-Kubo thermal conductivity to give scaled CMD thermal conductivities which are in agreement with experiment, which we find unlikely.

In light of this observation and those made by Turney *et al.*[27] which were mentioned in Chapter 4, it seems that to scale the overall thermal conductivity in solids requires one to scale the contributions to the thermal conductivity from each phonon mode individually by the ratio of the heat capacities for that mode. Therefore, in order to calculate the quantum mechanical thermal conductivity of solids using CMD it is possible that one would require a method that allows one to calculate the contributions to the thermal conductivity from each phonon separately, which unfortunately neither of the methods developed in this Chapter from the hydrodynamic theory provide. This may be supported by the fact that the rapidly decaying component due to the high frequency phonons in the HFACF shown for the $T = 10\,\mathrm{K}$ and $\rho_m = 1820\,\mathrm{kg\,m^{-3}}$ state point in Fig. 6.1 contributes only $\approx 1\%$ to the integrated Green-Kubo thermal conductivity.[76] It is, however, these phonons whose heat capacities will be most affected by nuclear quantum effects.[27] The vast majority of the thermal conductivity is therefore contributed by low frequency phonons for which the heat capacity is approximately classical. Scaling the whole thermal conductivity by the overall ratio of the PIMD and the CMD constant volume heat capacities would therefore cause the contribution to the thermal conductivity from these low frequency phonons to be underestimated. Thus, while we have managed to show in this Chapter that it is possible to develop a hydrodynamic theory of the thermal conductivity of solids that agrees reasonably well with the Green-Kubo approach in the classical limit, extending this to include nuclear quantum effects using methods like CMD remains an unsolved and very challenging problem.

# 7
# Conclusions

Within this thesis we have explored whether nuclear quantum effects may be included in the prediction of the thermal conductivity using computer simulations through path integral based approaches like centroid molecular dynamics (CMD).[12–17] We began in Chapter 2 by discussing some of the background theory which underpins how path integrals may be used to calculate the quantum mechanical values of both static properties exactly using path integral molecular dynamics (PIMD) and dynamic properties approximately using CMD. We also introduced some of the details and techniques which are necessary to understand how these simulations are undertaken in practice.

The theory of the thermal conductivity of liquids from the perspective of linearised hydrodynamics was then discussed in Chapter 3, and this framework was used to present one way in which the most popular method to compute the thermal conductivity within purely classical simulations, the Green-Kubo relation, may be derived.[84] We then explored some of the reasons as to why the previously attempted generalisations of the classical Green-Kubo method to path integral based approaches which approximately incorporate nuclear quantum effects into the dynamics have been largely unsuccessful.[19; 24; 25; 116]

In an effort to find an alternative approach which would be more amenable to such a generalisation, we described how the thermal diffusivity (the ratio of the

thermal conductivity and the constant volume heat capacity) may be related to the equilibrium density fluctuations in the liquid phase using the hydrodynamic theory.[84; 85; 117] We used this approach in conjunction with CMD in Chapter 4 to calculate the quantum mechanical thermal diffusivity of liquid parahydrogen. By precomputation of the centroid potential of mean force at each state point we were able to perform our CMD calculations with the same computational effort as a purely classical molecular dynamics calculation.[21] We found that the CMD estimate of the thermal diffusivity actually agreed well with experiment, but that the CMD estimate of the constant volume heat capacity was rather poor. When the thermal diffusivity obtained from CMD was combined with the constant volume heat capacity calculated from PIMD, then we found a thermal conductivity in close agreement with the experimental measurements.

However, the simulations necessary to find the thermal diffusivity from the equilibrium density fluctuations were found to be very computationally expensive, much more so than they would have been using the CMD generalisation of the Green-Kubo method.[19] By using an argument that CMD is nothing more than classical molecular dynamics on an effective potential, we obtained a means of correcting the CMD Green-Kubo thermal conductivity using a simple scaling by the ratio of the CMD and the PIMD constant volume heat capacities - and found that this gave equivalent results to the equilibrium density fluctuation method but with greatly reduced computational cost. This allowed us to efficiently calculate the quantum mechanical thermal conductivity using CMD for liquid parahydrogen and also for liquid helium with greater accuracy than any previous theoretical investigation that we are aware of.[19; 24; 25] In particular, we were able to correctly reproduce the position of the experimentally observed peak in the temperature dependence of the thermal conductivity along the saturation line of liquid parahydrogen,[81] as well as the increase in the thermal conductivity with increasing temperature in liquid helium.[138]

The same idea of scaling the CMD Green-Kubo thermal conductivity was then applied to the more challenging application of liquid water in Chapter 5,

which we chose to model using the q-TIP4P/F potential.[32] We used approximate centroid potentials of mean force calculated by Dr. Joseph Lawrence using iterative Boltzmann inversion[130], which again allowed us to perform our CMD simulations with the same effort as classical molecular dynamics. Here we observed that the CMD Green-Kubo thermal conductivity was negligibly different from the Green-Kubo thermal conductivity that was calculated from a purely classical simulation at temperatures above 300 K, consistent with the observations made about other dynamical properties using this potential.[172] Therefore, it turns out in this case that one could simply scale the classical Green-Kubo thermal conductivities by the ratio of the PIMD to classical constant volume heat capacities and obtain equivalent results to scaling the CMD Green-Kubo thermal conductivities. Unfortunately, the final temperature dependence of the predicted scaled CMD thermal conductivities did not display as close an agreement with experiment as they did for the liquid parahydrogen or the liquid helium calculations presented in Chapter 4. Nevertheless, the scaled results seem to at least give a qualitative improvement compared to the unscaled classical and CMD Green-Kubo q-TIP4P/F thermal conductivities, and they were not any worse than previous classical investigations on simple water models.[153] Furthermore, it is unclear whether the simplistic model of the interactions in liquid water represented by the q-TIP4P/F potential is sufficient to capture the thermal conductivity accurately.

Finally, we explored whether the arguments developed for determining the thermal diffusivity of a system from the equilibrium density fluctuations in the liquid phase in Chapters 3 and 4 could also be used within the solid phase in the classical limit. We presented the necessary adaptations which are required to extend the hydrodynamic theory to anisotropic crystalline solids,[175] and then applied these to the case of Lennard-Jones argon. We were able to use the equilibrium density fluctuations in the solid phase to obtain thermal conductivities which were in reasonable agreement with those calculated from the Green-Kubo relation at temperatures above 30 K. Below this temperature, the equilibrium density fluctuations became dominated by an oscillating sound wave component and the

fraction of the signal which was most sensitive to the thermal diffusivity became very small due to the ratio of the constant volume and the constant pressure heat capacities, $\gamma$, approaching unity. This made it difficult to determine the thermal diffusivity from fitting the equilibrium density fluctuations to an appropriate functional form at low temperatures, and since $\gamma \approx 1$ in a typical solid,[182] this means that using the equilibrium density fluctuations to determine the thermal conductivity will not generally be a viable approach for solids.

In the case where $\gamma \to 1$ the thermal conductivity may instead be found from the equilibrium local temperature fluctuations, where the proportions of the thermal diffusion and the sound wave components are switched compared to the equilibrium density fluctuations. Fitting the equilibrium local temperature fluctuations to the functional form predicted by the hydrodynamic theory enabled us to obtain a thermal conductivity which was also in reasonable agreement with the Green-Kubo thermal conductivity at 10 K. However, neither of these methods for thermal conductivity determination based on the hydrodynamic theory competed with the efficiency of the Green-Kubo method due to an unfavourable dependence of the fitted thermal diffusivity on the size of the system used in the simulations.

We ended Chapter 6 by arguing that although the hydrodynamic model for the equilibrium local density and local temperature fluctuations can (with some adaptations) be applied to the solid phase, the scaling of the CMD thermal conductivity by the ratio of the quantum to CMD constant volume heat capacities probably cannot. Instead, one would likely need to correct for the inaccurate CMD estimate of the constant volume heat capacity using a more sophisticated procedure involving separately scaling the contribution to the thermal conductivity from each phonon by the ratio of the quantum to CMD heat capacities of that phonon.[27] Therefore, whilst we have developed an approach which seems to allow for accurate determination of the quantum mechanical thermal conductivity in simple liquids using CMD, extension of this to finding the quantum mechanical thermal conductivity of crystalline solids appears to be more difficult.

Nevertheless, we are hopeful that the progress made within this thesis for the liquid phase will provide a useful foundation to build upon for extensions towards more complex applications in the future. In particular, it will be interesting to see how well CMD performs when applied to the thermal conductivity of amorphous solids and also whether it is ultimately possible to find a way to successfully apply CMD in some form to the quantum mechanical thermal conductivity of crystalline solids.

# Bibliography


[1] E. S. Toberer, L. L. Baranowski, and C. Dames, *Annual Review of Materials Research* **42**, 179 (2012).

[2] X. Gu, Z. Fan, and H. Bao, *Journal of Applied Physics* **130**, 210902 (2021).

[3] D. G. Cahill, W. K. Ford, K. E. Goodson, G. D. Mahan, A. Majumdar, H. J. Maris, R. Merlin, and S. R. Phillpot, *Journal of Applied Physics* **93**, 793 (2003).

[4] D. G. Cahill, P. V. Braun, G. Chen, D. R. Clarke, S. Fan, K. E. Goodson, P. Keblinski, W. P. King, G. D. Mahan, A. Majumdar, et al., *Applied Physics Reviews* **1**, 011305 (2014).

[5] F. Müller-Plathe, *The Journal of Chemical Physics* **106**, 6082 (1997).

[6] D. Evans and G. Morriss, *Statistical Mechanics of Nonequilibrium Liquids*, DOAB Directory of Open Access Books, ANU E Press, 2007.

[7] C. J. Glassbrenner and G. A. Slack, *Physical Review* **134**, A1058 (1964).

[8] D. K. Christen and G. L. Pollack, *Physical Review B* **12**, 3380 (1975).

[9] S. G. Volz and G. Chen, *Physical Review B* **61**, 2651 (2000).

[10] B. Le Neindre, P. Bury, R. Tufeu, and B. Vodar, *Journal of Chemical and Engineering Data* **21**, 265 (1976).

[11] V. C. Chamorro, C. Tempra, and P. Jungwirth, *The Journal of Physical Chemistry B* **125**, 4514 (2021).

[12] J. Cao and G. A. Voth, *The Journal of Chemical Physics* **100**, 5093 (1994).

[13] J. Cao and G. A. Voth, *The Journal of Chemical Physics* **100**, 5106 (1994).

[14] J. Cao and G. A. Voth, *The Journal of Chemical Physics* **101**, 6157 (1994).

[15] J. Cao and G. A. Voth, *The Journal of Chemical Physics* **101**, 6168 (1994).

[16] J. Cao and G. A. Voth, *The Journal of Chemical Physics* **101**, 6184 (1994).

[17] T. D. Hone, P. J. Rossky, and G. A. Voth, *The Journal of Chemical Physics* **124**, 154103 (2006).

[18] I. R. Craig and D. E. Manolopoulos, *The Journal of Chemical Physics* **121**, 3368 (2004).

[19] Y. Yonetani and K. Kinugawa, *The Journal of Chemical Physics* **120**, 10624 (2004).

[20] T. D. Hone and G. A. Voth, *The Journal of Chemical Physics* **121**, 6412 (2004).

[21] T. D. Hone, S. Izvekov, and G. A. Voth, *The Journal of Chemical Physics* **122**, 054105 (2005).

[22] T. F. Miller and D. E. Manolopoulos, *The Journal of Chemical Physics* **122**, 184503 (2005).

[23] T. F. Miller and D. E. Manolopoulos, *The Journal of Chemical Physics* **123**, 154504 (2005).

[24] H. Imaoka and K. Kinugawa, *Chemical Physics Letters* **671**, 174 (2017).

[25] J. Liu, B. J. Alder, and W. H. Miller, *The Journal of Chemical Physics* **135**, 114105 (2011).

[26] J. Turney, E. Landry, A. McGaughey, and C. Amon, *Physical Review B* **79**, 064301 (2009).

[27] J. Turney, A. McGaughey, and C. Amon, *Physical Review B* **79**, 224305 (2009).

[28] R. Anderson, The case for cryoelectronics, in *Proceedings of First International Caracas Conference on Devices, Circuits and Systems*, pp. 1–5, IEEE, 1995.

[29] M. P. Allen and D. J. Tildesley, *Computer Simulation of Liquids*, Clarendon Press, USA, 1989.

[30] D. Frenkel and B. Smit, *Understanding Molecular Simulation: From Algorithms to Applications*, Computational science, Elsevier Science, 2001.

[31] S. Miura, S. Okazaki, and K. Kinugawa, *The Journal of Chemical Physics* **110**, 4523 (1999).

[32] S. Habershon, T. E. Markland, and D. E. Manolopoulos, *The Journal of Chemical Physics* **131**, 024501 (2009).

[33] D. M. Wilkins, D. E. Manolopoulos, S. Pipolo, D. Laage, and J. T. Hynes, *The Journal of Physical Chemistry Letters* **8**, 2602 (2017).

[34] R. Feynman, A. Hibbs, and D. Styer, *Quantum Mechanics and Path Integrals*, Dover Books on Physics, Dover Publications, 2010.

[35] M. Parrinello and A. Rahman, *The Journal of Chemical Physics* **80**, 860 (1984).

[36] H. F. Trotter, *Proceedings of the American Mathematical Society* **10**, 545 (1959).

[37] M. Suzuki, *Journal of Mathematical Physics* **26**, 601 (1985).

[38] R. W. Hall and B. J. Berne, *The Journal of Chemical Physics* **81**, 3641 (1984).

[39] D. Chandler and P. G. Wolynes, *The Journal of Chemical Physics* **74**, 4078 (1981).

[40] M. Ceriotti, M. Parrinello, T. E. Markland, and D. E. Manolopoulos, *The Journal of Chemical Physics* **133**, 124104 (2010).

[41] R. Korol, N. Bou-Rabee, and T. F. Miller, *The Journal of Chemical Physics* **151**, 124103 (2019).

[42] R. Korol, J. L. Rosa-Raíces, N. Bou-Rabee, and T. F. Miller, *The Journal of Chemical Physics* **152**, 104102 (2020).

[43] M. F. Herman, E. J. Bruskin, and B. J. Berne, *The Journal of Chemical Physics* **76**, 5150 (1982).

[44] T. M. Yamamoto, *The Journal of Chemical Physics* **123**, 104101 (2005).

[45] M. Tuckerman, B. J. Berne, and G. J. Martyna, *The Journal of Chemical Physics* **97**, 1990 (1992).

[46] M. E. Tuckerman, B. J. Berne, G. J. Martyna, and M. L. Klein, *The Journal of Chemical Physics* **99**, 2796 (1993).

[47] T. E. Markland and D. E. Manolopoulos, *Chemical Physics Letters* **464**, 256 (2008).

[48] S. A. Chin, *Physics Letters A* **226**, 344 (1997).

[49] M. Takahashi and M. Imada, *Journal of the Physical Society of Japan* **53**, 3765 (1984).

[50] V. Kapil, J. Behler, and M. Ceriotti, *The Journal of Chemical Physics* **145**, 234103 (2016).

[51] R. P. Feynman and H. Kleinert, *Physical Review A* **34**, 5080 (1986).

[52] R. Kubo, *Journal of the Physical Society of Japan* **12**, 570 (1957).

[53] B. J. Braams and D. E. Manolopoulos, *The Journal of Chemical Physics* **125**, 124105 (2006).

[54] M. Rossi, M. Ceriotti, and D. E. Manolopoulos, *The Journal of Chemical Physics* **140**, 234116 (2014).

[55] A. Witt, S. D. Ivanov, M. Shiga, H. Forbert, and D. Marx, *The Journal of Chemical Physics* **130**, 194510 (2009).

[56] T. J. H. Hele, M. J. Willatt, A. Muolo, and S. C. Althorpe, *The Journal of Chemical Physics* **142**, 191101 (2015).

[57] I. R. Craig and D. E. Manolopoulos, *The Journal of Chemical Physics* **123**, 034102 (2005).

[58] E. Geva, Q. Shi, and G. A. Voth, *The Journal of Chemical Physics* **115**, 9209 (2001).

[59] S. Habershon, G. S. Fanourgakis, and D. E. Manolopoulos, *The Journal of Chemical Physics* **129**, 074501 (2008).

[60] S. Habershon, B. J. Braams, and D. E. Manolopoulos, *The Journal of Chemical Physics* **127**, 174108 (2007).

[61] R. E. Peierls, *Quantum Theory of Solids*, Oxford University Press, 2001.

[62] P. Carruthers, *Reviews of Modern Physics* **33**, 92 (1961).

[63] D. K. Christen and G. L. Pollack, *Physical Review B* **12**, 3380 (1975).

[64] P. Debye, *Annalen der Physik* **344**, 789 (1912).

[65] D. He, S. Buyukdagli, and B. Hu, *Physical Review E* **78**, 061103 (2008).

[66] J. Callaway, *Physical Review* **113**, 1046 (1959).

[67] D. A. Broido, A. Ward, and N. Mingo, *Physical Review B* **72**, 014308 (2005).

[68] J. Li, L. Porter, and S. Yip, *Journal of Nuclear Materials* **255**, 139 (1998).

[69] Y. Lee, S. Lee, and G. S. Hwang, *Physical Review B* **83**, 125202 (2011).

[70] O. N. Bedoya-Martínez, J.-L. Barrat, and D. Rodney, *Physical Review B* **89**, 014303 (2014).

[71] M. Mertig, G. Pompe, and E. Hegenbarth, *Solid State Communications* **49**, 369 (1984).

[72] J. Che, T. Çağin, W. Deng, and W. A. Goddard III, *The Journal of Chemical Physics* **113**, 6888 (2000).

[73] Y. H. Lee, R. Biswas, C. M. Soukoulis, C. Wang, C. Chan, and K. Ho, *Physical Review B* **43**, 6573 (1991).

[74] P. K. Schelling, S. R. Phillpot, and P. Keblinski, *Physical Review B* **65**, 144306 (2002).

[75] K. V. Tretiakov and S. Scandolo, *The Journal of Chemical Physics* **120**, 3765 (2004).

[76] A. McGaughey and M. Kaviany, *International Journal of Heat and Mass Transfer* **47**, 1783 (2004).

[77] Y. He, I. Savić, D. Donadio, and G. Galli, *Phys. Chem. Chem. Phys.* **14**, 16209 (2012).

[78] Y.-G. Yoon, R. Car, D. J. Srolovitz, and S. Scandolo, *Physical Review B* **70**, 012302 (2004).

[79] R. Vogelsang, C. Hoheisel, and G. Ciccotti, *The Journal of Chemical Physics* **86**, 6371 (1987).

[80] B. C. Sakiadis and J. Coates, *AIChE Journal* **1**, 275 (1955).

[81] H. M. Roder and D. E. Diller, *The Journal of Chemical Physics* **52**, 5928 (1970).

[82] M. L. Ramires, C. A. Nieto de Castro, Y. Nagasaka, A. Nagashima, M. J. Assael, and W. A. Wakeham, *Journal of Physical and Chemical Reference Data* **24**, 1377 (1995).

[83] R. Kubo, M. Yokota, and S. Nakajima, *Journal of the Physical Society of Japan* **12**, 1203 (1957).

[84] J. Hansen and I. McDonald, *Theory of Simple Liquids: with Applications to Soft Matter*, Elsevier Science, 2013.

[85] B. Berne and R. Pecora, *Dynamic Light Scattering: With Applications to Chemistry, Biology, and Physics*, Dover Books on Physics Series, Dover Publications, 2000.

[86] J. Boon and S. Yip, *Molecular Hydrodynamics*, Dover Books on Physics, Dover Publications, 1991.

[87] L. P. Kadanoff and P. C. Martin, *Annals of Physics* **24**, 419 (1963).

[88] S. Baroni, R. Bertossa, L. Ercole, F. Grasselli, and A. Marcolongo, *Handbook of Materials Modeling: Applications: Current and Emerging Materials* , 809 (2020).

[89] L. Landau and E. Lifshitz, *Fluid Mechanics: Landau and Lifshitz: Course of Theoretical Physics, Volume 6*, Number v. 6, Elsevier Science, 2013.

[90] Z. Guo, A. Verma, X. Wu, F. Sun, A. Hickman, T. Masui, A. Kuramata, M. Higashiwaki, D. Jena, and T. Luo, *Applied Physics Letters* **106**, 111909 (2015).

[91] G. A. Slack, *Physical Review* **127**, 694 (1962).

[92] A. Fiorentino and S. Baroni, *Physical Review B* **107**, 054311 (2023).

[93] J. Irving and J. G. Kirkwood, *The Journal of Chemical Physics* **18**, 817 (1950).

[94] R. J. Hardy, *The Journal of Chemical Physics* **76**, 622 (1982).

[95] B. Todd, P. J. Daivis, and D. J. Evans, *Physical Review E* **51**, 4362 (1995).

[96] P. Boone, H. Babaei, and C. E. Wilmer, *Journal of Chemical Theory and Computation* **15**, 5579 (2019).

[97] A. Kinaci, J. B. Haskins, and T. Çağin, *The Journal of Chemical Physics* **137**, 014106 (2012).

[98] P. C. Howell, *The Journal of Chemical Physics* **137**, 224111 (2012).

[99] L. Ercole, A. Marcolongo, P. Umari, and S. Baroni, *Journal of Low Temperature Physics* **185**, 79 (2016).

[100] A. J. C. Ladd, B. Moran, and W. G. Hoover, *Physical Review B* **34**, 5058 (1986).

[101] A. Marcolongo, P. Umari, and S. Baroni, *Nature Physics* **12**, 80 (2016).

[102] M. Pulighеddu, F. Gygi, and G. Galli, *Physical Review Materials* **1**, 060802 (2017).

[103] E. Lampin, P. Palla, P.-A. Francioso, and F. Cleri, *Journal of Applied Physics* **114**, 033525 (2013).

[104] D. P. Sellan, E. S. Landry, J. Turney, A. J. McGaughey, and C. H. Amon, *Physical Review B* **81**, 214305 (2010).

[105] C. Carbogno, R. Ramprasad, and M. Scheffler, *Physical Review Letters* **118**, 175901 (2017).

[106] J. Kang and L.-W. Wang, *Physical Review B* **96**, 020302 (2017).

[107] B. Cheng and D. Frenkel, *Physical Review Letters* **125**, 130602 (2020).

[108] R. Li, Z. Liu, A. Rohskopf, K. Gordiz, A. Henry, E. Lee, and T. Luo, *Applied Physics Letters* **117**, 152102 (2020).

[109] L. d. S. Oliveira and P. A. Greaney, *Physical Review E* **95**, 023308 (2017).

[110] I. F. Silvera and V. V. Goldman, *The Journal of Chemical Physics* **69**, 4209 (1978).

[111] H. Wang, X. Sun, and W. H. Miller, *The Journal of Chemical Physics* **108**, 9726 (1998).

[112] Q. Shi and E. Geva, *The Journal of Chemical Physics* **118**, 8173 (2003).

[113] B. J. Sutherland, W. H. Moore, and D. E. Manolopoulos, *The Journal of Chemical Physics* **154**, 174104 (2021).

[114] A. I. Krivchikov, O. A. Korolyuk, V. V. Sumarokov, J. Mucha, P. Stachowiak, and A. Jeżowski, *Low Temperature Physics* **29**, 527 (2003).

[115] S. Habershon and D. E. Manolopoulos, *The Journal of Chemical Physics* **131**, 244518 (2009).

[116] R. Luo and K. Yu, *The Journal of Chemical Physics* **153**, 194105 (2020).

[117] R. D. Mountain, *Reviews of Modern Physics* **38**, 205 (1966).

[118] M. Schoen, R. Vogelsang, and C. Hoheisel, *Molecular Physics* **57**, 445 (1986).

[119] D. Bertolini and A. Tani, *Physical Review E* **51**, 1091 (1995).

[120] I. De Schepper, E. Cohen, C. Bruin, J. van Rijs, W. Montfrooij, and L. De Graaf, *Physical Review A* **38**, 271 (1988).

[121] I. R. Craig and D. E. Manolopoulos, *Chemical Physics* **322**, 236 (2006), Real-time dynamics in complex quantum systems.

[122] R. D. Goodwin, *J. Res. Natl. Bur. Stand.(US) C* **65**, 231 (1961).

[123] H. M. Roder, *Survey of the properties of the hydrogen isotopes below their critical temperatures*, volume 641, US Government Printing Office, 1973.

[124] G. Buntkowsky, F. Theiss, J. Lins, Y. A. Miloslavina, L. Wienands, A. Kiryutin, and A. Yurkovskaya, *RSC Advances* **12**, 12477 (2022).

[125] G. Bussi and M. Parrinello, *Computer Physics Communications* **179**, 26 (2008).

[126] C. Li and G. A. Voth, *Journal of Chemical Theory and Computation* **18**, 599 (2022).

[127] T. D. Loose, P. G. Sahrmann, and G. A. Voth, *arXiv preprint arXiv:2208.07973* (2022).

[128] F. Musil, I. Zaporozhets, F. Noé, C. Clementi, and V. Kapil, *arXiv preprint arXiv:2208.06205* (2022).

[129] T. Fletcher, A. Zhu, J. E. Lawrence, and D. E. Manolopoulos, *The Journal of Chemical Physics* **155**, 231101 (2021).

[130] A. Soper, *Chemical Physics* **202**, 295 (1996).

[131] D. Reith, M. Pütz, and F. Müller-Plathe, *Journal of Computational Chemistry* **24**, 1624 (2003).

[132] D. Borgis, R. Assaraf, B. Rotenberg, and R. Vuilleumier, *Molecular Physics* **111**, 3486 (2013).

[133] B. Rotenberg, *The Journal of Chemical Physics* **153**, 150902 (2020).

[134] B. N. Esel'son, Y. P. Blagoi, V. Grigor'ev, V. Manzhelii, and S. Mikhailenko, Properties of Liquid and Solid Hydrogen (Svoistva Zhidkogo i Tverdogo Vodoroda)., Technical report, NATIONAL STANDARD REFERENCE DATA SYSTEM, 1971.

[135] B. J. Braams, T. F. Miller, and D. E. Manolopoulos, *Chemical Physics Letters* **418**, 179 (2006).

[136] D. Scharf, G. J. Martyna, and M. L. Klein, *Fizika Nizkikh Temperatur* **19**, 516 (1993).

[137] V. Kapil, J. Wieme, S. Vandenbrande, A. Lamaire, V. Van Speybroeck, and M. Ceriotti, *Journal of Chemical Theory and Computation* **15**, 3237 (2019).

[138] R. J. Donnelly and C. F. Barenghi, *Journal of Physical and Chemical Reference Data* **27**, 1217 (1998).

[139] R. A. Aziz, M. Slaman, A. Koide, A. Allnatt, and W. J. Meath, *Molecular Physics* **77**, 321 (1992).

[140] E. W. Lemmon, I. H. Bell, M. L. Huber, and M. O. McLinden, "Thermophysical Properties of Fluid Systems" in NIST Chemistry WebBook, (retrieved December 14, 2022).

[141] G. R. Medders, V. Babin, and F. Paesani, *Journal of Chemical Theory and Computation* **10**, 2906 (2014).

[142] P. Ren and J. W. Ponder, *The Journal of Physical Chemistry B* **107**, 5933 (2003).

[143] H. Berendsen, J. Grigera, and T. Straatsma, *Journal of Physical Chemistry* **91**, 6269 (1987).

[144] W. L. Jorgensen, J. Chandrasekhar, J. D. Madura, R. W. Impey, and M. L. Klein, *The Journal of Chemical Physics* **79**, 926 (1983).

[145] J. L. Abascal and C. Vega, *The Journal of Chemical Physics* **123**, 234505 (2005).

[146] C. Vega and J. L. Abascal, *Phys. Chem. Chem. Phys.* **13**, 19663 (2011).

[147] G. A. Cisneros, K. T. Wikfeldt, L. Ojamäe, J. Lu, Y. Xu, H. Torabifard, A. P. Bartók, G. Csányi, V. Molinero, and F. Paesani, *Chemical Reviews* **116**, 7501 (2016).

[148] M. A. González and J. L. Abascal, *The Journal of Chemical Physics* **135**, 224516 (2011).

[149] D. M. Ferguson, *Journal of Computational Chemistry* **16**, 501 (1995).

[150] L. Hernández de la Peña and P. Kusalik, *The Journal of Chemical Physics* **121**, 5992 (2004).

[151] F. Paesani, W. Zhang, D. A. Case, T. E. Cheatham III, and G. A. Voth, *The Journal of Chemical Physics* **125**, 184507 (2006).

[152] C. McBride, C. Vega, E. G. Noya, R. Ramírez, and L. M. Sesé, *The Journal of Chemical Physics* **131**, 024506 (2009).

[153] S. H. Lee, *Molecular Physics* **112**, 2155 (2014).

[154] N. Karasawa and W. A. Goddard III, *The Journal of Physical Chemistry* **93**, 7320 (1989).

[155] J. Beckers, C. Lowe, and S. De Leeuw, *Molecular Simulation* **20**, 369 (1998).

[156] R. Henderson, *Physics Letters A* **49**, 197 (1974).

[157] E. R. Chan, A. Striolo, C. McCabe, P. T. Cummings, and S. C. Glotzer, *The Journal of Chemical Physics* **127**, 114102 (2007).

[158] R. Potestio, *JUnQ* **3**, 13 (2013).

[159] P. Ganguly and N. F. van der Vegt, *Journal of Chemical Theory and Computation* **9**, 5247 (2013).

[160] B. Bayramoglu and R. Faller, *Macromolecules* **45**, 9205 (2012).

[161] V. Agrawal, G. Arya, and J. Oswald, *Macromolecules* **47**, 3378 (2014).

[162] A. Villa, N. F. van der Vegt, and C. Peter, *Physical Chemistry Chemical Physics* **11**, 2068 (2009).

[163] Y. Wu, H. L. Tepper, and G. A. Voth, *The Journal of Chemical Physics* **124**, 024503 (2006).

[164] S. Jang, S. Jang, and G. A. Voth, *The Journal of Chemical Physics* **115**, 7832 (2001).

[165] F. Römer, A. Lervik, and F. Bresme, *The Journal of Chemical Physics* **137**, 074503 (2012).

[166] T. W. Sirk, S. Moore, and E. F. Brown, *The Journal of Chemical Physics* **138**, 064505 (2013).

[167] Y. Mao and Y. Zhang, *Chemical Physics Letters* **542**, 37 (2012).

[168] S. H. Lee and J. Kim, *Molecular Physics* **117**, 1926 (2019).

[169] G. Marechal and J.-P. Ryckaert, *Chemical Physics Letters* **101**, 548 (1983).

[170] P. J. Daivis and D. J. Evans, *Molecular Physics* **81**, 1289 (1994).

[171] J. Petravic, *The Journal of Chemical Physics* **123**, 174503 (2005).

[172] A. Eltareb, G. E. Lopez, and N. Giovambattista, *Physical Chemistry Chemical Physics* **23**, 6914 (2021).

[173] L. Landau, E. Lifšic, E. Lifshitz, A. Kosevich, J. Sykes, L. Pitaevskii, and W. Reid, *Theory of Elasticity: Volume 7*, Course of theoretical physics, Elsevier Science, 1986.

[174] P. C. Martin, O. Parodi, and P. S. Pershan, *Physical Review A* **6**, 2401 (1972).

[175] P. D. Fleming III and C. Cohen, *Physical Review B* **13**, 500 (1976).

[176] M. Sprik, R. W. Impey, and M. L. Klein, *Physical Review B* **29**, 4368 (1984).

[177] G. Clavier, N. Desbiens, E. Bourasseau, V. Lachet, N. Brusselle-Dupend, and B. Rousseau, *Molecular Simulation* **43**, 1413 (2017).

[178] H. Zaoui, P. L. Palla, F. Cleri, and E. Lampin, *Physical Review B* **94**, 054304 (2016).

[179] O. Peterson, D. Batchelder, and R. Simmons, *Physical Review* **150**, 703 (1966).

[180] J. Chen, G. Zhang, and B. Li, *Physics Letters A* **374**, 2392 (2010).

[181] H. Wang and W. Chu, *Journal of Alloys and Compounds* **485**, 488 (2009).

[182] E. Gopal, *Specific Heats at Low Temperatures*, The International Cryogenics Monograph Series, Springer US, 2012.

[183] G. Keeler and D. Batchelder, *Journal of Physics C: Solid State Physics* **3**, 510 (1970).

[184] A. Singh and E. B. Tadmor, *Journal of Computational Physics* **299**, 667 (2015).

[185] P. Schofield, *Proceedings of the Physical Society (1958-1967)* **88**, 149 (1966).

[186] P. Schofield, Physics of Simple Liquids, 1968.

[187] J. Copley and S. Lovesey, *Reports on Progress in Physics* **38**, 461 (1975).

[188] N. W. Ashcroft and N. D. Mermin, *Solid state physics*, Cengage Learning, 2022.